

**UNI-AXIAL STRETCHING GENERATED
POLY(E-CAPROLACTONE) FILM FOR HUMAN
VASCULAR TISSUE ENGINEERING APPLICATION**

ZUYONG WANG

**NATIONAL UNIVERSITY OF
SINGAPORE**

2013

**UNI-AXIAL STRETCHING GENERATED
POLY(E-CAPROLACTONE) FILM FOR HUMAN
VASCULAR TISSUE ENGINEERING APPLICATION**

ZUYONG WANG

(M.Sc.), XMU

**A THESIS SUBMITTED
FOR THE DEGREE OF DOCTOR OF PHILOSOPHY
DEPARTMENT OF MECHANICAL ENGINEERING
NATIONAL UNIVERSITY OF SINGAPORE**

2013

Declaration

I hereby declare that this thesis is my original work and it has been written by me in its entirety. I have duly acknowledged all the sources of information which have been used in the thesis.

This thesis has also not been submitted for any degree in any university previously.



Wang Zuyong

7 August 2013

Acknowledgements

I am especially grateful to Assistant Professor Thian Eng San, Professor Teoh Swee Hin, Associate Professor Hong Minghui and Associate Professor Jerry Chan for their scientific guidance, generous support and complete trust during my PhD training and this thesis writing. Of many times, they have each dedicated to sit down with me to guide and advise me in scientific thinking, planning, and how to learn, write and make presentations for academic research. They have led me into the universe of science and inspired me with enthusiasm to think about and explore the unknown fields of science. I am greatly indebted to them for many opportunities that they have laid out for encouraging me to be independent and beyond the limits.

It is also very fortunate and privileged that I can work with so many colleagues and friends from the BIOMAT Group, the Laser Technology Group and the Experimental Fetal Medicine Group, especially Erin Teo, Mark Chong, Zhiyong Zhang, Feng Wen, Kay Siang Tiaw, Min Tang, Ming Tseng, Yuchun Liu, Qinyuan Zhang, Poon Nian Lim, Lei Chang, Jing Lim, Zaichun Chen, Dedy Sandikin, Nuryanti Johana, Zhuo Wang, Jason Feng, Yi Min Tan, Lan Yin Lee, Rueyna Lam, Xu Le, Zheren Du, Jing Yang, Yiguo Chen, Tsungsheng Kao, Fangfang Luo, Yiping Fan, Lay Geok Tan, Citra Mattarn, Yeo Su Li, Caolemeng Bao, Xiaohui Yang, Chin Wen and Niraja Mohan Dighe for their great help and stimulation in such a delightful working

Acknowledgements

environment! I am also grateful to Guorui Jing, Dan Kai, Peiling Zhu, Tao Li, Wei'an Zhang and Ying Su for their friendship and kind help in experiments.

I would like to thank Ms Sharen Teo (Mechanical Engineering), Ms Ginny Chen (Obstetrics and Gynecology) and Ms Lin Koh Hwee (Electrical and Computer Engineering) for their kind help in the administrative stuffs. I would also like to thank Mr Thomas Tan, Mr Hong Wei Ng and Mr Khalim Abdul for their kind assistance in materials lab these years.

Last but not least, I would like to owe my deepest gratitude to my family, in particular my parents for their consistent care and love. Their moral edification, encouragement and unwavering support have always kept me to strive for the excellence.

The work of this thesis was carried out in the BIOMAT Lab, the Experimental Fetal Medicine Lab and the Laser Microprocessing Lab, with funding support from the Ministry of Education, Singapore. I would also like to thank National University of Singapore for awarding me a Research Scholarship.

Table of Content

Declaration	i
Acknowledgements	ii
Table of Content	iv
Abstract	viii
List of Acronyms.....	ix
List of Tables.....	xii
List of Figures	xiv
Chapter 1 Introduction	1
1.1 Background.....	1
1.2 Objectives	5
1.3 Scope	6
1.4 Novelty	8
Chapter 2 Literature Review.....	9
2.1 Human Vascular System and Regeneration	9
2.1.1 Blood Vessel Structure	9
2.1.2 Vascular Grafts.....	11
2.1.3 BM Architecture and Function	15
2.1.4 Vascular Neotissue Regeneration.....	18
2.2 Stem Cells for Engineered BM.....	19
2.2.1 Stem Cells.....	19
2.2.2 Stem Cells for VTE Applications.....	21
2.2.3 MSCs Differentiation into SMCs	23
2.3 Geometric Cues for Engineered BM	27
2.3.1 Fabrication of Anisotropic Geometries	28
2.3.2 Vascular Cell Responses to Geometric Cues	35
2.3.2.1 Cellular Alignment and Elongation.....	35
2.3.2.2 Cellular Migration	38
2.3.2.3 Cellular Adhesion and Proliferation.....	38
2.3.2.4 Cellular Differentiation	39
2.3.3 Current Applications of Geometric Cues for TEVG.....	42
2.3.4 Stability and Degradation Behaviour of Geometric Cues	42
2.3.4.1 Factors Influencing Degradation	43
2.3.4.2 Degradation and TEVG Properties.....	47

2.4 Porous Patterns for Engineered BM	51
2.4.1 Techniques for Pore Incorporation	51
2.4.2 Vascular Cell Responses to Porous Patterns	58
2.4.3 Porous Patterns and Current Vascular Scaffold Design	59
Chapter 3 Uniaxial Stretching for Generation of Three-Dimensional Anisotropic Geometries on Poly(ϵ-caprolactone) Films	61
3.1 Introduction	61
3.2 Materials and Methods	63
3.2.1 Experimental Design	63
3.2.2 Materials	63
3.2.3 Generation of PCL 3D Anisotropic Geometries	64
3.2.4 Field Emission Scanning Electron Microscopy (FESEM)	65
3.2.5 Atomic Force Microscopy (AFM)	65
3.2.6 Water Contact Angle (WCA)	66
3.2.7 Differential Scanning Calorimeter (DSC)	66
3.2.8 Polarized Light Microscopy (PLM)	66
3.2.9 Cellular Isolation and <i>In Vitro</i> Culture	67
3.2.10 Confocal Laser Scanning Microscopy (CLSM)	67
3.2.11 Cellular Alignment and Elongation Analysis	68
3.2.12 Cellular Proliferation Assay	69
3.2.13 Data Analysis	69
3.3 Results	69
3.3.1 Biomimetic 3D Self-Assembling PCL Anisotropic Geometries	69
3.3.2 Effects of Stretching Temperature (T_s) and Draw Ratio (DR) on Ridge-Length and Inter-Ridge-Distance	72
3.3.3 Surface Modification	74
3.3.4 Aligned Cellular Growth	76
3.3.5 Dynamic and Long-Term Cellular Alignment	78
3.3.6 Cytotoxicity and Cellular Proliferation	81
3.4 Discussion	82
3.5 Summary	89
Chapter 4 Regulated Mesenchymal Stem Cell Behaviour via Anisotropic Geometries for Vascular Tissue Engineering	91
4.1 Introduction	91
4.2 Materials and Methods	93
4.2.1 Experimental Design	93
4.2.2 Materials	94
4.2.3 Sample Preparation	95
4.2.4 Field Emission Scanning Electron Microscopy (FESEM)	95
4.2.5 Atomic Force Microscopy (AFM)	95
4.2.6 Tensile Testing	95
4.2.7 Cell Isolation and Culture	96
4.2.8 Confocal Laser Scanning Microscopy (CLSM)	96
4.2.9 Cell Alignment and Elongation	96
4.2.10 Cell Nucleus Alignment and Elongation	97

Table of Content

4.2.11 Real-time Quantitative Reverse Transcription Polymerase Chain Reaction (qRT-PCR)	97
4.2.12 Immunocytochemistry Assays.....	98
4.2.13 Flow Cytometry.....	99
4.2.14 Data Analysis.....	100
4.3 Results	100
4.3.1 Stem Cell Immunophenotype of Isolated Human MSCs	100
4.3.2 Anisotropic 3D Ridge/Groove Arrays on PCL Films	101
4.3.3 Film Mechanical Properties.....	103
4.3.4 MSCs Alignment and Elongation.....	106
4.3.5 Reorganised MSCs Cytoskeleton and Nucleus Deformation.....	108
4.3.6 MSCs Differentiation	109
4.3.7 3D Vascular Scaffold Construction.....	114
4.4 Discussion.....	116
4.5 Summary.....	121
Chapter 5 Degradation Behaviour of Anisotropic Geometries and Mesenchymal Stem Cell Responses	123
5.1 Introduction	123
5.2 Materials and Methods	125
5.2.1 Experimental Design	125
5.2.2 Materials	126
5.2.3 Sample Preparation.....	126
5.2.4 Hydrolysis.....	126
5.2.5 Field Emission Scanning Electron Microscopy (FESEM).....	126
5.2.6 Water Contact Angle (WCA)	126
5.2.7 Weight Loss.....	127
5.2.8 Tensile Testing	127
5.2.9 Cell Isolation and Culture.....	127
5.2.10 Confocal Laser Scanning Microscopy (CLSM)	128
5.2.11 Cell Nucleus Alignment and Elongation.....	128
5.2.12 Data Analysis.....	128
5.3 Results	128
5.3.1 Stability of UX _{HP} -PCL Ridge/Groove Arrays.....	128
5.3.2 Morphological Evolution.....	129
5.3.3 Film Weight Loss Behaviour.....	131
5.3.4 Surface Hydrophilicity Changes.....	132
5.3.5 Film Mechanical Property Evolution	133
5.3.6 Stem Cell Responses	134
5.4 Discussion.....	138
5.5 Summary.....	144
Chapter 6 A Combination of Uniaxial Stretching and Femtosecond Laser Drilling for Engineered Vascular Basement Membrane	146
6.1 Introduction	146
6.2 Materials and Methods	148
6.2.1 Experimental Design	148

Table of Content

6.2.2 Materials	149
6.2.3 Sample Preparation.....	149
6.2.4 Field Emission Scanning Electron Microscopy (FESEM).....	150
6.2.5 Nutrition Diffusion Test	150
6.2.6 Cell Isolation and Culture.....	151
6.2.7 MSCs and HUVECs Co-culture	151
6.2.8 Confocal Laser Scanning Microscopy (CLSM).....	152
6.2.9 Cellular Alignment	153
6.2.10 NO Assay.....	153
6.2.11 Data Analysis.....	154
6.3 Results	154
6.3.1 Anisotropic Geometries and Pore Patterns on PCL Films	154
6.3.2 Tailorability of Pore Position and Diameter.....	156
6.3.3 Enhanced Permeability for MSCs Adhesion and Proliferation.....	158
6.3.4 MSCs Alignment.....	160
6.3.5 Direct MSCs-HUVECs Interaction	164
6.4 Discussion.....	168
6.5 Summary.....	174
Chapter 7 Conclusions	176
Chapter 8 Future Work	179
References	182
Appendices - List of Related Publications.....	204

Abstract

Poor scaffold function could impair vascular tissue regeneration, limiting the clinical translation of tissue-engineered vascular grafts. In this work, poly(ϵ -caprolactone) (PCL) films with anisotropic geometries and micropore patterns were developed and fabricated, to mimic the extracellular matrices (ECM) for the complex architecture reconstruction of blood vessels. Uniaxial stretching induced three-dimensional orientated ridge/groove arrays on PCL films with enhanced mechanical properties. Mesenchymal stem cells (MSCs) grew and aligned well on the PCL films with up-regulated expression of contractile smooth muscle cell genes. In addition, the PCL films exhibited inherent stability in an erosive environment, thereby better retaining the anisotropic geometries. PCL films with micropore patterns could be achieved via femtosecond laser drilling, which mimicked the vascular basement membrane for nutrient permeability, MSCs alignment on one surface of the films, and rapid endothelialisation on the opposite surface of the films. In short, this thesis explores the use of anisotropic geometries and micropore patterns for the generation of multi-functional film scaffolds that are capable of mimicking ECM for facilitating vascular tissue regeneration.

List of Acronyms

3D	Three-Dimensional
aTE	Anisotropic Tissue Engineering
AFM	Atomic Force Microscopy
BM	Basement Membrane
BSA	Bovine Serum Albumin
CLSM	Confocal Laser Scanning Microscopy
CNSI	Cell Nucleus Shape Index
CS-PCL	Cast-Stretched Poly(ϵ -caprolactone)
DAPI	4',6-Diamidino-2-Phenylindole
DGC	Dystrophin–Glycoprotein Complex
DMEM	Dulbecco's Modified Eagle Medium
DRG	Dorsal Root Ganglia
DSC	Differential Scanning Calorimeter
ECM	Extracellular Matrices
ECs	Endothelial Cells
EDTA	Ethylenediaminetetraacetic Acid
ePTFE	Expanded Polytetrafluoroethylene
FACS	Fluorescence-Activated Cell Sorting
FBs	Fibroblasts
FBS	Fetal Bovine Serum
FDA	Fluorescein Diacetate
FESEM	Field Emission Scanning Electron Microscopy
FITC	Fluorescein Isothiocyanate
Fn	Fibronectin
GAPDH	Glyceraldehyde-3-Phosphate Dehydrogenase
GCNF	Glial Cell Line-Derived Neurotrophic Factor
GFP	Green Fluorescence Protein

HP-PCL	Heat-Pressed Poly(ϵ -caprolactone)
HSPGs	Heparin-Sulfate Proteoglycans
HUVECs	Human Umbilical Vein Endothelial Cells
IGF-1	Insulin-Like Growth Factor 1
LN	Laminin
MCP-1	Monocyte Chemoattractant Protein-1
MMPs	Matrix Metalloproteinase
MSCs	Mesenchymal Stem Cells
NO	Nitric Oxide
PBS	Phosphate Buffer Saline
PCL	poly(ϵ -caprolactone)
PDLA	Poly(D-lacticacid)
PET	Polyethylene Terephthalate
PFA	Paraformaldehyde
PGA	Polyglycolic Acid
PI	Propidium Iodide
PLA	Polylactic Acid
PLGA	Poly(lactic-co-glycolic acid)
PLM	Polarized Light Microscopy
PMMA	Poly(methyl methacrylate)
PS	Penicillin-Streptomycin
PTFE	Polytetrafluoroethylene
PU	Polyurethanes
PUX _{HP} -PCL	Porous Uniaxial-Stretched Heat-Pressing Poly(ϵ -caprolactone)
qRT-PCR	Quantitative Reverse Transcription Polymerase Chain Reaction
SC-PCL	Solvent-Casted Poly(ϵ -caprolactone)
SM- α -actin	Smooth Muscle Alpha Actin
SMCs	Smooth Muscle Cells
SM-MHC	Smooth Muscle Myosin Heavy Chain
TCP	Tissue Culture Plate
TE	Tissue Engineering
TEVG	Tissue-Engineered Vascular Grafts
TGF- β 1	Transforming Growth Factor Beta 1
UX _{HP} -PCL	Uniaxial-Stretched Heat-Pressing Poly(ϵ -caprolactone)

VTE	Vascular Tissue Engineering
vWF	von Willebrand Factor
WCA	Water Contact Angle

List of Tables

Table 1-1	Applications of PCL in various tissue regeneration
Table 2-1	Strategies to biomimic the micro-environment of tunica media
Table 2-2	Characteristics of an ideal vascular graft (Adapted from [Bujan <i>et al.</i> 2004; Chlupac <i>et al.</i> 2009])
Table 2-3	The advantages and limitations of current vascular grafts
Table 2-4	Function of human vascular BM
Table 2-5	Minimal criteria for the identification of MSCs
Table 2-6	Advantages of using MSCs for vascular tissue regeneration as compared to SMCs
Table 2-7	Criteria for MSCs differentiation towards vascular cells
Table 2-8	Effects of biochemical factors on MSCs differentiation
Table 2-9	Technologies for the fabrication of anisotropic topographical geometry cues
Table 2-10	Factors influencing TE scaffold degradation
Table 2-11	The influences of degradation on TE scaffold properties
Table 2-12	Technologies for the incorporation of pores into films

Table 3-1	Inter-ridge-distance and ridge-length of UX _{HP} -PCL ridge/groove arrays (n = 4)
Table 3-2	Effects of uniaxial stretching on PCL film crystallinity
Table 4-1	Compiled list of gene targets probed for SMC contractile markers
Table 4-2	Compiled list of monoclonal antibodies for SMCs contractile markers
Table 4-3	Stem cell immunophenotype of isolated MSCs (Passage 6)
Table 4-4	Film mechanical properties and theoretical burst stress (n = 3)

List of Figures

- Figure 1-1** Schematic diagram illustrating the scope of experimental parts including Chapter 3 (i), Chapter 4 (ii), Chapter 5 (iii), and Chapter 6 (iv). [Page 7]
- Figure 2-1** Schematic diagram illustrating the vascular structure of normal artery and vein. (Adapted from the webpage of University of Miami, 2013 [31]) [Page 10]
- Figure 2-2** Publication and citation numbers in vascular tissue engineering (VTE). (According to the Web of Science, 2013) [Page 14]
- Figure 2-3** Mechanism for vascular neotissue regeneration. BMCs release MCP-1 and recruit Mon/Mac towards the grafts **(A)**. Mon/Mac infiltrate and release multiple angiogenic cytokines and growth factors (e.g. VEGF) during scaffold degradation, to recruit SMCs and ECs onto grafts **(B)**. Mon/Mac migrate away after complete scaffold degradation leaving behind autologous TEVG **(C)**. (BMC: bone marrow stem cells; MCP-1: monocyte chemoattractant protein-1; Mon/Mac: monocyte/macrophage; VEGF: vascular endothelial growth factor) (Adapted from Roh *et al.* 2010 [80]) [Page 19]
- Figure 2-4** Schematic diagram illustrating the positive and negative resist for lithography. (Adapted from Roach *et al.* 2010 [129]) [Page 31]
- Figure 3-1** Uniaxial stretching of PCL films resulted in anisotropic geometries. **(A)** Field emission scanning electron microscopy (FESEM) image of HP-PCL revealed a flat surface (Scale bar = 200 μm). **(B)** Low and high magnified FESEM images of UX_{HP}-PCL revealed anisotropic geometries (Double-headed arrow: stretching direction; Scale bar = 200 and 20 μm). **(C)** Atomic force microscopy (AFM) images of UX_{HP}-PCL. [Page 71]

- Figure 3-2** Morphological consistency of UX_{HP}-PCL. Representative regions (2x2 mm²; Y-0 to Y-4) from the film center to the edge, and regions (X-0 to X-5) from the film center to the two ends with an inter-region-distance of ~2 cm. FESEM images revealed similar inter-ridge-distance within regions of X-0 → X-3 and Y-0 → Y-4 (Double-headed arrow: stretching direction; Scale bar = 100 μm). * represents the significant difference as compared to the inter-ridge-distance of film central region (n = 4; *, p <0.05). [Page 72]
- Figure 3-3** FESEM images of UX_{HP}-PCL fabricated at a consistent *DR* of 4 and different *T_s* (21 °C, 37 °C and 54 °C), or consistent *T_s* of 54 °C and different *DR* (2, 3 and 4; Scale bar = 50 μm). [Page 73]
- Figure 3-4** Increased surface hydrophilicity of UX_{HP}-PCL. **(A)** WCA before hydrolysis. UX_{HP}-PCL revealed a WCA in parallel direction being similar to that of HP-PCL, but with an additional increase (~7 °) in perpendicular direction. * represents the significant difference as compared to WCA in the parallel direction (n = 5; ***, p <0.001; NS, p >0.05). **(B)** WCA after hydrolysis (NaOH, 3M). UX_{HP}-PCL achieved enhanced surface hydrophilicity, with continuous WCA decrease in both directions (n = 3). [Page 75]
- Figure 3-5** Morphological stability of UX_{HP}-PCL during surface modification. FESEM images revealed well-maintained ridge/groove shapes for hydrolysis (NaOH solution, 3M) of different time (Dark arrows: local integrity of ridge surface; Scale bar = 10 μm). [Page 75]
- Figure 3-6** Confocal laser scanning microscopy (CLSM) images of cytoskeletal (Phalloidin: red, F-actin; DAPI: blue, DNA; Scale bar = 200 μm) and cytoplasmic (FDA: green, live cells; PI: red, dead cells; Scale bar = 500 μm) staining of MSCs (Passage-6, 5k per cm², for 5 days of culture) on UX_{HP}-PCL anisotropic geometries and HP-PCL flat surface (Control; White arrow: ridge direction; Scale bar = 500 μm). MSCs cultured with UX_{HP}-PCL anisotropic geometries aligned and elongated preferentially towards the ridge direction. In contrast, MSCs organised randomly in control group. [Page 76]
- Figure 3-7** Consistent MSCs alignment. **(A)** UX_{HP}-PCL sample of 1x1 cm². **(B)** CLSM images of MSCs organization in representative zones (Z1-Z5) revealed consistent cell alignment in a controlled direction along ridges (Phalloidin: red, F-actin; DAPI: blue, DNA; White arrow: ridge direction; Scale bar = 500 μm). [Page 77]

- Figure 3-8** (A) Quantitative analysis of cell arrangement angles. The angles of MSCs (Passage-6, 5k per cm², for 5 days of culture) on UX_{HP}-PCL concentrated within a small range of $\pm 15^\circ$, while cell angle frequency of control group (HP-PCL flat surface) approximated to that of an isotropic sample (Red line: frequency of MSCs angle distribution; Dashed-dark line: frequency of cell angle distribution of an isotropic sample, which is $\sim 0.56\%$; Dashed-blue line: ridge direction; Solid-blue line: preferential cell orientation). (B) MSCs alignment efficiency represented by the normalised cell number within $\pm 10^\circ$ (Dashed-dark lines: expected values of a perfectly isotropic sample, which is $\sim 11.7\%$). (C) MSCs elongation represented by CSI (CSI of 1 representing a circle). MSCs on UX_{HP}-PCL achieved significant increase in cellular alignment and elongation as compared to control. * represents the significant difference compared with that of control group (n = 3; ***, p < 0.001). [Page 78]
- Figure 3-9** Dynamic cell alignment and elongation. (A) CLSM images of MSCs revealed aligned growth towards the anisotropic geometries of UX_{HP}-PCL over the investigated period (Control: HP-PCL flat surface; White arrow: ridge direction; Scale bar = 500 μm). (B) Frequency distributions of MSCs angles on UX_{HP}-PCL anisotropic geometries. Cell arrangement angles fell into a narrower range with increasing the culture time. (C & D) Dynamic cell alignment and elongation. MSCs on UX_{HP}-PCL achieved the rapid increase in cell alignment and elongation during initial culture of 3 days, and kept the efficiencies un-increased for further culture. * represents the significant difference compared with that of control group at each time point (n = 3; **, p < 0.01; ***, p < 0.001; NS, p > 0.05). [Page 80]
- Figure 3-10** Long-term cell alignment capability. CLSM images from FDA/PI live-cell staining revealed a long-term aligned growth of MSCs on UX_{HP}-PCL after achieving confluence, but local cellular alignment only in control group (White arrow: ridge direction; Scale bar = 500 μm). [Page 81]
- Figure 3-11** MSCs proliferation on UX_{HP}-PCL anisotropic geometries, HP-PCL flat surface and TCP flat surface (Positive control). UX_{HP}-PCL ridge/grooves supported MSCs growth with similar proliferation to that on HP-PCL flat surface, approaching that of positive control group with increased culture time (n = 5; ***, p < 0.001; NS, p > 0.05). [Page 82]
- Figure 3-12** Anisotropic polyethylene (PE) geometries. Commercial PE films were stretched at T_s of 70 $^\circ\text{C}$ and DR of 4. (A) Light microscopy

- and AFM images revealed orientated wave-like geometries on PE films after uniaxial stretching, but non-anisotropic structures on un-stretched films (Double-headed arrows: stretching direction; Scale bar = 40 μm). **(B)** Typical height profile of uniaxial-stretched PE films [along the red-line shown in AFM images]. [Page 84]
- Figure 3-13** Polarised light microscopy (PLM) images of HP-PCL and UX_{HP}-PCL. Uniaxial stretching resulted in orientated molecular chains of UX_{HP}-PCL. [Page 85]
- Figure 3-14** Ridges and grooves of UX_{HP}-PCL subjected to alkaline hydrolysis (NaOH, 3M) for 12 hr **(A)** and 20 days **(B)**. FESEM images of ridges exhibited thorn-like structures (Dark arrows; ~ 50 nm in width) perpendicular to stretching direction, and larger resistance against hydrolysis as indicated from the less caves presented than grooves did (Double-headed arrows: stretching direction; White arrows: caves in the grooves; Scale bar = 2 and 200 μm). [Page 85]
- Figure 3-15** Schematic diagram illustrating formation of UX_{HP}-PCL ridges and grooves. Uniaxial stretching re-orientated the multilayered lamellas of HP-PCL, which self-packed into new crystals along stretching direction. During that process, film superficial amorphous regions formed into grooves because of being easily deformed, while the crystals experienced less deformation and were revealed out from film surface as elongated ridges. [Page 86]
- Figure 4-1** Light microscopy images of *in vitro* culture expanded human MSCs (Passage-6). [Page 101]
- Figure 4-2** **(A)** Field emission scanning electron microscopy (FESEM) images of SC-PCL, HP-PCL and CS-PCL revealed different surface morphologies (Scale bar = 200 μm). **(B)** FESEM and atomic force microscopy (AFM) images of UX_{SC}-PCL, UX_{HP}-PCL and UX_{CS}-PCL revealed film morphologies of anisotropic geometries (Scale bar = 50 μm for FESEM images). [Page 102]
- Figure 4-3** **(A)** Inter-ridge-distance. **(B)** Ridge-depth. Among three-stretched PCL films, UX_{HP}-PCL ridge/groove arrays revealed medium inter-ridge-distance and ridge-depth ($n = 3$; ***, $p < 0.001$; NS, $p > 0.05$). [Page 103]
- Figure 4-4** **(A)** Tensile stress-strain curves of PCL films. **(B)** Enlarged stress-strain curves of UX_{HP}-PCL and HP-PCL. UX_{HP}-PCL exhibited continuous stress increase after achieving the linear stress-strain segment, which was similar to those of UX_{SC}-PCL and UX_{CS}-PCL,

and different from that of HP-PCL. [Page 104]

- Figure 4-5** Confocal laser scanning microscopy (CLSM) images of MSCs. Cells (Passage-3, 5 k/cm²) were cultured in D10 for 4 days and stained with cytoplasm using FDA (Green colour). **(A)** MSCs on un-stretched PCL film surfaces exhibited random organisation. **(B)** MSCs aligned towards the ridge/grooves of UX_{SC}-PCL and UX_{HP}-PCL, but randomly organized on UX_{CS}-PCL. (Double-headed arrows: ridge direction (Scale bar = 250 μm). [Page 106]
- Figure 4-6** Quantitative analysis of MSCs alignment and elongation. Cells (Passage-3, 5 k/cm², for 4 days in D10) were examined by CLSM using FDA live-cell cytoplasmic staining. **(A)** Cell alignment efficiency described by the normalised cell number in ±10°. **(B)** Cell elongation described by the ratio of long-to-short elliptic axis. Compared to UX_{CS}-PCL and UX_{SC}-PCL, UX_{HP}-PCL organized MSCs with better cellular alignment efficiency and elongation (n = 3; ***, p < 0.001; **, p < 0.01; *, p < 0.05; NS, p > 0.05). [Page 107]
- Figure 4-7** Cytoskeletal reorganisation of MSCs on UX_{HP}-PCL. Cells (Passage-6, 5 k/cm², for 5 days of culture in D10) were stained with F-actin (Red colour) and DNA (Blue colour), and examined using CLSM. **(A)** MSCs on HP-PCL flat surfaces. **(B)** MSCs on UX_{HP}-PCL ridge/groove arrays (Double-headed arrows: ridge direction; Scale bar = 50 μm). [Page 108]
- Figure 4-8** MSCs nucleus deformation on UX_{HP}-PCL. Cells (Passage-6, 5 k/cm², for 5 days of culture in D10) were stained with DNA using DAPI (Blue colour). **(A)** CLSM images of MSCs nuclei on HP-PCL and UX_{HP}-PCL surfaces (Double-headed arrows: direction of PCL ridge/groove arrays; Scale bar = 100 μm). **(B)** Quantitative analysis of nucleus alignment and elongation (n = 3; ***, p < 0.001). [Page 109]
- Figure 4-9** Gene expression change of SMCs contractile markers in MSCs on UX_{HP}-PCL. Cells (Passage-6, 5 k/cm²) were cultured with tissue culture plate (TCP, Control group) flat surfaces, HP-PCL flat surfaces and UX_{HP}-PCL ridge/grooves in D10 for 5 days. Quantitative reverse transcription polymerase chain reaction (qRT-PCR) analysis showed that UX_{HP}-PCL up-regulated the expression levels of ACTA2, CNN1 and MYH11 in MSCs. (n = 3; vs HP-PCL group: ***, p < 0.001; NS, p = 0.15). [Page 111]
- Figure 4-10** Protein expression change of SMCs contractile markers in MSCs on UX_{HP}-PCL. Cells (Passage-6, 5 k/cm²) were cultured on HP-

PCL flat surfaces and UX_{HP}-PCL ridge/grooves in D10 for 5 days, and immunocytochemistry-labeled with IgG isotypes (Negative control) and SMCs contractile markers: SM- α -actin for early-term differentiation **(A)**, calponin for middle-term differentiation **(B)**, and SM-MHC for late-term differentiation **(C)**. MSCs on UX_{HP}-PCL positively expressed SMCs contractile filaments in the ordered organisation towards ridges (DNA: blue colour; SMCs contractile markers: green colour; Double-headed arrows: direction of PCL ridge/groove arrays; Scale bar = 50 μ m). [Page 113]

Figure 4-11 Quantitative analysis of the protein expression of SM- α -actin, calponin and SM-MHC. **(A)** Positive cell number. **(B)** Fluorescence intensity. Flow cytometry (FACS) analysis showed that MSCs (Passage-6, 5 k/cm², for 5 days of culture in D10) on UX_{HP}-PCL achieved enhanced expression of SMCs contractile markers in both positive cell number and expression intensity (n = 3; ***, p <0.001; **, p <0.01; *, p <0.05). [Page 114]

Figure 4-12 **(A)** Schematic diagram for engineering 3D vascular scaffolds (Red arrows: flow direction; blue arrows: ridge direction). **(B)** A small-diameter 3D tubular scaffolds from UX_{HP}-PCL. FESEM images revealed ridge/grooves similarly presented on both wall surfaces in a direction perpendicular to the tube (Blue arrows: ridge direction; Scale bar = 100 μ m). **(C)** Patency of the 3D tubular scaffolds from UX_{HP}-PCL, UX_{CS}-PCL and UX_{SC}-PCL after immersion in culture medium. **(D)** Engineering of layered-MSCs/PCL/MSCs with similar direction in different layers (Blue arrows: ridge direction; scale bar = 200 μ m). [Page 116]

Figure 5-1 Morphological stability of UX_{HP}-PCL ridge/groove arrays against degradation. Film samples were hydrolysed in an alkaline medium for 20 days at room temperature. Field emission scanning electron microscopy (FESEM) images reveal overall ridge/groove arrays that still existed on UX_{HP}-PCL (FS: flat surfaces; R: ridges; G: grooves; Double-headed arrow: stretching direction; Scale bar = 200 and 20 μ m for low and high magnified FESEM images, respectively). [Page 129]

Figure 5-2 Morphological evolution of UX_{HP}-PCL ridge/groove arrays with alkaline hydrolysis at room temperature for day 0-30. Degradation of UX_{HP}-PCL ridge/groove arrays occurred on film surfaces with ridges being degraded into small parallel ridge-islands (FS: flat surfaces; R: ridges; G: grooves; Double-headed arrow: stretching direction; Scale bar = 20 μ m). [Page 130]

- Figure 5-3** Morphologies of UX_{HP}-PCL ridge/groove arrays (**A**) and HP-PCL flat surfaces (**B**) after 30 days of degradation. FESEM images reveal integrated surfaces with overall orientated geometries on UX_{HP}-PCL. In contrast, HP-PCL flat surfaces were degraded into fragments (Double-headed arrow: stretching direction; Scale bar = 100 μ m). [Page 131]
- Figure 5-4** Film weight loss of PCL films hydrolysed in an alkaline medium at room temperature for 0-39 days. UX_{HP}-PCL ridge/groove arrays followed an “S-shape” behaviour of film weight loss, while HP-PCL flat surfaces experienced a “parabola-shape” behaviour (FS: flat surfaces; R: ridges; G: grooves; n = 5). [Page 132]
- Figure 5-5** Surface hydrophilicity of PCL films with alkaline hydrolysis for different time. UX_{HP}-PCL ridge/groove arrays obtained increased surface hydrophilicity after degradation, and retained similar water contact angle (WCA) of $>40^\circ$ in both parallel (//) and perpendicular (\perp) directions for 20 days of degradation (FS: flat surfaces; R: ridges; G: grooves; n = 5). [Page 133]
- Figure 5-6** Film mechanical properties of PCL films after alkaline hydrolysis at room temperature for different time. (**A**) Typical tensile stress-strain curves. (**B**) Film yield stress, yield strain, Yong's Modulus, and ultimate stress and strain. Over the investigated degradation period, UX_{HP}-PCL ridge/groove arrays experienced slight increase in film yield stress and strain, resulting in less change at film Yong's Modulus (FS: flat surfaces; R: ridges; G: grooves; n = 3). [Page 134]
- Figure 5-7** Cellular responses to geometric degradation of UX_{HP}-PCL ridge/groove arrays. Human MSCs (P6, 5k per cm^2) were cultured on UX_{HP}-PCL ridge/groove arrays hydrolysed in an alkaline medium for different time (0-30 days), and stained using TRITC-conjugated phalloidin (Red colour: F-actin, cytoskeleton) and DAPI (Blue colour: DNA, nuclei). (**A**) MSCs on HP-PCL flat surfaces organised randomly (Neg Ctrl; Dot line: nucleus angle frequency of an Isotropic sample with a value of $\sim 0.56\%$). (**B**) MSCs on hydrolysed UX_{HP}-PCL ridge/groove arrays (Double-headed white arrows: ridge direction). (**C**) Nucleus alignment described as a normalised nucleus number in $\pm 10^\circ$ (Dot line: nucleus alignment of an Isotropic sample with a value of $\sim 11.7\%$). (**D**) Nucleus elongation described by a CNSI. A CNSI of 1 represents a circle (*, ** and *** represent significant differences as compared to Neg Ctrl; n = 3; *, p < 0.05; **, p < 0.01; ***, p < 0.001) [Page 137]

- Figure 5-8** Summarised relationships among film weight loss of UX_{HP}-PCL, geometric evolution of ridge/grooves and MSCs responses. At less than ~20 % film weight loss, degradation resulted in gradually rougher surfaces with stable MSCs alignment. At more than ~20 % film weight loss, ridges degraded into small ridge-islands, leading to MSCs response with declined nucleus alignment and elongation (Hollow arrows: concaves at ridge-edges in [C] and direct loss of ridge-islands in [D]). [Page 144]
- Figure 6-1** Uniaxial stretching and femtosecond laser drilling of PCL films resulted in orientated ridge/groove arrays and pore patterns. (A) HP-PCL flat surfaces. (B) UX_{HP}-PCL ridge/groove arrays (double-headed arrows: redge direction). (C) PUX_{HP}-PCL with orientated ridge/groove arrays and pore patterns (Scale bar = 500 μm). [Page 155]
- Figure 6-2** (A) Pore morphologies top and bottom film surfaces. FESEM images of PUX_{HP}-PCL reveal through-hole after femtosecond laser drilling, which was rounded with lip-like melting and formed into an ellipse-like shape towards ridges (Scale bar = 20 and 200 μm for high and low magnifications, respectively). (B) Pore morphologies on HP-PCL top film surface revealed more rounded and more ejection (Scale bar = 50 and 500 μm for the high and low magnifications, respectively). [Page 156]
- Figure 6-3** Control of pore position. (A) x-axis was defined as the ridge direction, while y-axis was perpendicular to ridges. (B) Different pore patterns on PUX_{HP}-PCL (Scale bar = 500 μm). [Page 157]
- Figure 6-4** (A) Light microscopy images of melting ejection. Higher E_{pulse} produced thicker ejection fibers ($N_{\text{pulse}} = 20$), while higher N_{pulse} resulted in less ejection ($E_{\text{pulse}} = 20 \mu\text{J}$). (B) Influences of E_{pulse} and N_{pulse} . Pore diameters increased with raised E_{pulse} ($N_{\text{pulse}} = 20$), but exhibited less changes when N_{pulse} was varied ($E_{\text{pulse}} = 20 \mu\text{J}$; $n = 6$). [Page 158]
- Figure 6-5** Permeability evolution of PUX_{HP}-PCL. Cumulative concentration of FITC-dextran increased with diffusion time, and achieved ~100 % of diffusion at 288 hrs (FITC-dextran: marker molecule; UX_{HP}-PCL: control group; $n = 6$). [Page 159]
- Figure 6-6** (A) Schematic diagram illustrating the experimental design. MSCs seeded on PUX_{HP}-PCL in D10 and D0 were set as positive (P-Ctrl) and negative (N-Ctrl) control, respectively. (B) Cellular adhesion

- and proliferation on PUX_{HP}-PCL. Cells (Passage-6, 5k per cm²) were seeded and cultured for 1 and 3 days. MSCs on PUX_{HP}-PCL achieved increased cell adhesion (day 1) and proliferation (day 3) as compared to those of UX_{HP}-PCL group (n = 3; ***, p <0.001; NS, p >0.05). [Page 160]
- Figure 6-7** Pore influence on MSCs alignment. **(A)** UX_{HP}-PCL. MSCs aligned on UX_{HP}-PCL towards the ridge directions. **(B-E)** PUX_{HP}-PCL. MSCs exhibited aligned growth towards the ridge/groove arrays when they could extend freely, half-cell alignment when cellular extension was obstructed only at one end, and disturbed alignment when MSCs extension was obstructed at one end and the other end attached to substrate/cells that were not in ridge direction (Double-headed arrows: ridge direction; Green arrows: free extension of cells; Yellow arrows: cell extension being obstructed and attached to substrate or cells; Scale bar = 100 μm). [Page 161]
- Figure 6-8** Influence of pore pattern on MSCs alignment. **(A)** CLSM images reveal different MSCs organisation on PUX_{HP}-PCL (Red arrows: cells disturbed by pores; Scale bar = 200 μm). **(B)** Normalised MSCs alignment efficiency. MSCs exhibited the declined degree of alignment efficiency towards ridge/grooves depending on pore patterns (n = 3; ***, p <0.001; NS, p >0.05). [Page 162]
- Figure 6-9** Non-interfered MSCs alignment on PUX_{HP}-PCL. Cells (Pasage-6, 5k per cm²) seeded on PCL films were cultured for pre-determined time. **(A)** DIC images of HP-PCL, PHP-PCL, UX_{HP}-PCL and PUX_{HP}-PCL (Inter-pore-distance: 500 μm; Double-headed arrows: ridge direction). **(B)** Normalised cell alignment efficiency. MSCs alignment on PUX_{HP}-PCL achieved significant increase than that of PHP-PCL, and was non-reduced as compared to that of UX_{HP}-PCL (n = 3; ***, p <0.001; NS, p >0.05). **(C)** Cellular organisation at a confluence status. MSCs after 8 days of culture still retained aligned growth on UX_{HP}-PCL and PUX_{HP}-PCL in a controllable direction towards ridges (Double-headed arrows: ridge direction). [Page 163]
- Figure 6-10** Cellular ingrowth of MSCs into PUX_{HP}-PCL via (i) bridging, (ii) sidewall depth and (iii) coverage. Cells (Passage-6, 5k per cm²) seeded on PUX_{HP}-PCL:X500Y500 were cultured for 3 days in D10 (Red arrows: cellular anchors that adhered to the pore sidewall; Blue arrows: cellular anchors that extended into the pore depth; Scale bar = 20 μm). [Page 165]
- Figure 6-11** Direct MSCs-HUVECs contact. PHK26-labeled MSCs (Red colour; Passage-6, 10k per cm²) seeded on one surface of PUX_{HP}-

PCL:X500Y500 were cultured in D10 for 1 day, and GFP-labeled HUVECs (Green colour; Passage-6, 15k per cm²) were then seeded onto the other film surface and co-cultured in EGM10 for further 3 days. **(A)** 3D construction of section-scanning CLSM images from DIC, Green and Red channels. Yellow colour represented the colocalisation of green and red colours. **(B)** Crossing-section view. Yellow colour distributed not only around the green and/or red colour areas but also within each other (Scale bar = 20 µm). [Page 166]

Figure 6-12 **(A)** CLSM images of cell-contact between GFP-labeled HUVECs (Green colour) and PHK26-labeled MSCs (Red colour) for 2 and 5 days of co-culture in EGM10 (Scale bar = 500 µm). **(B)** Normalised pore number that occurred HUVECs-MSCs contact (n = 4). [Page 167]

Figure 6-13 Influence of direct MSCs-HUVECs interaction. **(A)** Total system NO level. Direct cell-cell interaction increased the total NO level of HUVECs/MSCs co-culture system, while in-directed interaction declined the system total NO level (n = 4; *, p <0.05; **, p <0.01; ***, p <0.001). **(B)** HUVECs adhesion and proliferation. Direct cell-cell interaction increased HUVECs proliferation as compared to that of co-culture system with in-direct cell-cell interaction and single-culture system (n = 3; *, p <0.05; ***, p <0.001; NS, p >0.05). [Page 168]

Chapter 1 Introduction

1.1 Background

There is great unmet need for vascular grafts. According to the World Health Organisation's report, cardiovascular disease is the leading cause of death globally [1]. In the U.S., over 60 million Americans live with the influences of heart attacks or strokes [2-4], and in Europe, almost one half of the death is associated with atherosclerosis [5]. In developing countries such as China, the death rates related to cardiovascular diseases will surge up to 73 % by 2030 [6]. Surgical bypass is the procedure of choice in a number of patients for cardiovascular disease therapy [7]. There are ~1.4 million arterial bypass operations performed annually in the U.S. alone [4, 8]. Surgical bypass is also considered to be more cost-effective and preserve the quality of patient's life better than other therapeutic strategies such as amputation [8]. However, ~7 % of 17.5 million patients worldwide who require surgical bypass procedures do not have suitable vessels for use [9].

The patient's own arteries or veins remain the gold standard of vascular grafts for surgical bypassing [8]. For patients who do not have suitable own vessels, vascular grafts from foreign tissues (e.g. the same or different species) and synthetic materials are used for surgical bypassing. However, long-term patency rates remain the major concern of current vascular grafts, in particularly for small-diameter bypass grafting (e.g. the coronary arteries) [4, 10]. The 5-year patency of autografts (patient's own

vessels) and synthetic grafts for the above-the-knee femoropopliteal arteries is only ~74 and ~39 %, respectively [8]. Besides that, availability is the other major limitation for autografts [2, 11, 12] and any vessel harvest is associated with indispensable donor site [13], while allografts, xenografts and synthetic grafts often accompany with toxicity and immune-rejection. New strategies for an ideal vascular graft have become in an urgent need for cardiovascular disease therapy.

Vascular tissue engineering (VTE), a new developing field, has emerged and achieved considerable advances over the past 10 years. The ultimate goal of VTE is to generate autologous tissue-engineered vascular grafts (TEVG) that not only are living, immunocompatible and capable of physiological response as autologous grafts, but also have sufficient availability, meet patient-specific requires and minimise the procedures and time required before implantation, finally approaching the "off-the-shelf" idea [14]. There are four basic concepts for VTE including the cells, scaffolds, signals, and engineering techniques [14, 15], among which cells and scaffolds are the key components of TEVG.

Vascular scaffolds provide the temporal mechanical support to withstand the hemodynamic strength and strain. They are also crucial for the vascular tissue remodeling via delivering biochemical and/or mechanical signals for the cell behaviour regulation such as spreading, growth, migration, differentiation and the secretion of extracellular matrices (ECM) [16]. The materials of vascular scaffolds can be natural or synthetic polymers [15]. Polyglycolic acid (PGA), polylactic acid (PLA) and poly(ϵ -caprolactone) (PCL) are the most widely used synthetic polymers in biomedicine [14]. However, vascular scaffolds from PGA after the surgical sutures

tend to lose their mechanical strength over 2-4 weeks post-implantation [15]. Furthermore, both PGA and PLA are easy to undergo plastic deformation and failure when exposed to long-term cyclic strain [17], limiting their applications as suitable materials for mechano-active tissue regeneration (e.g. TEVG). In contrast, PCL is a versatile biomaterial and has been extensively applied for regeneration of various tissues (Table 1-1). PCL has superior mechanical properties [17]. *In vivo*, PCL degrades slowly via the hydrolysis of ester linkages and eliminates the resultant fragments by giant cells and macrophages [14, 15]. Another unique property of PCL is its rubbery state at room temperature because of its low glass transition temperature of about $-60\text{ }^{\circ}\text{C}$ [17]. Therefore, PCL is most suitable for the design of long-term implantable system such as TEVG. The first human clinical study based on PCL and its co-polymer scaffolds conducted recently in Japan gave promising long-term outcomes [14].

Table 1-1: Applications of PCL in various tissue regeneration

Tissue Engineering	Specific Applications	Ref.
Bone	(i) Fused deposition modeled porous 3D scaffolds for critical-size femoral defects repair; (ii) Porous scaffolds with platelet-rich plasma for orthotopic defect repair: vascular ingrowth and functional integration.	[18, 19]
Blood Vessel	(i) Bi-axial-stretched film with CD34 modification for hemo-compatibility and construction of tunica intima and media; (ii) Electropun fibrous film for endothelium regeneration; (iii) Rolled sheets for media reconstruction.	[20-22]
Skin	(i) Bi-axial stretched film for dermal fibroblast growth.	[23]
Nerve	(i) Electropun fibers for peripheral nerve regeneration.	[24]

Vascular cells are responsible for the neotissue and function regeneration. These include the endothelial cells (ECs), smooth muscle cells (SMCs) and fibroblasts (FBs). ECs function as the thromboresistance, antipseudointimal hyperplasia and inhibition of SMCs migration, overgrowth and ECM secretion [15]. SMCs and FBs contribute to the structural integrity, mechanical support and vasoactive responses. Furthermore, SMCs and FBs can also stabilise the ECs-composed intima [25]. Besides those cells, stem cells have gained more attention in recent years, and serve as an alternative vascular cell source, due to the self-renewability and potential differentiation into vascular cells [26].

Currently, VTE, however, is far away from the generation of an ideal graft that should be engineered, autologous and "off-the-shelf" [27]. The major problem is that TEVG from the current manipulations does not match the compliance of native vessels [27]. The cells and filaments are not able to organise in the specific circumferential alignment of native vessels [14, 28]. SMCs have limited renew capability, and are easy to lose their contractile apparatus and shift into a synthetic phenotype, resulting in the over cell proliferation and ECM secretion, the migration into intimal regions, and final regulation failure of blood pressure and flow [15, 29].

To overcome the problems of current TEVG, major efforts have been directed to understand the importance of vascular cell micro-environment, and mimic it for the design of *de novo* vascular scaffolds. In native vessels, one important structure is the basement membrane (BM), the two sides of which are located with the orientated SMCs and ECs. It has been known that BM plays a crucial role in the vascular development and physiological function such as the anti-thrombosis, compliance,

selective permeability and patency of blood vessels [9, 30]. Importantly, the recent study demonstrated that BM is a meshwork composed of orientated fibers and interconnected pores [9]. Such complex architecture should have important impacts on the vascular cell organisation and function, and have potential to facilitate better compliance for TEVG.

1.2 Objectives

This project aims to develop novel functional vascular scaffolds that mimic the complex architecture of BM, with capability to guide the ordered organisation and differentiation of stem cells, and support the rapid endothelialisation. For this objective, PCL will be used as the scaffold materials, and mesenchymal stem cells (MSCs) and ECs will be used as the cell sources for the tunica media and intima, respectively.

- **Specific Aim-1:** Uniaxial stretching of PCL films results in the orientated three-dimensional (3D) ridge/groove arrays, with robust capability to support effective and long-term stem cell alignment.
- **Specific Aim-2:** Uniaxial-stretched PCL films, with elevated mechanical properties and 3D orientated ridge/groove arrays, promote the alignment and differentiation of MSCs into a contractile SMCs-like phenotype, and facilitate the tubular scaffold construction.
- **Specific Aim-3:** Uniaxial-stretched PCL films obtain enhanced stability against erosive environments, with better-retained surface hydrophilicity, mechanical properties, and 3D orientated ridge/groove arrays for the prolonged cell regulation.

- **Specific Aim-4:** A combination of uniaxial stretching and femtosecond laser drilling results in engineered BM, with 3D orientated ridge/groove arrays and microporous patterns for the ordered MSCs organisation and rapid endothelialisation from ECs.

1.3 Scope

Chapter 1 is the introduction, which gives a brief background and specifies the research objectives and novelty of VTE applications.

Chapter 2 is the literature review, which focuses on current research progress related to the objectives of this project including the human blood vessels and regeneration, stem cells for VTE applications, geometric cues for engineered BM, and porous patterns for engineered BM.

Chapters 3-6 are the experimental parts. As shown in Figure 1-1, Chapter 3 will focus on the development of using uniaxial stretching to generate orientated ridge/groove arrays on PCL films for stem cell organisation control. A series of materials and cellular characterisations will be performed. Chapter 4 will focus on PCL film selection, which should have sufficient mechanical properties and proper geometries for MSCs alignment, differentiation and TEVG scaffold construction. Based on Chapter 4, Chapter 5 will focus on the understanding of how erosive environment influence the orientated ridge/groove arrays on selected PCL films, changes of film properties, and further MSCs responses. Chapter 6 will focus on the using of femtosecond laser beam to drill micropore patterns on the selected films. Therefore, the PCL films will have orientated ridge/groove arrays and microporous patterns.

Parameters for femtosecond laser drilling and materials characterisations will be done. Biological studies including the nutrient diffusion, MSCs alignment and direct cell-cell interaction between MSCs and ECs will be performed for evaluating the performances of PCL films as the engineered BM for VTE applications.

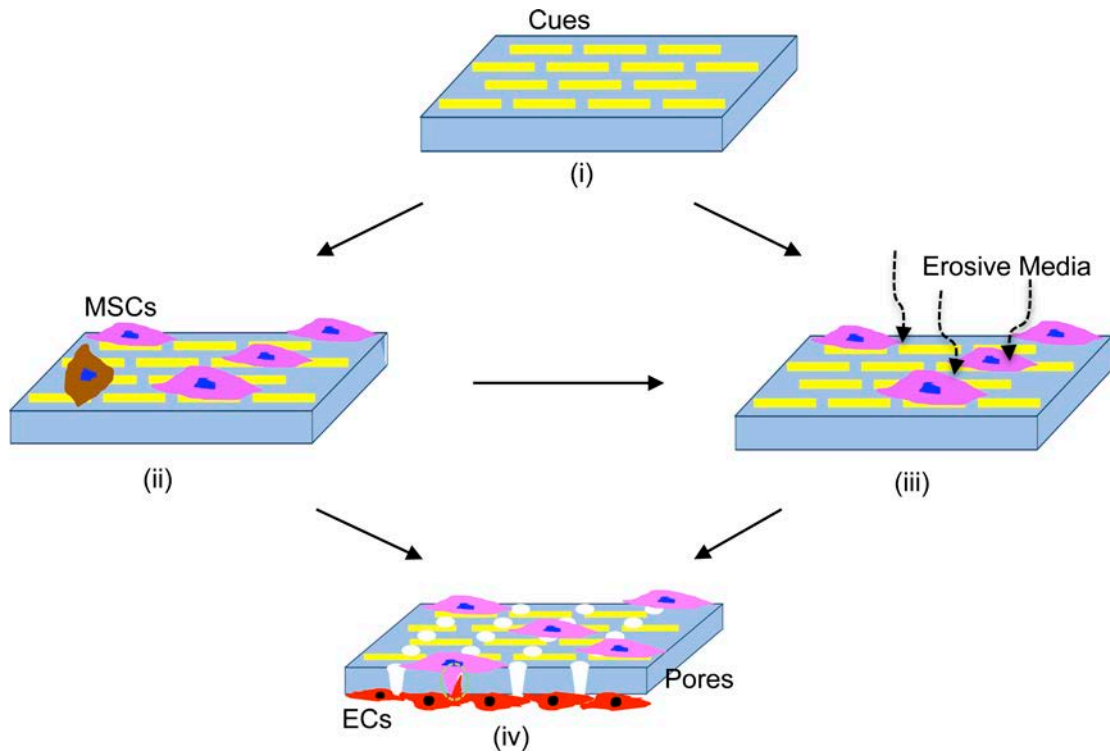


Figure 1-1: Schematic diagram illustrating the scope of experimental parts including Chapter 3 (i), Chapter 4 (ii), Chapter 5 (iii), and Chapter 6 (iv).

Chapter 7 is the conclusions, which will focus on the summarisation of main conclusions that this project contributed.

Chapter 8 is the future work, which will focus on the examination of limitations of current work, and point out the potential directions for future research.

1.4 Novelty

The unmatched compliance of TEVG remains a major challenge for VTE. This project using a biomimical strategy to incorporate anisotropic geometries and microporous patterns on PCL films will facilitate the development of functional scaffolds for TEVG to approach the compliance of native vessels. The PCL films will function as an engineered BM for aligned cell organisation as in native tunica media and rapid endothelialisation on the opposite film surface as tunica intima. Therefore, this work will provide a novel multi-functional PCL film as an engineered BM for VTE application. The work will also enhance the understanding on how geometric cues regulate MSCs fate, how pores influence cellular alignment towards the anisotropic geometries, and how direct cell-cell interaction affects the endothelialisation.

This project will develop two innovative methods. The first technique is using uniaxial stretching to produce film geometric cues in a solvent-free and simple manner. The other technique is using a combination of uniaxial stretching and femtosecond laser drilling for fabricating multi-functional films with anisotropic geometric cues and microporous patterns in a controllable manner (e.g. pore size and position) for non-inferential cellular alignment. These two techniques should facilitate the development of function vascular scaffolds for an "off-the-shelf" TEVG.

Chapter 2 Literature Review

2.1 Human Vascular System and Regeneration

2.1.1 Blood Vessel Structure

Blood vessels extend throughout the body and form into a circulation system for gas and nutrient exchange, waste transport and immune defense. Human vascular system includes arteries that carry nutrient and oxygenated blood away from the heart to the body; capillaries that response to the exchange of nutrient and oxygen among the arteries, tissue and veins; and veins that carry blood back into the heart. Except for the capillaries, all arteries and veins in large, middle and small diameters posses three-layered structures [16]. From the luminal side outward, they are tunica intima, media and adventitia, mainly composed of ECs, SMCs and FBs, respectively (Figure 2-1) [31].

Tunica intima consists of ECs monolayer, forming as a tight nonthrombogenic barrier between lumen side and the rest of vessel wall. This layer function as (i) anti-thrombosis, (ii) anti-infection/inflammation from the underlying tissues, and (iii) regulation signals to SMCs [32]. To biomimic the micro-environment of tunica intima, strategies can be utilising the flow shear stress for mechanical biomimicry and modifying the scaffold surface for anti-thrombosis (e.g. heparin and CD34) [33-35]. Seeding of ECs has also been used for the increased patency of vascular grafts [36].

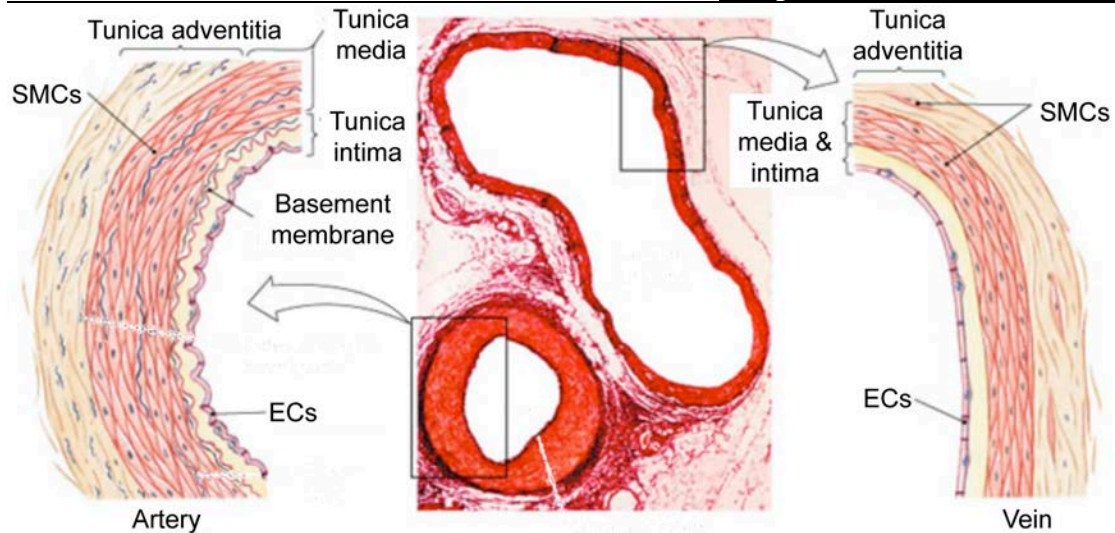


Figure 2-1: Schematic diagram illustrating the vascular structure of normal artery and vein. (Adapted from the webpage of University of Miami, 2013 [31])

Tunica media has an anisotropic architecture consisting of SMCs and ECM of collagen type I and III, elastin, and other proteins and proteoglycans [32]. In the development of blood vessels, SMCs secrete ECM in an ordered organisation [16]. Elastin arranges as fenestrated sheets, and is connected by the collagen fibers, proteoglycan thin layers and SMCs [37]. It has been known that elastin and collagen account for ~50 % of the dry weight of vessels [38]. Elimination of SMCs does not alter significantly the static mechanical properties of mature arteries [39], suggesting that before successful remodeling, vascular scaffolds should be able to provide sufficient burst strength support. SMCs embedded in the collagen-enriched ECM and organised into the circumferential alignment with a herringbone helical arrangement [40]. Tunica media contributes most to (i) the secretion, integrity and mechanical support [16], (ii) vasoactive response to signals from ECs (e.g. cytokines) [32], and (iii) regulation on ECs [15]. Studies to biomimic tunica media include the targeting of biochemical components, mechanical stimuli and geometric architecture (Table 2-1) [28, 41, 42].

The adventitia consists of FBs and loose collagen-enriched ECM, serving two main functions to support vascular wall and anchor vessels to the surrounding tissue as well as regulate endothelium function [15, 32].

Table 2-1: Strategies to biomimic the micro-environment of tunica media

	Natural Tunica Media	Signal Pathways	VTE Scaffolds	Function	Ref.
Biochemical components	Elastin	Non-integrin heterotrimer G-protein-coupled pathway	Recombinant elastin-like polypeptides on PU fibers	Contractile phenotypes with organised actin stress fibers and biological markers	[41]
Mechanical Stimuli	Cyclical strain	RhoA/ROCK and (FAK)/c- Src pathway	Equiaxial and uniaxial strain	Up-regulated expression of contractile SMCs markers via cyclical uniaxial strain	[42]
Geometric Morphologies	Anisotropic organisation	Mechano-transduction	An amphiphilic comb polymer micropatterns	Increased SMCs contractile marker expression	[28]

2.1.2 Vascular Grafts

An ideal vascular graft for the surgical bypassing should meet the requirements of the four aspects (Table 2-2): safety (e.g. anti-infection, biocompatibility and appropriate mechanical properties), function (e.g. long-term patency, growth potential and vasoactive responses), operation (e.g. ease of handling and non-leaking), and availability (e.g. off-the-shelf supply, ease of storage and low cost) [8, 11, 12, 16, 17, 43]. Current vascular grafts can be divided into five categories namely autografts, allografts, xenografts, synthetic grafts and TEVG.

Autografts possess the most of physiological properties and are biocompatible without either toxicity or immune-rejection. Long-term performances of these grafts

demonstrate the highest percent of 5-year patency among the current grafts, and good compliance and healing with rare formation of intimal hyperplasia [8, 13, 44-46]. Allografts can be obtained from cadaver donors, and have been demonstrated with poor patency than that of autografts, but better than that of synthetic grafts [47]. Xenografts have "off-the-shelf" availability from bovine arteries. These grafts can be considered as the treated natural materials from a decellularisation process, and have been demonstrated with lower infection, thrombosis and reintervention rate than those of synthetic grafts. Being similar to xenografts, synthetic grafts can also be "off-the-shelf" and are mostly based on polyethylene terephthalate (PET), polytetrafluoroethylene (PTFE) and polyurethanes (PU). However, as shown in Table 2-3, these grafts are still far away from the characteristics of an ideal vascular graft. Intimal hyperplasia at distal anastomosis and thrombogenicity of artificial surface are the main reasons that result in mechanical and diameter mismatch between the vascular grafts and native arteries, lack of ECs and de-differentiation of SMCs.

Table 2-2: Characteristics of an ideal vascular graft

Safety	Function	Operation	Availability
Sufficient mechanical support: flow stress and long-term cyclic strain [8, 17]	Long-term patency: resistance to thrombosis, aneurysm and/or calcification in vivo [8, 11, 16, 43]	Surgical handling: suturability and simplicity [8]	"Off-the-shelf": various diameters and lengths [8, 11]
Biocompatibility: no toxicity or immunogenicity [8]	Mechanical matching: vasoactive response, structure remodeling and incorporation to host tissue [11, 16]	Being leak-proof: at the distal anastomosis [12]	Storage: easy [11]
Infection: no [8]	Living and growth potential: [16, 43]		Cost: reasonable manufacturing fee [8]

Table 2-3: The advantages and limitations of current vascular grafts (Adapted from Bujan *et al.* 2004; Chlupac *et al.* 2009)

	Autograft Artery	Autograft Vein	Allograft	Xenograft	Synthetic Grafts
Examples	Internal and external iliac, superficial femoral, internal thoracic arteries	Great saphenous, arm, popliteal and superficial femoral veins	Arteries and large saphenous, umbilical and cryopreserved veins	Bovine carotid or internal thoracic arteries	Woven and knitted PET-based Terylene or Dacron; Porous ePTFE-based Teflon or Gore-Tex; Fibrillar and foamy PU scaffolds
First Trial	Jaboulay and Briau at 1896	Goyannes <i>et al.</i> at 1906	Gross <i>et al.</i> used allo-arteries at 1948	Hurt <i>et al.</i> at 1983	Ku <i>et al.</i> at 1957
Safety	+++	+++	++	++	+++
Function	Very good	~65-75% 5-year patency; Complete healing with rare aneurysms or intimal hyperplasia	~60% 5-year patency; Un-complete healing with degenerative disease and calcifications	~59% 5-year patency; Diseases with calcification, intimal hyperplasia and transmission	~40% 5-year patency; Diseases with intimal hyperplasia; thrombosis, obstruction, suture and aneurysms
Operation	+	+	++	++	+++
Availability	Very limited with a length at several cm	Limited with a diameter of ~1-6 mm and length of <1 m	Limited/good with a length of <1 m	Good with a length of <40 cm	Very good with a diameter of <30 mm and length of <1 m
Ref.	[8, 44]	[8, 13, 44-46]	[8, 44, 48]	[8, 44, 49, 50]	[8, 44, 51-54]

Symbols: +++, Favourable; ++, Less favourable; +, Unfavourable.

Recently, VTE has been proposed for generating engineered, autologous, and "off-the-shelf" TEVG. As shown in Figure 2-2, this is a rapidly developing field. The average citation of VTE in the past 20 years is even higher than that of bone TE (26.3 vs 22.4). VTE is to biomimic the cellular microenvironment for vascular tissue remodeling, strategies of which can be divided into three major categories: (i) biochemical factors (e.g. cytokines and transcription factors), (ii) mechanical stimuli (e.g. stress and strain), and (iii) geometric cues (e.g. ridge/groove arrays and pits).

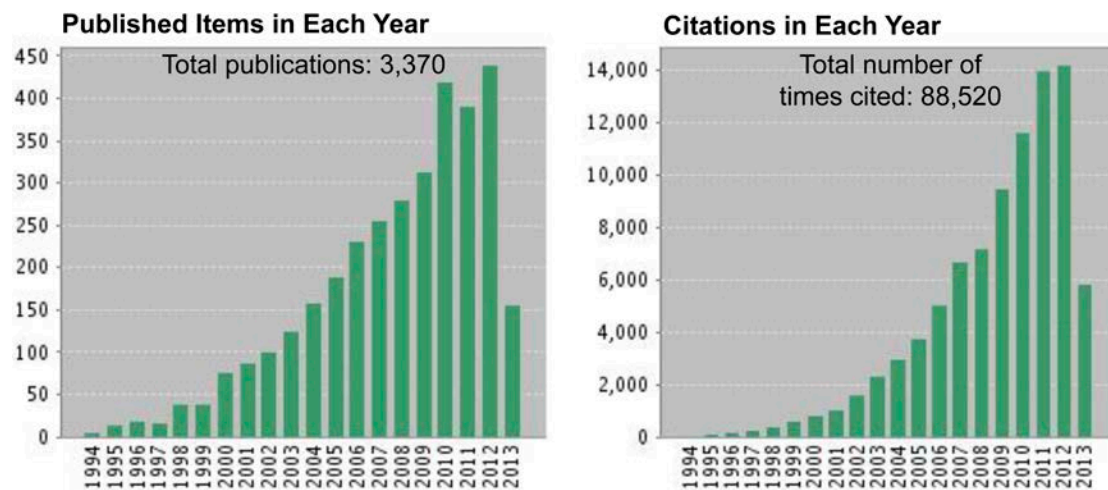


Figure 2-2: Publication and citation numbers in vascular tissue engineering (VTE). (According to the Web of Science, 2013)

For example, the healthy vessels contain lots of type IV collagen and laminin (LN) in tunica media [16]. Vascular scaffolds, in incorporation of LN, have been shown to promote SMCs expression of contractile apparatus [55]. Growth factors such as transforming growth factor beta 1 (TGF- β 1), insulin-like growth factor 1 (IGF-1), heparin and Ang-II have also been used for VTE to promote SMCs differentiation [56]. However, these factors are known to have side effects, if optimal conditions had not been achieved, and could result in atherosclerosis [57]. Recently, mechanical stimuli such as shear stress [58] and cyclic stretch [59-61] have been shown to be

beneficial in regulating vascular cells. However, mechanical stimuli are not suitable for the generation of an "off-the-shelf" TEVG, as the operation is complex and difficult to be replicated *in vivo*. The latest strategy known as geometric cues is designing specific geometric structures to biomimic the complex vascular architecture for cellular behaviour control [59]. Promising outcomes using geometric cues have been shown to align vascular cell organisation as in native vessels [2, 3, 40, 62]. Moreover, compared to the former two strategies, geometric cues could allow the incorporation into the scaffolds for implantation, and are easy available and operation without side effects.

2.1.3 BM Architecture and Function

BM is an important structural feature and cell regulator of native vessels, and localises between tunica intima and media. Constituents of BM are the large insoluble molecules including heparin-sulfate proteoglycans (HSPGs), type IV collagen, LN, and enactin/nidogen. Minimal components include SPARC/BM-40/osteopontin, type XV and XVIII collagen, fibulins, and agrin [63, 64]. These constituents come together to form sheet-like meshwork via a process known as "self-assembly" [64], with a complex architecture consisting of orientated fibers and pores in submicron and nanoscales [9]. Thickness and the pore and fiber diameters vary significantly at different locations and physiological statuses [9, 65]. Large vessels generally have larger pores and fiber diameters than the small ones.

BM Function. The function of BM can be summarised into three aspects namely structural support, vascular development and physiological regulation (Table 2-4). For example, BM helps the maintenance of vascular shape and mechanical support. In

normal vessels, BM serves as a basolateral for both ECs and SMCs, and separates them from each other [64, 66], while in the diseased vessels, SMCs run across BM and migrate into intima, resulting in thrombosis. Vascular diseases such as the Alport syndrome and Knoblach syndrome are often associated with the disordered function of BM [67].

Table 2-4: Function of human vascular BM

Vascular BM	Important Functions	Ref.
Structural Support	<ul style="list-style-type: none"> (i) Compartments to separate the endothelium from the vascular stroma; (ii) Basolateral for the ECs and SMCs; (iii) Vascular shape maintenance; (iv) Mechanical responses to the pulsatile blood flow and vasoconstriction 	[64, 66]
Vascular Development	<ul style="list-style-type: none"> (i) Direct cell-cell contact between pericytes and ECs; (ii) Alteration of the components and structures; (iii) Vascular maturation: SMCs recruitment 	[64, 68, 69]
Biochemical Regulation	<ul style="list-style-type: none"> (i) Vascular hemostasis; (ii) ECs: shape, migration, proliferation and differentiation; (iii) SMCs: orientated organisation, proliferation, activation of contractile function; (iv) Cell-cell interaction: selective permeability for nutrition and growth factors (e.g. VWF) from ECs, SMC and others 	[66, 68, 70]

During vascular development, mesenchymally divided pericytes embed into BM, and interact intimately with ECs through a direct cell-cell contact and interdigitation [69], revealing final similarities (e.g. the contractile function) to SMCs in larger vessels. Furthermore, the meshwork of BM could accumulate von Willebrand factor (vWF) to recruit SMCs for vascular modeling [68].

Interestingly, BM also plays a crucial role for the physiological regulation of vascular vessels. BM of normal blood vessels is shared by SMCs and ECs on its both surfaces, and directly interacts with them to transmit signals. During vascular remodeling process, SMCs anchor BM via a dystrophin–glycoprotein complex (DGC) to bind to LN [71, 72]. The SMCs multi-layers organise along a similar direction according to BM fibers [70]. Besides those, type IV collagen and LN of BM are crucial for the maintenance of SMCs contractile phenotypes [15], while SMCs *in vitro* tend to lose the contractile phenotype and shift into a synthetic status, with over-secretion of ECM, but lack of organised contractile apparatus [29, 69]. ECs anchor BM via an interaction between integrin and LN or type IV collagen [64]. The late one is able to promote ECs proliferation and migration. Moreover, BM geometric architecture has been shown to influence the shape, migration, proliferation and differentiation of ECs [9].

BM Biomimicry. Currently, BM biomimicry for VTE focuses on the chemical components such as LN, type IV collagen. Study has suggested that LN could up-regulate contractile markers' expression in SMCs [55], while electrospun nanofibrous scaffolds in incorporation of type IV collagen triple peptides (Cys-Ala-Gly), resulted in significant increase of ECs adhesion, but decrease of SMCs adhesion [73]. Compared to BM components, researches that biomimic the BM geometric architectures are very limited [68, 74-77]. These include the decellularized arteries and veins [76, 77], amniotic membranes [74], and porous or nano/micropatterned polymeric films [75]. A study by Liliensiek *et al.* [9] firstly preformed a thorough characterisation on human BM architecture. However, so far, no scaffold design for VTE that targets to biomimic the BM complex architecture has been proposed.

2.1.4 Vascular Neotissue Regeneration

Vascular neotissue regeneration of TEVG has been predicated from the direct contribution of seeded cells when scaffolds degrade [78]. However, the early evidence that significant cell loss (up to ~95 %) occurred after the first 24 h exposure to pulsatile flow [79] suggested that the seeded cells might not have direct contribution as cellular components to vascular neotissue. Recently, the study performed by Roh *et al.* [80] exhibited how the neotissue regeneration occurred for TEVG *in vivo*. The results suggested that TEVG transformed into mature vessel might follow an inflammation-mediated remodeling (Figure 2-3), which involved the protein absorption (e.g. the integrin of inflammatory to recognise the biomaterials surface), complement activation for mediating the inflammation, macrophage adhesion to biomaterials via chemkines, giant cell formation for the degradation of large biomaterials fragments (e.g. reactive oxygen intermediates, oxygen free radicals, enzymes and acid), and ECM remodeling (e.g. M-2 macrophage for ECM secretion and degradation) [15]. Stem cells on seeded grafts could act as an indirect role for the macrophage recruitment, but not as a direct cell component of neotissue. However, other study also showed that stem cells could be retained when they got differentiation into SMCs [81]. Nevertheless, these observations clearly pointed out that vascular scaffolds should have (i) sufficient open interconnected pores to facilitate cell transmural recruitment, and (ii) capability of guiding the cell reorganisation. These further emphasise the importance of vascular BM architecture, and should give helpful guidance for vascular scaffold design. Besides that, stem cells have shown the important role in vascular neotissue regeneration, and are promising for VTE applications.

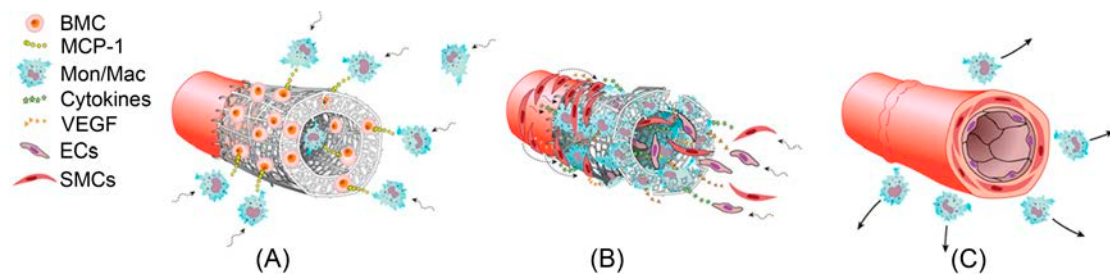


Figure 2-3: Mechanism for vascular neotissue regeneration. BMCs release MCP-1 and recruit Mon/Mac towards the grafts (A). Mon/Mac infiltrate and release multiple angiogenic cytokines and growth factors (e.g. VEGF) during scaffold degradation, to recruit SMCs and ECs onto grafts (B). Mon/Mac migrate away after complete scaffold degradation leaving behind autologous TEVG (C). (BMC: bone marrow stem cells; MCP-1: monocyte chemoattractant protein-1; Mon/Mac: monocyte/macrophage; VEGF: vascular endothelial growth factor) (Adapted from Roh *et al.* 2010 [80])

2.2 Stem Cells for Engineered BM

The gold standard of cellular source for TEVG is the patients' autologous cells including FBs, SMCs and ECs. However, the mature differentiated cells have a limited self-renewed capability, and tend to lose their activity during the *in vitro* culture expansion [11, 82]. Stem cells have shown to be promising potential cell source for VTE applications [83-85]. This section summarises the exciting work that has been reported in this area, with a focus on the applications and current research challenges.

2.2.1 Stem Cells

Stem cells have tremendous potential for regenerative medicine such as VTE [85]. Compared to the traditional cell sources, stem cells are easily available from various tissues (e.g. muscle, bone marrow and fat [84]), and have high expansion potential [86], reproducible phenotype [85] and potential to differentiate into functional vascular cells (e.g. SMCs [87] and ECs [88]). Current methods for the isolation of stem cells include the (i) Percoll[®] gradient centrifugation, (ii) selection via the

preferential cell adhesion, and (iii) sorting via immunophenotyping [84, 85]. These isolated stem cells can be the mononuclear cells from bone marrow (BM-MNCs), MSCs from fat, bone marrow and muscle, pericytes from capillaries and endothelial precursor cells (EPCs) from bone marrow and cord blood.

BM-MNCs are a heterogeneous population including MSCs, ECs, EPCs and other cells and therefore, could be used as the cell source for SMCs and/or ECs [84]. BM-MNCs can be pre-differentiated before implantation (e.g. SMCs [89]) or implanted in their undifferentiated status as the first human clinical study conducted in Japan [14]. However, it is still unclear why TEVG with BM-MNCs after implantation resulted in a graft composed of SMCs and ECs, although the inflammatory has been considered to be crucial for the vascular remodeling [80, 84]. Pericytes have also been used as a SMCs source for TEVG construction [90], while EPCs are mostly used as the cell source instead of ECs for vascularisation [91].

Compared to the BM-MNCs, pericytes and EPCs, MSCs are a homogeneous population with a typical immunophenotype (Table 2-5), and can be harvested from almost every organ, faster expansion to the differentiated vascular cells, and lacking expression of major histocompatibility complex (MHC) II antigens [84, 92]. TEVG from MSCs could be capable of significantly saving the waiting time to obtain the clinically required cell numbers and allowing the immune-privilege for allogeneic cell delivery [93], leading to the "off-the-shelf" vascular grafts. Furthermore, recent study demonstrated that bone marrow derived MSCs (BM-MSCs) have antithrombotic properties to inhibit platelet adhesion as ECs do [94]. These unique properties make MSCs to be attractive for TEVG construction.

Table 2-5: Minimal criteria for the identification of MSCs*

Criteria	Performances
Morphology	Plastic adhesion
Immuno-phenotype	Positivity (>95 %) for CD73, CD90 and CD105 surface molecules; Negativity (>95%) for CD14, CD34, CD45 and human leukocyte antigen-DR (HLA-DR) surface molecules
Stemness	Multi-differentiation potential to fat, cartilage and bone

*According to the Mesenchymal and Tissue Stem Cell Committee of the International Society for Cellular therapy (ISCT) (Adapted from Mariani *et al.* 2012 [95]).

2.2.2 Stem Cells for VTE Applications

MSCs have been the subject of intensive study for VTE [15]. Gong *et al.* [96] studied the differentiation of BM-MSCs into SMCs using a bioreactor system and successfully constructed a small-diameter TEVG. Wang *et al.* [97] used human adipose MSCs and PGA mesh, in incorporation of growth factors and a pulsatile bioreactor system, obtained the similar small-diameter TEVG expressing the SMCs phenotype. Compared to the traditional cell source-SMCs, MSCs possess several advantages for TEVG generation (Table 2-6). Interestingly, although MSCs are multi-differentiated, lots of current studies utilised MSCs as a cell source instead of SMCs. This could be a reasonable trend as MSCs themselves share certain SMCs phenotype [87, 96]. Furthermore, MSCs are found to secrete growth factors (e.g. MCP-1) to recruit ECs from circulation system for endothelialisation [80].

In vivo animal studies using MSCs-seeded TEVG have provided encouraging results [15]. Hashi *et al.* [94] engineered a small-diameter TEVG using BM-MSCs and PLLA mats, and found that MSCs-seeded grafts exhibited a long-term patency, while scaffolds alone resulted in obvious platelet adhesion and thrombus formation. Zhang

et al. [98] engineered a three-layered tubular scaffold seeded with MSCs and implanted it into a dog model. The grafts exhibited a long-term patency (3 months) with confluent ECs on lumen. Zhao *et al.* [99] implanted the decellularised arterial scaffold with pre-differentiated MSCs seeding into a sheep model, and found that the grafts remained patency and antithrombotic over 5 months, while unseeded grafts failed in 2 weeks.

Table 2-6: Advantages of using MSCs for vascular tissue regeneration as compared to SMCs

Characteristics	SMCs	MSCs	Ref.
Accessibility	Limited self-renew ability; Autologous; Over proliferation in dedifferentiated status → intimal hyperplasia	Easy accessibility; Autologous and allogeneic cell; Self-renewable and high expansion potential	[86]
Phenotype	Dedifferentiation → lose of the contractile apparatus	Reproducible phenotype and stemness within 1-million-fold expansion; Lack of sufficient SMCs contractile markers	[86]
Immune Response	Positive expression of MHC II and T cell co-stimulators → immune-rejection for allogeneic cells; Potential tumor formation	Lack of MHC II and co-stimulator for T cells (CD 40, 80 and 86) → immune-privilege for allogeneic cells and differentiation; No tumor formation potential; Ameliorate tissue damage via a paracrine mechanism	[15, 85, 92, 93]

Interestingly, Mirza *et al.* [81] used green fluorescence protein (GFP)-labeled MSCs and seeded them on a PU scaffold. Using a rat model, they found that MSCs-seeded group caused better endothelisation. Interestingly, they observed the co-expressed GFP and SMC markers in MSCs, supporting the hypothesis that MSCs can differentiate into SMCs *in vivo*, and be retained if they differentiated into SMCs

successfully. However, the MSCs-differentiated SMCs exhibited a slight difference in phenotype from mature SMCs, indicating that probably only a partial differentiation occurred for MSCs [85]. In the next section, the focus will be on how physiological environment to differentiate MSCs and what kinds of strategies could be performed potentially for TEVG biomimicry.

2.2.3 MSCs Differentiation into SMCs

MSCs to function as the cell source for TEVG are needed to differentiate into SMCs or ECs. Such immunophenotype differentiation towards vascular cells can be distinguished by the expression of identified biomarkers and functional assays [85]. Table 2-7 summarises the criteria used for MSCs differentiation identification.

Table 2-7: Criteria for MSCs differentiation towards vascular cells

Vascular Cells	Performances	Ref.
SMCs	Positive immunophenotype: Early-term marker: SM- α -actin, SM22; Middle-term: calponin; Late-term: SM-MHC, smoothelin	[87, 100]
ECs	Positive immunophenotype: Platelet ECs adhesion molecular: CD31; Vascular endothelial (VE)-cadherin; Von Willibrand Factor (vWF); Functional assay: Tubular formation; Uptake of acetylated low-density lipoproteins	[85]

It is worth noting that smooth muscle (SM) alpha actin (SM- α -actin) and calponin can also be positively expressed in undifferentiated MSCs, while the late-term markers of smoothelin and SM myosin heavy chain (SM-MHC) can only be observed in the mature contractile SMCs [96, 100]. It should also note that MSCs, although there exists standard criteria for distinguishing the differentiation, could have slight

variation in the growth capability, gene expression and differentiated potential. For example, the MSCs from umbilical cord have been reported to have the longest and highest proliferated potential during *in vitro* expansion [101]. However, they could not differentiate towards an adipogenic lineage [102]. Such variations should be taken into consideration when MSCs were used for VTE applications. Differentiation of MSCs into vascular cells could be triggered by growth factors, mechanical stimuli and artificial scaffold matrix.

Growth Factors. Growth factors are multifaceted in regulating MSCs fate. As shown in Table 2-8, the growth factors used for vascular cell differentiation include TGF- β 1, BMP, PDGF, FGF and VEGF [85]. TGF- β 1 is known to differentiate MSCs towards a SMCs-like phenotype, while PDGF and VEGF could differentiate MSCs following ECs pathways. An interesting thing is that these factors can also be released from SMCs, ECs and even MSCs themselves (e.g. PDGF, VEGF, MPC-1) [83], suggesting that vascular cells could communicate each other via a paracrine pathway. Besides the growth factors, biochemical factors such as all-trans retinoic acid have also been used to differentiate MSCs into SMCs [57, 103]. Interestingly, recent studies have observed that a combination of different growth/biochemical factors made MSCs differentiate into SMCs to be more effective than the single factor [57, 87]. However, these factors are generally derived from animals, expensive to use, and difficult to control the optimum concentration for effective differentiation [104]. The mechanism that MSCs differentiation triggered by these growth factors remained not well-known, and side effects have often occurred. For example, TGF- β 1 and BMP4 could also promote MSCs differentiation into osteoblasts and adipocytes, leading to potential atherosclerosis during the vascular tissue remodeling [57]. Similarly, retinoic acid has

also been known as a powerful teratogen [104].

Table 2-8: Effects of biochemical factors on MSCs differentiation

Biochemical Factors	Cell Sources	Key Results	Ref.
VEGF	Human bone marrow MSCs	Increased KDR and FLT-1 expression (2 % serum); Capillary-like structures	[105]
TGF- β 1	Human embryonic MSCs Human bone marrow MSCs	Increased SM- α -actin, calponin and SM-MHC expression: → TGF β 1/Alk5 pathway (0 % serum) → Notch signaling (10 % serum) → ERK/MAPK inhibition	[106-108]
All-trans retinoic acid	Rabbit & human bone marrow MSCs	Increased myocardin, caldesmon, SM22 and SM-MHC	[57, 103]
BMP4	Human adipose MSCs	Increased SM- α -actin, SM22, calponin and SM-MHC expression (TGF- β 1, 1 % serum); Contractile property	[87]

Mechanical Stimulation. Mechanical stimuli are to biomimic the mechanical environment that vascular cells encounter. In native blood vessels, ECs within endothelium experience continuous fluid shear stress of 10-20 dynes/cm³ [109]. Meanwhile, both ECs on lumen and SMCs in tunica media are subjected to cyclic strain from pulsatile stress (5-30 % strain and 30-90 cycles/min [110]). Therefore, *in vitro* shear stress and strain models have been developed for understanding the mechanical influence on MSCs differentiation [85].

Contrary results have been observed for the shear stress studies. One group exposed fibroblast-like stromal cells to shear flow, and found that cells could have enhanced expression of SMCs-specific markers [111]. In contrast, the other study carried out by Wang *et al.* [112] observed that murine embryonic MSCs subjected to shear flow

differentiated towards ECs-like cells. However, studies have not examined the ECs or SMCs markers when the differentiation of MSCs into SMCs or ECs was argued, respectively. Therefore, the findings are not sufficient to claim that MSCs have gotten a full differentiation. One possible reason for the contrary observation might be that stimuli from flow shear stress are un-specific for MSCs differentiation. An interesting thing is that both studies have found that MSCs did align along a direction parallel to the flow. However, in native vessels, SMCs are perpendicular to the blood flow. Using flow shear stimuli to trigger circumferential alignment of SMCs remains a big challenge.

The strain model can be uniaxial or equiaxial that involves cells cultured on an elastic substrate [85]. Kurpinski *et al.* [60] demonstrated that uniaxial strain could increase the calponin expression in MSCs, decline the cartilage matrix markers, and align MSCs being perpendicular to the strain axis, whereas equiaxial strain tended to decrease the SMCs makers' expression [85]. These exciting findings suggest that mechanical strain could be a suitable strategy for MSCs differentiation. However, both the uniaxial and equiaxial strains exist in native vessels. How MSCs response to the strains *in vivo* is still unknown. An important observation is that when uniaxial strain was applied parallel to a micropatterned substrate, MSCs exhibited enhanced SMCs markers' expression, while when uniaxial strain was perpendicular to the micropatterns, MSCs showed a decline expression of SMCs markers [60], indicating that geometric structures could influence MSCs differentiation.

Artificial Scaffold Matrix. Scaffold matrix serves as a "niche" for MSCs, of which scaffold rigidity and surface geometric structures could influence MSCs behaviour.

Rigidity is known as a bulk property of vascular scaffolds and characterised by the Young's Modulus. The rigidity of native tissues from brain to bone varies within three-orders magnitude [85]. It has been hypothesised that soft scaffold matrix could mimic the brain and induce MSCs differentiation in a neurogenic pathway. A stiffer one mimics the muscle and differentiates MSCs following a myogenic pathway, and a rigid one mimics the bone and differentiates MSCs along an osteogenic pathway [15]. Park *et al.* [113] demonstrated that MSCs cultured on stiffer substrates expressed the higher myogenic SM- α -actin and calponin 1, but elevated the expression of chondrogenic marker of collagen-II and adipogenic marker of lipoprotein lipase on soft substrates. Moreover, stiffer substrates appeared to facilitate the stress filament formation via a Rho GTPase in-dependent pathway. However, the organisation of cells and stress filaments remains in a random manner, deviated from the ordered architecture of native vessels, while the recent study demonstrated that cellular alignment was important for muscle cells (e.g. cardiomyocyte) to realise the contractile function [114]. Geometric structures refer to the surface nano/micropatterns of VTE scaffolds. Such cues have shown to be promising potential in regulating cellular alignment and SMCs markers expression [28, 115].

2.3 Geometric Cues for Engineered BM

On tunica media side of BM, SMCs organise into a circumferential alignment. Various strategies have been proposed for VTE to realise cell alignment, which can be divided into two categories: chemical cues (e.g. glial cell line-derived neurotrophic factor (GDNF) and fibronectin (Fn)) and physical cues such as the mechanical stimuli (e.g. cyclic strain [60], shear stress [116]), electrical cues [117] and topographical geometries. Among these strategies, geometric cues hold great potential for TEVG

applications because they have no requirement of external stimuli, and are more stable than chemical cues in regards to the surgical durability and degradation resistance.

2.3.1 Fabrication of Anisotropic Geometries

For anisotropic tissues (e.g. TEVG), the geometric cues used can typically be divided into two main categories: orientated fibers [118] and ridge/groove arrays [2]. Fibrous geometric cues possess a unique advantage of high porosity, and can be generated from the adapted electrospinning and flow shear [118, 119], while the substrates with ridge/groove arrays have better mechanical properties, and are able to be fabricated from various methods such as lithography [104], soft lithography [120], direct laser writing [121] and using abrasives [122]. Table 2-9 summarises the strategies that are mostly used for the generation of anisotropic geometry cues for TE applications.

Electrospinning. Electrospinning uses an adapted collector such as the two frames and the rotating disc or mandrel instead of the traditional flat one. On the traditional flat collector, electrospun fibers are often deposited as randomly orientated and nonwoven mats, due to the bending instability of the spinning jet [118]. Interestingly, with rotating of a disc, highly orientated fibers can be obtained [123]. Similarly, orientated fibers have been obtained by using a rotating mandrel [124]. Comparatively, electrospinning using a disc is able to generate highly orientated fibers at a relatively smaller rotating speed, while electrospinning using a mandrel generally requires a speed larger than 1,000 rpm. Several reasons could contribute to the fiber orientation, which include the dramatic increase of field strength at the disc edge, uniaxial pulling from rotating as well as the air flow [118]. However, these two

methods are easy to induce discontinuous fibers due to the large pulling from rotating, and peeling is difficult. An alternative method using a collector consisting of two conductive frames separated by a void gap has also been demonstrated to align fibers effectively [125]. The underlying mechanism has been proposed that under electrostatic forces in the opposite directions, fibers between the two frames could be stretched to align themselves perpendicular to the edge of the gap [118]. Compared to the rotating disc or mandrel, this method facilitates the transfer of aligned fibers to other substrate and allows the stack of aligned fibers at different angles in alternative layers. However, the width of the gap is limited up to several centimeters [118, 125].

Orientated fibrous mats from electrospinning hold advantages of a high porosity and could be applicable for large scale of biomaterials. Limitations of such technologies include: (i) the use of chemical solvents, since the potential risk of residuals leads to problems with regard to the safety considerations [126], (ii) the use of a high voltage and complex setup, but a low efficiency of aligned fiber yield, (iii) the poor mechanical property that remains a big concern on the applications of electrospinning fibers for mechano-active tissue regeneration (e.g. TEVG with a burst strength robust enough) [27, 127].

Flow Shear. Orientated fibers from flow shear are using a hydrodynamic flow. A study carried out by Lanfer *et al.* [128] firstly reported this method with a setup of the microfluidic system, substrate and collagen solution. Flow shear allows the preparation of aligned collagen fibers with a variable orientation, density and morphologies. A mechanism behind the fiber orientation involves the combination of collagen fibrillogenesis and flow shear force. If one end of the fibril attaches to the

substrate surface, the streaming fluid can align the remaining part in a position of low hydrodynamic resistance [128]. Compared to electrospinning, this technique is easier and safer for operation, and has a potential to be applicable for a large scale production. However, this method remains being limited for TE applications due to problems such as too small area of fibrous mats (limited to several square millimeters), in-homogenous morphologies and low alignment efficiency. In addition, how to peel fibers from substrates for further processing steps and applications is also a big problem yet to be solved.

Lithography. Lithographic processing involves a wide range of techniques that allow specific well-defined geometric structures to be realised for the copy of biological patterns (e.g. cells, ECM fibers and proteins) [129]. Such methods utilise UV, X-ray, and the beams of electrons and ions, and share an underlying principle to transfer the patterns from a master. The procedures include coating of surface, exposure to irradiation, development and washing. The mask used can be a negative or positive resist that occurs cross-links or deteriorates after the action of exposure (Figure 2-4). Direct lithography allows the precise control of structure parameters (e.g. groove width and depth) and is capable of fabricating various designed geometries (Table 2-9). However, it requires a complementary set of patterning tools and processes, and the use of toxic chemical solvents for the developmental procedures [121, 126, 129]. Furthermore, direct lithography is compatible with a limited scale of materials that should be photo-resistant such as silicon [130] and PUA [104], while these materials often have little value for the translational research as they are not biodegradable [131].

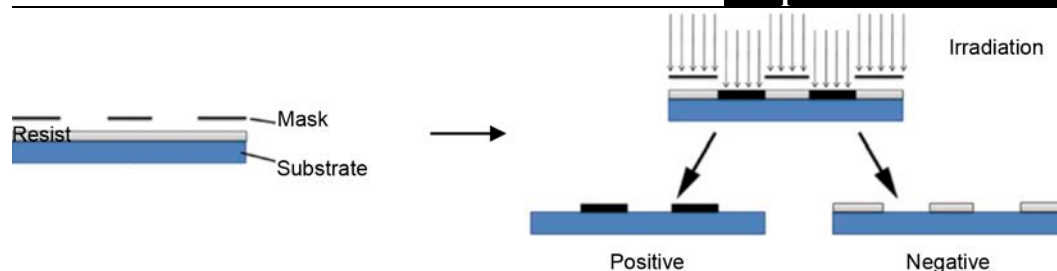


Figure 2-4: Schematic diagram illustrating the positive and negative resist for lithography. (Adapted from Roach *et al.* 2010 [129])

Soft Lithography. Soft lithography is the most common and widely used method for nano/micropatterns via self-assembly and replica modeling, with feature sizes ranging from nano to hundreds of micrometers [132]. During the process, an elastomeric stamp of patterned relief structures on its surface is applied to create the patterned structures (Table 2-9). Compared to the direct lithography, soft lithography extends the applicability of lithography to many biodegradable polymers such as collagen [3], PLA [117], PCL [132], poly(methyl methacrylate) (PMMA) [133] and poly(lactic-co-glycolic acid) (PLGA) [134]). Moreover, it allows fabrication of structures in different shapes. However, soft lithography needs a pre-fabricated model and has an additional procedure to peel substrate from the model, which often results in structural defects for the large-scale feature generation [126, 132]. Furthermore, geometric cues generated from this technique require the use of chemical solvents, and often lack porosity that fibrous mats have.

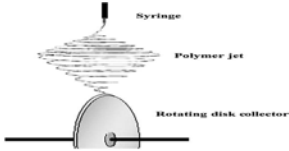
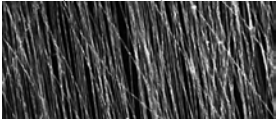
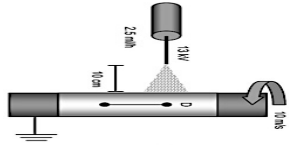
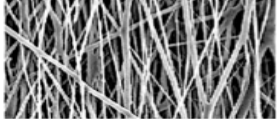
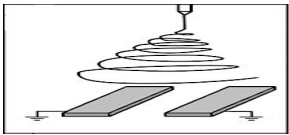
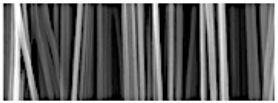
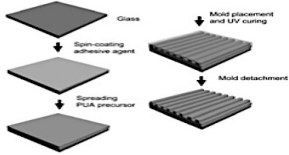
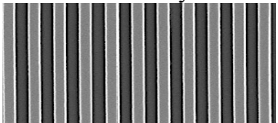
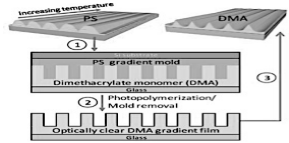
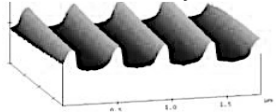
Direct Laser Writing. Direct laser writing offers an excellent strategy for TE to create geometric cues at precise structure parameter control. Compared to electrospinning and soft lithography, this technique avoids the involvement of toxic solvents, and fabricates structures in a rapid, non-contact and single-step manner [121]. So far, direct laser writing has been developed for biomaterials such as PCL

[135], PLC [121] and poly(D-lactic acid) (PDLA) [132]. The underlying mechanism, applications and unmet problems in regard of direct laser writing for biomedical applications will be reviewed in Section 2.4 in detail.

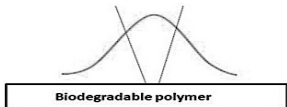
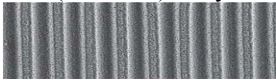
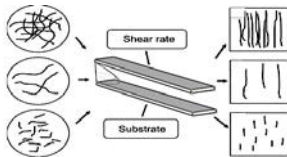
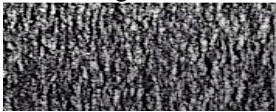
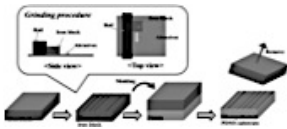




Abrasive. Another method for the generation of orientated ridge/groove arrays is using abrasives, with the first report performed by Shimizu *et al.* [122]. This technique allows fabrication in a simple and low-cost manner. Firstly, the micropatterns are created on an iron block through grinding on sandpaper in one direction, which is then used as a model to transfer geometries on PDMS substrate. Structural parameters can be variable if different sandpapers were used. However, topographical features generated from this method result in destruction of substrates accompanying with non-clean features. Furthermore, using abrasives probably requires the substrates to be more rigid with a large thickness, and might not be suitable for the thin film surface patterning that is extensively applied for VTE [22].

Besides the orientated fibers and ridge/groove arrays, topographical features generated from top-down freezing and self-forming ion beam procedures have also been reported as cues to regulate cellular behaviour [136, 137]. However, to-date no ideal geometric cues to biomimic the BM have been proposed. It has become an urgent need to develop novel strategies for creating geometric cues in a reproducible, simple, solvent-free and homogeneous manner for facilitating the "off-the-shelf" TEVG. Moreover, the strategies should also allow geometric cues to be compatible with sufficient porosity and ease of construction for 3D tubular scaffolds.

Table 2-9: Technologies for the fabrication of anisotropic topographical geometry cues

Strategies	Setup*	Examples*	Advantages	Main Limitations	Ref.	
Electrospinning	(i) Disk Rotating			Highly orientated fibers with high porosity Being applicable for various polymers	Potential toxic residue due to the use of solvent; Low efficiency with a complex setup;	[123]
	(ii) Mandrel Rotating				Poor mechanical properties; Safety concern for the high voltage and rotating speed	[124]
	(iii) Two Frames					
Lithography	(i) Direct Lithography			Precise control of parameters; Various geometries	Cumbersome set of patterning tools and procedures; Toxic solvent use; Limited applicable materials	[104]
	(ii) Soft Lithography			Various shapes with proper tunable parameters; Increased scale for applicability	Cumbersome set of patterning tools and procedures; Toxic solvent use	[120]

Continued

Direct Laser Writing		P(LLA-CL) arrays 	Precise control of parameters; Various geometries	High cost with specific technique require;	[121]
Flow Shear		Collagen fibers 	Easy and safe operation	Low efficiency of alignment; Use of solvent; Difficult for a large scale	[119]
Abrasive		PDMS arrays 	Highly orientated features	Limited to stiff materials	[122]
Top-Down Freezing Procedure		Collagen walls 	High porosity	Specific technique require	[136]
Self-Forming Ion Beam Procedure	<i>Under patent</i>	Silicon waves 	Disconnected and orientated waves	Poor performance on cell alignment	[137]

*Figures were adapted in sequence from Xu *et al.* 2004; Baker *et al.* 2008; Li *et al.* 2004; Lee *et al.* 2012; Sun *et al.* 2010; Yeong *et al.* 2010; Lanfer *et al.* 2010; Shimizu *et al.* 2009; Bozkurt *et al.* 2009; and Tocce *et al.* 2010, respectively.

Abbreviations: P(LLA-CL): copolymer of PLA and PCL; PUA: polyurethane acrylate; DMA: dimethacrylate; and PDMS: polydimethylsiloxane.

2.3.2 Vascular Cell Responses to Geometric Cues

Cells can recognise the anisotropy of engineered architecture from fibers and ridge/groove arrays in either nano or micron-scales. Compared to the isotropic morphologies, vascular cells such as FBs [138, 139], SMCs [28, 123, 140], ECs [134] and MSCs [43, 113, 141] on the orientated fibers and ridge/groove arrays have revealed a robust capability of self-alignment. The cellular alignment in TE has also been observed for cardiomyocytes [142], C2C12 myoblasts [122], schwann cells [143], osteoblasts [144, 145], liver carcinoma cells [146].

2.3.2.1 Cellular Alignment and Elongation

Cellular response to the topographical features is intuitive, and has been used for cell behaviour control since 1964 [147]. It is generally accepted that cells elongate and align towards the anisotropic features via a mechanism known as "contact guidance". During the dynamic process, focal adhesions and actin filaments are confined on intervening ridges, leading to orientation of the long axe of focal adhesions along the anisotropic features [142, 148]. The recent study using a ridge/groove gradient further explores the underlying mechanisms, and suggests that the orientation of focal adhesion is because of the anisotropic rigidity and deformation resistance of ridge/groove arrays that stabilise the focal adhesions enriched on ridges for a final co-orientation with ridges [138]. On the other hand, promotion of cell marginal expansion in the ridge direction in incorporation of the inhibition of cell lateral extension across grooves, might also contribute to the elongated cell morphology [149]. This mechanism can be evidenced by the rapid retraction of protrusion along the perpendicular direction of ridges and invading in the parallel direction [150].

Orientated Ridge/Groove Arrays. The scale of ridge/groove arrays is crucial for eliciting cell responses. Recent studies have shown that ridge depth can dictate the extent to which cells will respond to a given lateral dimension [137, 145]. Human corneal epithelial cells (HCECs) do not preferentially align to the underlying arrays when the ridge depth is less than 150 nm [151]. While when the ridge depth increases from 150 to 800 nm, enhanced cell alignment and elongation have been observed [137, 145, 151]. Interestingly, the minimal ridge depth reported for osteoblasts can be as small as 33 nm [144, 145]. This indicates that cells might have specific requirements on ridge depth. Such phenomena can be reasonable as cells from different tissues are surrounded with ECM at different scales (e.g. sub-micron to micron-scale ECM for HCECs [137] and nonmetric ECM for bone [145])

Cells are known to align less on ridge/groove arrays with nanodimensions and more on features with micron dimensions [144]. The increase in groove width is found to increase the cellular alignment and elongation for HCECs [137]. Cells on the features with a width of 4 μm have much higher alignment efficiency as compared to the nanoscale geometries. However, too big sizes especially for a groove width of $>50 \mu\text{m}$, often result in delayed and lower alignment, and cellular confluence is required before alignment occurs [126]. As early as 1970s, Ohara and Buck [145, 148] have hypothesised that cells cannot align to geometric features if focal adhesions fail to sense the arrays with an excessive pitch. The delayed alignment of cells are probably because that if the groove width were larger than the cell dimensions, the focal adhesions will sense the underlying substrates as isotropic rigidity for the cells, resulting in cell morphologies as that observed on flat surfaces [138].

Beside the ridge depth and width, the presence of crossing ridges can also affect cellular alignment towards the ridges [139]. Too small an aspect ratio between the parallel and perpendicular directions could result in significant reduced cell alignment.

Orientated Fibrous Mats. Anisotropic fibrous mats are well-studied for neural regeneration to provide spatial guidance for the neurite extension following the fiber directions [147]. However, *in vivo* study showed that neurite preferred to grow perpendicularly in the direction of fiber alignment at the implant-brain interface [152]. A "Janus feature" is observed for dorsal root ganglia (DRG) cultured at border between the random and aligned fibers, which indicates a radial organisation of neurite on the random fiber side, but orientated growth at the side with aligned fibers [131]. Interestingly, DRG on an double-layered mats are able to sense both the anisotropy of fiber layers instead of the top-layer only [131]. A further study suggests the neurite can align following the crossing fibers, while DRG remain in the mats direction [143]. Orientated fibers are also used to biomimic the ECM of tunica media, and realise SMCs to align into a spindle-like contractile phenotype [123].

Other Factors. Mechanical stimuli (e.g. cyclic strain) impacted on nanopatterns could cause cellular reorientation in a perpendicular direction to ridges [144], suggesting that cells probably have preferential response to the mechanical stimuli. Furthermore, cell seeding density and serum of medium can also influence cellular alignment to the anisotropic features. Higher seeding density can result in better initial cell alignment [43, 114], while the lack of serum dramatically inhibits HCECs alignment, compared to the culture in normal medium [153].

2.3.2.2 Cellular Migration

Cell migration plays a critical role in a variety of physiological and pathological phenomena [139]. The migration of FBs, SMCs, ECs and MSCs can contribute to vascular wound healing and tissue regeneration [80]. It has been known that compared to continuous surfaces, FBs on orientated ridge/groove arrays have considerable enhancement at the migration along ridge direction, [138]. The presence of crossing ridges can further increase cell mobility, particularly for the grids that have a smaller size than the cells [139]. Similarly, ECs have also been found to migrate preferentially along the long axis of ridges [154]. Moreover, on a ridge/groove gradient (1-9.1 μm in groove width), FBs exhibited a migration speed dependent on the ridge density, with the fastest speed observed on an intermediate density of ridge patterns, but lower speeds on the denser or sparse ridge patterns [138]. In addition, lower ridge depth tends to fast cellular migration along the ridges [139]. All these studies suggest that vascular scaffolds with anisotropic ridge/groove arrays could be able to guide cell migration during vascular remodeling.

2.3.2.3 Cellular Adhesion and Proliferation

Cellular adhesion and proliferation are other vital functions that may affect the development of TEVG. Xu *et al.* [123] demonstrated that SMCs grew on the aligned fibers of an average diameter of 500 nm achieved increased rates of adhesion and proliferation. In contrast, Thakar *et al.* [61, 155] cultured SMCs on orientated ridge/groove arrays and observed reduced SMCs proliferation and DNA synthesis (10 and 2.8 μm in groove width and depth, respectively). ECs from rat arteries have been shown to enhance the cell proliferation on titanium nano/micropatterns [156], while

cells from human umbilical veins tend to respond as decreased proliferation to small ridge/groove arrays (e.g. 400 and 80 nm pitch) [154]. Besides these, C2C12 myoblasts exhibit similar proliferation on the flat and micropatterned surfaces [122]. These observations suggest that cell proliferation on geometric cues is heterogeneous, depending on the substrate and cell source. Interestingly, HCECs on the nanopatterns (e.g. 400 nm pitch) are observed with enhanced adhesion strength against flow shear [130]. Such function of ridge/groove arrays should benefit the recruited ECs adhesion for stable endothelialisation.

2.3.2.4 Cellular Differentiation

To increase the possibility of *in vivo* adaptation, vascular grafts are expected to be capable of maintaining an appropriate phenotype of cells as in native healthy blood vessels [157]. It has become clear that topographical geometry cues are crucial in regulating the cell shape and function for VTE applications. Mechanism behind these regulations is known as a mechano-transduction pathway that could be direct and/or indirect [144]. Direct mechanotransduction relies on the links between a cell shape and nucleus through the cytoskeleton and nuclear lamins. Cellular elongation orientates cytoskeleton, up-regulates and move nuclear lamins onto the nucleus periphery, and deforms nucleus shapes, resulting in genomic adaptation [158]. Indirect mechanotransduction involves chemical signaling cascades that can be initiated by focal adhesion-associated proteins [159], and probably includes the integrin-mediated Rho GTPase and the FAK signaling network [160].

SMCs. SMCs of current TEVG are easy to lose their contractile apparatus and shift into a synthetic phenotype, with excessive proliferation, ECM secretion, and

migration into the intimal regions that lead to intimal hyperplasia [15, 29]. These SMCs typically exhibit the "hill and valley" morphologies, well spread, and random organisation [56]. Furthermore, the recent opinion suggests that synthetic phenotype of SMCs dominates with increasing passage number in culture, although the status is reversible both *in vitro* and *in vivo* [28]. Thakar *et al.* [61] suggested that micropatterned topographies could be used for SMCs regulation. In a recent study, they observed that micropatterned geometric cues could regulate SMCs as what TGF- β 1 does [155]. Williams *et al.* [28] confirmed the findings. In the study, micropatterns were found to be as effective as TGF- β 1 on up-regulating the expression of SM- α -actin and SM-MHC in the low passage SMCs. However, the regulation seems to be cell passage dependent, as the enhancement has not been observed for the large passage SMCs. Another study carried out by Cao *et al.* [115] cultured primary SMCs on microchannel scaffolds and observed similar effects on up-regulated SMCs contractile markers' expression including the SM- α -actin, calponin and SM-MHC. This study further indicated that the total amount of deposited elastin and collagen could be lower, when SMCs got aligned and elongated. These observations suggest that topographical geometric cues are capable of regulating the expression of SMCs contractile genes, although SMCs exhibit inherent limitations for TEVG construction.

MSCs. The effects of topographical geometric cues on MSCs differentiation are complex. Xie *et al.* [161] cultured human embryonic MSCs on the random and aligned fibrous mats, and found that after retinoic treatment, MSCs on the aligned fibers achieved enhanced differentiation into the neural lineage with guided neurite outgrowth. Similar observations are found for MSCs cultured on nanoscale ridge/groove arrays, even without drug treatment [104]. These findings suggest that

topographical geometries are capable of inducing neural gene expression in MSCs, regardless if the substrate is fibrous or solid bulk. Furthermore, the study represents a great advantage in the protocols for MSCs differentiation because the authors avoided the use of growth factors. However, differentiated direction of MSCs induced by topographical geometric cues appears to be dependent on the sources of stem cells. Dang *et al.* [141] demonstrated that MSCs from bone marrow on the aligned fibrous mats could obtain the induced myogenic differentiation, and Li *et al.* [162] further suggested that MSCs on the orientated ridge/groove arrays could selectively differentiate towards the myogenic lineages, with up-regulated myogenic gene expression but reduced expression in the osteogenic and neural genes. Similar observations were found on the aligned fibrous mats [163]. However, these studies have not performed the investigation on the contractile SMCs markers' expression, although MSCs have shown potential to differentiate into SMCs for VTE applications.

Clearly, the regulation of topographical geometric cues is profound on the cellular function differentiation. The expression of contractile SMCs markers could be up-regulated through using geometric cues. However, such influence has not been studied for MSCs. On the other hand, MSCs are promising for differentiation into SMCs, and on the orientated ridge/groove arrays, they can self-align into the elongated shapes, which have been known as an indicator of SMCs differentiation [126, 164]. Therefore, it should become an interest for VTE applications if topographical geometries alone could promote the SMCs contractile markers' expression in MSCs.

2.3.3 Current Applications of Geometric Cues for TEVG

The applications of topographical geometric cues for VTE are currently on the bench-top analysis [2, 165]. Zorlutuna *et al.* [2, 3] developed a vascular scaffold with nanopatterns on both the inner and outer sides, and further demonstrated increased ultimate tensile stress of the grafts through SMCs alignment, with a Young's Modulus in the range of native arteries and veins. Recently, Jana *et al.* [165] using a novel electrospinning setup successfully obtained 3D tubular scaffolds with circumferentially aligned fibers and SMCs. These achievements reveal promising potential of incorporating the geometric cues for TEVG design. Interestingly, a recent study also suggested that geometric cues could influence the contractile function of cell/material constructs through affecting the organisation of actin cytoskeleton and focal adhesion complexes [114]. Besides those, geometric cues have effects on the orientated remodeling of the underlying ECM [140], leading to the increased mechanical properties of the aligned cell/material constructs [166]. Furthermore, the orientated ECM have been shown to allow continuous cell alignment even when substrates were removed [141] and support 3D cellular alignment construction according to the underlying ECM organisation via a matrix metalloproteinases-mediated (MMPs) pathway [146].

2.3.4 Stability and Degradation Behaviour of Geometric Cues

While topographical geometries are promising for VTE scaffolds to biomimic the BM anisotropic architecture for compliance matching through potential cell alignment and functional differentiation, design of an ideal VTE scaffold should consider the degradation behaviour of geometric structures because scaffold's properties will be deteriorated after being implanted into the *in vivo* circulation system which filled with

various erosive biochemical agents, cells and hemodynamic forces. The degradation properties are therefore of crucial importance in the design of biomaterials for VTE applications.

2.3.4.1 Factors Influencing Degradation

Biodegradability refers to the degradability of an implantable polymer giving fragments, which can move away from the site through fluid transfer, but not necessarily from the body [167]. However, bioresorbability is total elimination of the initial foreign materials either through filtration or metabolisation of the degraded bio-products with no residual side effects [167]. Biopolymers such as silks degrade in the presence of enzymes (e.g. MMPs), while the synthetic polymers mainly follow a hydrolytic pathway [168]. PCL is one bioresorbable synthetic polymer [17]. Similar to PLA, PGA and PLGA, PCL degrades by the random hydrolysis of ester bonds. However, PCL has clear advantages over other synthetic biomaterials in several aspects of degradation: (i) no side effects of by-products, (ii) a wide range of tailorable degradation rates, and (iii) the unique mechanical performances to withstand hemodynamic forces [17, 169].

Degradation studies can be performed both *in vivo* and *in vitro*. While evaluation from the *in vivo* studies provide closer physiological environment biomimicry, *in vitro* degradation for synthetic polymers is approximated to *in vivo* one, and the information can be used as an initial estimate of the degradation rate and other corresponding properties [170]. Moreover, *in vitro* degradation can allow the accomplished degradation profile in an acceptable timeframe, particularly for the biomaterials with slow degradation. Importantly, *in vitro* degradation allows

environmental parameters to be controlled, while *in vivo* studies are often affected by the animal species and different implant positions [168]. Typical *in vitro* model consists of soaking the biomaterials in an aqueous solution at 37 °C and similar pH to the body fluids [170]. Accelerated models can be adapted from temperature at an elevated one (e.g. 80 °C for PCL [171]) or the pH to be a lower and higher one (e.g. 5M NaOH for PCL [172]).

PCL has been known to undergo a two-stage degradation progress [17]: (i) non-enzymatic hydrolytic cleavage of ester groups, and (ii) intracellular metabolisation via the citric acid cycle. The hydrolytic process can be divided into three main steps [17, 170, 173]: (i) diffusion of medium into bulk polymer, which is strongly affected by the surface hydrophilicity, pore size and porosity, and swelling effects; (ii) polymer degradation to generate soluble cyclic oligomers and monomers; and (iii) weight loss via the diffusion of fragments. Table 2-10 summarises the main influence factors for the hydrolytic process, including degradation environment, materials properties and scaffold characteristics. It is worth noting that scaffold dimension and pore/porosity play an important role in determining the degradation manner. Scaffolds with a large wall thickness and small porosity could result in the accumulation of carboxyl end groups, lower the pH value, and lead to autocatalysis for a rapid degradation [170]. The underlying mechanism is that the diffusion of products is lower than the polymer degradation [173]. Such degradation behaviour has been known as "bulk erosion" whereas when diffusion is faster than polymer degradation, "surface erosion" can occur. It should also be noted that *in vitro* enzymatic degradation could result in a faster mass loss (e.g. lipase [174, 175]). However, such enzyme has not been found in the human body [176]. Interestingly, the presence of cells accelerates PCL

degradation rates [177], which probably explained the reason of rapid degradation *in vivo* than *in vitro*.

Table 2-10: Factors influencing TE scaffold degradation

Influence Factors	Typical Examples	Ref.	
Environment	(i) Enzymes	PCL particles: PBS < lipase, with changed degradation mechanism	[174, 175]
	(ii) Bacteria	Faster degradation that preferred in amorphous area via a chain scission mechanism	[178]
	(iii) Cells	PCL degradation rate: PBS < DMEM < DMEM + fibroblast	[177]
	(iv) <i>In vivo</i>	PLGA (50:50) and PCL fibers: <i>in vitro</i> < <i>in vivo</i>	[179, 180]
Molecules	(i) Molecular structure	<i>In vitro</i> PBS buffer: star-shaped and network PCL degraded faster than linear one	[172, 173]
		<i>In vitro</i> enzyme: network PCL degraded slower than the linear one in lipase	[175]
	(ii) Composition	<i>In vivo</i> PCL/collagen VTE scaffolds: better consistence of properties than PCL fibers alone; Unchanged degradability for PCL/PEO as compared to PCL alone, due to phase change; Increased PCL degradation by CaP	[171, 179, 181, 182]
Scaffolds	(iii) Modification	UV treatment of PCL increased the degradation with changed rate profile; NaOH treated PCL enhanced the degradation in enzymes	[178, 183]
	(i) Dimension	Bulk erosion mostly for thick materials and surface one for thin materials	[170]
	(ii) Surface/volume ratio	Higher surface area ratio, faster degradation	[184]
	(iii) Pore size and porosity	<i>In vitro</i> and <i>in vivo</i> : larger surface/internal pore sizes and porosity increased the degradation	[185]

Abbreviations: PCL: Poly(ϵ -caprolactone); PLGA: poly(*d,l*-lactic-co-glycolic acid); PEO: poly(ethylene oxide); PBS: phosphate buffered saline; DMEM: dulbecco's modified Eagle's medium

2.3.4.2 Degradation and TEVG Properties

The effects of degradation on TE scaffold properties are generally described using the changes of molecular weight, polydispersity, by-product release, medium pH changes, weight loss, dimension changes, and mechanical loss [170]. Wu and Ding [186] performed an *in vitro* study on the degradation of PLGA 3D porous scaffolds (Table 2-11). For the first time, they suggested the three stages for the changes of scaffold properties. Interestingly, PLGA scaffolds during the first 10 weeks exhibited a consistent structural integrity and unchanged mechanical properties, but reduced relative number (M_n/M_{n_0}) and viscosity (M_v/M_{v_0}) of average molecular weight. The next stage corresponded to the weight loss, structural deformation and mechanical deterioration, and the third stage referred to the scaffold disruption. To closer mimic the vascular environment, Cao *et al.* [185] designed a flow system for studying the *in vitro* degradation of PLGA scaffolds under hydromechanics. They found that the surface pore sizes were crucial for scaffold function changes (Table 2-10). However, they did not compare scaffold degradation in static and fluid flow environments. Another VTE-related work by Theiler *et al.* [173] studied the degradation of PCL micropatterns. Although their interest focused on the effects of molecular structure on PCL degradation rate, the results showed that micropatterns were completely removed at a very small mass loss (<15 %), indicating geometric failure at very early of degradation. One interesting work performed by Sung *et al.* [187] linked the scaffold degradation to cell response and further *in vivo* performances. The key findings of (i) faster degradation resulted in poorer cell viability; and (ii) PCL facilitated proper inflammatory and angiogenesis better than PLGA were probably because of the autocatalysis-induced acidification.

The performances of VTE scaffolds subjected to the *in vivo* degradation have been studied in several animal models (Table 2-11). Jeong *et al.* [188] implanted PLCL scaffolds using a nude mice subcutaneous dorsum model, and found that the PLCL scaffolds had slow degradation with an excellent tissue compliance with the SMCs by investigating the SMCs makers' expression. Pektok *et al.* [176] compared the PCL and expanded polytetrafluoroethylene (ePTFE) scaffolds. They found that PCL grafts degraded slowly, with no stenosis and faster endothelialization, extracellular matrix formation and neoangiogenesis than the undegradable ePTFE grafts. Moreover, macrophages and fibroblasts presented with PCL grafts indicating inflammatory occurred. These studies clearly suggested that PCL scaffolds were promising for VTE applications. A slow degradation of VTE scaffold with proper inflammatory could facilitate the vascular neotissue remodeling [189]. Such proposal could be evidenced by the recent study that compared the different degradation rates of scaffolds for heat repairmen [190]. They concluded that degradation rate influenced the functional benefits of patch replacement, and a moderately slow degrading provided improved outcomes.

On the aspects of degradation, several characteristics have been proposed for an idea TEVG scaffold: (i) degradation products should be biocompatible, with proper inflammatory for cellular recruitment, ECM deposition and neoangiogenesis [176, 191]; (ii) degradation rate should be comparable to the neotissue growth [191]; (iii) dynamical compliance of mechanical properties [17]; (iv) sufficient porosity, pore size and interconnectivity to avoid autocatalysis for cell ingrowth, requirements of oxygen, nutrients and waste removal and cell-cell communication [187, 192]; (v)

stability-enhanced geometric cues for guiding cell and ECM reorganisation during remodeling.

Table 2-11: The influences of degradation on TE scaffold properties

Degradation Models	Key Performances	Ref.
<i>In vitro</i> PBS, PH7.4, 37 °C; 3D PLGA porous scaffolds	(i) stage I: constant structural integrity and mechanical property; reduced M_n/M_{n_0} and M_v/M_{v_0} ; (ii) stage II: slight structural change; reduced E/E_0 ; weight loss; (iii) stage III: significant weight loss to complete solution	[170, 186, 193]
TEVG <i>in vivo</i> Nude mice subcutaneous dorsum; PLCL pre-seeded with SMCs	(i) Slow degradation with ~81 % mass loss after 15 wk; (ii) Rapid M_n loss: ~54 % retention at 3rd wk and ~23 % at 15 wk; increased M_w/M_n for chain scission; (iii) Caprolactone degraded faster than lactide	[188]
Sprague–Dawley rats subcutaneous pockets;	Slower degradation: more neovascularization and thicker fibrous capsule (using a PLLA/PGA porous film)	[189]
Rat abdominal aorta; PCL fibers	(i) Gradual degradation with ~20 % M_w loss and ~22 % M_n loss up to 24 wk; (ii) Degradation triggered by cell infiltrates: macrophages, fibroblasts and new capillaries (<12 wk) and giant cell at outside (just after implanation)	[176]
Rabbit aortoiliac bypass; PCL/collagen fibrous scaffold	Reduced but still comparable biomechanical strength to native artery	[169]
Porcine coronary artery; Commercialized PLLA scaffolds coated with PDLLA	Complete bioresorption with gradually reduced molecular weight and no significant inflammatory up to 3 years	[194]

Abbreviations: *PLGA*: poly(*d,l*-lactide-co-glycolide); *PLCL*: poly(*l*-lactide-co- ϵ -caprolactone); *PCL*: Poly(ϵ -caprolactone); *PLLA*: poly-*L*-lactide; *PDLLA*: poly-*d, l*-lactide.

2.4 Porous Patterns for Engineered BM

Vascular BM serves critical signaling roles for vascular cells, and the fibrous architectures are organised with circumferential alignment and high porosity [9]. While many techniques allow the fabrication of scaffolds with anisotropic geometric cues for organised cell alignment as in native tunica media, less of them simultaneously provide the interconnected porous structures as what present on BM. It has been generally accepted that 3D TE scaffolds should have sufficient pores, porosity and interconnectivity for the requirements of oxygen, nutrients, and waste removal [192]. Artificial tissue without pores could have a maximum thickness of ~150-200 μm for gas exchange [195]. Secondly, TEVG scaffolds, if there were no or too small pores, would result in bad cellular infiltration, and slower transmural (out-to-lumen or lumen-to-out) and anastomotic (limited to <1 cm [196]) tissue ingrowth (e.g. only ~600 μm thickness of cell ingrowth for the aligned PCL fibrous mats for 12 weeks *in vivo* [166]) [197, 198]. Moreover, presence of the pores can increase elasticity and reduce compliance mismatching [198]. In the coming section, methods for the pore incorporation into scaffolds will be reviewed, with an aim to create the engineered BM with anisotropic geometric cues and interconnected pores simultaneously.

2.4.1 Techniques for Pore Incorporation

Current techniques for the incorporation of pores into TE scaffolds include: (i) electrospinning, (ii) leaching, (iii) phase separation, (iv) direct/soft lithography, and (v) direct laser writing. Table 2-12 summarises the techniques, the resulted morphologies, and their benefits and limitations.

Electrospinning. Procedures for electrospinning and lithography have been reviewed in Section 2.3.1. It is worth noting that although electrospinning allows simultaneous generation of the aligned fibers and interconnected pores, such porous mats have inherent limitations for the *in vivo* application. The smaller rotating speed lowers the fiber alignment, while the higher rotating speed, although it allows highly aligned fibers, results in significant fiber packing with reduced pore size and inhibited cell/tissue ingrowth [118, 124]. Recently, Baker *et al.* [124] utilising a selective removal of sacrificial fibers (e.g. PEO) offset the packing effect and achieved highly aligned fibers with a large porosity. Apart from the great advantages achieved, the high porous aligned fiber mats are far away for VTE application due to the poor mechanical properties and significant dimensional deformation when they are contacted with liquid.

Lithography and Phase Separation. The direct and soft lithography for pore generation hold a great advantage in the precise pore size and position control. Such techniques have achieved the application for 3D tissue construction *in vitro* and exhibited robust capability of cellular infiltration [199, 200]. However, it seems difficult for such methods to integrate the orientated ridge/groove arrays and pore patterns together. Being similar to lithography, phase separation has also met problems to incorporate anisotropic geometries on scaffold surfaces although it allows excellent pore generation in 3D scaffolds [201].

Leaching. To create anisotropic geometry cues and pores simultaneously, one promising method is leaching. Using this technique, Sarkar *et al.* [40], Papenburg *et*

al. [62], and Yucel *et al.* [202] reported the substrates with micropatterned structures and interconnected porosity. The principle can be divided into two parts: (i) biodegradable polymers (e.g. PLGA, PMMA) solution mixed with the porogens for pore generation, and (ii) casting of polymer/porogen solution into a nano/micropatterned model for anisotropic geometries' generation. The procedures are similar to those of soft lithography, with a combination of leaching and soft lithography. The porogens used can be salt [186], sugar [40] and/or water-soluble polymers such as PEO [124] and PEG [202], and the pore size and porosity can be varied by controlling the size and concentration of porogens [198]. Although the porous micropatterned substrates have been demonstrated to allow proper nutrient diffusion and cell alignment [40, 62], several problems remain not yet to be resolved, and limit the VTE applications. Firstly, although the pores could be interconnected, they are difficult to allow cell migration across the scaffolds for vascular neotissue regeneration as well as direct cell-cell interaction. Secondly, while the precise control of pore size is important, the pore size generated from leaching is not homogeneous, As required, the pore size should be sufficient for cell ingrowth, yet small enough to prevent excessive blood leakage [198]. Thirdly, the pore position generated from leaching seems difficult to be controlled. Fourth, while the large pore size and porosity would give better interconnectivity and avoid the autocatalytic erosion [187], they have been observed to induce poor durability [197] and significant reduction in cell alignment [40].

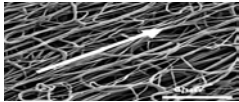
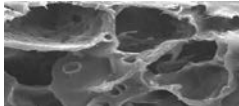
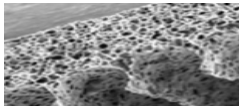
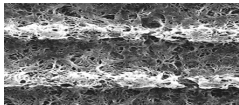
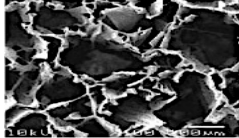
Direct Laser Writing. Recently, more attention has been attracted to a newly emerging technique of direct laser writing for TE. Tiaw *et al.* [135] reported the use of femtosecond and excimer lasers for the direct drilling of biodegradable polymers

(e.g. PCL). At the same time, Aguilar *et al.* [203] reported the quite similar findings and studied the molecule structural changes. Both studies confirmed that direct laser writing could be an excellent technique for micropatterning the biodegradable polymers without significant change of bulk properties. Based on the above findings, Yeong *et al.* [121] applied the Ti-sapphire femtosecond laser wrote orientated ridge/groove arrays on PLC films, and achieved highly aligned cell organisation when cell were seeded. The major advantages of direct laser writing compared to other techniques for anisotropic geometric cues' generation are described in Section 2.3.1. For pore generation, Tiaw *et al.* [135, 204] reported the use of Ti:Sapphire doped crystal femtosecond, KrF excimer laser and diode-pumped solid state Nd:YAG laser for drilling pores on bi-axial-stretched PCL films. Compared to the above reviewed techniques (e.g. electrospinning, leaching, lithography and phase separation), direct laser writing has advantages of the integrity of precise control at the pore size and position [135]. Moreover, pores penetrated the scaffolds are in a linear manner that would facilitate vascular cell migration and transmural tissue ingrowth, as well as the cell-cell communication similar to that of cells on the two sides of BM [205]. Direct laser writing is different from the lithography, phase separation or leaching that require the one-step fabrication and in theory, could be compatible with the current techniques (for geometric cues generation) to further create porous patterns on the aligned fibrous mats or ridge/groove arrays.

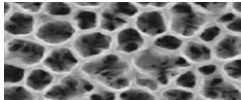
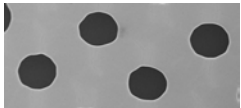
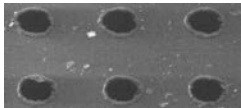
To-date, the laser used for TE scaffolds can be divided into two categories: (i) long pulse laser (>10 ns) and (ii) short pulse laser ($\times 10^{-15}$ s). The long pulse laser (e.g. CO₂ laser, UV laser) are mostly used for engineered plastics such as PMMA, PLLA [206]. These lasers breakdown the polymers through the high-energy photon absorption

[204], and generate a pulse longer than the thermal wave propagated in polymers, leading to possible thermal-induced material changes [121]. Femtosecond lasers (e.g. Ti:Sapphire femtosecond laser) breakdown polymers through a multi-photon absorption [204] and can remove almost any target materials due to the high peak energy ($>10^{12}$ w/cm²) [121, 135]. The basic science underling the femtosecond laser ablation involves five phenomena: (i) ionizing of targeted materials at the early of laser pulse time; (ii) absorption of free electrons; (iii) formation of a strong electric field due to the electrons that break free from the bulk materials; (iv) ions out of the bulk materials if electron energy is larger than binding energy; and (v) materials remove [135].

Table 2-12: Technologies for the incorporation of pores into films

Strategies	Examples*	Advantages	Limitations	Ref.
Electrospinning (Rotating disk and mandrel)	PCL 	Simultaneous alignment and pores	Solvent-usage and potential residues; High speed → higher fiber packing → small pores → no cell infiltration	[152]
Leaching	Salt PLGA 	High porosity and interconnectivity; Easy control of porosity and mean size of pores; Potential one-step for incorporation of patterns and pores;	Solvent usage and potential residues of solvents and porogens; Inhomogeneous pore size; Difficult for cell infiltration	[189]
	Sugar PCL 	Potential tissue-scaffold integrity		[62]
	Polymers (PEO, PEG) PHBV-PLGA 			[202]
Phase Separation	PLGA 	Better resistance to degradation; Larger porosity and surface area than leached scaffolds; Less solvent residues	Inhomogeneous pores: graded reduce in pore size from inner to surface; Larger foreign body giant cell response and less tissue ingrowth; Use of solvent and potential residues	[185, 201]

Continued

Direct Lithography	<p>Silicon</p> 	<p>Precise pore shape and position; Direct punching</p>	<p>Mask-required and Limited applicability for photo resistant materials; Toxic solvent usage</p>	[207]
Soft Lithography	<p>PDMS</p> 	<p>Applicable for biodegradable materials; Precise pore shape and position</p>	<p>Solvent usage and potential residues; Cumbersome set of tools and procedures (e.g. model-needed);</p>	[208]
Direct Laser Writing	<p>PCL</p> 	<p>Applicable for biodegradable materials; Precise pore shape and position; Direct punching and simple procedures</p>	<p>Expensive-equipment require; Time-consume for a large number of pores or patterns</p>	[204]

*Figures were adapted in sequence from Nisbet *et al.* 2009; Kaushiba *et al.* 2007; Papenburg *et al.* 2007; Yucel *et al.* 2010; Safinia *et al.* 2008; Khung *et al.* 2008; Wang *et al.* 2009; Tiaw *et al.* 2008, respectively.

Abbreviations: *PCL*: poly(ϵ -caprolactone); *PLGA*: poly(*d,l*-lactide-co-glycolide); *PEG*: polyethylene glycol; *PEO*: poly(ethylene oxide); *PHBV*: poly(3-hydroxybutyrate-co-3-hydroxyvalerate); *PDMS*: polydimethylsiloxane.

2.4.2 Vascular Cell Responses to Porous Patterns

The nano/micro-structural features of BM are known as a crucial indicator for healthy status. Liliensiek *et al.* [9] firstly examined the porous morphologies of human vascular BM, and pointed out the importance of VTE applications. Their subsequent studies explored the effects of mimicking the aligned BM fibrous structures on human ECs regulation [154, 209]. However, the porous structures have not been incorporated into their studies. Currently, studies in regards to the regulation of pores have been performed on various cell types (e.g. FBs [210], SMCs [211], ECs [210], HECEs [212], MSCs [213]). From these studies, the presence of pores on the substrates has shown to affect cell adhesion, morphology, proliferation and differentiation. O'Brien *et al.* [214] observed that cellular attachment on collagen–glycosaminoglycan scaffolds decreased with increasing the mean pore size. Such finding was confirmed by Khung *et al.* [207] using a porous gradient with an average pore size from 600 to 3000 nm. Their results further suggested that cells could even sense a feature size as small as ~20 nm. Moreover, Karuri *et al.* [212] demonstrated that cells on nanoscale pores exhibited fastened adhesion against flow shear with more numerous filopodia and retraction fibers than the cells on microporous features. The reason could be that the pore edges facilitate cell-substrate adhesion by acting as nucleation for the cells-materials interaction. Interestingly, ECs have been suggested to preferentially adhere to pores less than 80 μm , while SMCs and FBs preferred a pore size of 63-150 μm and 38-150 μm of PLLA scaffolds, respectively [210, 211, 214].

Besides the adhesion, pores have shown significant impacts on the cellular morphology and migration. Wang *et al.* [208] showed that pores could inhibit cell

spreading, with a slower spreading for the pores at a small diameter. Cells exhibited confined morphologies with more and longer protrusions stretched out towards sidewalls as compared on the flat surfaces. These morphology and migration changes increased the cell activity, but lowered the alkaline phosphatase activity in Caco-2 cells. Such differentiated effects have also been observed in MSCs on PMMA porous substrates [213]. Clearly, cells are responsive to the porous features of scaffolds. However, how vascular cells (e.g. SMCs, ECs and MSCs) respond to the combined anisotropic geometries and porous structures of BM remains unknown.

2.4.3 Porous Patterns and Current Vascular Scaffold Design

Pores have been incorporated for TEVG design. Kaushiva *et al.* [189] using salt leaching developed a PLLA/PLGA film with an average pore size of $\sim 60 \mu\text{m}$, and found that slow degraded films with had better capillarity ingrowth and thinner fibrous capsule. Hu *et al.* [215] developed a microporous fibrous VET scaffold using electrospinning, and found that the micropores ($\sim 125\text{-}250 \mu\text{m}$) could support SMCs ingrowth both *in vitro* and *in vivo* and promote SMCs differentiation. Both studies have suggested that pores could not only facilitate the capillary ingrowth, but also promote cellular differentiation. However, the films generated from leaching and electrospinning are poor in mechanical stability and limited at cell organisation control. Another group led by Matsuda [197, 216] in Japan utilised elastomeric PU films and KrF excimer laser drilling for producing microporous VTE scaffolds. They found that pore patterns did increase the scaffold elasticity, and pores promoted the endothelialisation on lumen surface with a thin intimal tissue. However, their design lacked the capability of aligning SMCs on tunica media side. Recently, Sarkar *et al.* [40] and Papenburg *et al.* [62] firstly created porous micropatterned PLGA substrates

through sugar leaching, and carried out a feasibility study on stacking the substrates into multi-layered cell/material architectures as tunica media. Although the substrates were designed for the tunica media conduction only and have been found with limitations in cell alignment and nutrient diffusion of 3D construction, they have stimulated an ambitious idea for me to incorporate the anisotropic geometric cues and micropore patterns on bioresorbable thin films as an engineered BM, to facilitate the aligned and differentiated MSCs organization on the tunica media side, and promote endothelialisation on the lumen side.

Chapter 3 Uniaxial Stretching for Generation of Three-Dimensional Anisotropic Geometries on Poly(ϵ -caprolactone) Films

3.1 Introduction

Proper tissue function and regeneration rely on robust spatiotemporal control of cellular microenvironments [217]. *In vivo*, many tissues such as skeletal and myocardial muscles, blood vessels, nerves as well as bone are physiologically anisotropic, with architectures consisting of highly aligned cells and cell-matrices [218, 219]. Such alignment plays an important role in dictating tissue functions. For example, the aligned organisation of cardiomyocytes and fibroblasts is critical to the electrical and mechanical properties of the heart [220], whereas circumferential alignment of smooth muscle cells (SMCs) in blood vessels is required for the generation of contractile force and modulation of vascular tone [61, 221]. However, the inability of scaffolds to guide cell behaviour has often resulted in poor cell and cell-matrix organisation [222, 223]. Tissue constructs based on such scaffolds will have limited capability of eliciting function regeneration, especially for anisotropic tissues.

Scaffolds with versatile topographical geometries, have been shown to deliver cell-matrix-regulator signals to regulate cell behaviour, and serve as powerful artificial

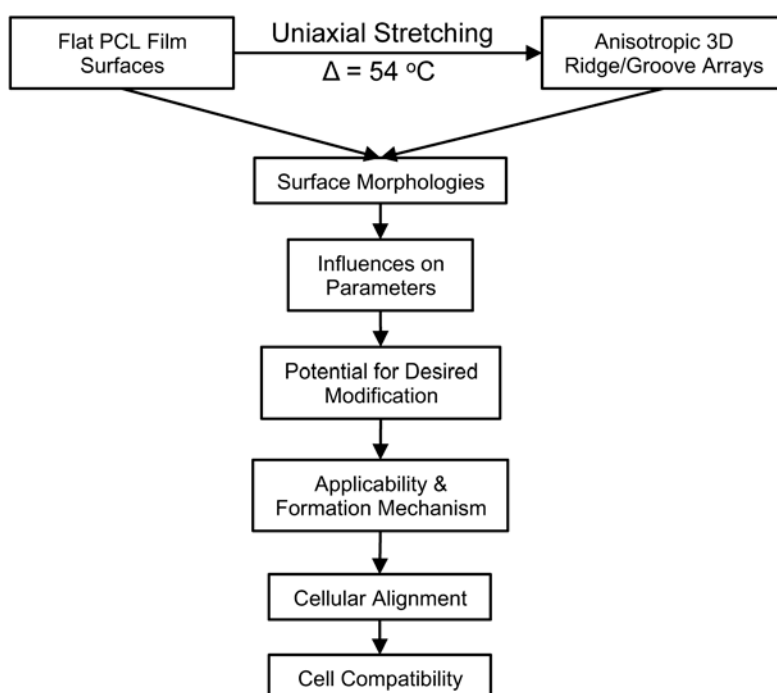
microenvironments for recapitulating tissue architectures and functions [217, 224]. Chapter 2, Section 2.3.1 reviews the different development of geometries, fabrication techniques, and the related cellular performances in regenerative medicine. The two main strategies for incorporating of geometric cues on poly(ϵ -caprolactone) (PCL) films are soft-lithography and electrospinning. However, geometric cues generated from soft-lithography typically requires mechanical separation of PCL films from the mould, which often results in the formation of defects on surface features [132]. In addition, this technique refers to a cumbersome set of patterning tools and procedures [122, 225]. Modified electrospinning set-up using a rotating mandrel or void gap has been used to generate orientated PCL nanofibrous meshes. However, the poor film mechanical property remains a concern. In particular, both soft-lithography and electrospinning methods use chemical solvents (e.g. chloroform, tetrahydrofuran, acetone and ethyl acetate) [132, 226, 227], and the potential risk of residuals leads to problems with regard to safety concerns. Hence, it is imperative to develop alternative strategies that eliminate the use of solvents and be simple and reproducible for the incorporation of geometric cues on PCL films.

In this work, a novel method of uniaxial stretching has been developed to create PCL films with biomimetic 3D self-assembling anisotropic geometric cues, which allows the fabrication in a simple, solvent-free and reproducible manner. A robust and long-term capability of eliciting stem cell alignment in a controllable direction has also been demonstrated for potential VTE application.

3.2 Materials and Methods

3.2.1 Experimental Design

A novel fabrication for geometric cues is being developed for PCL films (Scheme 3-1). A series of materials and cellular characterisations have been performed focusing on the aspects of morphological features, formation mechanism, parameter control, potential for desired modification and regulations on stem cell behaviour.



Scheme 3-1: Schematic diagram illustrating the experimental design in this work. PCL films with flat surfaces were subjected to uniaxial stretching at 54 °C. Surface morphologies and the performances on cellular alignment and elongation were examined to understand that whether the generated geometric features can function as cues. Influences on parameter's control, potential for surface modification, applicability and formation mechanism and cell cytotoxicity were also studied for developing uniaxial stretching as a novel technique for fabrication of film geometric cues.

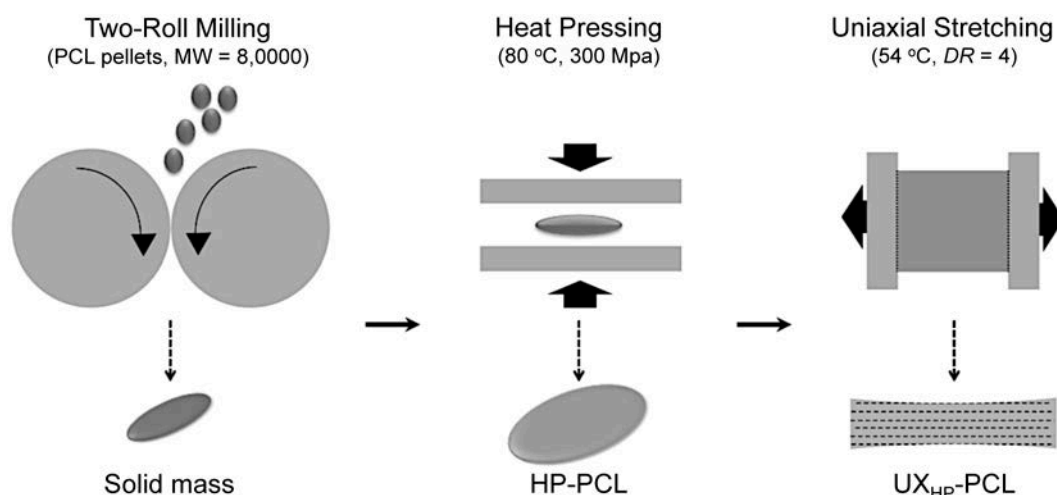
3.2.2 Materials

PCL (MW 80,000), phosphate buffer saline (PBS), penicillin-streptomycin (PS), TRITC-conjugated phalloidin, paraformaldehyde (PFA), triton-X 100, bovine serum albumin (BSA), fluorescein diacetate (FDA), propidium iodide (PI) and 4',6-diamidino-2-phenylindole (DAPI) were purchased from Sigma-Aldrich (Singapore).

Dulbecco's modified eagle medium (DMEM), trypsin- ethylenediaminetetraacetic acid (EDTA) and fetal bovine serum (FBS) were purchased from Life Technologies (Singapore). Cell strainers, tissue culture plates (TCP) and flash and low-adhesion cell culture plate were purchased from BD Bioscience (Singapore), Thermo Fisher Scientific (USA), Nunc (Singapore) and Corning (Costar, Singapore), respectively.

3.2.3 Generation of PCL 3D Anisotropic Geometries

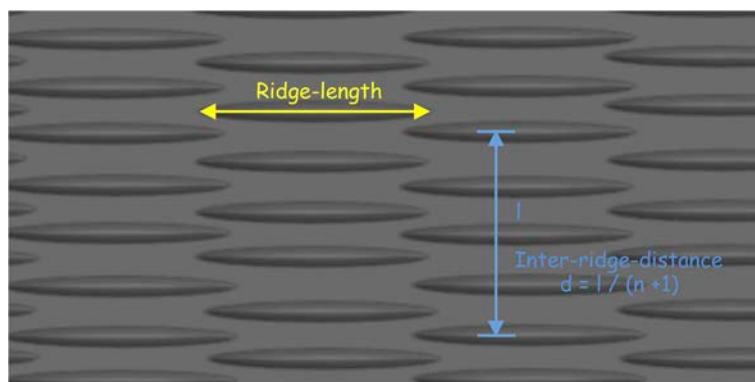
As shown in Scheme 3-2, heat-press PCL (HP-PCL, $\sim 120 \mu\text{m}$ in thickness) films were fabricated via two-roll milling and subsequent pressing at $80 \text{ }^\circ\text{C}$, 300 MPa [228]. Anisotropic geometries were created on PCL films using a solvent-free method. Briefly, HP-PCL were cut into rectangular pieces ($5 \times 3 \text{ cm}^2$), heated to $54 \text{ }^\circ\text{C}$ and subjected to uniaxial stretching before cooling down to room temperature. The HP-PCL after uniaxial stretching was named as UX_{HP} -PCL.



Scheme 3-2: Schematic diagram illustrating PCL film fabrication. Anisotropic 3D ridge/groove arrays on UX_{HP} -PCL were obtained by uniaxial stretching of HP-PCL (*DR*: draw ratio).

3.2.4 Field Emission Scanning Electron Microscopy (FESEM)

The morphologies of PCL films before and after uniaxial stretching were examined by FESEM (S-4300, Hitachi, Japan). Briefly, samples were sputter-coated with gold at 10 mA for 30 s. Images were taken at a voltage of 15 kV. Ridge orientation, inter-ridge-distance and ridge-length were measured from FESEM images using the built-in functions of NIH ImageJ (USA). Briefly, angle-variation was described as the mean of standard variations of ridge orientation. Inter-ridge-distance was measured by drawing lines perpendicular to the stretch direction, and described as the length of a line divided by the crossed ridge number (Scheme 3-3). Ridge-length was measured by drawing a straight line from the start point to the end point of individual ridge. Four samples were used for each measurement above.



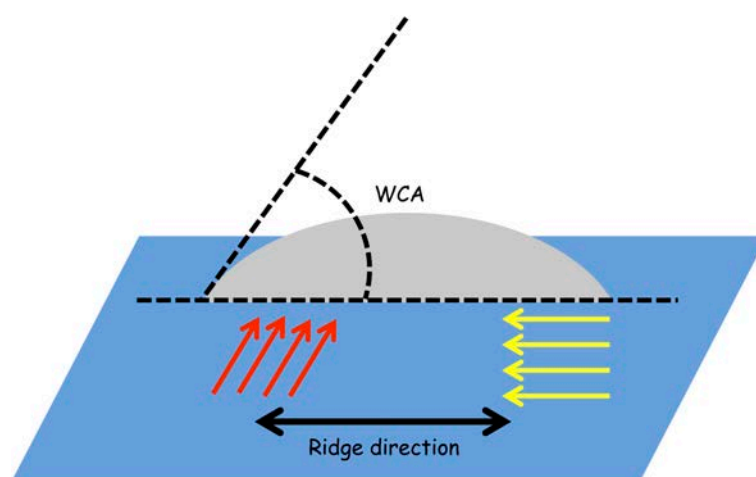
Scheme 3-3: Schematic diagram illustrating the measurement of ridge-length and inter-ridge-distance. Ridge-length is equal to the length of a line from the start point to the end point of individual ridge. Inter-ridge-distance is defined as $d = l / (n + 1)$, where d is the average distance between two ridges, l is the length of a cross line, and n is the number of ridges the line crossed.

3.2.5 Atomic Force Microscopy (AFM)

PCL film morphologies were examined using AFM (MFP-3D, Asylum Research, USA). Images were captured using a tapping scan over an area of $60 \times 60 \mu\text{m}^2$ on film surfaces. Height-profile was analysed via Igor Pro6 (USA).

3.2.6 Water Contact Angle (WCA)

Surface hydrophilicity was evaluated by WCA measurement using a video contact angle system (Advanced Surface Technologies, VCA2000, USA). Briefly, a drop volume of 1 μl was used, and images were taken 5 s after the drop dispersion for full drop development. Measurement was performed followed two mutually perpendicular directions. On UX_{HP}-PCL, one direction was towards the ridges (Scheme 3-4). Three samples and five random positions of each sample were analysed.



Scheme 3-4: Schematic diagram illustrating the measurement of water contact angles (WCA) on UX_{HP}-PCL (Yellow and Red arrows: direction of WCA measurement followed).

3.2.7 Differential Scanning Calorimeter (DSC)

DSC (DSC60, Shimadzu, Japan) was used to examine the crystallinity of PCL films. Briefly, a scanning range from 20 to 90 °C was performed at a heating rate of 10 °C/min in air ambient. PCL film crystallinity was determined by comparing with 100 % crystalline PCL, which has an enthalpy of fusion of 139.5 J/g [228].

3.2.8 Polarized Light Microscopy (PLM)

The effect of uniaxial stretching on PCL molecular chain reorientation was examined using PLM (EMM0307, Nikon, Japan) with a magnification of x400.

3.2.9 Cellular Isolation and *In Vitro* Culture

Human tissue collection for research purposes was approved by the Domain Specific Review Board of National Healthcare Group, in compliance with international guidelines regarding the use of fetal tissue for research [229]. In all cases, patients gave separate written consent for the use of collected tissues.

Human mesenchymal stem cells (MSCs) were isolated as previously described [229]. Briefly, single-cell suspension was obtained by flashing femurs using a 22-gauge needle. Tissue fragments were removed by passing the suspension through a cell strainer (40 μm). Cells (10^6 per cm^2) were seeded on tissue culture flask (75 ml) and cultured in D10 medium (DMEM + 10 % FBS + 1 % PS). Non-adherent cells were removed by changing the medium at day 3. Adherent cells (MSCs) were recovered from the primary culture after one week. *In vitro* culture expanded MSCs (Passage-6) were characterised with positive expression of stem cell phenotype.

3.2.10 Confocal Laser Scanning Microscopy (CLSM)

The responses of MSCs to PCL film anisotropic geometries were investigated using cytoskeletal and cytoplasmic staining. The flat surface of HP-PCL was used as a control group. Cells were immediately examined using CLSM (FV1000, Olympus, Japan).

Cytoskeletal staining:

MSCs after culture for pre-determined period were fixed using PFA (3.7 % in PBS) for 15 min, followed by permeabilisation using Triton-X 100 (0.1 % in PBS) for 10

min, and blocking using BSA solution (2 % in PBS) for 30 min. Cells were then incubated with TRITC-conjugated phalloidin (1:200 in PBS) for 1 hour to label the F-actin cytoskeleton. After washing thrice with PBS, cells were further incubated with DAPI (1:1000) for 5 min to visualise nuclei.

Cytoplasmic staining:

Live MSCs were incubated with FDA (8 µg/ml) for 10 min. After removing the FDA solution, cells were further incubated with PI (4 µg/ml) for 5 min, followed by washing thrice with PBS.

3.2.11 Cellular Alignment and Elongation Analysis

Images of live cells were analysed using the built-in function of NIH ImageJ software (USA) as described in previous report [146]. For single-cell analysis, MSCs were analysed at sub-confluence on PCL films. All cells in contact with other cells and cells contact with the image edges were manually removed from the data sets. Cellular arrangement angle was defined as the orientation of the major elliptic axis of individual cell. Preferential cell orientation was defined as the angle that a range of 10° below and above it has the largest cell number. The preferential cell orientation was set as 0°, and all the cellular angles and ridge direction were normalised to it. Cell number within each degree from -90 to +89° was calculated and normalised such that the total sum was unity, and plotted as a curve to describe the frequency distribution of cell angles. Cells with angles fell into $\pm 10^\circ$ were considered to be aligned [230]. Cellular elongation was described using a cell shape index (CSI, circularity = $4\pi \cdot \text{area} / \text{perimeter}^2$) [146]. Three samples and four random regions of each sample were analysed.

3.2.12 Cellular Proliferation Assay

The effect of UX_{HP}-PCL anisotropic geometries on MSCs proliferation was investigated using a colorimetric MTS assay (CellTiter 96 AQueous One solution, Promega, Madison, WI) [223]. HP-PCL and TCP flat surfaces were set as positive controls, and five samples were used. Briefly, cells after culture for pre-determined period were washed with PBS and incubated with 20 % MTS reagent in serum-free medium for 3 h at 37 °C. The absorbance of obtained dye was measured at 490 nm using a spectrophotometric plate reader (FLUOstar Optima, BMG Lab Technologies, Offenburg, Germany).

3.2.13 Data Analysis

Data analysis was performed on Prism 5 software. Results were reported as mean ± SD. A value of $p < 0.05$ was considered to be statistically significant.

3.3 Results

3.3.1 Biomimetic 3D Self-Assembling PCL Anisotropic Geometries

Figure 3-1A reveals a relatively flat surface for HP-PCL. Uniaxial stretching resulted in anisotropic geometries on UX_{HP}-PCL consisting of two distinct portions: (1) 3D micro-scaled ridges that were discontinuous and preferentially orientated towards the stretching direction, with variations of ridge angles being less than $\pm 1.56^\circ$ (Figures 3-1B and C), and (2) continuous grooves that separated the ridges from each other. AFM examination of UX_{HP}-PCL revealed similar results as observed from FESEM, with a typical height-profile of ridge-depths varying from 200 to 900 nm (Figure 3-1D).

Figure 3-2 shows the morphological consistency of UX_{HP} -PCL. FESEM images of representative regions (X-0 \rightarrow X-5, Y-0 \rightarrow Y-4) revealed anisotropic geometries in a consistent orientation on the whole film surface of UX_{HP} -PCL. The inter-ridge-distance of regions from X-0 to X-5 tended to increase slightly. However, no significant change was observed in the regions from X-0 to X-3 ($p > 0.05$). Moreover, the anisotropic geometries did not exhibit conspicuous changes at inter-ridge-distance for the regions from Y-0 to Y-5, although some inter-ridge-distance reduction was found at the region near the film edge (Y-4; $p > 0.05$).

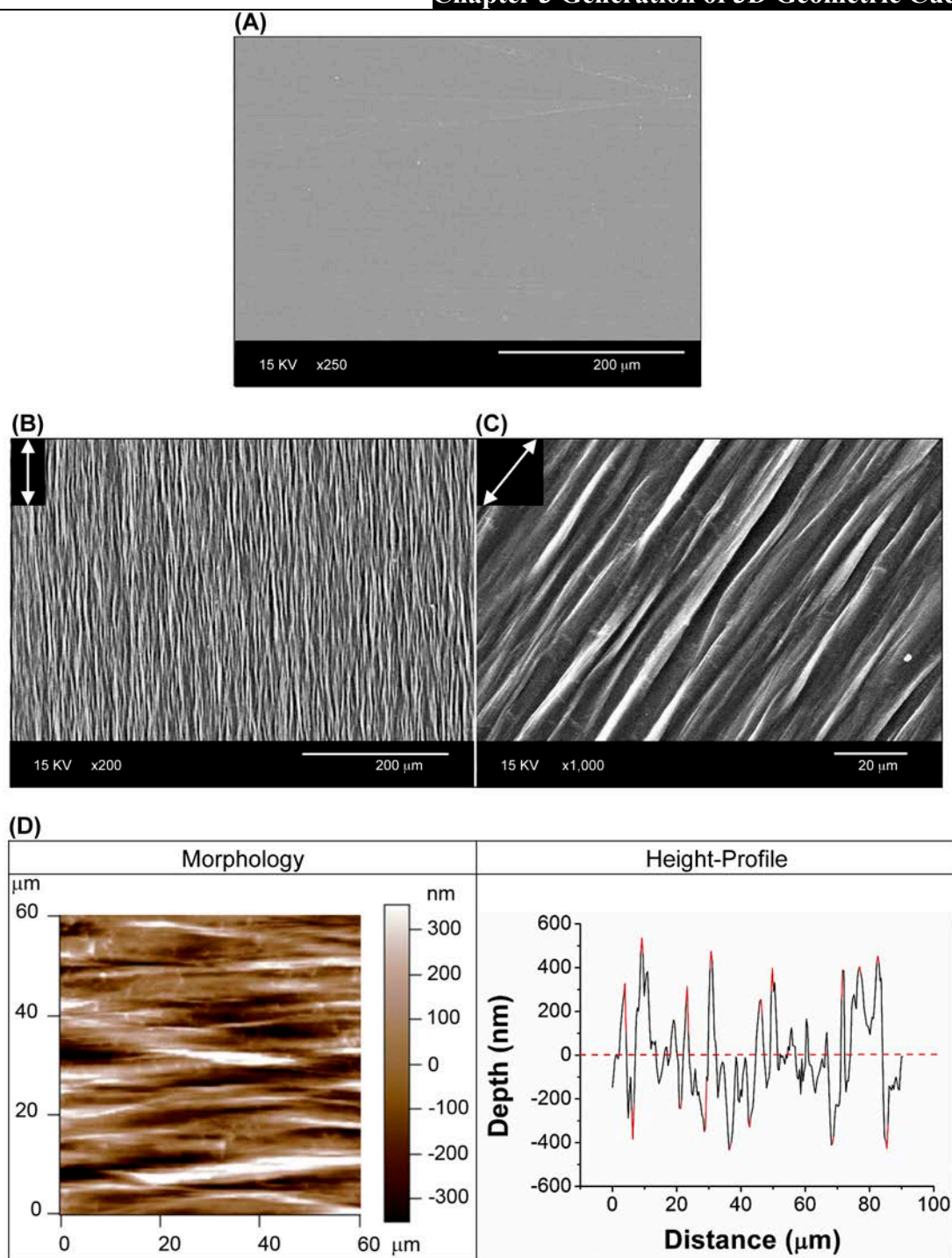


Figure 3-1: Uniaxial stretching of PCL films resulted in anisotropic geometries. (A) Field emission scanning electron microscopy (FESEM) image of HP-PCL revealed a flat surface (Scale bar = 200 μm). (B) Low and high magnified FESEM images of UX_{HP}-PCL revealed anisotropic geometries (Double-headed arrow: stretching direction; Scale bar = 200 and 20 μm). (C) Atomic force microscopy (AFM) images of UX_{HP}-PCL.

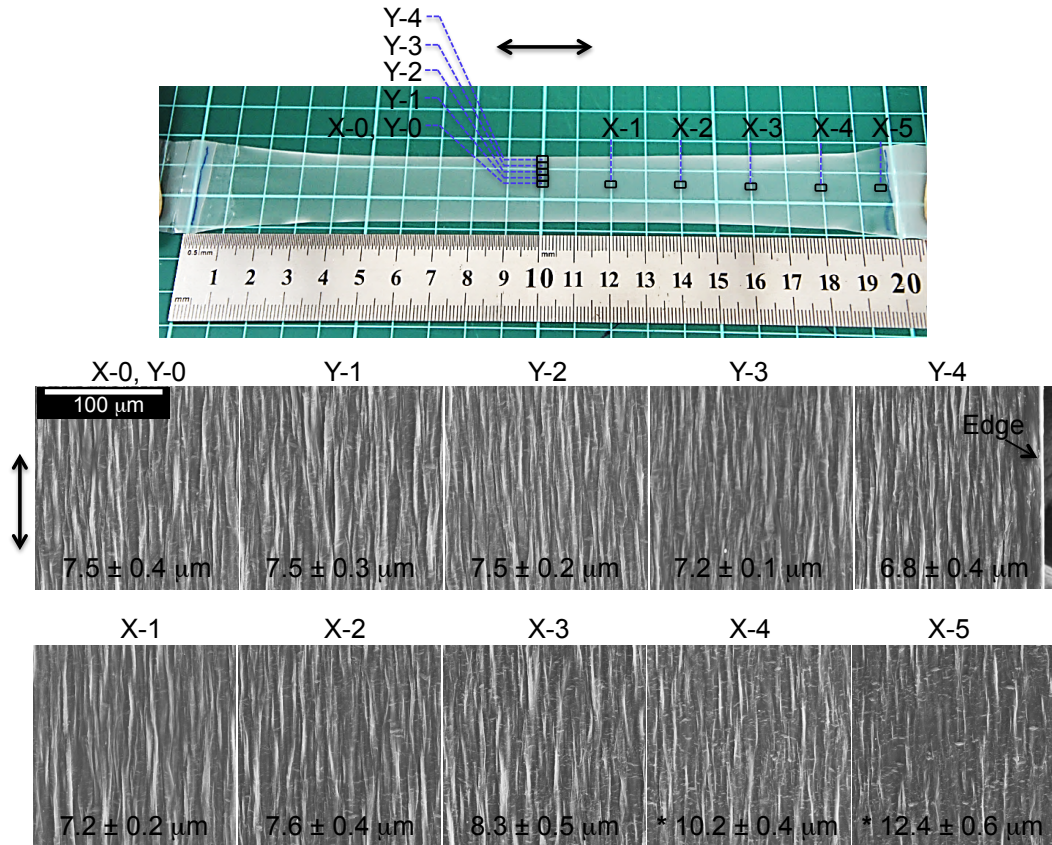


Figure 3-2: Morphological consistency of UX_{HP} -PCL. Representative regions ($2 \times 2 \text{ mm}^2$; Y-0 to Y-4) from the film center to the edge, and regions (X-0 to X-5) from the film center to the two ends with an inter-region-distance of $\sim 2 \text{ cm}$. FESEM images revealed similar inter-ridge-distance within regions of X-0 \rightarrow X-3 and Y-0 \rightarrow Y-4 (Double-headed arrow: stretching direction; Scale bar = $100 \mu\text{m}$). * represents the significant difference as compared to the inter-ridge-distance of film central region ($n = 4$; *, $p < 0.05$).

3.3.2 Effects of Stretching Temperature (T_s) and Draw Ratio (DR) on Ridge-Length and Inter-Ridge-Distance

Figure 3-3 shows the influences of T_s and DR on the anisotropic geometries of UX_{HP} -PCL. At elevated T_s , more ridges were formed on UX_{HP} -PCL, with the ridge/groove shapes becoming clearer. However, DR did not show such effect on the geometries. Quantitative analysis of the anisotropic geometries of UX_{HP} -PCL showed that when T_s and DR increased, the inter-ridge-distance tended to be reduced, and the ridge-length was increased, indicating proper tailorability of the geometries in a certain range (Table 3-1).

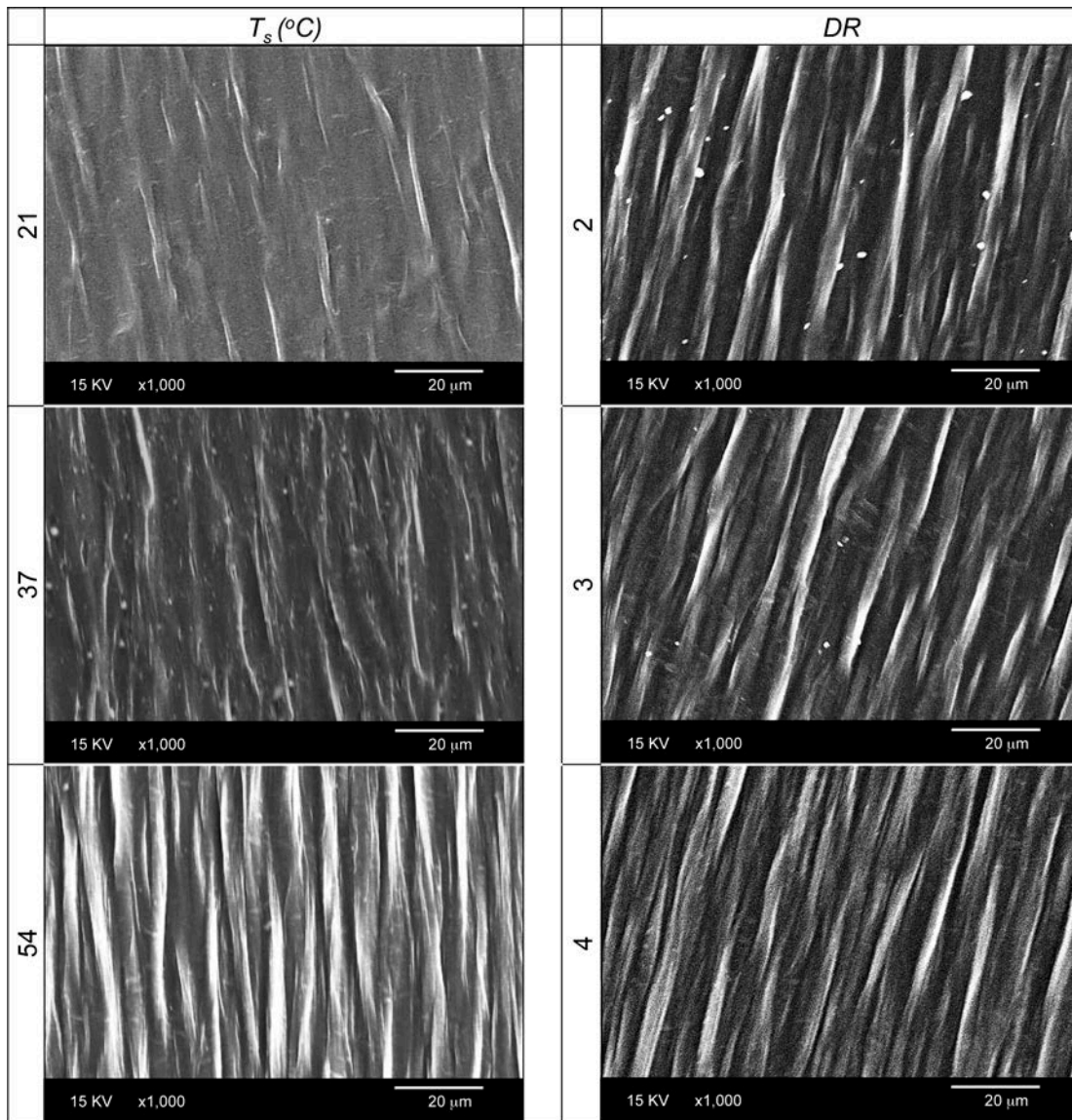


Figure 3-3: FESEM images of UX_{HP}-PCL fabricated at a consistent *DR* of 4 and different *T_s* (21 °C, 37 °C and 54 °C) or consistent *T_s* of 54 °C and different *DR* (2, 3 and 4; Scale bar = 50 μm).

Table 3-1: Inter-ridge-distance and ridge-length of UX_{HP}-PCL ridge/groove arrays (n = 4)

Structural Parameters (μm)	<i>T_s</i> (°C)			<i>DR</i>		
	21	37	54	2	3	4
Inter-ridge-distance	15.7 ± 1.1	11.2 ± 1.4	6.1 ± 0.9	17.4 ± 0.4	11.6 ± 2.5	6.9 ± 0.8
Ridge-length	28.1 ± 3.7	42.8 ± 7.4	89.0 ± 11.2	62.9 ± 5.0	66.6 ± 10.9	92.2 ± 9.2

3.3.3 Surface Modification

Figure 3-4A shows that the surface of UX_{HP} -PCL anisotropic geometries was relatively hydrophobic (WCA $>80^\circ$). The WCA on UX_{HP} -PCL anisotropic geometries in their parallel direction was similar to that on HP-PCL flat surface (82.3 vs 82.6° , $p >0.05$). Moreover, UX_{HP} -PCL anisotropic geometries exhibited anisotropic surface hydrophilicity, with additional increase in WCA of $\sim 7^\circ$ in their perpendicular direction than in the parallel direction ($p <0.001$). However, the surface hydrophilicity was isotropic for HP-PCL flat surface, with similar WCA along the two mutually perpendicular directions (81.8 vs 82.6° , $p >0.05$). Compared to HP-PCL flat surface, uniaxial stretching made the anisotropic geometries of UX_{HP} -PCL to be more hydrophobic, with larger WCA in their perpendicular direction ($p <0.001$).

PCL is relatively hydrophobic for cell attachment [17, 231]. Figure 3-4B shows the modification of UX_{HP} -PCL anisotropic geometries via alkaline hydrolysis for achieving enhanced surface hydrophilicity. The WCA on UX_{HP} -PCL anisotropic geometries gradually decreased with increasing hydrolysing time. Comparatively, the decline of WCA in the perpendicular direction of UX_{HP} -PCL anisotropic geometries was slower than that in the parallel direction, resulting in an increased WCA difference between the two mutually perpendicular directions. The rate of WCA decline on UX_{HP} -PCL anisotropic geometries in the parallel direction was similar to that on HP-PCL flat surface, achieving a desired WCA range for cell growth (50 - 60°) after 24 hr of hydrolysis [232]. Moreover, FESEM images of UX_{HP} -PCL anisotropic geometries revealed well-maintained ridge/groove shapes over the investigated period (Figure 3-5). The surface of ridges exhibited more local integrity than that on groove surface after 12 hr of hydrolysis, indicating larger resistance against hydrolysis.

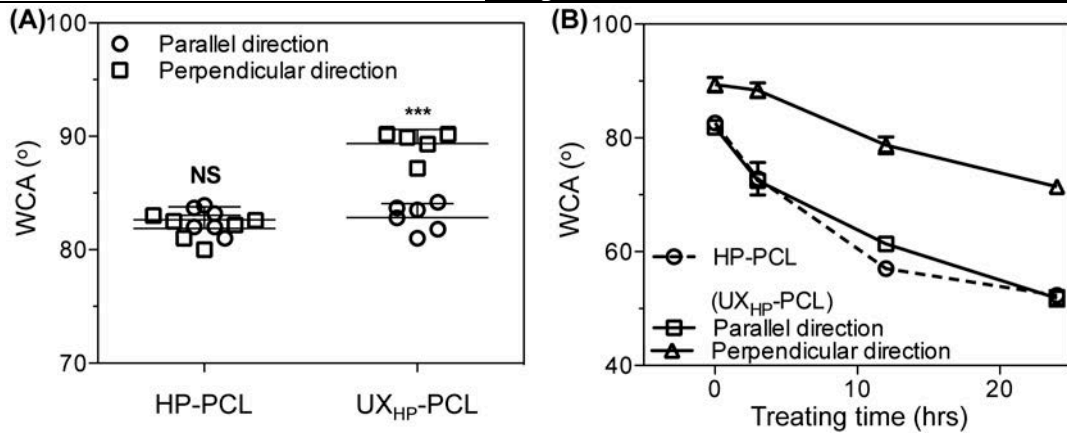


Figure 3-4: Increased surface hydrophilicity of UX_{HP}-PCL. **(A)** WCA before hydrolysis. UX_{HP}-PCL revealed a WCA in parallel direction being similar to that of HP-PCL, but with an additional increase (~7 °) in perpendicular direction. * represents the significant difference as compared to WCA in the parallel direction (n = 5; ***, p < 0.001; NS, p > 0.05). **(B)** WCA after hydrolysis (NaOH, 3M). UX_{HP}-PCL achieved enhanced surface hydrophilicity, with continuous WCA decrease in both directions (n = 3).

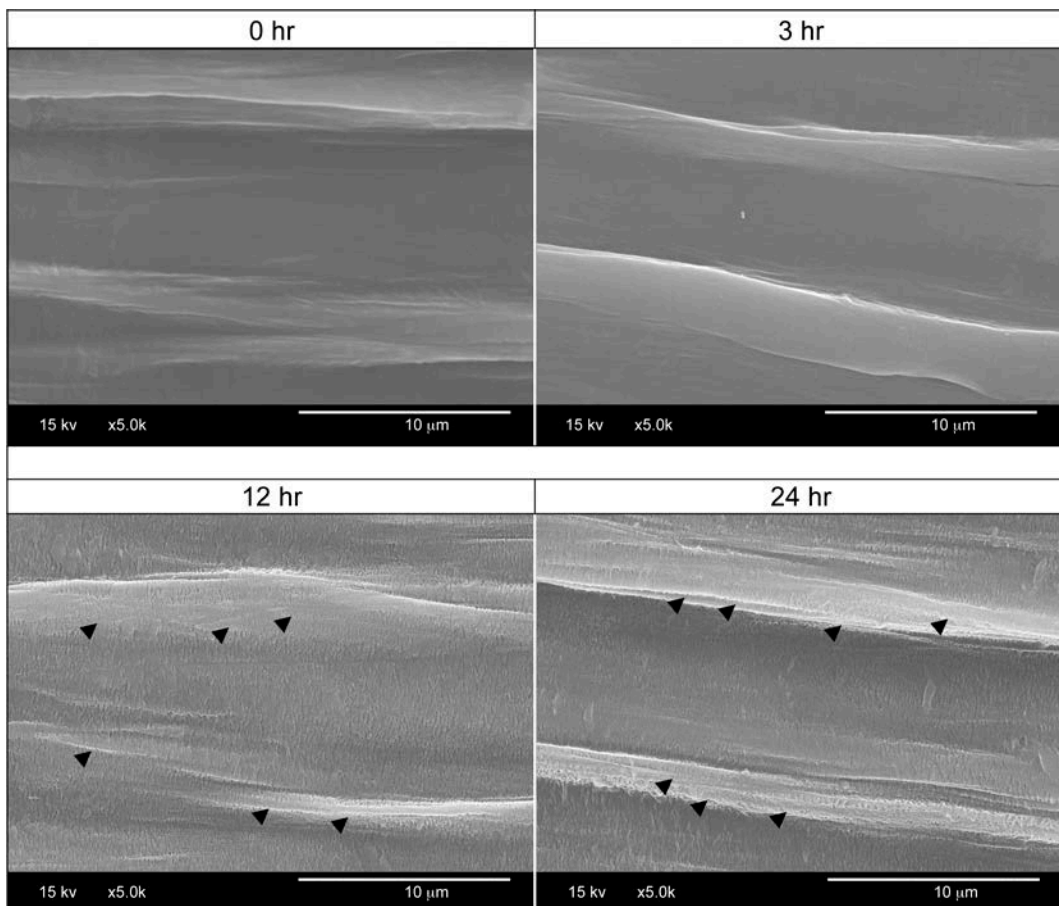


Figure 3-5: Morphological stability of UX_{HP}-PCL during surface modification. FESEM images revealed well-maintained ridge/groove shapes for hydrolysis (NaOH solution, 3M) of different time (Dark arrows: local integrity of ridge surface; Scale bar = 10 μm).

3.3.4 Aligned Cellular Growth

The UX_{HP}-PCL anisotropic geometries were further evaluated via interaction with MSCs *in vitro*. Figure 3-6 reveals an aligned and elongated growth of MSCs on UX_{HP}-PCL anisotropic geometries, with orientations preferentially towards the geometries after 5 days of culture. In contrast, MSCs on HP-PCL flat surface (control) did not exhibit any trend of alignment. Moreover, live staining of MSCs using FDA/PI dyes to avoid potential artifacts arising from the fixation process revealed distinct cellular alignment and elongation on UX_{HP}-PCL anisotropic geometries. The alignment of MSCs was observed to be present in a consistent direction on the whole UX_{HP}-PCL sample (1x1 cm²) as indicated by the cell organisation in different regions (Z1-Z5; Figure 3-7).

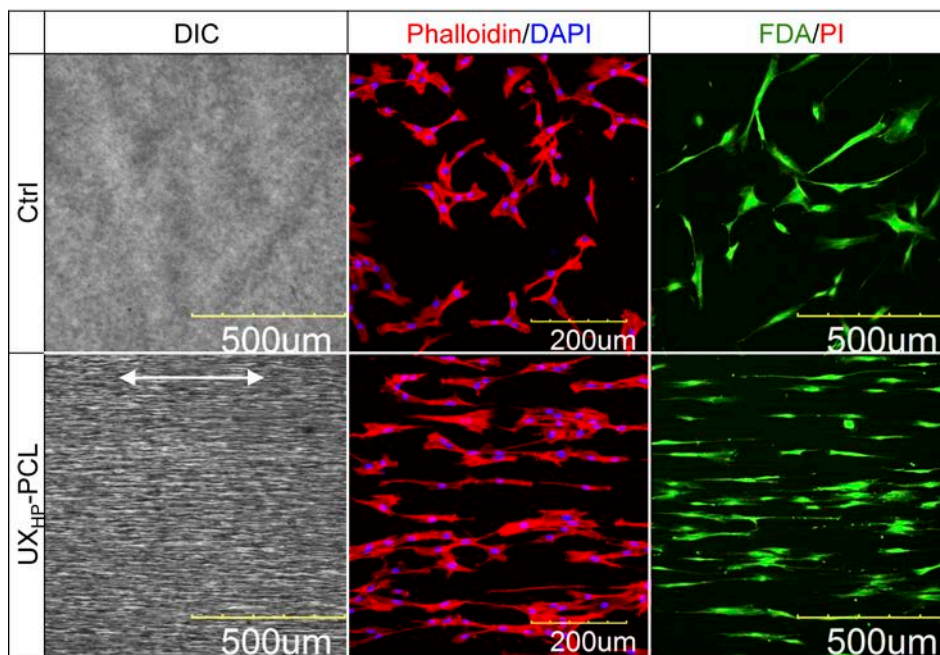


Figure 3-6: Confocal laser scanning microscopy (CLSM) images of cytoskeletal (Phalloidin: red, F-actin; DAPI: blue, DNA; Scale bar = 200 µm) and cytoplasmic (FDA: green, live cells; PI: red, dead cells; Scale bar = 500 µm) staining of MSCs (Passage-6, 5k per cm², for 5 days of culture) on UX_{HP}-PCL anisotropic geometries and HP-PCL flat surface (Control; White arrow: ridge direction; Scale bar = 500 µm). MSCs cultured with UX_{HP}-PCL anisotropic geometries aligned and elongated preferentially towards the ridge direction. In contrast, MSCs organised randomly in control group.

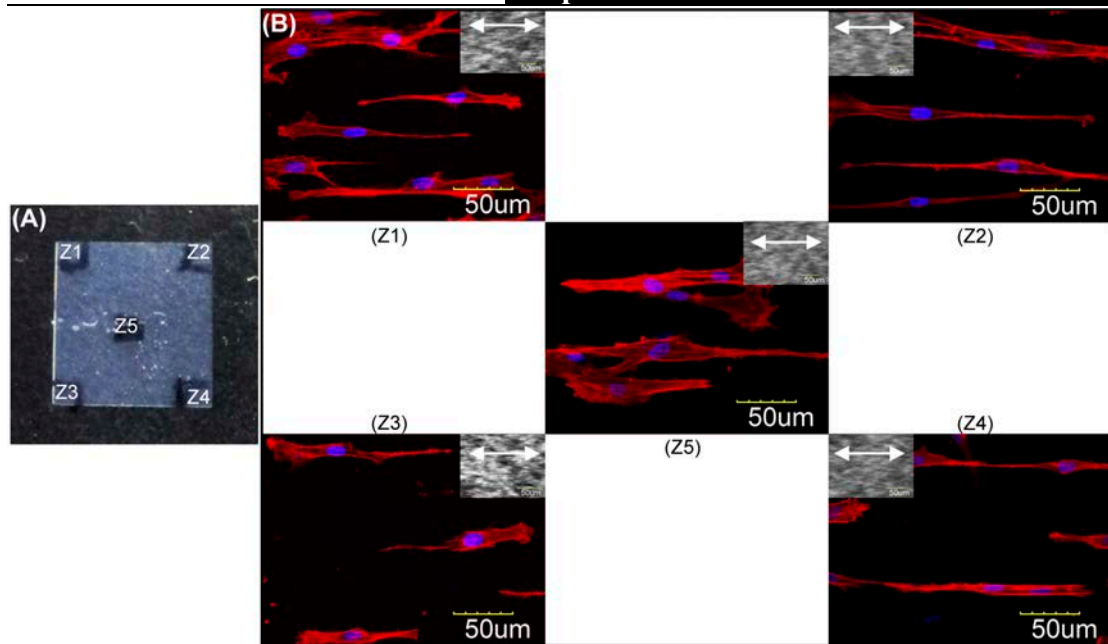


Figure 3-7: Consistent MSCs alignment. (A) UX_{HP}-PCL sample of 1x1 cm². (B) CLSM images of MSCs organization in representative zones (Z1-Z5) revealed consistent cell alignment in a controlled direction along ridges (Phalloidin: red, F-actin; DAPI: blue, DNA; White arrow: ridge direction; Scale bar = 500 μm).

Quantitatively, the angulation of MSCs on UX_{HP}-PCL anisotropic geometries was confined in a small range of -15 to $+15$ °, with a preferential orientation approximately parallel to the geometries (Angle-shift: 1.3 ± 0.9 °; Figure 3-8A). In contrast, the cellular arrangement angles of control group were evenly distributed, approaching the frequency distribution curve of a perfectly isotropic sample. Quantitative analysis of cellular alignment and elongation showed that MSCs cultured with UX_{HP}-PCL anisotropic geometries achieved significant increase in the normalised cell number in ± 10 ° (3.9x of control, $p < 0.001$; Figure 3-8B) and decrease in the CSI (0.7x of control, $p < 0.001$; Figure 3-8C).

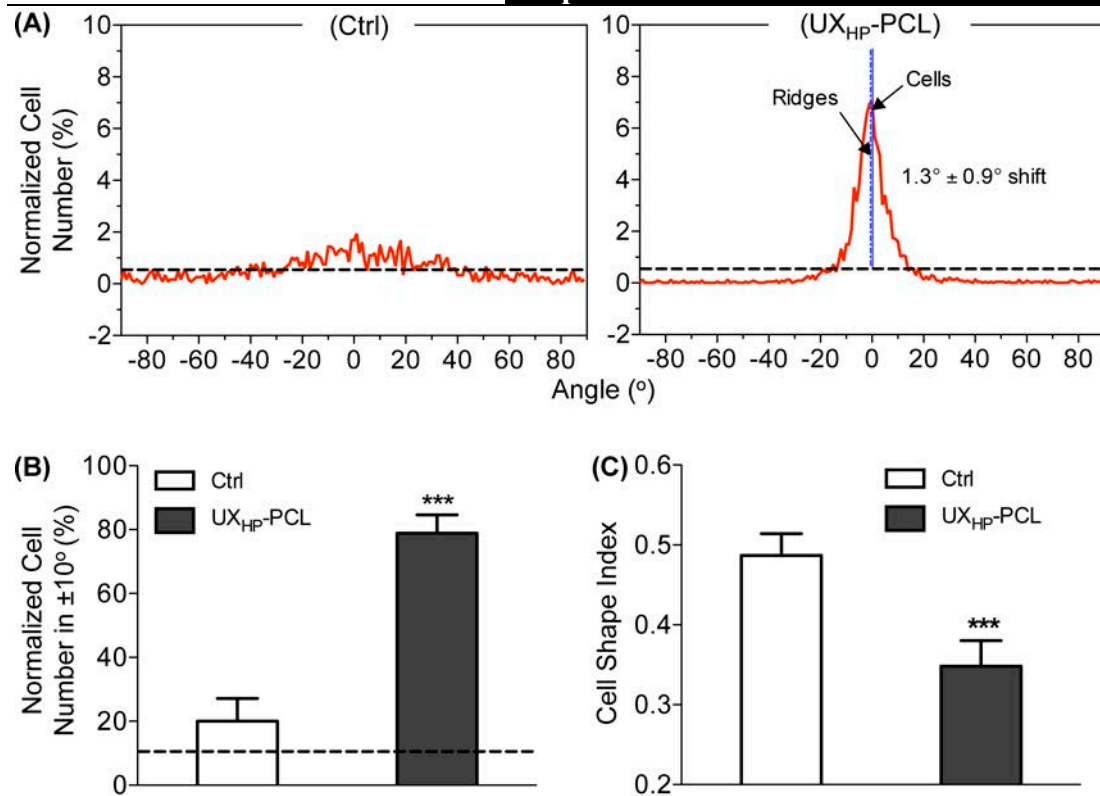


Figure 3-8: (A) Quantitative analysis of cellular arrangement angles. The angles of MSCs (Passage-6, 5k per cm², for 5 days of culture) on UX_{HP}-PCL concentrated within a small range of $\pm 15^\circ$, while cell angle frequency of control group (HP-PCL flat surface) approximated to that of an isotropic sample (Red line: frequency of MSCs angle distribution; Dashed-dark line: frequency of cellular angle distribution of an isotropic sample, which is $\sim 0.56\%$; Dashed-blue line: ridge direction; Solid-blue line: preferential cell orientation). (B) MSCs alignment represented by the normalised cell number within $\pm 10^\circ$ (Dashed-dark lines: expected values of a perfectly isotropic sample, which is $\sim 11.7\%$). (C) MSCs elongation represented by CSI (CSI of 1 representing a circle). MSCs cultured with UX_{HP}-PCL anisotropic geometries achieved significant increase in cellular alignment and elongation as compared to control. * represents the significant difference compared with that of control group ($n = 3$; ***, $p < 0.001$).

3.3.5 Dynamic and Long-Term Cellular Alignment

Figure 3-9 shows the dynamic organisation and morphology of MSCs on UX_{HP}-PCL anisotropic geometries. MSCs on UX_{HP}-PCL were found to align towards the anisotropic geometries after 12 hr of culture, exhibiting a wide range (-30 to $+10^\circ$) for cellular arrangement angles to distribute (Figures 3-9A and B). However, MSCs seemed to adjust towards the anisotropic geometries, leading to a narrower angle range at day 3, and maintained with minimal changes up to day 10. In contrast, MSCs

in the control group were observed to distribute randomly over the investigated period.

Quantitatively, MSCs for the initial culture of 12 hr on both UX_{HP}-PCL anisotropic geometries and HP-PCL flat surface revealed large CSI (>0.8) and low alignment efficiency (<35 %; Figures 3-9C and D). MSC alignment greatly increased from 12 hr to day 3, (1.3x increase, $p < 0.001$), and exhibited slight, continuous increment over day 3-10 (80.3 vs 85.4 %, $p > 0.05$; Figure 3-9C). Meanwhile, the CSI of MSCs on UX_{HP}-PCL anisotropic geometries reduced rapidly from 12 hr to day 3 (1.3x reduction, $p < 0.001$) and remained stable over day 3-10 (0.35 vs 0.32, $p > 0.05$; Figure 3-9D). Compared to the control, MSCs interacting with UX_{HP}-PCL anisotropic geometries achieved considerable increase in cellular alignment efficiency (Day 3, 2.8x of control, $p < 0.001$; Day 10, 2.8x of control, $p < 0.001$) and a significant reduction in CSI (Day 3, 0.9x of control, $p < 0.01$; Day 10, 0.8x of control, $p < 0.001$). The aligned and elongated growth of MSCs was maintained on UX_{HP}-PCL anisotropic geometries in a consistent orientation along the geometries, even when cells got confluent (15 days of culturing; Figure 3-10). In contrast, MSCs of the control group revealed local alignment only.

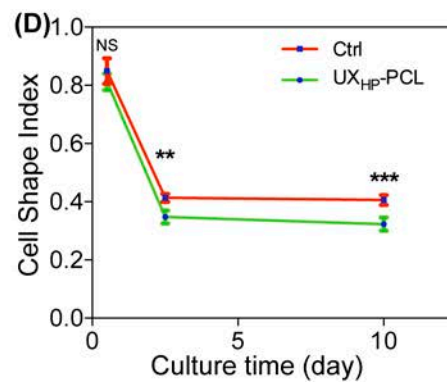
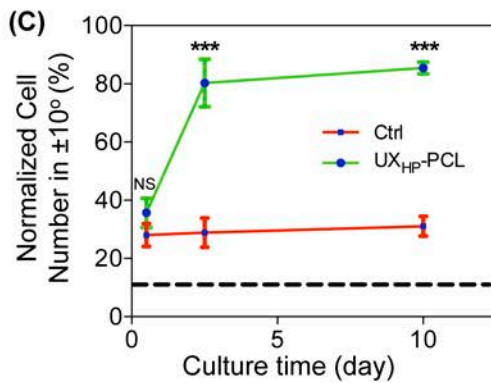
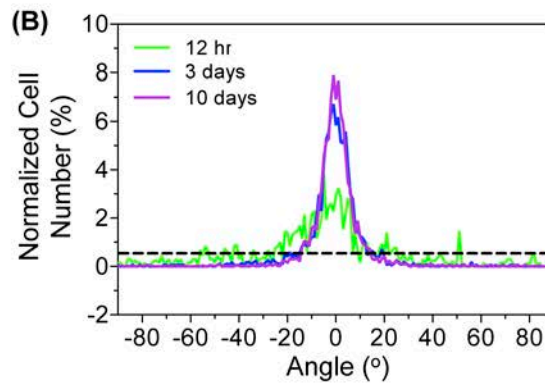
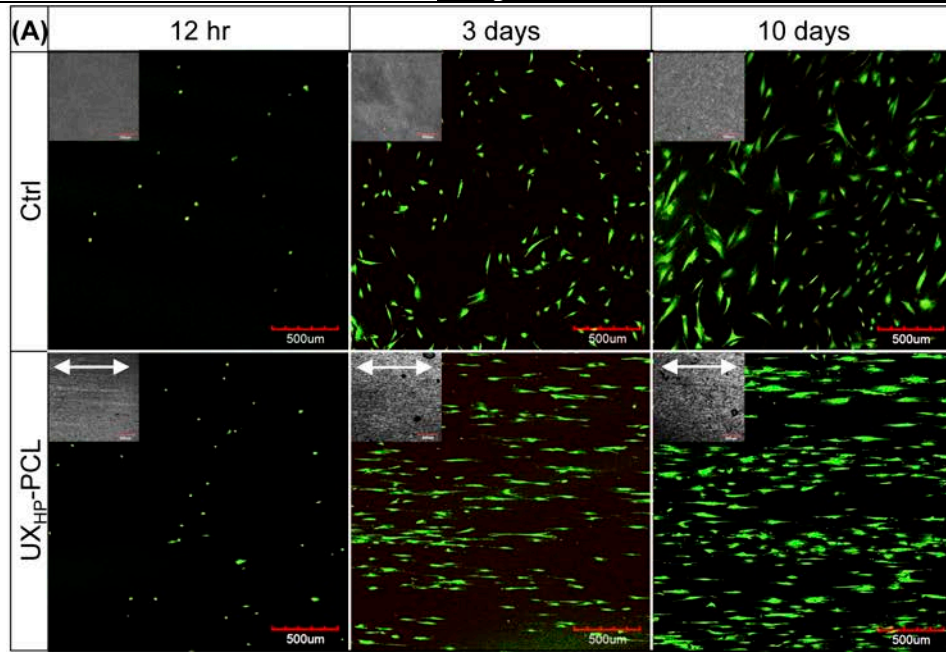


Figure 3-9: Dynamic cell alignment and elongation. **(A)** CLSM images of MSCs revealed aligned growth towards the anisotropic geometries of UX_{HP}-PCL over the investigated period (Control: HP-PCL flat surface; White arrow: ridge direction; Scale bar = 500 μm). **(B)** Frequency distributions of MSCs angles on UX_{HP}-PCL anisotropic geometries. Cell arrangement angles fell into a narrower range with increasing the culture time. **(C & D)** Dynamic cell alignment and elongation. MSCs on UX_{HP}-PCL achieved the rapid increase in cell alignment and elongation during initial culture of 3 days, and kept the efficiencies un-increased for further culture. * represents the significant difference compared with that of control group at each time point (n = 3; **, p < 0.01; ***, p < 0.001; NS, p > 0.05).

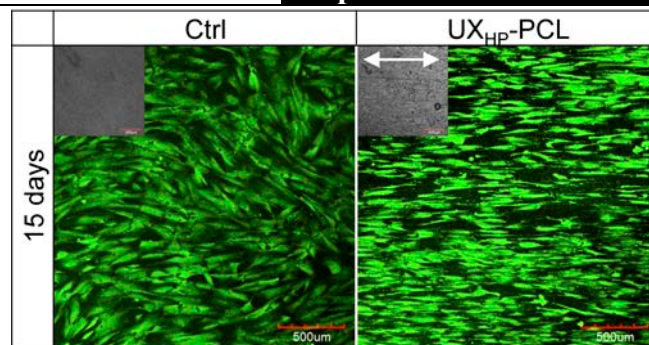


Figure 3-10: Long-term cell alignment capability. CLSM images from FDA/PI live-cell staining revealed a long-term aligned growth of MSCs on UX_{HP}-PCL after achieving confluence, but local cellular alignment only in control group (White arrow: ridge direction; Scale bar = 500 µm).

3.3.6 Cytotoxicity and Cellular Proliferation

Cytotoxicity of MSCs was evaluated by FDA/PI staining. MSCs after 0.5, 3, 5, 10 and 15 days of culturing on UX_{HP}-PCL anisotropic geometries revealed 100 % FDA-stained live cells (Green colour), without the presence of PI-stained dead cells (Red colour; Figures 3-6, 9A and 10). Results from MTS assay showed that MSCs proliferated well (Day 3 vs Day 6, $p < 0.001$; Day 6 vs Day 12: $p < 0.001$), with similar phenomena being observed on HP-PCL flat surface ($p > 0.05$; Figure 3-11). With increasing culture time, MSCs proliferation on UX_{HP}-PCL anisotropic geometries approached that on positive control group.

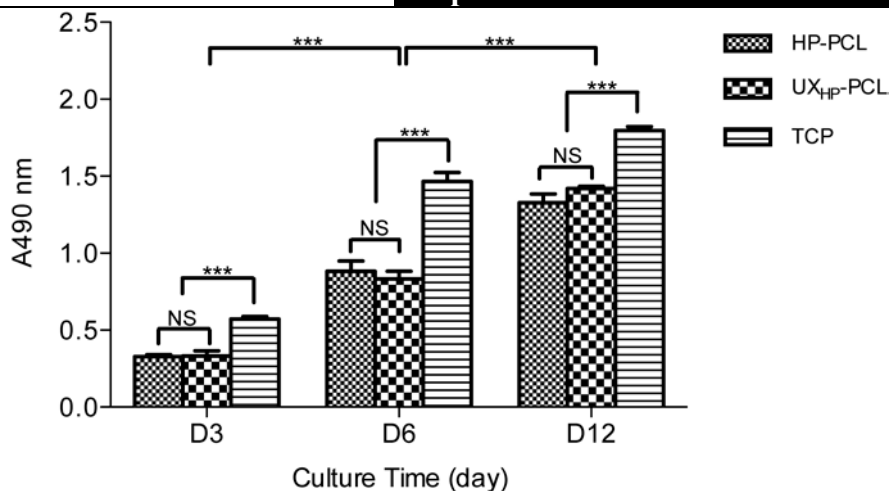


Figure 3-11: MSCs proliferation on UX_{HP}-PCL anisotropic geometries, HP-PCL flat surface and TCP flat surface (Positive control). UX_{HP}-PCL ridge/grooves supported MSCs growth with similar proliferation to that on HP-PCL flat surface, approaching that of positive control group with increased culture time (n = 5; ***, p < 0.001; NS, p > 0.05).

3.4 Discussion

In this study, a novel technique of uniaxial stretching was developed to create anisotropic geometries on PCL films. The anisotropic geometries of UX_{HP}-PCL consisted of self-assembling, highly orientated micro-3D ridges and grooves, with inter-ridge-distance and ridge-length being variable by T_s and DR . The anisotropic geometries enabled MSCs growth, with significant increase in the average cell alignment and elongation on UX_{HP}-PCL for over two weeks. Previous studies using soft-lithography and electrospinning methods have attempted to incorporate anisotropic geometries on PCL films. However, these techniques have considerable drawbacks such as unstable yield, non-uniform geometries in a large area, tedious procedures and/or chemical solvent usage and residual remains [132, 226, 227]. The method as described in this study had added advantages in providing a solvent-free, reproducible and simple fabrication for facilitating the incorporation of anisotropic topographies on PCL thin films. On the other hand, although PCL films have been used extensively in many applications, most of them lack functional topography

geometries [22, 233, 234]. The use of uniaxial stretching has achieved unique anisotropic geometries on PCL film surfaces. This strategy could enable a whole new range of complementary applications of PCL films for controlling cellular alignment and elongation in biomimetic tissue engineering.

It should be noted that uniaxial stretching in this work was applied mainly to PCL films. This method, however, could also be applicable to other thermoplastic polymers. In Figure 3-12, uniaxial stretching of polyethylene (PE) films resulted in similarly orientated wave-like structures as those observed on PCL films. To the best knowledge, the presenting method of uniaxial stretching is suitable for semi-crystalline polymers because the formation of micro-ridges required polymeric crystals. In this study, uniaxial stretching resulted in the micro-ridges and grooves on UX_{HP}-PCL. Meanwhile, it orientated the PCL molecular chains (Figure 3-13) with increased film crystallinity (Table 3-2), suggesting that recrystallisation of PCL crystals occurred, and a correlation between them and the resulted geometries structures existed. The thorn-like structures (~50 nm of width) and their perpendicular orientations to the stretching direction (Figure 3-14) agreed with the characteristics of the multilayered lamellas of polymeric films after uniaxial stretching [235]. Further degradation revealed a larger resistance of the ridges to hydrolysis, suggesting that the ridges were generated from the recrystallised PCL crystals [236]. Because the crystalline structures were more rigid than the amorphous structures, the recrystallised PCL crystals during uniaxial stretching would experience less deformation, while the superficial amorphous regions were easy to be deformed and formed into grooves to reveal the crystals from film surface as ridges (Figure 3-15).

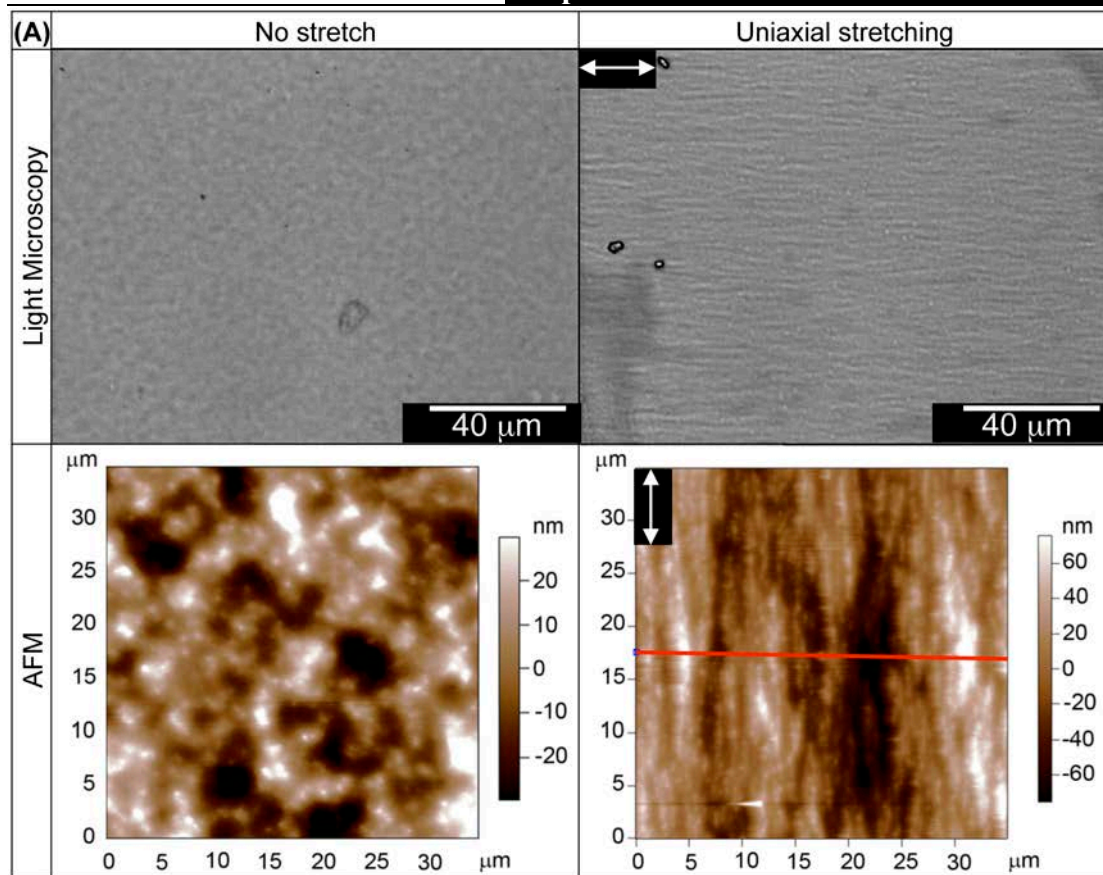


Figure 3-12: Anisotropic polyethylene (PE) geometries. Commercial PE films were stretched at T_s of 70 °C and DR of 4. **(A)** Light microscopy and AFM images revealed orientated wave-like geometries on PE films after uniaxial stretching, but non-anisotropic structures on un-stretched films (Double-headed arrows: stretching direction; Scale bar = 40 μm). **(B)** Typical height profile of uniaxial-stretched PE films [along the red-line shown in AFM images].

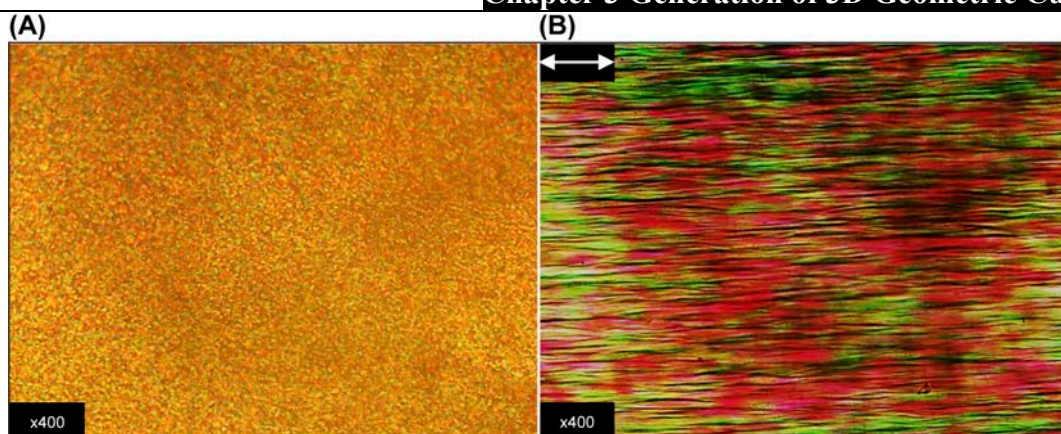


Figure 3-13: Polarised light microscopy (PLM) images of HP-PCL and UX_{HP}-PCL. Uniaxial stretching resulted in orientated molecular chains of UX_{HP}-PCL.

Table 3-2: Effects of uniaxial stretching on PCL film crystallinity

Films	HP-PCL	UX _{HP} -PCL
Crystallinity (%)	36.2	54.0

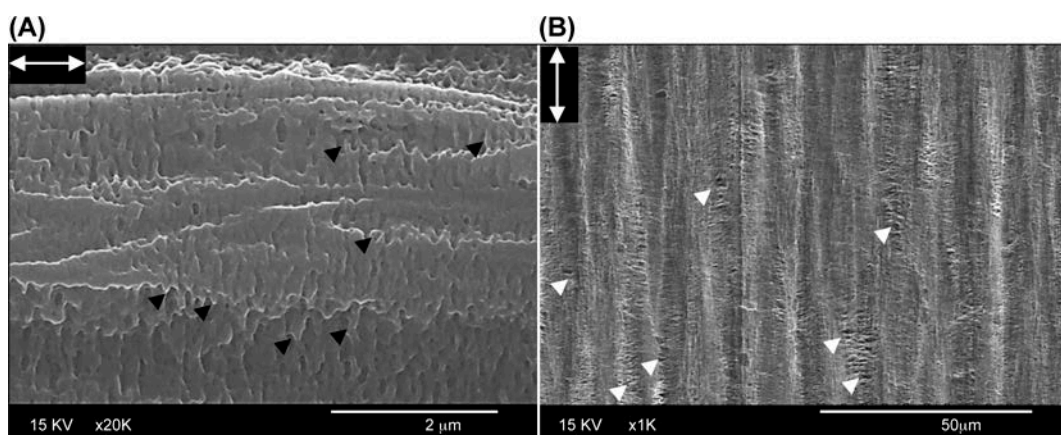


Figure 3-14: Ridges and grooves of UX_{HP}-PCL subjected to alkaline hydrolysis (NaOH, 3M) for 12 hr (A) and 20 days (B). FESEM images of ridges exhibited thorn-like structures (Dark arrows; ~50 nm in width) perpendicular to stretching direction, and larger resistance against hydrolysis as indicated from the less caves presented than grooves did (Double-headed arrows: stretching direction; White arrows: caves in the grooves; Scale bar = 2 and 200 μm).

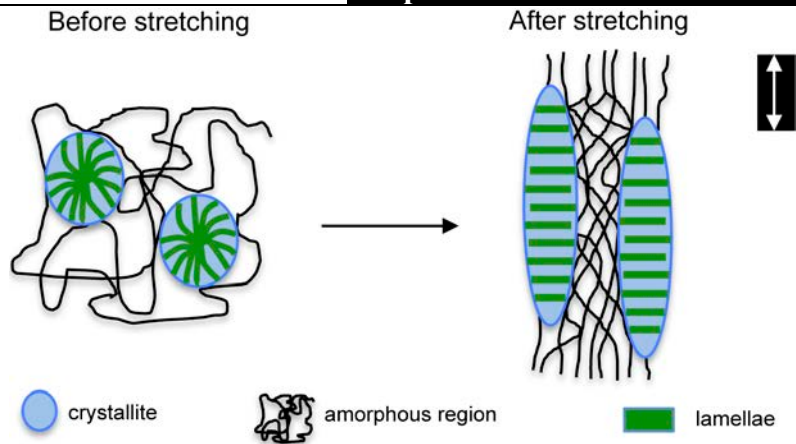


Figure 3-15: Schematic diagram illustrating formation of UX_{HP} -PCL ridges and grooves. Uniaxial stretching re-orientated the multilayered lamellas of HP-PCL, which self-packed into new crystals along stretching direction. During that process, film superficial amorphous regions formed into grooves because of being easily deformed, while the crystals experienced less deformation and were revealed out from film surface as elongated ridges.

It should also be noted that during the initial elastic deformation, the center of UX_{HP} -PCL might experience a larger extent of stretching than the film at the two ends. This effect probably resulted in the smaller inter-ridge-distance observed in the film center because of larger Poisson's contraction [237]. However, most regions of UX_{HP} -PCL from the center to the two ends might experience similar extent of stretching because the changes of film contraction existed mainly near the film ends, and no significant difference of inter-ridge-distance was found in the regions of film central area (X-0 to X-3). Additionally, boundary effects could exist during the stretching process. A reduction in the inter-ridge-distance was found in the regions near the film edge (Y-4), probably because of the larger DR that the edge parts experienced [238]. However, the reduction observed was limited to the film edge location and did not result in distinct morphology difference as compared to the film center. In addition, all the film samples used in this work were taken from film central area of Y-0 to Y-2 and X-0 to X-3.

The UX_{HP}-PCL exhibited anisotropy in both geometric structures and surface hydrophilicity. However, due to the intrinsic properties of low melting point (~60 °C) and ester bond, PCL surfaces were susceptible to undergo the subsequent modification steps such as plasma and hydrolysis treatment [17]. Interestingly, the micro-ridges and grooves of UX_{HP}-PCL were shown to be resistant to hydrolysis within the period investigated, suggesting that the anisotropic geometries conferred by uniaxial stretching could undergo proper modification for incorporating more desired physicochemical characteristics such as RGD-peptides and CD34, on UX_{HP}-PCL for specific applications [222, 239]. The anisotropic surface hydrophilicity observed on UX_{HP}-PCL could be attributed by the increased surface roughness in perpendicular direction due to the presence of 3D micro-ridges and grooves [240]. It was worthy to note that during the hydrolysis period, the anisotropy of surface hydrophilicity was retained. This suggested that in addition to “contact guidance”, alterations to the physico-chemical interactions at the biomaterial surface might be introduced to induce gradients that further influence and initiate cellular alignment [146, 241].

The biological benefits of UX_{HP}-PCL were demonstrated in modulating MSCs behaviour. MSCs were selected because of their potential as a cell source for tissue engineering [242]. UX_{HP}-PCL anisotropic geometries were capable of eliciting MSCs alignment in a controllable direction, as demonstrated by both cytoskeletal and cytoplasmic staining. Ridge-depth, during the cell-substrate interaction, has been known to influence cellular responses to a given lateral dimension [243, 244]. The MSCs alignment on UX_{HP}-PCL anisotropic geometries suggested that the ridge-depth conferred by uniaxial stretching was able to facilitate cellular responses to the geometric structures. A limitation of the current process as compared to other

microfabrication techniques was the inability to control precisely ridge-depth, which ranged from 200 to 900 nm in the UX_{HP}-PCL. An “optimum” ridge-depth, however, remains to be elucidated, with recent studies suggesting that topography heterogeneity, rather than absolute dimensions, are more physiologically relevant [138]. Further work was warranted to better understand the influence of heterogeneous ridge-depth on MSCs responses including differentiation and function.

Cell alignment in previous studies has been relatively loosely defined such as the cumulative cell number within $\pm 10^\circ$ [230], $\pm 15^\circ$ [121] and $\pm 30^\circ$ [245]. Here, a more accurate measurement was employed. Although geometric dimensions tend to influence the interaction between cells and substrates, the reported alignment efficiency of MSCs on UX_{HP}-PCL ($>85\%$, $\pm 10^\circ$) was comparable with the previous reports on PCL micropatterns [227] and considerably higher than those on other reported patterns (e.g. Silicon: $\sim 50\%$, $\pm 10^\circ$ [230]; PLLA-PCL: $<70\%$, $\pm 15^\circ$ [121]). It was likely that both the 3D micro-ridge/grooves and anisotropic surface hydrophilicity acted as cues to contribute simultaneously to the high alignment efficiency [146, 241]. Interestingly, the MSC alignment as observed was a dynamic one. MSCs were able to adjust their orientations according to the ridges, which achieved high degree of cellular alignment over time. It has been known that substrates with microdimensions had better ability to modulate cell alignment than those with nanodimensions [219]. However, too large a dimension, particularly in groove-width larger than 50 μm , often resulted in delayed and low alignment efficiency, and cellular confluence was required before alignment occurred [146, 246]. In comparison, MSCs were able to align rapidly on UX_{HP}-PCL anisotropic geometries despite low cell density.

One important aspect concerning the actual applications of anisotropic topography to generate aligned tissue constructs was the consistent regulation of cues on cellular alignment. Here, the aligned MSC organisation within the entire film remained for more than two weeks, with no observed reduction in the alignment efficiency, suggesting the ability of UX_{HP}-PCL in facilitating long-term MSCs alignment. Moreover, the alignment orientation of MSCs was consistent over time, with a controllable direction determined by the ridges. In contrast, cell alignment on chemical patterns was known to undergo changes in cellular orientations during cell proliferation [245], likely attributed to the preference of cells to 3D topographical structures over 2D chemical cues [247]. This demonstrated a consistent elicitation of UX_{HP}-PCL topographies on MSC alignment. In potential applications of engineering 3D layer-stacked cell-scaffold constructs, the orientation of cell alignment in each layer could be tailored by the adjustment of placed film angles. Meanwhile, UX_{HP}-PCL anisotropic geometries increased MSC elongation as compared to the control group, with stable cellular elongation after 3 days of culturing. Such consistent regulation in cellular alignment and elongation was known to have profound effects on MSC fate including differentiation towards muscle cells [246, 248]. Moreover, UX_{HP}-PCL did not present any cytotoxicity, but allowed MSCs to proliferate over time. The anisotropic topographies of UX_{HP}-PCL achieved robust spatial and temporal regulation of MSC elongation and alignment.

3.5 Summary

In this work, a novel solvent-free, reproducible and simple method of uniaxial stretching was developed to create geometric cues on bioresorbable films for stem cell

alignment control. Results showed that uniaxial stretching of PCL films resulted in anisotropic geometries, consisting of 3D self-assembling micro-ridges and grooves (Ridge-length: $\sim 90 \mu\text{m}$, Inter-ridge-distance: $\sim 6 \mu\text{m}$, Ridge-depth: 200-900 nm) that highly orientated and homogeneously distributed towards the stretching direction over film surface. The inter-ridge-distance and ridge-length could be varied through changing of stretch temperature and draw ratio. The PCL ridge/groove arrays allowed surface modification such as hydrolysis for achieving improved hydrophilicity, while maintaining the ridges and grooves well. MSCs cultured with the PCL ridge/groove arrays revealed an aligned organisation in a controllable orientation along the ridges, without indication of cytotoxicity or reduction in cellular proliferation. Compared to HP-PCL flat surfaces, MSCs interacting with the anisotropic geometries achieved larger increase in cellular alignment ($>85\%$) and elongation for a prolonged period (>2 weeks). These results demonstrated that uniaxial stretching could have potential in patterning film surface for biomimetic VTE applications. PCL films with anisotropic ridge/groove arrays could be used as “functional cues” for eliciting cell alignment and elongation as well as “basic units” in conjunction with stem cells for regenerating complex tissue such as blood vessels that require high cellular alignment and anisotropic functions.

Chapter 4 Regulated Mesenchymal Stem Cell Behaviour via Anisotropic Geometries for Vascular Tissue Engineering

4.1 Introduction

Tissue engineering (TE) offers a novel therapy to improve or regenerate vascular function using a combination of biomaterials, cells and engineering techniques [11, 16]. As an essential structure, tunica media is crucial for healthy artery functions to maintain the endothelium phenotypes, support mechanical strength and regulate blood pressure by contraction and relaxation to a variety of stimulus [16, 249]. These have been known to rely on the specific architectures of tunica media, which composed of circumferentially aligned vascular smooth muscle cells (SMCs) and elastin/collagen-enriched extracellular matrices (ECM) [16, 28, 115, 215, 249].

Geometric features consisting of orientated fibers [250] and ridge/groove arrays [2] have been designed to mimic the anisotropy in tunica media architectures for vascular tissue regeneration. It has been known that SMCs cultured on ridge/groove arrays achieved reduced cell proliferation rates and anisotropic patterns as in native tunica media [2, 61, 155]. Moreover, geometric features have shown potential to modulate SMCs phenotypes towards the contractile status [28, 115]. Despite these great achievements of basic research, the incorporation of geometric features onto three-

dimensional (3D) tubular vascular scaffolds remains a challenging issue yet to be solved. Currently available techniques such as soft-lithography, electrospinning and direct-laser-writing often involved tedious procedures and/or chemical solvent usage and residue [251]. Furthermore, both soft-lithography and direct-laser-writing are more suitable for thick substrates than thin films in a small area, hampering the generation of "off-the-shelf", non-cytotoxic and cost-effective vascular grafts.

Traditionally, patient-specific SMCs have been utilised as a classic cell source for tunica media regeneration [252]. Recent studies, however, found that adult mature SMCs have limited proliferation with decreased collagen and elastin secretion, and tend to de-differentiate towards the synthetic status, leading to construction of vascular grafts becoming difficult [85, 96, 249]. Mesenchymal stem cells (MSCs) are potentially useful for vascular tissue regeneration [85]. *In vitro*, MSCs can be expanded and differentiated into SMCs under stimulus of various biochemical factors including transforming growth factor (TGF- β 1), platelet-derived growth factor and ascorbic acid [57, 85, 96, 249]. Moreover, MSCs as compared to adult mature SMCs have advantages in antithromogenicity [94], easy access [85] and lack of expression of major histocompatibility complex II antigens to response for immune rejection [93]. However, using growth factors to differentiate MSCs is expensive. Optimal concentration is difficult to control and the side effects of growth factors may result in atherosclerosis [57].

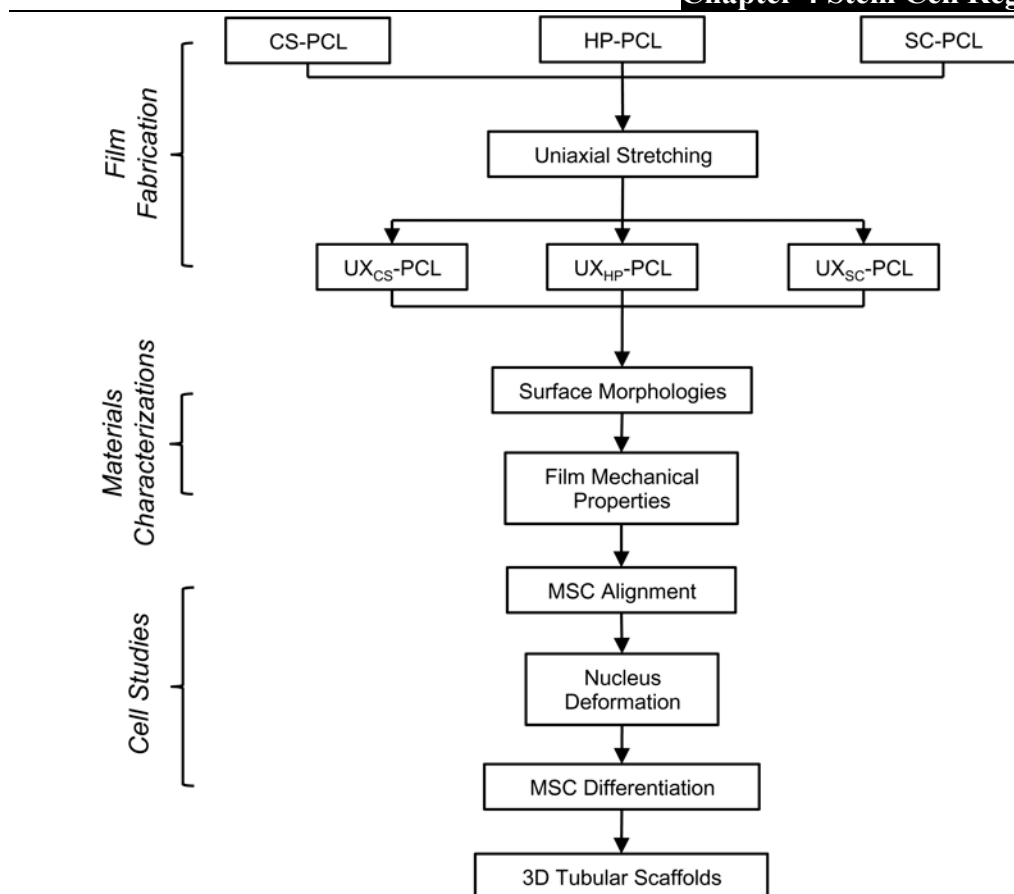
In Chapter 3, poly(ϵ -caprolactone) (PCL) film geometric cues have been developed using uniaxial stretching, and shown robust capability of aligning MSCs. In this work, PCL films with the ridge/groove arrays are applied to biomimic the anisotropy of

vascular basement membrane (BM) and modulate MSCs behaviour for vascular TE (VTE) application. The PCL films have been shown to up-regulate the expression of SMCs contractile markers in MSCs, and facilitate the construction of 3D tubular VTE scaffolds. This work would support the potential of using geometric cues to biomimic BM anisotropy in conjunction with stem cells for VTE application.

4.2 Materials and Methods

4.2.1 Experimental Design

PCL films with biomimetic 3D geometric cues in incorporation of human MSCs were utilised towards vascular TE application. As shown in Scheme 4-1, uniaxial stretching was applied on PCL films fabricated from different methods. Selection of PCL films has been performed, and the PCL films with best mechanical property and proper geometries were utilised to promote regulate MSCs function towards a contractile SMCs-like phenotype and for the construction of 3D vascular scaffolds.



Scheme 4-1: Schematic diagram illustrating the experimental design. Uniaxial stretching was applied to generate ridge/groove arrays on various PCL films. Materials characterisations focused on surface morphologies and film mechanical properties. *In vitro* cellular studies included MSCs alignment, cytoskeleton and nucleus changes, and the expression of SMCs contractile markers. Finally, PCL films with ridge/groove arrays in incorporation of MSCs were used for the construction of 3D tubular VTE scaffolds.

4.2.2 Materials

Monoclonal mouse anti-human smooth muscle α -actin (SM- α -actin), calponin, myosin heavy chain (SM-MHC), IgG2a and IgG1 were purchased from Dako (Singapore). Goat anti-mouse IgG (H+L)-fluorescein isothiocyanate (FITC) was obtained from Life Technologies (Singapore). RNeasy mini kit and RT² first strand kit were obtained from Qiagen (Singapore). Other materials and cells used were obtained as described in Chapter 3, Section 3.2.2.

4.2.3 Sample Preparation

PCL pellets were dissolved in dichloromethane to obtain PCL solution at a concentration of 2 wt.%. Solvent-cast PCL (SC-PCL) films were obtained through casting of the PCL solution into a glass mold followed by evaporation in a fume hood. Cast-stretch PCL (CS-PCL) films were obtained using an in-house developed machine via cast extrusion. Heat-press PCL (HP-PCL) films were fabricated via heat press of PCL solid mass at 80 °C and 300 MPa. The PCL films were then subjected to uniaxial stretching at a temperature of 54 °C and a draw ratio of 4 [126], and named as UX_{SC}-PCL, UX_{CS}-PCL and UX_{HP}-PCL, respectively.

4.2.4 Field Emission Scanning Electron Microscopy (FESEM)

PCL film morphologies were examined via FESEM (S-4300, Hitachi, Japan). Inter-ridge-distance was measured following the description in Chapter 3, Section 3.2.4. Three samples were used for each kind of PCL film.

4.2.5 Atomic Force Microscopy (AFM)

PCL film morphologies were also examined via AFM (MFP-3D, Asylum Research, USA) examination. Ridge-depth was measured following the description in Chapter 3, Section 3.3.5. Data were present as the average of the mean from each measurement. Three samples were used for each kind of PCL film.

4.2.6 Tensile Testing

PCL films were cut into rectangular shapes measuring 5x30 mm². Thickness was measured using a Digimatic Micrometer (APB-1D, Mitutoyo Corporation, Japan) at 5 random positions of each sample. Tensile testing was performed using a tensile test

machine (Model 3345, Instron, USA) with a load cell of 100 N and a pulling rate of 10 mm/min. An offset-strain of 0.005 was used to determine the yield stress and strain for UX_{CS}-PCL, UX_{SC}-PCL and UX_{HP}-PCL. A low yield point just beyond the maximum point after linear-elastic region was used to determine the yield stress of HP-PCL. The corresponding strain at linear-elastic part was determined as the yield strain. Three samples were used for each kind of PCL film.

4.2.7 Cell Isolation and Culture

MSCs were isolated and cultured following the description in Chapter 3, Section 3.2.9. In this work, MSCs used were within Passage-6.

4.2.8 Confocal Laser Scanning Microscopy (CLSM)

Images of fluorescence-labeled cells were examined using CLSM (CLSM, FV1000, Olympus, Japan) following the description in Chapter 3, Section 3.2.10.

4.2.9 Cell Alignment and Elongation

MSCs were labeled via both fixed-cell cytoskeletal and live-cell cytoplasmic staining using TRITC-conjugated phalloidin and FDA, respectively. Cellular angles were analysed from the CLSM images of live cells using the built-in function of NIH ImageJ software (USA). The method was described in Chapter 3, Section 3.2.11. Cells with angles that fall into $\pm 10^\circ$ were considered to be aligned [126]. The alignment efficiency was described as the normalised cell number within $\pm 10^\circ$. A perfectly isotropic sample would be expected to have an alignment efficiency of $\sim 11.7\%$. The cell elongation was described using a long-to-short elliptic axis index, which was equal to the ratio of major and minor elliptic axis of a cell. A circle would

have a long-to-short index of 100 %. Three copies were used and four random regions per copy were analysed for each PCL film sample.

4.2.10 Cell Nucleus Alignment and Elongation

Cell nuclei were visualised using DAPI and images were captured via CLSM following the description in Chapter 3, Section 3.2.10. The angle of cell nucleus was analysed using the built-in function of ImageJ. Cellular nuclei with angles that fall into $\pm 10^\circ$ were considered to be aligned. Alignment efficiency was described as a percentage number of aligned nuclei. A perfectly isotropic sample would be expected to have an alignment efficiency of $\sim 11.7\%$. Nucleus elongation was determined using a cell nucleus shape index (CNSI, circularity = $4\pi \cdot \text{area} / \text{perimeter}^2$), with a CNSI of 1 representing a circle. Three samples were used and four random regions per sample were analysed for each kind of PCL film.

4.2.11 Real-time Quantitative Reverse Transcription Polymerase Chain Reaction (qRT-PCR)

Real-time qRT-PCR was performed to investigate the expression of interested gene targets (Table 4-1) in MSCs. Briefly, MSCs seeded on TCP flat surfaces (control group), HP-PCL flat surfaces and UX_{HP}-PCL ridge/groove arrays were cultured in D10 under identical conditions for 5 days. Total RNA was extracted using RNeasy mini kit. cDNA was synthesized using RT² first strand kit. qRT-PCR was performed on a ABI Prism 7000 real-time detection system (AB Applied Biosystem, USA) for 45 cycles. Primers specific to the targeted genes were obtained from PrimerBank (<http://pga.mgh.harvard.edu/primerbank/>). The normalised expression levels of each gene targeted were determined by comparing the quantified cDNA transcript level to

that of glyceraldehyde-3-phosphate dehydrogenase (GAPDH, used as the internal standard) [126]. The results were finally normalised to the relative expression levels of each gene of TCP group. Three experiments and triplicates were done.

Table 4-1: Compiled list of gene targets probed for SMC contractile markers

GenBank Accession Number	Gene Target	Sequence (5'-3')	Amplicon Length (bp)
NM_001256799	GAPDH	ACAGTTGCCATGTAGACC TTTTTGGTTGAGCACAGG	95
NM_001613	ACTA2	AGATCAAGATCATTGCCCC TTCATCGTATTCTGTTTGC	116
NM_001299	CNN1	CATCATTCTTTGCGAATTCATC CAATTTTGGGTTGACTCATTG	75
NM_022844	MYH11	CTATCTGCTAGAAAAATCACGG CACTTCTCATCTTCTCCTTG	104

4.2.12 Immunocytochemistry Assays

Immunocytochemistry assays were performed to investigate the expression of contractile SMCs markers in MSCs at protein level. MSCs seeded on HP-PCL flat surfaces and UX_{HP}-PCL ridge/groove arrays were cultured in D10 for 5 days. After fixation, permeabilisation and blocking, cells were incubated with primary monoclonal antibodies (Table 4-2) for 60 min at room temperature. Cells incubated with the corresponding IgG isotype of each primary antibody were set as negative control (Neg Ctrl). After washing thrice with PBS, cells were further incubated with the second antibody (goat anti-mouse IgG-FITC) for another 60 min at room temperature. After washing thrice with PBS, cells were then incubated with DAPI (1:1000 in PBS) for 5 min for the nucleus visualisation. Cell images were captured by CLSM. The parameters used for each SMCs contractile marker were kept the same for all groups.

Table 4-2: Compiled list of monoclonal antibodies for SMCs contractile markers

1 st Monoclonal Antibodies (Mouse anti-human SM)	IgG Isotypes	Dilution in 1-wt% BSA Solution (v/v)
SM- α -actin	IgG 2a k	1:100
Calponin	IgG 1 k	1:100
SM myosin heavy chain (SM-MHC)	IgG 1 k	1:50
2 nd antibody (Goat anti-mouse IgG-FITC)	/	1:500

4.2.13 Flow Cytometry

Intracellular Quantitative Analysis: Fluorescence-activated cell sorting (FACS) was applied to quantify the protein expression levels of targeted SMCs contractile markers. MSCs were seeded and cultured following the description in Chapter 4, Section 4.2.12. After 5 days of culture, cells were treated with trypsin-EDTA (0.25 %) and collected through centrifugation (400 rcf, 5 min). Cells were then incubated with SMCs-specific primary monoclonal antibodies and related IgG isotypes (Neg Ctrl). Intracellular fluorescence was detected using a flow cytometry (Beckman, USA) equipped with an argon laser emission of 488 nm. Data were analysed from 10,000 cells per sample using the built-in function of Summit V4.3.02 software (Beckman, USA). The gate was set with a positive cell number in Neg Ctrl being less than 0.5 %. Three experiments and triplicates were carried out.

Extracellular Quantitative Analysis: Cellular surface protein expression of targeted markers on the isolated MSCs was analysed using FACS. Briefly, MSCs were cultured in cell culture flask to get ~75 % confluence. Cells were then trypsinised, fixed and incubated with monoclonal antibodies that were specific for stem cell immunophenotype and related IgG1 isotypes (Neg Ctrl). Cellular fluorescence was

determined and analysed following the description in Section 4.2.13 (Intracellular Quantitative Analysis).

4.2.14 Data Analysis

Data analysis was performed on Prism 5 software. Results were reported as mean \pm SD. A value of $p < 0.05$ was considered to be statistically significant.

4.3 Results

4.3.1 Stem Cell Immunophenotype of Isolated Human MSCs

In vitro isolated, culture-expanded human MSCs (Passage-6) grew as plastic-adherent cells (Figure 4-1). FACS analysis of surface markers' expression of the cells revealed typical stem cell immunophenotype, which was negative (<1.5 %) for the haemopoietic and endothelial markers: CD19, CD31 and CD34, and positive (>95 %) for the mesenchymal markers: CD73 (SH-3, SH-4), CD105 (SH-2) and cell adhesion molecules: CD90 (Table 4-3). These observations suggested that the isolated, culture-expanded MSCs were stem cells [253].

Table 4-3: Stem cell immunophenotype of isolated MSCs (Passage 6)

Stem-Cell-Specific Monoclonal Antibodies	IgG Isolypes	Positive Cell Number	
		Neg Ctrl (%)	Experimental (%)
CD73 IgG1-APC	IgG1-APC	0.05	99.95
CD45 IgG1-FITC	IgG1-FITC	0.33	0.36
CD90 IgG1-FITC			99.76
CD19 IgG1-RPE	IgG1-RPE	0.05	0.03
CD34 IgG1-RPE			1.22
CD105 IgG1-RPE			99.48

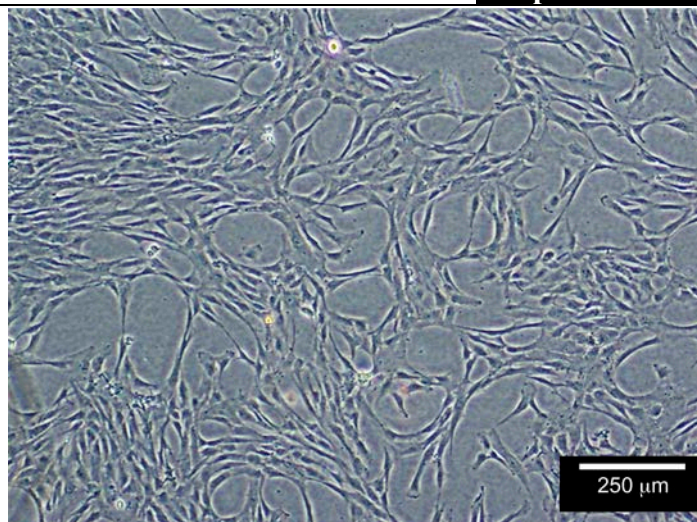


Figure 4-1: Light microscopy images of *in vitro* culture expanded human MSCs (Passage-6).

4.3.2 Anisotropic 3D Ridge/Groove Arrays on PCL Films

As shown in Figure 4-2A, FESEM images of PCL films revealed different morphologies. SC-PCL, HP-PCL and CS-PCL exhibited honeycomb-like surfaces, flat surfaces with some indentations, and smooth surfaces, respectively. Interestingly, FESEM images of all these PCL films after uniaxial stretching showed anisotropic geometries, consisting of highly orientated micro-3D ridges and grooves following the stretching direction (Figure 4-2B). The ridge/groove arrays were confirmed by the examination of AFM.

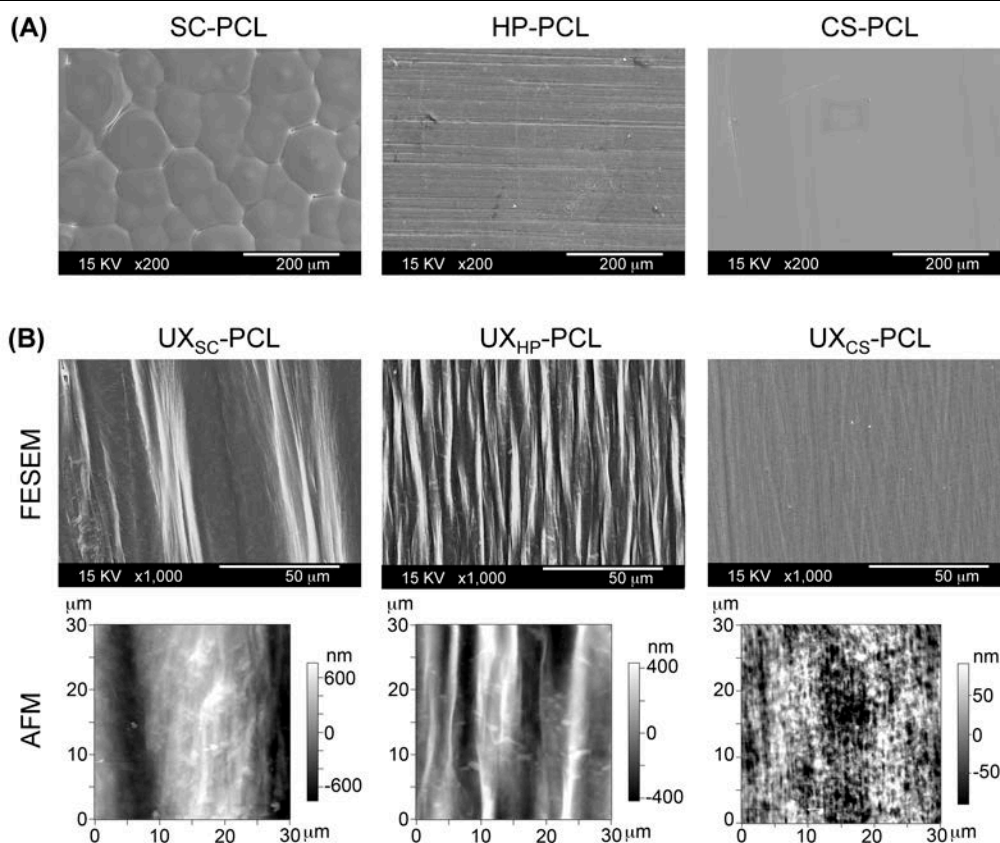


Figure 4-2: (A) Field emission scanning electron microscopy (FESEM) images of SC-PCL, HP-PCL and CS-PCL revealed different surface morphologies (Scale bar = 200 μm). (B) FESEM and atomic force microscopy (AFM) images of UX_{SC}-PCL, UX_{HP}-PCL and UX_{CS}-PCL revealed film morphologies of anisotropic geometries (Scale bar = 50 μm for FESEM images).

As shown in Figure 4-3A, the ridge/groove arrays of UX_{SC}-PCL revealed the widest inter-ridge-distance among the three films investigated (9.0x of UX_{HP}-PCL and 10.2x of UX_{CS}-PCL, $p < 0.001$). UX_{HP}-PCL and UX_{CS}-PCL exhibited similar inter-ridge-distance ($p > 0.05$) of ~ 5 μm. Furthermore, Figure 4-3B shows that UX_{SC}-PCL also possessed the largest ridge-depth, which was 2.9x of UX_{HP}-PCL and 17.5x of UX_{CS}-PCL ($p < 0.001$). The ridge/groove arrays of UX_{HP}-PCL exhibited a larger ridge-depth than that of UX_{CS}-PCL (5.1x increase, $p < 0.001$).

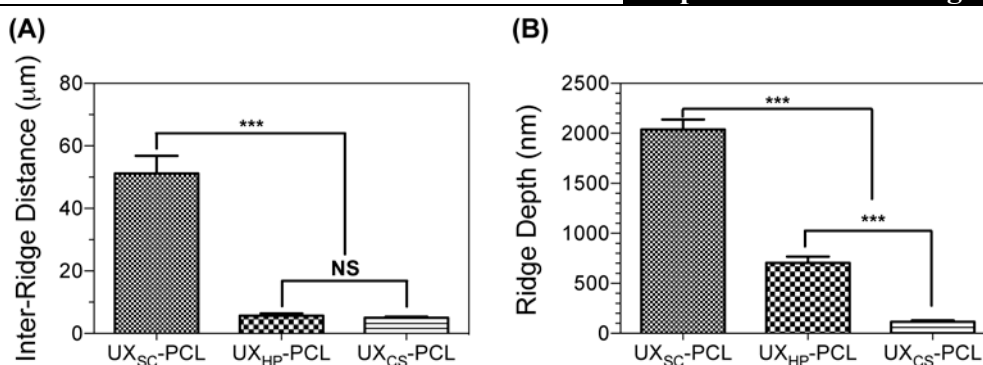


Figure 4-3: (A) Inter-ridge-distance. (B) Ridge-depth. Among three-stretched PCL films, UX_{HP}-PCL ridge/groove arrays revealed medium inter-ridge-distance and ridge-depth. (n = 3; ***, p < 0.001; NS, p > 0.05)

4.3.3 Film Mechanical Properties

As shown in Figure 4-4A, tensile testing of UX_{SC}-PCL, UX_{CS}-PCL and UX_{HP}-PCL exhibited similar stress-strain correlations, with the curves consisting of linear segments up to the proportionality limit and non-linear parts characterising with increased elongation, but non-corresponding rise in the loading stress. Analysis from the stress-strain curves showed that UX_{HP}-PCL ridge/groove arrays as compared to UX_{SC}-PCL and UX_{CS}-PCL had better film mechanical performances in regards to the yield stress (0.3-0.5x increase, p < 0.05), Young's Modulus (2.1-2.6x increase, p < 0.001), ultimate stress (0.8-2.4x increase, p < 0.001) and ultimate strain (0.3-0.5x increase, p < 0.001; Table 4-4). Moreover, the film yield strain of UX_{HP}-PCL ridge/groove arrays was similar to that of UX_{CS}-PCL ridge/groove arrays (p > 0.05) and much larger than that of UX_{SC}-PCL ridge/groove arrays (0.9x increase, p < 0.001).

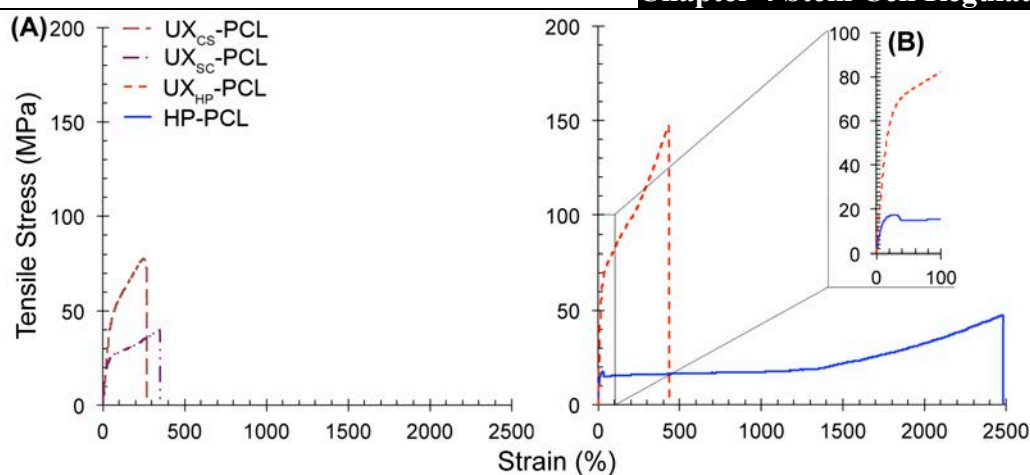


Figure 4-4: (A) Tensile stress-strain curves of PCL films. (B) Enlarged stress-strain curves of UX_{HP}-PCL and HP-PCL. UX_{HP}-PCL exhibited continuous stress increase after achieving the linear stress-strain segment, which was similar to those of UX_{SC}-PCL and UX_{CS}-PCL, and different from that of HP-PCL.

A comparison was then performed between HP-PCL flat surfaces and UX_{HP}-PCL ridge/groove arrays. As shown in Figure 4-4B, UX_{HP}-PCL ridge/groove arrays exhibited a different film stress-strain correlation from that of HP-PCL flat surfaces. The film stress-strain curve of HP-PCL flat surfaces after achieving the proportional limit experienced a dip in the stress value following with a considerable elongation, but less raise in loading stress. Furthermore, UX_{HP}-PCL ridge/groove arrays as compared to HP-PCL flat surfaces had significant increase in film yield stress (2.5x increase, $p < 0.001$), Young's Modulus (2.1x increase, $p < 0.001$) and ultimate stress (2.6x increase, $p < 0.001$; Table 4-4). Meanwhile, uniaxial stretching did not result in any obvious reduction in the film yield strain ($P > 0.05$).

Table 4-4: Film mechanical properties and theoretical burst stress (n = 3)

PCL film	Thickness (μm)	Yield stress (MPa)	Yield strain (%)	Young's Modulus (MPa)	Ultimate stress (MPa)	Ultimate strain (%)	Burst pressure* (mmHg)
UX _{CS} -PCL	24.7 \pm 5.6	42.8 \pm 8.1	35.8 \pm 4.3	107.3 \pm 23.4	81.0 \pm 4.2	277.5 \pm 10.6	2280.2 \pm 322.5
UX _{SC} -PCL	16.3 \pm 1.6	15.9 \pm 3.0	16.8 \pm 1.3	94.6 \pm 20.4	43.3 \pm 4.3	315.0 \pm 30.4	1305.1 \pm 322.5
UX _{HP} -PCL	37.9 \pm 5.5	55.7 \pm 7.2	31.3 \pm 2.8	336.8 \pm 34.9	145.9 \pm 15.0	419.3 \pm 15.0	5873.0 \pm 652.6
HP-PCL	169.7 \pm 17.1	16.0 \pm 3.0	30.7 \pm 2.8	109.2 \pm 33.2	40.9 \pm 9.8	2450.0 \pm 0.0	/

*TEVG scaffolds based on single film-layer with a radius of 2.3 mm.

4.3.4 MSCs Alignment and Elongation

Figure 4-5A shows the live-cell cytoplasmic staining of MSCs. CLSM images demonstrated that MSCs grew on the surfaces of CS-PCL, SC-PCL and HP-PCL exhibited random organisation. Interestingly, MSCs on UX_{SC}-PCL and UX_{HP}-PCL ridge/groove arrays achieved preferential aligned growth towards the ridge directions (Figure 4-5B). However, MSCs on UX_{CS}-PCL ridge/groove arrays were found to organise randomly (similar to CS-PCL flat surfaces).

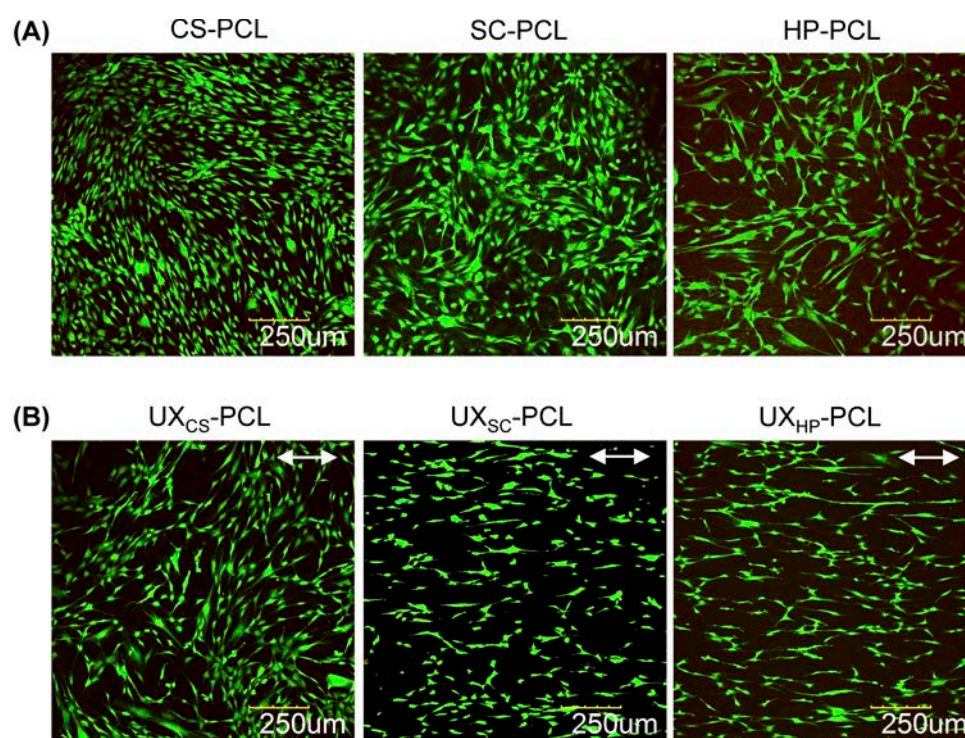


Figure 4-5: Confocal laser scanning microscopy (CLSM) images of MSCs. Cells (Passage-3, 5 k/cm²) were cultured in D10 for 4 days and stained with cytoplasm using FDA (Green colour). **(A)** MSCs on un-stretched PCL film surfaces exhibited random organisation. **(B)** MSCs aligned towards the ridge/grooves of UX_{SC}-PCL and UX_{HP}-PCL, but randomly organized on UX_{CS}-PCL (Double-headed arrows: ridge direction; Scale bar = 250 μm).

Quantitative analysis of cellular angles from the CLSM images showed that MSCs cultured on UX_{SC}-PCL and UX_{HP}-PCL ridge/groove arrays achieved considerable increase in cell alignment efficiencies as compared to those cells on SC-PCL (2.7x

increase, $p < 0.001$) and HP-PCL (2.7x increase, $p < 0.001$) surfaces, respectively (Figure 4-6A). However, MSCs on UX_{CS}-PCL ridge/groove arrays did not exhibit increased cellular alignment as compared to those cells on CS-PCL flat surfaces ($p > 0.05$). Interestingly, the alignment efficiencies for MSCs on the three un-stretched PCL film were less than 20 %, although they exhibited quite different morphologies.

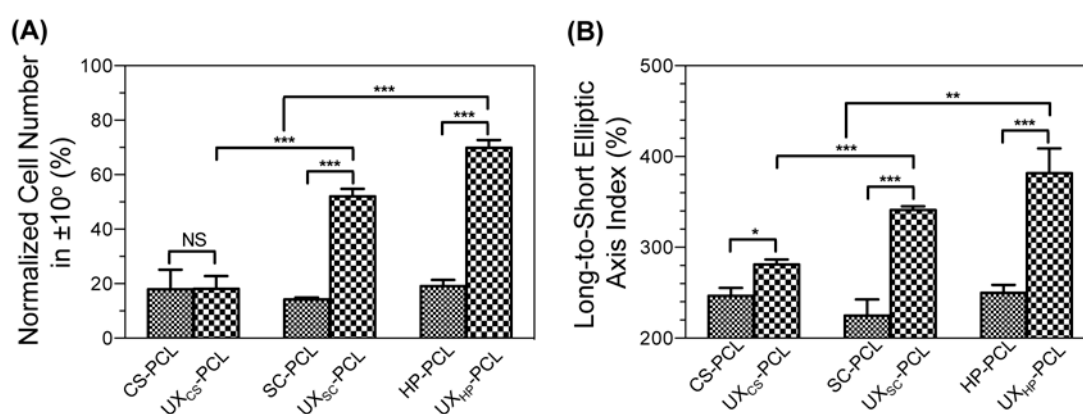


Figure 4-6: Quantitative analysis of MSCs alignment and elongation. Cells (Passage-3, 5 k/cm², for 4 days in D10) were examined by CLSM using FDA live-cell cytoplasmic staining. **(A)** Cell alignment efficiency described by the normalised cell number in $\pm 10^\circ$. **(B)** Cell elongation described by the ratio of long-to-short elliptic axis. Compared to UX_{CS}-PCL and UX_{HP}-PCL organized MSCs with better cellular alignment efficiency and elongation ($n = 3$; ***, $p < 0.001$; **, $p < 0.01$; *, $p < 0.05$; NS, $p > 0.05$).

Besides the increased cellular alignment, MSCs on UX_{SC}-PCL and UX_{HP}-PCL ridge/groove arrays also achieved considerable increase in cellular elongation (Figure 4-6B). The long-to-short elliptic index for MSCs on UX_{SC}-PCL and UX_{HP}-PCL ridge/groove arrays was 0.5-fold higher than those of the cells on SC-PCL and HP-PCL surfaces, respectively ($p < 0.001$). MSCs on UX_{CS}-PCL ridge/groove arrays also achieved increased cellular elongation as compared to cells on CS-PCL flat surfaces (0.1x increase, $p < 0.05$). This suggested that cell alignment might not be the only determination to cellular elongation.

Based on the analysis above, UX_{HP}-PCL ridge/groove arrays showed a larger capability of eliciting MSCs alignment (1.3x of UX_{SC}-PCL, 3.9x of UX_{CS}-PCL, $p < 0.001$) and elongation (1.1x of UX_{SC}-PCL, 1.4x of UX_{CS}-PCL, $p < 0.01$) than those of UX_{SC}-PCL and UX_{CS}-PCL ridge/groove arrays. Further optimisation was performed on UX_{HP}-PCL ridge/groove arrays.

4.3.5 Reorganised MSCs Cytoskeleton and Nucleus Deformation

Effects of UX_{HP}-PCL ridge/groove arrays on sub-cellular organelles of MSCs were further investigated. As shown in Figure 4-7A, CLSM images of F-actin-labeled cytoskeleton revealed a plasticity phenotype for MSCs on HP-PCL flat surfaces, with well spreading morphology and the more but random stress fibers. However, MSCs cultured on UX_{HP}-PCL ridge/groove arrays exhibited a typically contractile SMC-like phenotype, with spindle-like morphology, reduced spreading area, and the fewer and ordered stress fibers orientated towards the ridges (Figure 4-7B) [28, 56, 113].

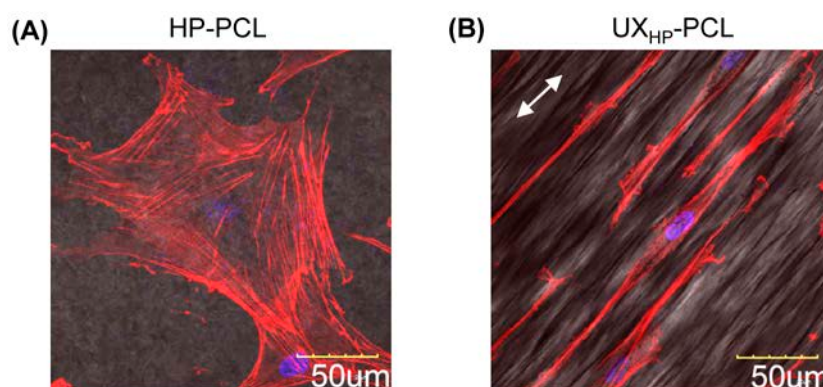


Figure 4-7: Cytoskeletal reorganisation of MSCs on UX_{HP}-PCL. Cells (Passage-6, 5 k/cm², for 5 days of culture in D10) were stained with F-actin (Red colour) and DNA (Blue colour), and examined using CLSM. **(A)** MSCs on HP-PCL flat surfaces. **(B)** MSCs on UX_{HP}-PCL ridge/groove arrays (Double-headed arrows: ridge direction; Scale bar = 50 μm).

Figure 4-8A shows the influences of UX_{HP}-PCL ridge/groove arrays on MSCs nuclei.

CLSM images of DNA-labeling exhibited obvious structure deformation of MSCs

nuclei, with orientated and elongated shapes towards UX_{HP}-PCL ridge/groove arrays. In contrast, MSCs nuclei were more rounded and randomly organised on HP-PCL flat surfaces. Comparatively, the nuclei for MSCs cultured on UX_{HP}-PCL ridge/groove arrays achieved considerable increase in the nucleus alignment as compared to those cells on HP-PCL flat surfaces (2.5x increase, $p < 0.001$; Figure 4-8B). Furthermore, MSCs nuclei exhibited increased nucleus elongation on PCL ridge/groove arrays, with significant decline at CNSI as compared to those cells on the PCL flat surfaces (0.28x reduction, $p < 0.001$; Figure 4-8C).

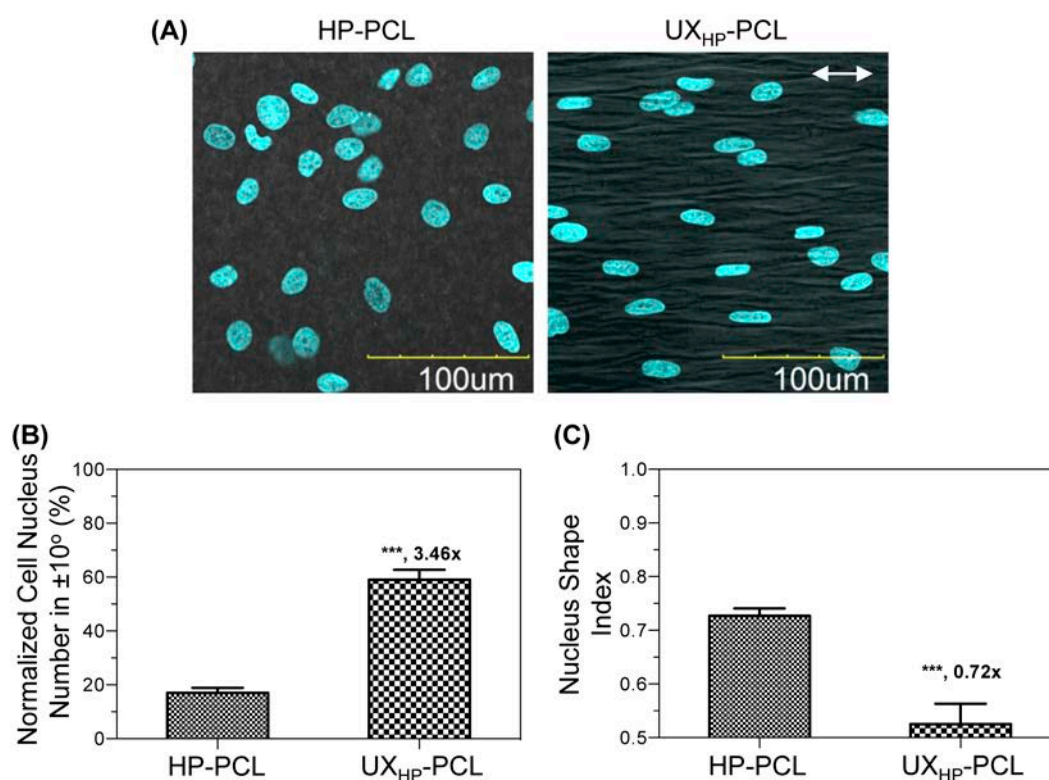


Figure 4-8: MSCs nucleus deformation on UX_{HP}-PCL. Cells (Passage-6, 5 k/cm², for 5 days of culture in D10) were stained with DNA using DAPI (Blue colour). (A) CLSM images of MSCs nuclei on HP-PCL and UX_{HP}-PCL surfaces (Double-headed arrows: direction of PCL ridge/groove arrays; Scale bar = 100 μm). (B) Quantitative analysis of nucleus alignment and elongation (n = 3; ***, $p < 0.001$).

4.3.6 MSCs Differentiation

Impacts of UX_{HP}-PCL ridge/groove arrays were linked to MSCs differentiation towards vascular TE applications. Results from qRT-PCR analysis showed that MSCs

obtained considerable increase in the targeted gene expression levels of ACTA2, CNN1 and MYH11 on UX_{HP}-PCL ridge/groove arrays, which were 3.2-fold, 2.8-fold and 0.4-fold higher than those of the control group of TCP flat surfaces, respectively (Figure 4-9). Here, ACTA2, CNN1 and MYH11 were the targeted gene markers for the early- (SM- α -actin), middle- (calponin) and late-term (SM-MHC) differentiation of vascular SMCs into a contractile phenotype, respectively [28, 56, 113, 249]. In contrast, MSCs on HP-PCL flat surfaces exhibited similar gene expression level for ACTA2, and lower levels for CNN1 and MYH11 as compared to those of the TCP control. Comparing HP-PCL and UX_{HP}-PCL groups, MSCs cultured on PCL ridge/groove arrays achieved increased gene expression levels of ACTA2 (2.7x increase, $p < 0.001$), CNN1 (3.8x increase, $p < 0.001$) and MYH11 (2.4x increase, $p = 0.15$).

Immunocytochemistry analysis was performed to understand the regulation of UX_{HP}-PCL ridge/groove arrays on the targeted gene expression at a more functional level of proteins. Figures 4-10A-C show the CLSM images of immunocytochemistry-labeled MSCs on HP-PCL flat surfaces and UX_{HP}-PCL ridge/groove arrays. Results revealed positive protein expression of SMCs contractile markers including SM- α -actin, calponin and SM-MHC in MSCs cultured with UX_{HP}-PCL ridge/groove arrays, although fluorescence intensity was reduced gradually for markers from the early- to late-term differentiation. No fluorescence was detected for MSCs in the isotype negative control (Neg Ctrl) of each investigated marker, demonstrating that the positive expression of contractile SMCs genes observed in MSCs at the protein level was not from the non-specific immune-conjunction.

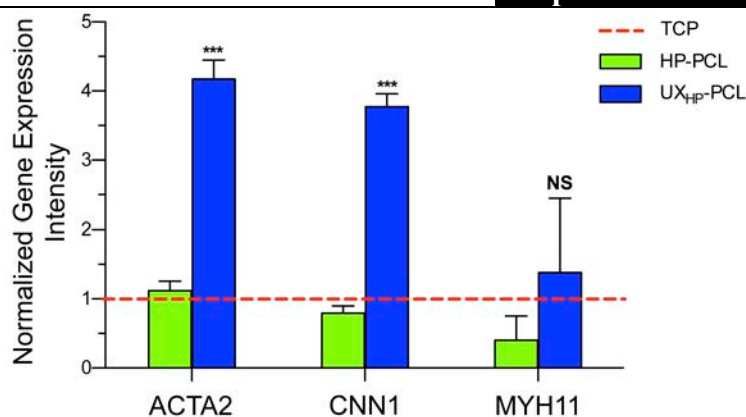
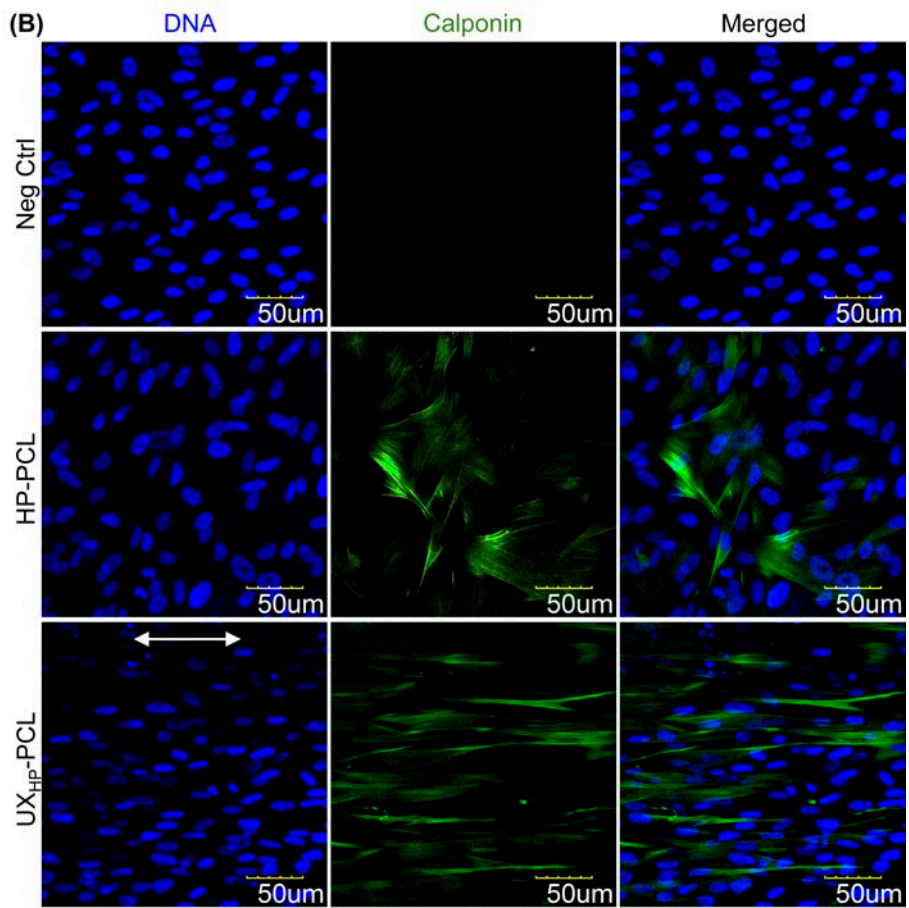
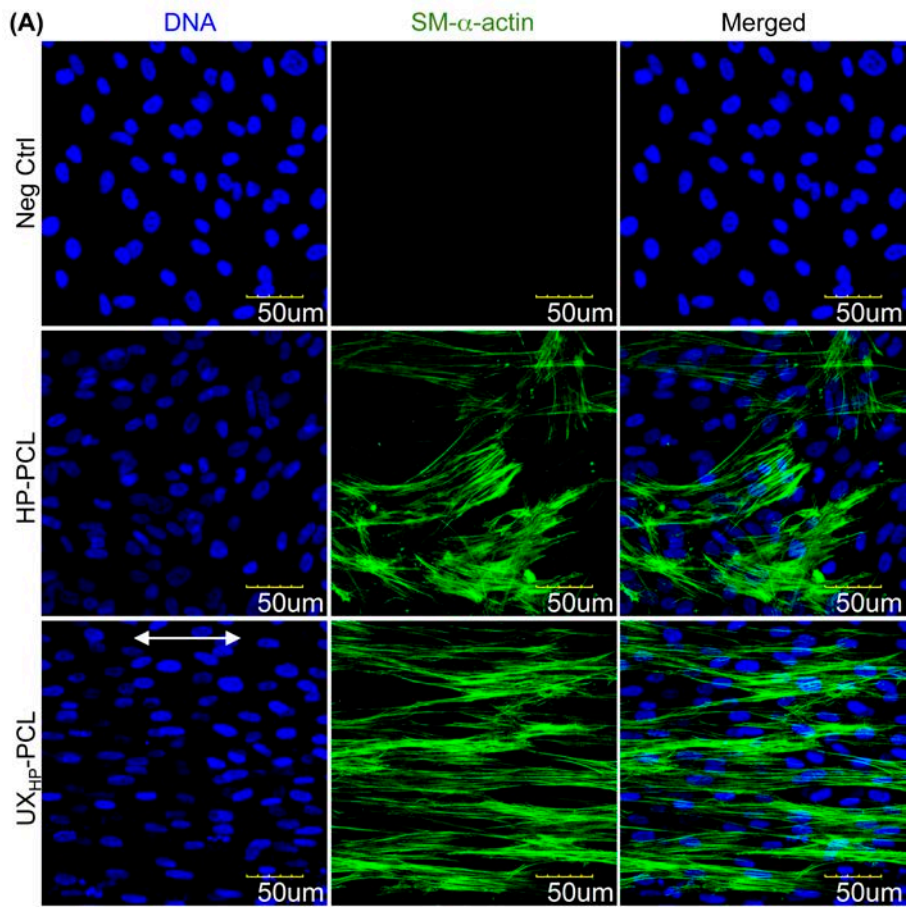


Figure 4-9: Gene expression change of SMCs contractile markers in MSCs on UX_{HP}-PCL. Cells (Passage-6, 5 k/cm²) were cultured with tissue culture plate (TCP, Control group) flat surfaces, HP-PCL flat surfaces and UX_{HP}-PCL ridge/grooves in D10 for 5 days. Quantitative reverse transcription polymerase chain reaction (qRT-PCR) analysis showed that UX_{HP}-PCL up-regulated the expression levels of ACTA2, CNN1 and MYH11 in MSCs. (n = 3; vs HP-PCL group: ***, p < 0.001; NS, p = 0.15).

Comparing HP-PCL and UX_{HP}-PCL groups, MSCs cultured on PCL ridge/groove arrays showed increased protein expression of SMCs contractile markers, with more positive-stained cells and higher fluorescence intensity. MSCs through interaction with UX_{HP}-PCL ridge/groove arrays further achieved ordered organisation of contractile SMCs-like stress filaments, preferentially orientated towards ridge directions, while the filaments organised randomly for MSCs on HP-PCL flat surfaces.



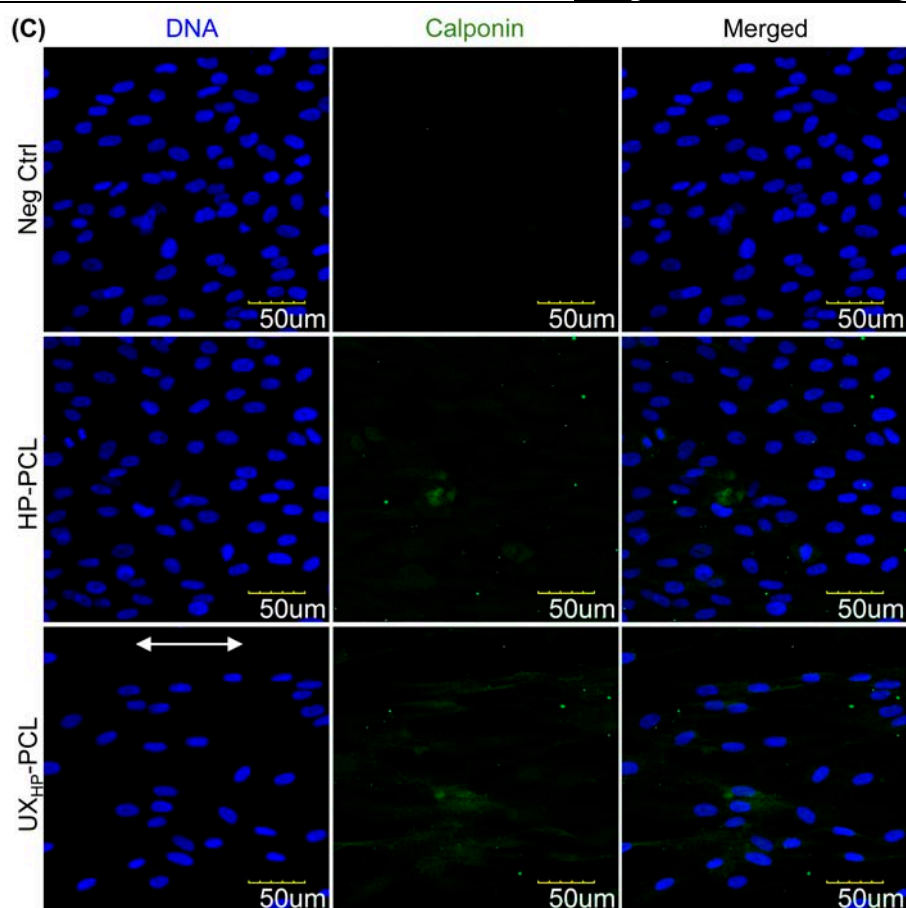


Figure 4-10: Protein expression change of SMCs contractile markers in MSCs on UX_{HP}-PCL. Cells (Passage-6, 5 k/cm²) were cultured on HP-PCL flat surfaces and UX_{HP}-PCL ridge/grooves in D10 for 5 days, and immunocytochemistry-labeled with IgG isotypes (Negative control) and SMCs contractile markers: SM- α -actin for early-term differentiation (A), calponin for middle-term differentiation (B), and SM-MHC for late-term differentiation (C). MSCs on UX_{HP}-PCL positively expressed SMCs contractile filaments in the ordered organisation towards ridges (DNA: blue colour; SMCs contractile markers: green colour; Double-headed arrows: direction of PCL ridge/groove arrays; Scale bar = 50 μ m).

Figures 4-11A and B exhibit the quantification of protein expression of SMCs contractile markers in MSCs. FACS analysis of the immunochemistry-labeled cells confirmed that MSCs on UX_{HP}-PCL ridge/groove arrays and HP-PCL flat surfaces positively expressed SMCs contractile markers. Positive cell number for the three investigated markers were larger than 30 % on both PCL film surfaces, but less than 0.5 % in the isotype Neg Ctrl ($p < 0.001$). Compared to HP-PCL group, MSCs on UX_{HP}-PCL ridge/groove arrays achieved significant increase in the positive cell number for the three SMCs contractile markers, with approximate 9.8, 7.9 and 11.3 %

increase for SM- α -actin, calponin and SM-MHC, respectively ($p < 0.001$; Figure 4-11A). Furthermore, MSCs obtained up-regulated expression intensity of SMCs contractile markers at the protein level, with the fluorescence detected being much higher than that of HP-PCL group (SM- α -actin, 23.5 % increase, $p < 0.001$; calponin, 24.3 % increase, $p < 0.05$; and SM-MHC, 17.1 % increase, $p < 0.01$; Figure 4-11B).

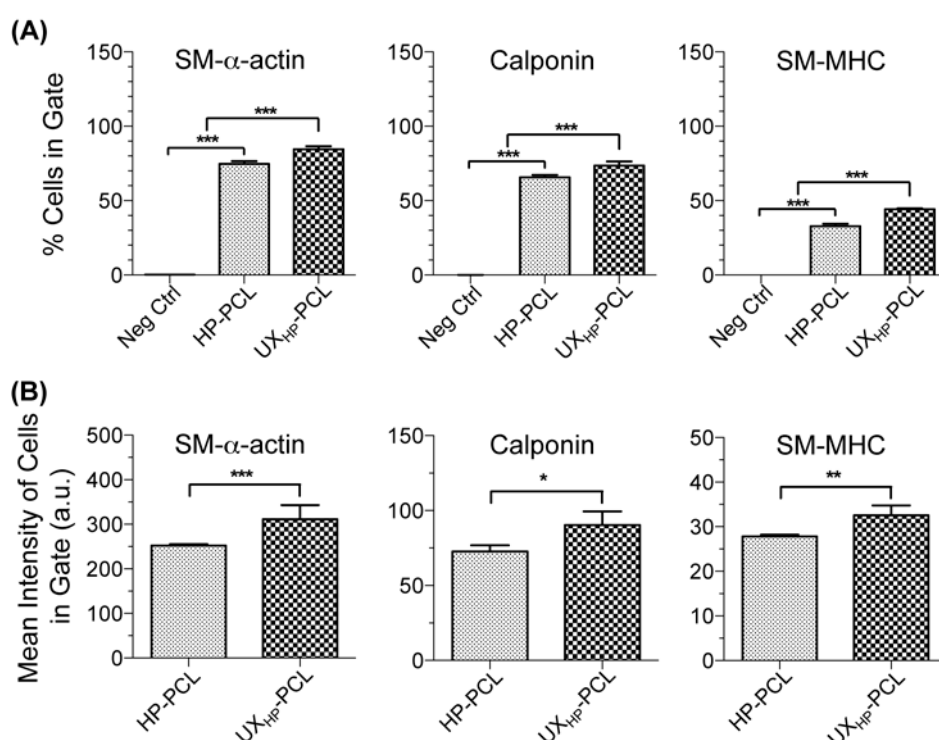


Figure 4-11: Quantitative analysis of the protein expression of SM- α -actin, calponin and SM-MHC. **(A)** Positive cell number. **(B)** Fluorescence intensity. Results from flow cytometry (FACS) showed that MSCs (Passage-6, 5 k/cm²) cultured with UX_{HP}-PCL ridge/groove arrays for 5 days achieved enhanced expression of SMCs contractile markers at the protein level, with increase in both positive cell number and expression intensity. (n = 3; ***, $p < 0.001$; **, $p < 0.01$; *, $p < 0.05$)

4.3.7 3D Vascular Scaffold Construction

Figure 4-12A shows the schematic for engineering of 3D tubular construction. Uniaxial-stretched PCL films were rolled around a round bar and sutured via heat welding. Figure 4-12B shows a UX_{HP}-PCL-based 3D tubular construction with a diameter of ~2.3 mm. FESEM images of the construction revealed similar ridge/groove arrays on both sides of the wall, with orientations being circularly

perpendicular to the inside flow. With an immersion test using culture medium, the construction from UX_{HP} -PCL ridge/groove arrays showed well-maintained tubular shapes and patency, while UX_{CS} -PCL and UX_{SC} -PCL ridge/groove arrays-based constructions obviously collapsed (Figure 4-12C). Furthermore, UX_{HP} -PCL ridge/groove arrays-based constructions showed a larger theoretic burst stress as compared to those of constructions from UX_{CS} -PCL and UX_{SC} -PCL ridge/groove arrays according to Laplace's Law (Table 4-4) [254]. Seeding MSCs on both sides of the wall, layered-MSCs/PCL/MSCs were achieved for 5 days of static culturing, with controlled orientations being the same in the three layers (Figure 4-12D).

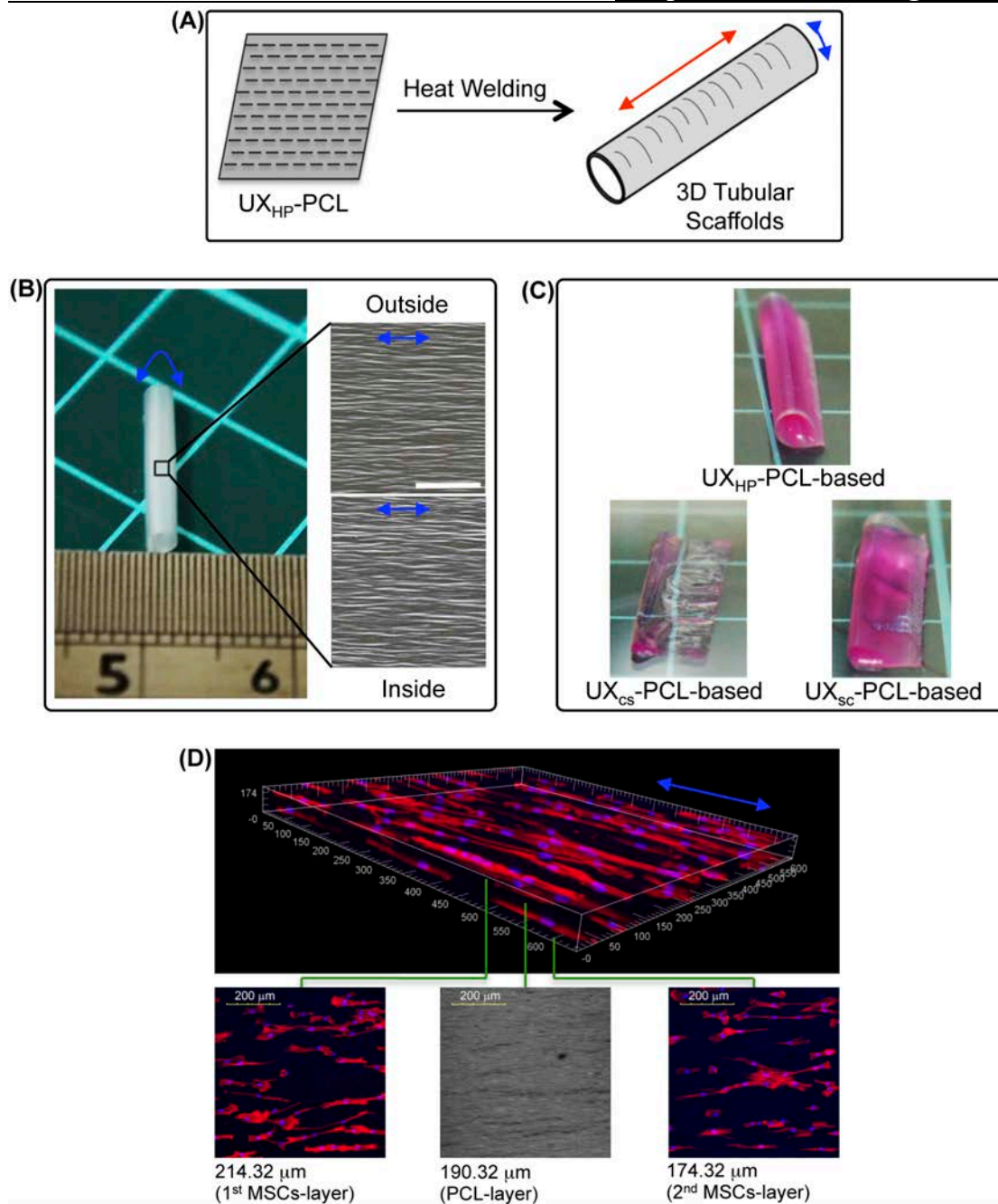


Figure 4-12: (A) Schematic diagram for engineering 3D vascular scaffolds (Red arrows: flow direction; blue arrows: ridge direction). (B) A small-diameter 3D tubular scaffolds from UX_{HP} -PCL. FESEM images revealed ridge/grooves similarly presented on both wall surfaces along a direction perpendicular to the tube (Blue arrows: ridge direction; Scale bar = 100 μ m). (C) Patency of the 3D tubular scaffolds from UX_{HP} -PCL, UX_{CS} -PCL and UX_{SC} -PCL after immersion in culture medium. (D) Engineering of layered-MSCs/PCL/MSCs with similar direction in different layers (Blue arrows: ridge direction; scale bar = 200 μ m).

4.4 Discussion

Geometric cues have offered a novel strategy to regenerate vascular tissue in anisotropic architectures. In this work, anisotropic ridge/groove arrays on PCL films

were generated to modulate human MSCs behaviour for vascular TE applications. Uniaxial stretching of different PCL films resulted in orientated ridge/groove arrays towards the stretching direction, with different ridge-depth and inter-ridge-distance. Compared to UX_{CS}-PCL and UX_{SC}-PCL, UX_{HP}-PCL exhibited better film mechanical properties and proper ridge-depth and inter-ridge-distance for higher efficiencies of MSCs alignment and elongation. UX_{HP}-PCL ridge/groove arrays modulated MSCs into a contractile SMCs-like phenotype, and up-regulated the expression of SM- α -actin, calponin and SM-MHC at both the gene and protein levels. Furthermore, UX_{HP}-PCL ridge/groove arrays facilitated the engineering of 3D tubular constructions and were able to generate a wall of layered-MSCs/PCL/MSCs with the anisotropy as in native tunica media.

It has been demonstrated that uniaxial stretching is capable of fabricating geometric cues and is applicable for semi-crystalline polymers such as PCL and polyethylene [126]. However, a concern was that whether it could be compatible with current film fabrication techniques. The results of this work demonstrated that uniaxial stretching produced orientated ridge/groove arrays on PCL films from different techniques such as heat-press, solvent-cast and cast-stretch, suggesting that uniaxial stretching could have a good compatibility with these techniques. Furthermore, uniaxial stretching of different PCL films resulted in variations in ridge-depth and inter-ridge-distance even at the same stretching temperature and draw ratio. This indicated that the film pre-fabrication could have significant influences on the parameters of the resulted ridge/groove arrays. These findings would facilitate the further development of uniaxial stretching to be a robust technique for the generation of film geometric cues.

Geometric cues to align cells are known via a mechanism of contact guidance [3, 146, 255]. The PCL ridge/groove arrays from uniaxial stretching have shown a capability of eliciting cellular alignment that could be effective as geometric cues generated from soft-lithography, electrospinning and direct-laser-writing [126]. The efforts presented in this study highlighted the importance of identifying factors that influenced MSCs alignment. Compared to UX_{CS} -PCL, the ridge/groove arrays of UX_{HP} -PCL had a similar inter-ridge-distance but much higher ridge-depth. MSCs on UX_{HP} -PCL aligned towards the ridge/groove arrays, but grew randomly on UX_{CS} -PCL surfaces. This indicated that the ridge-depth might be crucial for MSCs to align on the PCL ridge/groove arrays. Too small ridge-depth (e.g. ~ 116 nm of UX_{CS} -PCL ridge/groove arrays) would not result in expected responses to the geometries. Such phenomena supported that a threshold of ridge-depth might be existed to determine whether the geometric features could be recognised by the cells [256]. Comparing UX_{SC} -PCL and UX_{HP} -PCL, the former had ridge/groove arrays with larger ridge-depth. However, MSCs aligned to UX_{SC} -PCL ridge/groove arrays at a lower efficiency than that of cells on UX_{HP} -PCL ridge/groove arrays. This thus suggested that besides ridge-depth, inter-ridge-distance also impacted influences on MSCs responses, and cells tended to align at a higher efficiency to the PCL ridge/groove arrays with smaller inter-ridge-distances. These illustrated how geometric parameters are able to affect MSCs alignment to the PCL ridge/groove arrays.

Recently, more in-depth effects of geometric cues have been linked to cellular function differentiation, especially for stem cells [28, 104, 115, 141, 161, 162]. Here, MSCs cultured on UX_{HP} -PCL ridge/groove arrays were found to exhibit contractile vascular SMCs-like phenotype, with spindle-like morphology, smaller spreading area,

and the fewer cytoskeleton fibers [28, 155, 257]. Furthermore, MSCs on UX_{HP}-PCL ridge/groove arrays up-regulated the expression of SMCs contractile markers: SM- α -actin, calponin and SM-MHC. This has been demonstrated by both qRT-PCR and immunocytochemistry staining at both the gene and protein levels, respectively. These observations suggested that UX_{HP}-PCL ridge/groove arrays probably modulated MSCs to differentiate towards a contractile SMCs-like status. Such effects of UX_{HP}-PCL ridge/groove arrays on MSCs were in agreement with the previous findings in SMCs [28], and suggested that geometric cues could be used as tools for up-regulating the contractile SMCs-specific gene expression in MSCs and SMCs. Compared to the biochemical factors such as TGF- β 1 [10, 57, 249], ascorbic acid [57] and bone morphogenetic protein-4 [249], geometric cues were much cheaper with less side effects (e.g. atherosclerosis) and could provide continuous stimulation [126]. Besides these advantages, it should also be noted that the expression level of SMCs late-differentiation marker (SM-MHC) was still lower in MSCs than those of the early- and middle-term markers. This suggested that MSCs might not be fully differentiated, although the increased expression of investigated markers was observed.

It was generally suggested that geometric features to differentiate cell function through a mechanotransduction pathway [248]. Geometric structures adjusted the distribution of focal adhesion and cell migration and extension to align and elongate cells [114]. This resulted in re-orientation of cytoskeletons and tugging of nuclei to be aligned and elongated, leading to changes in the accessibility of transcriptional factors, structures of DNA and nucleus pores (affecting DNA, mRNA, protein factors, ion flux) and finally regulated the gene expression [258]. Here, MSCs aligned to UX_{HP}-PCL ridge/groove arrays and re-oriented the cytoskeletons. Furthermore, MSCs

nuclei were found to align and elongated significantly than cells on the PCL flat surfaces. These evidences indicated that MSCs up-regulated the expression of SMCs contractile markers could be attributed to the mechanotransduction mechanism via nucleus deformation. Meanwhile, the increased material stiffness of UX_{HP}-PCL ridge/groove arrays probably contributed to the higher expression of SMCs-specific genes in MSCs simultaneously, as recent evidences suggested that MSCs on stiff substrates could have up-regulated muscle cell gene expression [113, 259]. In addition, cellular source might influence the selective gene expression for stem cells on anisotropic geometric features. Studies suggested that stem cells divided from bone marrow (e.g. human fetal bone MSCs) tended to differentiate towards myocardial lineages [162, 163, 248], while embryonic stem cells followed the direction towards neurons regardless whether the cues were ridge/grooves arrays or fibrous substrates [104, 161]. The results presented in this study further demonstrated that MSCs also achieved enhanced expression of SMCs-specific genes on UX_{HP}-PCL ridge/groove arrays. Together with the previous findings, this work suggested that geometric cues could generally elevate the expression of both myogenic and SMCs-specific genes in MSCs [126, 162, 163, 248].

PCL films have been extensively used for vascular regeneration [22, 40, 176], due to their slow degradation and unique mechanical properties [17]. UX_{HP}-PCL ridge/groove arrays of this work were designed to biomimic the BM anisotropy for tunica media regeneration. Uniaxial stretching not only created the ridge/groove arrays, but also enhanced the film mechanical properties without sacrifice in its elasticity, indicating that 3D tubular scaffolds from UX_{HP}-PCL ridge/groove arrays would support enhanced mechanical support while not affecting the graft's

contraction/relaxation. Such retained film yield strain could be due to the heating effects that resulted in relax of stretched PCL molecular chains in amorphous regions. According to Laplace's Law [254], to estimate theoretic burst stress of vascular grafts, the geometry of 3D tubular scaffolds should be taken into consideration to avoid overestimation. Compared to UX_{SC} -PCL and UX_{CS} -PCL, the engineered 3D tubular scaffolds based on UX_{HP} -PCL exhibited the higher theoretic burst stress and no reduction in elasticity. Targeted for human mammary artery (ϕ : ~2.3 mm) application, the 3D tubular grafts based on UX_{HP} -PCL ridge/groove arrays could have a theoretic burst stress of >5000 mmHg, which would be enough to bear the pulsatile pressure in normal arteries [254]. Besides the safety ensuring, UX_{HP} -PCL-based tubular grafts exhibited a good capability of maintaining the patency shapes after filling with liquids. This would help the operative storability and simplicity of surgical handling [8, 260]. Such shape maintenance could be attributed to the better mechanical properties of UX_{HP} -PCL. In addition, the ridge/groove arrays were generated on films, which might also facilitate the 3D tubular geometry. MSCs on UX_{HP} -PCL ridge/groove arrays were demonstrated to express a contractile SMCs-like phenotype and up-regulate the expression of SM- α -actin, calponin and SM-MHC at both gene and protein levels. Meanwhile, the ridge/groove arrays of UX_{HP} -PCL-based 3D tubular grafts allowed construction of a wall of layered-MSCs/PCL/MSCs with similar anisotropy as in native tunica media.

4.5 Summary

In this work, biomimetic 3D anisotropic geometries were created on PCL films to biomimic the BM anisotropy for regulating phenotype. Results showed that uniaxial stretching of PCL films not only resulted in increased mechanical properties, but also

created 3D anisotropic ridge/groove arrays towards the stretching direction. Optimisation studies showed that MSCs on deeper but narrower ridge/groove arrays exhibited better alignment. Further studies demonstrated that MSCs cultured on PCL ridge/groove arrays expressed a contractile SMCs-like phenotype and up-regulated the expression of SM- α -actin, calponin and SM-MHC at gene and protein levels. Small-diameter tubular scaffolds engineered from the PCL film ridge/groove arrays allowed a wall of layered-MSCs/PCL/MSCs construction with similar anisotropy as in native media. These findings suggest that PCL film ridge/groove arrays could biomimic the BM anisotropy, and regulate MSCs behaviour for the applications in tunica media regeneration. This work also highlights the significant implications of using geometric cues and MSCs for vascular tissue regeneration.

Chapter 5 Degradation Behaviour of Anisotropic Geometries and Mesenchymal Stem Cell Responses

5.1 Introduction

Geometric cues have offered a novel strategy for vascular scaffolds to mimic the vascular basement membrane (BM) anisotropy and regulate cell behaviour in a precise and near-physiological fashion [224]. Geometric cues of TE scaffolds have been known to reorganise stem cells into specific tissue-like patterns or alignment [251]. TE scaffolds with versatile geometric features have also impacted upon the functional performances of cells (e.g. mobility [139], adhesion/proliferation [130], and differentiation [131, 224, 251]) and tissue constructions (e.g. anisotropy [261] and mechanical property [3]).

According to the material properties, geometric cues on scaffold's surfaces can typically be divided into two main categories: biodegradable and non-biodegradable. The latter one such as poly(dimethyl siloxane) (PDMS) micropatterns, however, have little value for translational research as they are not biodegradable [131]. Geometric features on biodegradable scaffolds such as collagen [3], poly(ϵ -caprolactone) (PCL) [131, 251] and poly(lactic acid) (PLA) [262] have achieved widespread applications

for tissue regeneration of blood vessels, skeletal and myocardial muscles, nerves and bone, and hold potential to be applied for translational research. However, upon implantation, biodegradable geometric cues are directly contacted to the environments *in vivo*, filled with various erosive fluids, biological enzymes and physiological inflammation responses [170]. Stability of geometric cues has thus been a concern for the successful functionalisation.

Accelerated hydrolysis *in vitro* using an acidic [184], alkaline [172] or basic medium [173] provides an efficient way to understand the influence of erosive environment on materials properties. Compared to *in vivo* studies, accelerated hydrolysis *in vitro* could function as an initial estimate and hold advantages to accomplish the degradation process in a more acceptable timeframe [170, 172, 175]. Hydrolytic degradation of poly(ϵ -hydroxy) esters *in vitro* can follow a surface or bulk erosion pathway [17]. Chapter 2, Section 2.3.4 reviews the main steps occurred for surface and bulk erosion, respectively. Currently, degradation studies have been extensively performed for different TE scaffolds (e.g. film [173, 263, 264], fiber [180], foam [17], bulk [182] and nano/microspheres [265, 266]). However, degradation behaviour of geometric cues is less well-known.

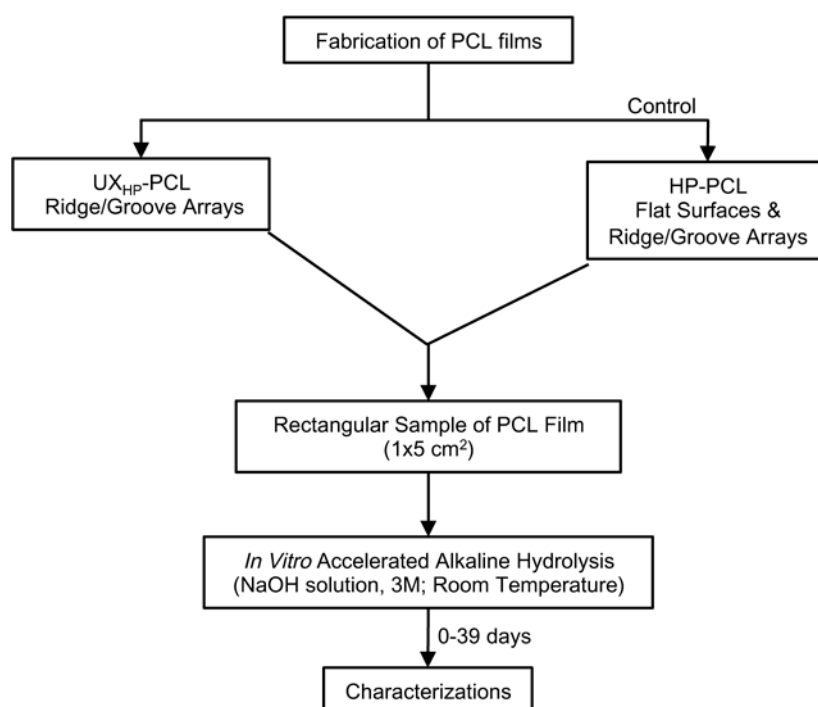
PCL is one promising synthetic poly(ϵ -hydroxy) esters with unique mechanical properties and slow degradation rates, allowing the applications for long-term vascular cell capture and tissue regeneration, especially for elder patients who had low healing capability [17, 173]. In previous Chapters 3 and 4, uniaxial-stretched heat-pressing PCL (UX_{HP}-PCL) films have shown promising capability to biomimic the anisotropy of vascular BM. The research interest of this work is focusing on the

stability of UX_{HP}-PCL ridge/groove arrays in erosive environment for providing the insights of how degradation affects geometric cues and further cellular responses in regards to VTE applications.

5.2 Materials and Methods

5.2.1 Experimental Design

As shown in Scheme 5-1, accelerated alkaline hydrolysis *in vitro* was performed for UX_{HP}-PCL ridge/groove arrays. For comparison, HP-PCL flat surfaces and ridge/groove arrays were used. Characterisation of topographical morphologies, film weight loss, surface hydrophilicity, mechanical properties and cellular responses have been carried out.



Scheme 5-1: Schematic diagram illustrating the experimental design. Anisotropic ridge/groove arrays were generated on UX_{HP}-PCL via uniaxial stretching of HP-PCL. Accelerated alkaline hydrolysis (NaOH solution, 3M) *in vitro* was performed at room temperature for 0-39 days. HP-PCL flat surfaces and ridge/groove arrays were used for comparison. Characterisations including morphology, weight loss, surface hydrophilicity, mechanical property and stem cell alignment have been performed.

5.2.2 Materials

Materials and mesenchymal stem cells (MSCs) in this work were obtained as described in Chapter 3, Section 3.2.2.

5.2.3 Sample Preparation

Flat surfaces and anisotropic ridge/groove arrays were created on heat-press PCL (HP-PCL) and uniaxial-stretch HP-PCL (UX_{HP} -PCL) films, respectively (Chapter 3, Section 3.2.3). Orientated ridge/groove arrays were also created on HP-PCL via direct-laser-writing [135].

5.2.4 Hydrolysis

Degradation behaviour of UX_{HP} -PCL ridge/groove arrays was studied via an accelerated alkaline hydrolysis *in vitro*. Briefly, PCL film samples were cut into rectangular shapes of dimensions measuring $1 \times 5 \text{ cm}^2$, and immersed in an aqueous alkaline medium at room temperature (NaOH solution, 3M, 10 ml per sample in a 6-well plate). Samples were taken out periodically, washed thrice with distilled water and dried in a dry cabinet for 1 week. For comparison, HP-PCL with flat surfaces and ridge/groove arrays were also hydrolysed in parallel.

5.2.5 Field Emission Scanning Electron Microscopy (FESEM)

FESEM characterisation was performed following the description in Chapter 3, Sections 3.2.4.

5.2.6 Water Contact Angle (WCA)

WCA characterisation was performed as described in Chapter 3, Section 3.2.6.

5.2.7 Weight Loss

Samples with initial weight of W_0 were degraded for pre-determined time. Superficial liquid was gently removed by using Kim Wipes (USA). Samples at this step had wet weight of W_{tw} . Samples after drying completely in a dry cabinet for 1 week had dry weight of W_{td} . Degradation degree of PCL films was presented as a percentage of weight loss calculated using the following equations (1) and (2):

$$\text{Weight loss at wet conditions } \%_{\text{wet}} = (W_0 - W_{tw}) / W_0 \times 100 \% \quad (1);$$

$$\text{Weight loss at dry conditions } \%_{\text{dry}} = (W_0 - W_{td}) / W_0 \times 100 \% \quad (2).$$

Five samples were used at each degradation time point per group.

5.2.8 Tensile Testing

After degradation for a pre-determined time, the thickness of PCL samples was measured. Tensile testing was performed as described in Chapter 4, Section 4.2.6 using dimensions measuring $5 \times 30 \text{ mm}^2$. An offset-strain of 0.005 was used to determine the yield stress and strain for UX_{HP}-PCL (day 0-30) and HP-PCL (day 30). A low yield point just beyond the maximum point after linear-elastic region was used to determine the yield stress for HP-PCL (day 0-20), and the corresponding strain at linear-elastic part was determined as the yield strain. Three samples were used at each degradation time point per group.

5.2.9 Cell Isolation and Culture

MSCs were isolated and culture expanded as described in Chapter 3, Section 3.2.9. MSCs used were within Passage-6.

5.2.10 Confocal Laser Scanning Microscopy (CLSM)

MSCs were labeled with cytoskeleton and DNA using TRITC-conjugated phalloidin and DAPI, respectively. Images of fluorescence-labeled cells were examined using CLSM (Chapter 3, Section 3.2.10).

5.2.11 Cell Nucleus Alignment and Elongation

The angles of MSCs nucleus were analysed as described in Chapter 4, Section 4.2.10. MSCs cultured on HP-PCL flat surfaces were set as negative control (Neg Ctrl). An isotropic sample would have an efficiency of ~11.7 % of nuclei to be aligned, and a cell nucleus shape index (CNSI) of 1 (a circle).

5.2.12 Data Analysis

Data analysis was performed on Prism 5 software. Results were reported as mean \pm SD. A value of $p < 0.05$ was considered to be statistically significant.

5.3 Results**5.3.1 Stability of UX_{HP}-PCL Ridge/Groove Arrays**

Figure 5-1 reveals preferentially orientated ridge/groove arrays on UX_{HP}-PCL along the stretching direction, while only some indentations on HP-PCL flat surfaces. To study the morphological resistance, 20 days of accelerated alkaline hydrolysis *in vitro* was performed for UX_{HP}-PCL ridge/groove arrays and HP-PCL flat surfaces and ridge/groove arrays. UX_{HP}-PCL ridge/groove arrays showed a larger morphological stability against degradation, with ridge shapes still existed, although increased surface roughness was observed. In contrast, HP-PCL flat surfaces degraded into

macroporous topographies, while the ridge structures of HP-PCL ridge/groove arrays were removed completely by degradation.

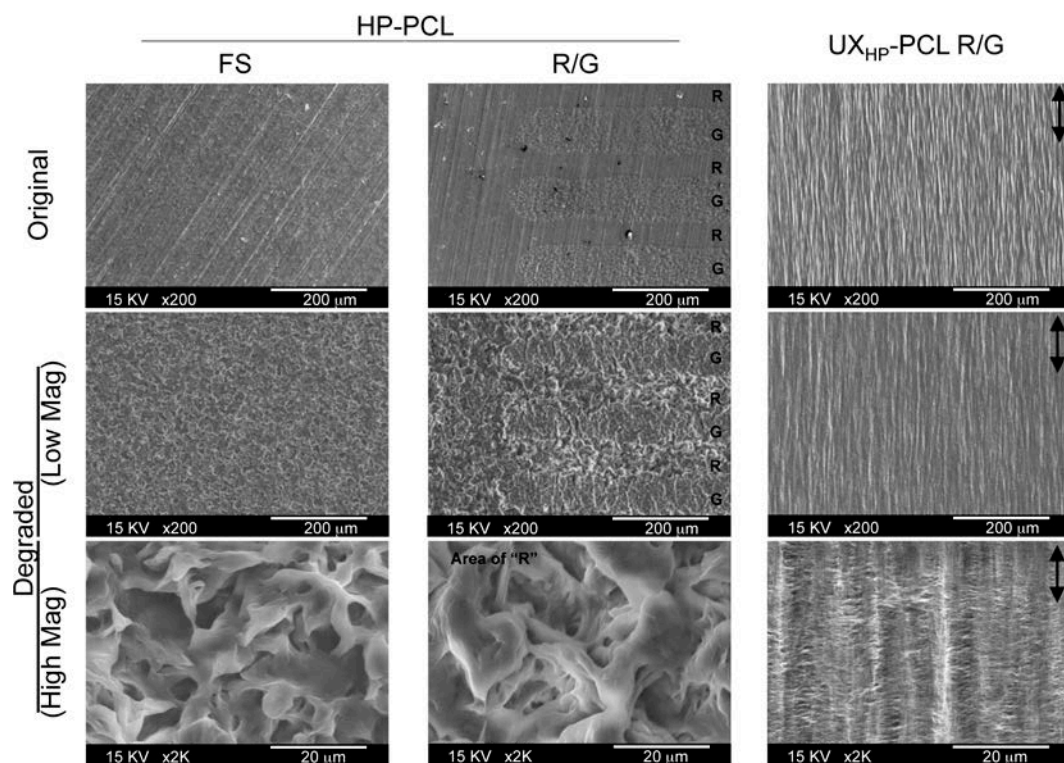


Figure 5-1: Morphological stability of UX_{HP} -PCL ridge/groove arrays against degradation. Film samples were hydrolysed in an alkaline medium for 20 days at room temperature. Field emission scanning electron microscopy (FESEM) images reveal overall ridge/groove arrays that still existed on UX_{HP} -PCL (FS: flat surfaces; R: ridges; G: grooves; Double-headed arrow: stretching direction; Scale bar = 200 and 20 μm for low and high magnified FESEM images, respectively).

5.3.2 Morphological Evolution

Time-dependent studies were performed to understand the influence of degradation on the morphological evolution of UX_{HP} -PCL ridge/groove arrays. As shown in Figure 5-2, FESEM images of UX_{HP} -PCL ridge/groove arrays revealed smooth surface structure before degradation. After hydrolysis for 2 days, degradation occurred throughout the surfaces of UX_{HP} -PCL ridge/groove arrays. Although rougher surfaces were observed with ongoing hydrolysis, UX_{HP} -PCL ridge/groove arrays were able to maintain the ridge shapes well till day 10.

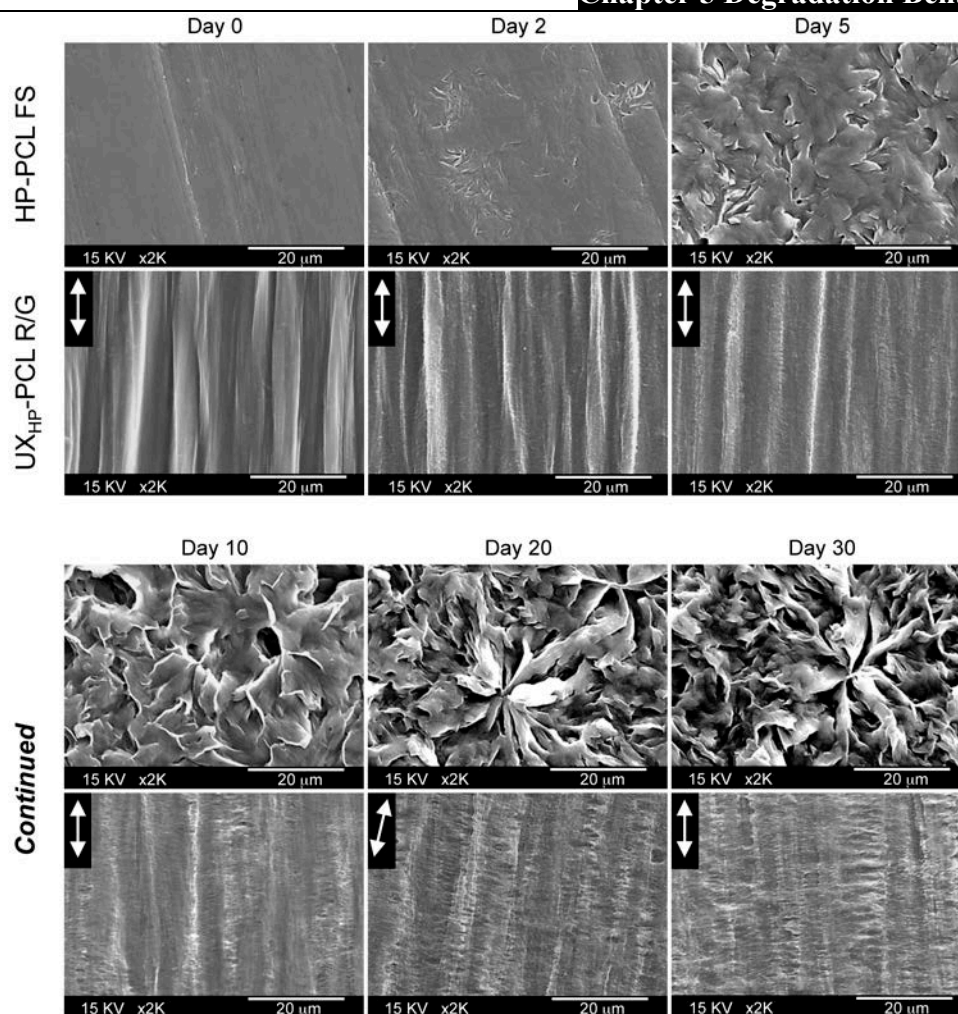


Figure 5-2: Morphological evolution of UX_{HP}-PCL ridge/groove arrays with alkaline hydrolysis at room temperature for day 0-30. Degradation of UX_{HP}-PCL ridge/groove arrays occurred on film surfaces with ridges being degraded into small parallel ridge-islands (FS: flat surfaces; R: ridges; G: grooves; Double-headed arrow: stretching direction; Scale bar = 20 μm).

Further hydrolysis resulted in small concaves formed at UX_{HP}-PCL ridge-edges, developing into a series of parallel grooves across the ridges. At day 30, ridges were found to transform into ridge-islands. Nevertheless, the overall geometries of UX_{HP}-PCL ridge/groove arrays still existed, as observed from the FESEM images over a large area (Figure 5-3A). In contrast, HP-PCL flat surfaces after only 5 days of hydrolysis were degraded completely with in-growing pores (Figure 5-2). Further hydrolysis of HP-PCL flat surfaces resulted in degradation invaded into the inside bulk of films, leading to fragments observed at day 30 (Figure 5-3B)

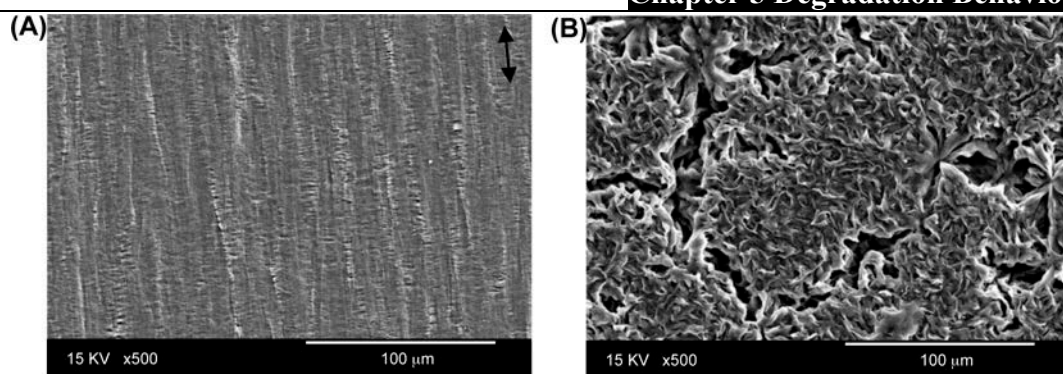


Figure 5-3: Morphologies of UX_{HP}-PCL ridge/groove arrays (A) and HP-PCL flat surfaces (B) after 30 days of degradation. FESEM images reveal integrated surfaces with overall orientated geometries on UX_{HP}-PCL. In contrast, HP-PCL flat surfaces were degraded into fragments (Double-headed arrow: stretching direction; Scale bar = 100 μm).

5.3.3 Film Weight Loss Behaviour

Figure 5-4 shows the influence of degradation on film weight loss of UX_{HP}-PCL ridge/groove arrays. Degradation resulted in an "S-shape" behaviour of film weight loss for UX_{HP}-PCL ridge/groove arrays, consisting of three phases: rapid weight loss (day 0-10) → slow weight loss (day 10-25) → rapid weight loss (day 25 onwards). In contrast, HP-PCL flat surfaces exhibited film weight loss as a "parabola-shape" behaviour, with two distinct phases: slow weight loss for day 0-5 and accelerated weight loss for day 5 onwards. Over the degradation period, the film weight loss curves at wet and dry conditions overlapped for UX_{HP}-PCL ridge/groove arrays with indication of little medium absorption, but exhibited clear deviation for HP-PCL flat surfaces after 5 days of hydrolysis, suggesting absorption of erosive medium.

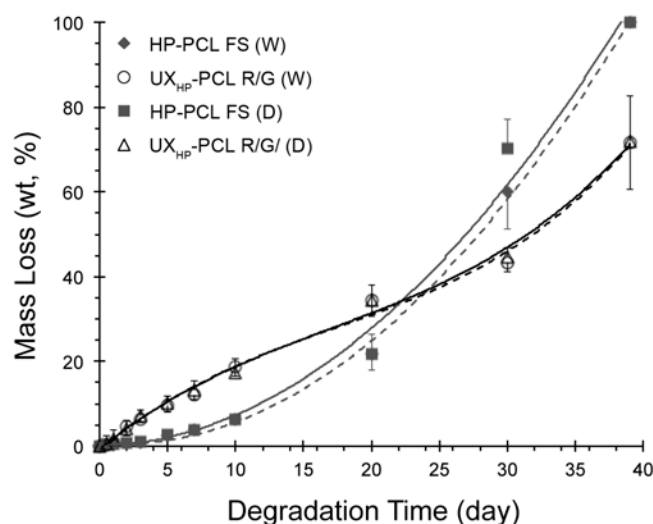


Figure 5-4: Film weight loss of PCL films hydrolysed in an alkaline medium at room temperature for 0-39 days. UX_{HP}-PCL ridge/groove arrays followed an “S-shape” behaviour of film weight loss, while HP-PCL flat surfaces experienced a “parabola-shape” behaviour (FS: flat surfaces; R: ridges; G: grooves; n = 5).

5.3.4 Surface Hydrophilicity Changes

Surface hydrophilicity is a crucial factor for the successful implementation of TE scaffolds, since a too hydrophobic or hydrophilic surface is not beneficial for cellular adhesion and proliferation [267]. Figure 5-5 shows the influence of degradation on surface hydrophilicity of UX_{HP}-PCL ridge/groove arrays. Results from WCA measurement exhibited that both UX_{HP}-PCL and HP-PCL surfaces were hydrophobic before hydrolysis, with WCA being larger than 80 °. After 2 days of degradation, increased surface hydrophilicity with a rapid decline in WCA was achieved for UX_{HP}-PCL ridge/groove arrays, in both parallel and perpendicular directions. Although further degradation resulted in continuous WCA reduction, the decline rate became much slower, especially in the parallel direction since the WCA change during day 2-20 was less than 7 °. In contrast, although HP-PCL flat surfaces also obtained enhanced hydrophilicity during the initial 2 days of degradation, they displayed a continuous and more rapid decline in WCA. The WCA change during day 2-20 was more than 25 °. At day 20, UX_{HP}-PCL ridge/groove arrays obtained similar WCA

larger than 40° in both directions ($p > 0.05$), while the WCA of HP-PCL flat surfaces was less than 18° .

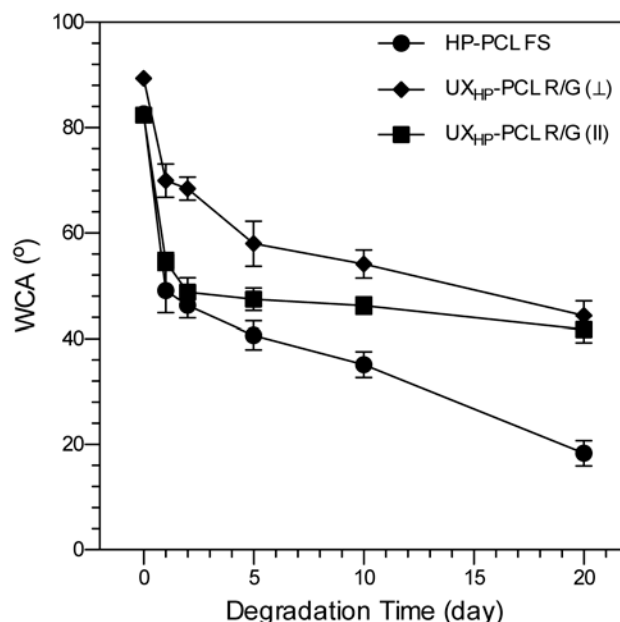


Figure 5-5: Surface hydrophilicity of PCL films with alkaline hydrolysis for different time. UX_{HP}-PCL ridge/groove arrays obtained increased surface hydrophilicity after degradation, and retained similar water contact angle (WCA) of $>40^\circ$ in both parallel (∥) and perpendicular (⊥) directions for 20 days of degradation (FS: flat surfaces; R: ridges; G: grooves; $n = 5$).

5.3.5 Film Mechanical Property Evolution

Figure 5-6A shows the effect of degradation on the changes of film tensile stress-strain curves. With the on-going degradation of UX_{HP}-PCL ridge/groove arrays and HP-PCL flat surfaces, film ultimate stress and strain generally declined. However, UX_{HP}-PCL ridge/groove arrays retained higher film ultimate stress (44 vs 16 % at day 30, 1.8x increase, $p < 0.05$) and strain (32 vs 3 % at day 30, 9.6x increase, $p < 0.01$) than those of HP-PCL flat surfaces (Figure 5-6B). Although the film Young's Modulus increased after degrading for 1 day, degradation for day 5 onwards tended to increase slightly both the film yield stress and strain for UX_{HP}-PCL ridge/groove arrays, resulting in less change to the film Young's Modulus. However, degradation

after day 5 showed a continuous decline at the film yield stress, yield strain and Young's Modulus for HP-PCL flat surfaces, especially after day 20.

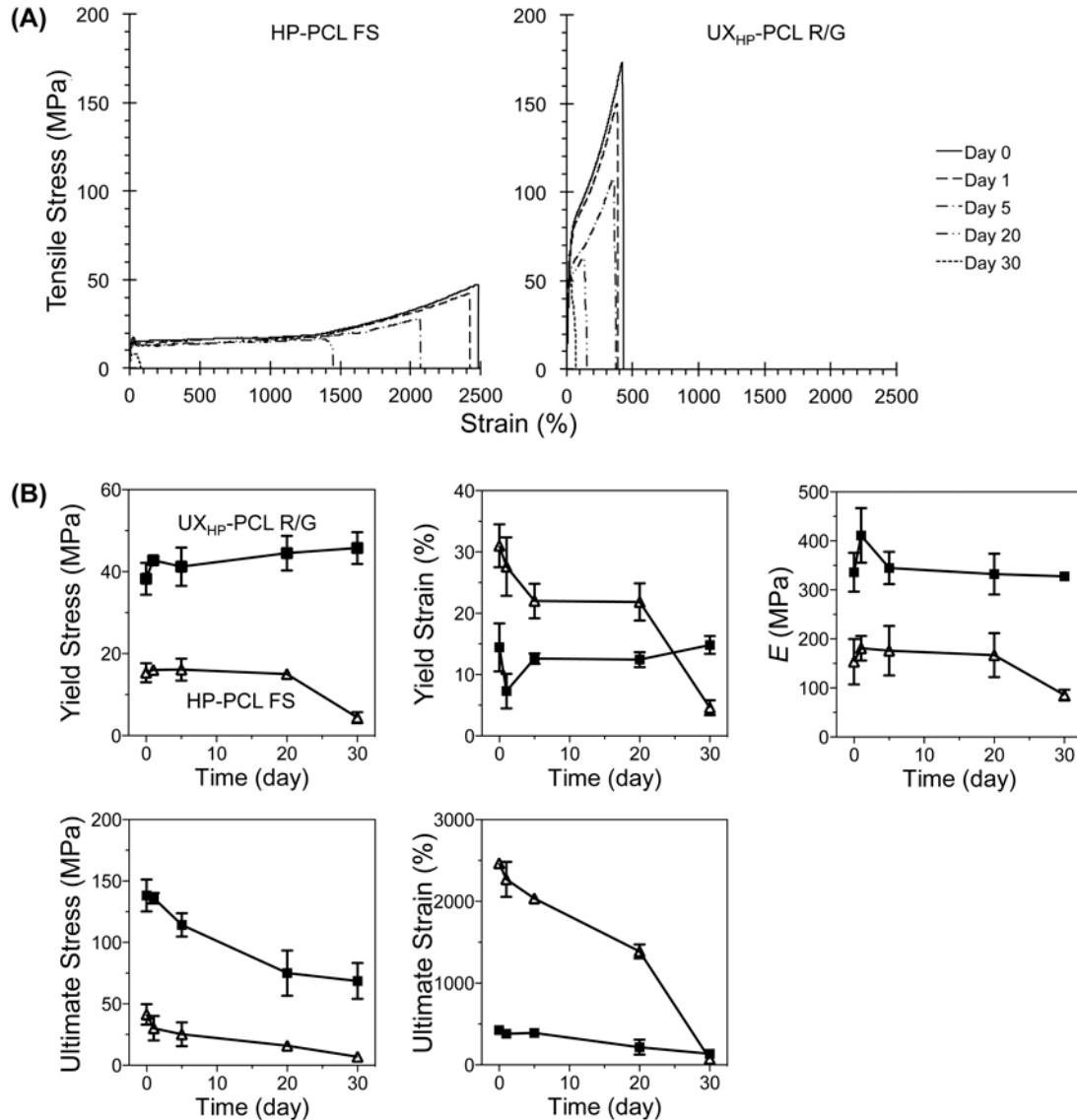


Figure 5-6: Film mechanical properties of PCL films after alkaline hydrolysis at room temperature for different time. (A) Typical tensile stress-strain curves. (B) Film yield stress, yield strain, Young's Modulus, and ultimate stress and strain. Over the investigated degradation period, UX_{HP}-PCL ridge/groove arrays experienced slight increase in film yield stress and strain, resulting in less change at film Young's Modulus (FS: flat surfaces; R: ridges; G: grooves; n = 3).

3.5.6 Stem Cell Responses

The effect of geometric degradation on cellular responses was evaluated by measuring human MSCs alignment on hydrolysed UX_{HP}-PCL ridge/groove arrays at different

degree. Figure 5-7A shows that MSCs cultured on HP-PCL flat surfaces (Neg Ctrl) organised randomly with less cellular elongation. Interestingly, MSCs cultured on UX_{HP}-PCL ridge/groove arrays hydrolysed different times exhibited different degree of aligned organisation and elongated cell shapes, with orientations towards the ridges (Figure 5-7B). For less than 10 days of hydrolysis, UX_{HP}-PCL ridge/groove arrays elicited better MSCs alignment and elongation. With further degradation, UX_{HP}-PCL ridge/groove arrays exhibited weaker guidance on MSCs reorganisation. However, certain degree of MSCs alignment and elongation could still be observed even at 30 days of degradation. It should also be noted that for more than 10 days of hydrolysis, the cell number on the confocal images tended to reduce gradually. This could be attributed to the continuous WCA reduction of UX_{HP}-PCL ridge/groove arrays that declined cellular adhesion/proliferation capability [267]. Moreover, the on-going hydrolysis caused increased width of the small crossing grooves within ridges, which has been known to increase cell mobility and result in loose cell adhesion [130, 138]. This probably resulted in cells being washed off easily during the intracellular staining process and therefore, resulting in the gradual reduced cell numbers on UX_{HP}-PCL with longer hydrolysis.

Analysis of MSCs nucleus angle frequency confirmed the observed cellular responses to the geometric degradation of UX_{HP}-PCL ridge/groove arrays (Figures 5-7A and B). The angle frequency of MSCs nuclei in Neg Ctrl exhibited as multi-peaks around the even distribution line of an Isotropic Ctrl. However, the angles of MSCs nuclei distributed into small angle-ranges, and presented as single dominating peak above the even distribution line of an Isotropic Ctrl. For UX_{HP}-PCL ridge/groove arrays with less than 10 days of hydrolysis, the single dominating peaks of MSCs nucleus angle

frequency showed similar peak-height and width. Quantitative analysis of the nuclei revealed non-significant differences at the nucleus alignment efficiencies of 40-48 % ($p > 0.05$) (Figure 5-7C) and elongation with CNSI of 0.7-0.8 ($p > 0.05$) (Figure 5-7D). For ongoing hydrolysis, the single dominating peaks of MSCs nucleus angle frequency showed gradual reduction in peak-height and increase in peak-width. Moreover, non-dominating peaks were observed for UX_{HP}-PCL ridge/groove arrays with more than 20 days of hydrolysis (Figure 5-7B). Correspondingly, the efficiencies of MSCs nucleus alignment and elongation were found to decrease gradually (Figures 5-7C and D). However, compared to Neg Ctrl, UX_{HP}-PCL ridge/groove arrays hydrolysed for 30 days still resulted in considerable increase in nucleus alignment (0.4x increase, $p < 0.05$) and elongation (0.1x reduction of CNSI, $p < 0.05$).

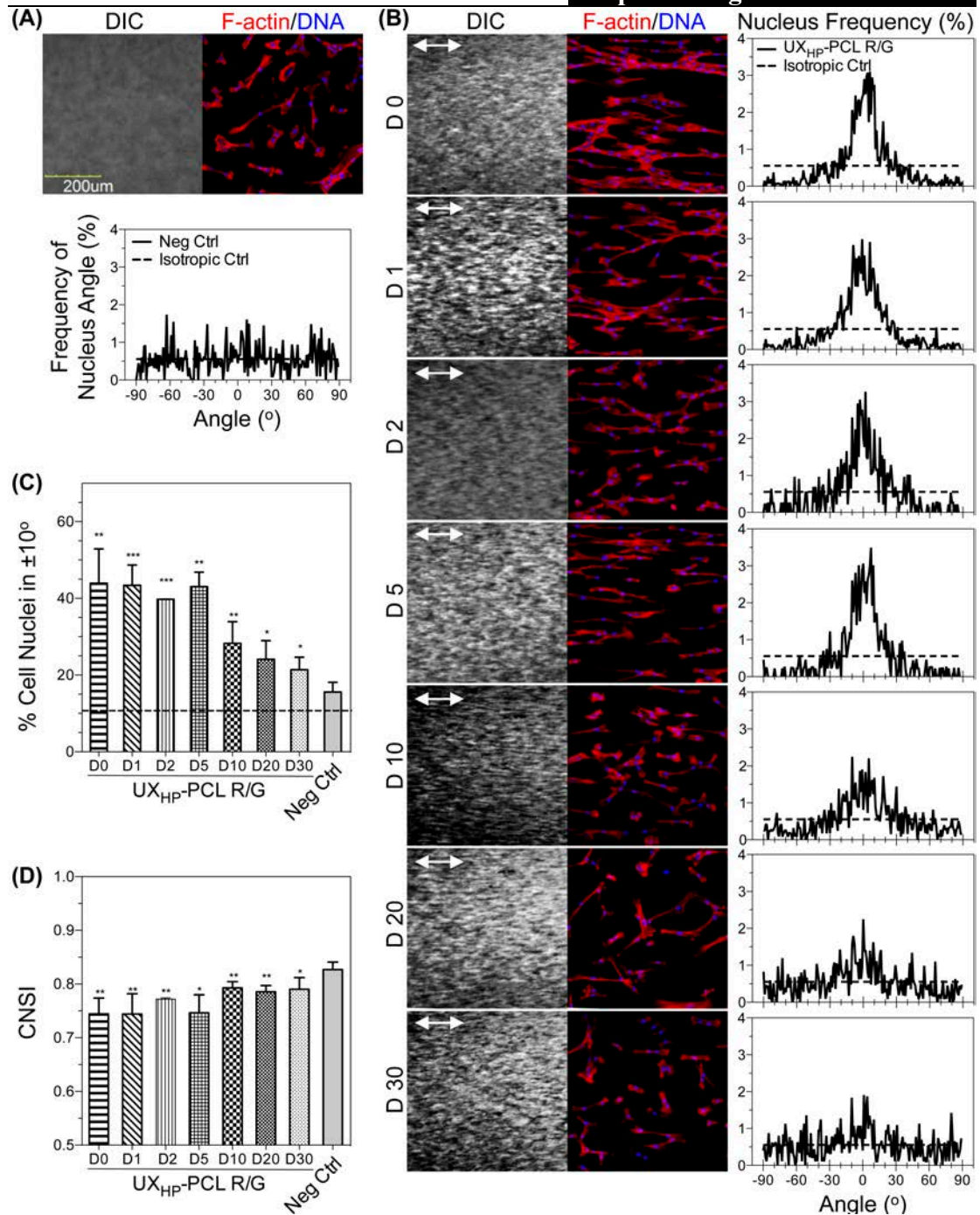


Figure 5-7: Cellular responses to geometric degradation of UX_{HP}-PCL ridge/groove arrays. Human MSCs (P6, 5k per cm²) were cultured on UX_{HP}-PCL ridge/groove arrays hydrolysed in an alkaline medium for different time (0-30 days), and stained using TRITC-conjugated phalloidin (Red colour: F-actin, cytoskeleton) and DAPI (Blue colour: DNA, nuclei). **(A)** MSCs on HP-PCL flat surfaces organised randomly (Neg Ctrl; Dot line: nucleus angle frequency of an Isotropic sample with a value of ~0.56 %). **(B)** MSCs on hydrolysed UX_{HP}-PCL ridge/groove arrays (Double-headed white arrows: ridge direction). **(C)** Nucleus alignment described as a normalised nucleus number in ±10° (Dot line: nucleus alignment of an Isotropic sample with a value of ~11.7 %). **(D)** Nucleus elongation described by a CNSI. A CNSI of 1 represents a circle (*, ** and *** represent significant differences as compared to Neg Ctrl; n = 3; *, p < 0.05; **, p < 0.01; ***, p < 0.001)

5.4 Discussion

Upon implantation of the engineered vascular scaffolds, geometric cues are contacted directly to the physiological erosive environments, and subjected to degradation inevitably *in vivo*. In this work, a degradation study on the stability of three-dimensional ridge/groove arrays on bioresorbable PCL films was performed. Results showed that UX_{HP}-PCL ridge/groove arrays achieved an enhanced morphological stability against degradation, compared to HP-PCL flat surfaces and ridge/groove arrays. UX_{HP}-PCL ridge/groove arrays followed a surface-controlled erosion, with an overall geometries be retained even at ~45 % film weight loss. During the investigated period of degradation, UX_{HP}-PCL ridge/groove arrays exhibited an "S-shape" behaviour of film weight loss, and maintained more stable surface hydrophilicity and film mechanical properties than those of HP-PCL flat surfaces. MSCs were able to align better towards UX_{HP}-PCL ridge/groove arrays when the geometries were retained, and became sensitive with gradually declined nucleus alignment and elongation to the geometric degradation of ridges.

Geometric cues have a larger surface/volume ratio than flat surfaces, and thus make them more susceptible to degradation in erosive environment [184]. In this study, HP-PCL flat surfaces were found to degrade completely into macroporous morphologies at ~5 % film weight loss. This phenomenon indicated that HP-PCL ridge/groove arrays could be degraded at an even smaller film weight loss. In fact, upon hydrolysis *in vitro*, the ridge areas of HP-PCL ridge/groove arrays were preferentially degraded and removed, further suggesting that geometric cues were susceptible to degradation, and could be removed in erosive environment with a small film weight loss.

Comparing HP-PCL flat surfaces and UX_{HP}-PCL ridge/groove arrays, original surface morphologies were well-maintained on UX_{HP}-PCL after the hydrolysis, suggesting that UX_{HP}-PCL ridge/groove arrays had an increased stability against degradation in erosive environment. Such enhancement was not due to the different surface geometries as HP-PCL ridge/groove arrays also lost the original ridges. It has been known that uniaxial stretching of polymeric films made closer chain packing, reduced free volume and restricted chain mobility, leading to inhibited penetration of erosive liquid into polymer bulk [236, 268, 269]. Meanwhile, PCL film crystallinity has been known to increase after uniaxial stretching [126]. This effect could also slow down the degradation of UX_{HP}-PCL ridge/groove arrays [126, 173]. Furthermore, UX_{HP}-PCL ridges were generated from the recrystallised PCL crystals [126]. Therefore, they had higher resistance against degradation than other regions [236], and probably resulted in the overall ridge/groove arrays being maintained. These suggested that uniaxial stretching could be the reason for the enhanced stability of UX_{HP}-PCL ridge/groove arrays against degradation.

UX_{HP}-PCL ridge/groove arrays exhibited a different morphological evolution from HP-PCL flat surfaces, suggesting that they might experience a different degradation mechanism [172]. It was valuable to note that over the investigated period, the degradation of UX_{HP}-PCL ridge/groove arrays occurred on film surfaces, without formation of in-growing or penetrating pores, while HP-PCL flat surfaces experienced interior degradation into the film bulk and presented as lots of in-growing macropores. These observations were in accordance with the commonly accepted fact for a surface and bulk-controlled erosion, respectively [17, 170, 172, 173]. The determining factor for which degradation takes place is the diffusion-reaction phenomena [17,

172]. The superficial degradation of UX_{HP}-PCL ridge/groove arrays suggested that the penetration of erosive liquid into PCL molecular chains was slower than that occurring for HP-PCL flat surfaces, because both PCL films had an identical hydrolysis rate constant of ester bonds [170]. This further explained the enhanced stability for UX_{HP}-PCL ridge/groove arrays, and agreed with the effect of uniaxial stretching that inhibited erosive liquid penetration [236, 268, 269].

One study has applied soft-lithography to micropattern PCL substrates with orientated ridge/groove arrays [173]. However, these structures have not obtained enhanced stability, and lost the geometries at less than 15 % weight loss during hydrolysis [173]. Similarly, HP-PCL ridge/groove arrays from direct-laser-writing during hydrolysis were found to preferentially remove the ridges and exhibited macroporous morphologies, which was similar the observations on HP-PCL flat surfaces. These suggested that apart from structure fabrication, techniques such as soft-lithography and direct-laser-writing were incapable of providing structures with enhanced stability. Comparatively, uniaxial stretching allowed not only the generation of ridge/groove arrays, but also the enhanced stability against degradation, facilitating the function of bioresorbable geometric cues in erosive environment. Furthermore, uniaxial stretching has been demonstrated to allow fabrication of geometric cues in a simple, solvent-free and reproducible manner, making it be a suitable method to generate film geometric cues for "off-the-shelf" and potentially clinical applications in vascular TE [126].

UX_{HP}-PCL ridge/groove arrays were found to follow an "S-shape" behaviour of film weight loss. Owing to the semi-crystalline properties, the initial film weight loss of

UX_{HP}-PCL ridge/groove arrays could be attributed to the preferential degradation in amorphous phases near the film surfaces [17]. Meanwhile, uniaxial stretching of polymeric films has often accompanied with surface wrinkling, cracking and residual tensile stress, which could facilitate erosive liquid penetration and/or molecular chain scission [17, 269, 270]. These probably resulted in the initially rapid film weight loss for UX_{HP}-PCL ridge/groove arrays. However, further degradation of UX_{HP}-PCL ridge/groove arrays resulted in reduced film weight loss rate, particularly for day 10-25. It was found that this period corresponded to the ridge disassembly. Since UX_{HP}-PCL ridges were generated from the recrystallised PCL crystals [126], they had closer chain packing and were more difficult for erosive liquid penetration than the superficial amorphous phases. Therefore, film weight loss rate during this period was reduced. Interestingly, accelerated film weight loss was obtained again from day 25 onwards. This was probably attributed to more surface areas being exposed as well as direct loss of small ridge-islands due to the formation of a series of parallel grooves across ridges [17, 184].

In regenerative medicine, PCL is known to exhibit slow degradation rates as compared to other biodegradable polymers (e.g. PLA and PGA) [17], and lots of efforts have been directed to accelerate the degradation rate of PCL [173]. However, these would not benefit the function of geometric cues, which relies on the shapes of surface structures. Moreover, the results of this work and together with previous findings, suggested that geometric features generated from methods such as soft-lithography and direct-laser-writing would be susceptible to erosive environment. It would be useful if PCL vascular TE scaffolds could have a faster degradation rate to give space for neotissue, while the functionalised geometric features remained

unaltered. Interestingly, UX_{HP}-PCL ridge/groove arrays exhibited a larger film weight loss than that of HP-PCL flat surfaces till ~35 % of the whole film weight, and then maintained the overall geometries. This was probably because of the generalist effects of uniaxial stretching that on one hand, accelerated the PCL film degradation [269, 270], and on the other hand conferred UX_{HP}-PCL ridges with enhanced resistance to degradation [126, 173, 236, 268, 269].

For the regeneration of vascular tissues, TE scaffolds should at least meet the basic safety requirements, although the complex mechanical property profile of blood vessels in most cases was beyond reach [173]. Although polymers such as PLA and PGA have achieved common use, they were susceptible to plastic deformation, limiting their use in mechano-active tissue reconstruction [17]. Comparatively, PCL is known to have superior mechanical performances [17, 173]. Meanwhile, UX_{HP}-PCL ridge/groove arrays have been demonstrated with enhanced mechanical properties, without scarifying the film elasticity. Here, the results further showed that UX_{HP}-PCL ridge/groove arrays under erosive environment could experience up to ~45 % film weight loss, without significant reduction in the film yield stress and strain. This indicated that *in vivo*, UX_{HP}-PCL ridge/groove arrays functioning as vascular geometric cues could also provide a stable mechanical support.

The changes of mechanical properties during degradation process are known to attributed to two opposite effects [175]: (1) the amorphous regions tended to hydrolyse faster than crystalline structures, leading to increased film crystallinity and Young's Modulus; and (2) the degradation generates mass loss and porosity inside or near the film's surface, resulting in a decreased Young's Modulus. The observation of

increased film yield stress, reduced yield strain and increased Yong's Modulus after the initial degradation for 1 day could be caused by the rapid weight loss in the superficial amorphous regions of UX_{HP}-PCL ridge/groove arrays [17]. Besides these, UX_{HP}-PCL ridge/groove arrays followed a surface-controlled erosion, which might also lead to a more stable film mechanical performance, as hydrolysis did not affect the internal bulk [17, 170, 173].

MSCs have shown to be a promising as vascular tunica media cell source, and UX_{HP}-PCL ridge/groove arrays exhibited robust regulation on MSCs alignment and elongation [126]. However, UX_{HP}-PCL ridge/groove arrays would undergo inevitable degradation *in vivo* [170], and whether they could support such regulation in a lasting manner as well as how vascular cells response to the structure geometric degradation remain unknown. The results of this work suggested a close correlation between the geometric degradation and stem cell responses. MSCs were found to align better on UX_{HP}-PCL ridge/groove arrays when the geometries were retained (Figures 5-8A and B). However, MSCs become sensitive to the geometric degradation of ridges with gradually declined nucleus alignment and elongation (Figures 5-8C and D). This could be attributed to the lowered height of ridges due to the ongoing hydrolysis, as studies suggested that ridge height could affect cell response to the given ridge/groove arrays [255, 271, 272], and lower ridges tended to result in decreased cell alignment [114, 273]. Besides this, the declined aspect ratio between ridges and grooves could also contribute to the observed reduction in MSCs nucleus alignment and elongation because of the presence of crossing grooves that divided ridges into small ridge-islands [139]. These observations suggested that stability-enhanced geometric cues would be preferable for vascular tissue regeneration. It was valuable to note that

because of uniaxial stretching, UX_{HP}-PCL ridge/groove arrays achieved an enhanced stability against degradation, and were able to maintain an overall geometries for increased MSCs nucleus alignment and elongation even at ~45 % film weight loss. These suggested that UX_{HP}-PCL ridge/groove arrays could provide a long lasting regulation on stem cells, and could be applied as suitable geometric cues for long-term vascular tissue regeneration with anisotropic architecture.

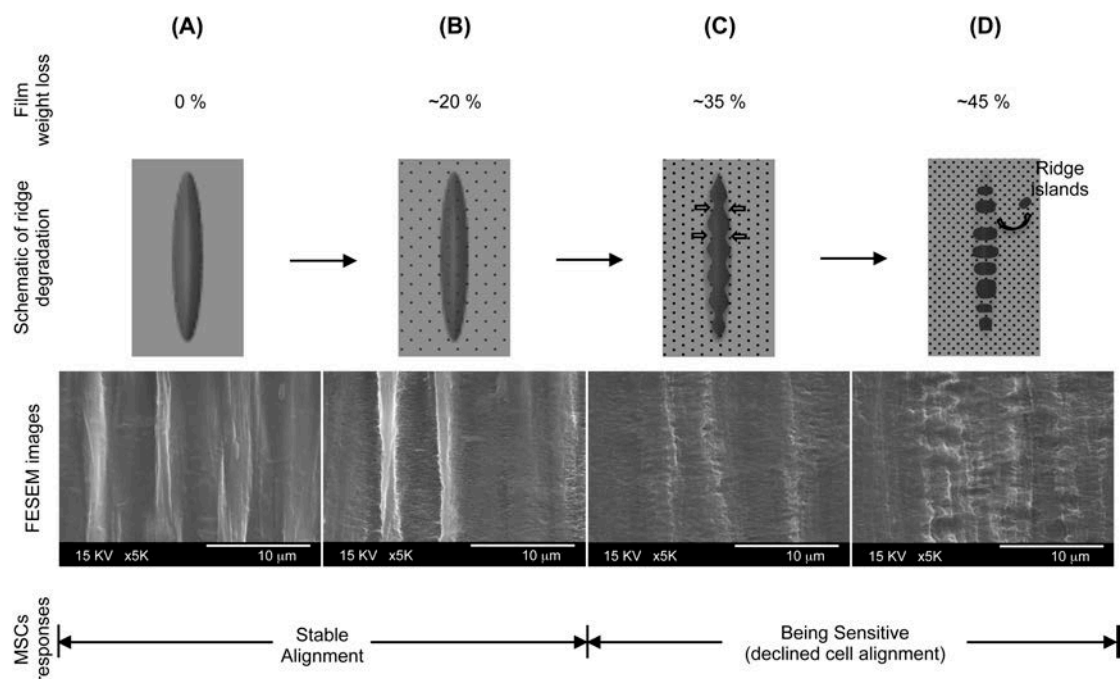


Figure 5-8: Summarised relationships among film weight loss of UX_{HP}-PCL, geometric evolution of ridge/grooves and MSCs responses. At less than ~20 % film weight loss, degradation resulted in gradually rougher surfaces with stable MSCs alignment. At more than ~20 % film weight loss, ridges degraded into small ridge-islands, leading to MSCs response with declined nucleus alignment and elongation (Hollow arrows: concaves at ridge-edges in [C] and direct loss of ridge-islands in [D]).

5.5 Summary

This work studied the influence of degradation on UX_{HP}-PCL ridge/groove arrays and further MSCs responses. UX_{HP}-PCL ridge/groove arrays achieved an enhanced morphological resistance to degradation in erosive environments, compared to the flat surfaces and ridge/groove arrays of HP-PCL. UX_{HP}-PCL ridge/groove arrays experienced a surface-controlled erosion, with overall geometries existed even at ~45

% film weight loss. During the investigated period of degradation, UX_{HP}-PCL ridge/groove arrays exhibited an "S-shape" behaviour of film weight loss, and maintained more a stable surface hydrophilicity and larger retainment of film mechanical properties than those of HP-PCL flat surfaces. MSCs tended to align better towards UX_{HP}-PCL ridge/groove arrays when the geometries were retained, and became sensitive with gradually declined nucleus alignment and elongation to the geometric degradation of ridges. It was concluded that uniaxial stretching could be used as a suitable method for the generation of film geometric cues with enhanced stability against degradation. This study also provides insights of how degradation to influence the geometric cues and further cell responses, and has implications for the design of biomaterials with stability-enhanced geometric cues for long-term vascular tissue regeneration.

Chapter 6 A Combination of Uniaxial Stretching and Femtosecond Laser Drilling for Engineered Vascular Basement Membrane

6.1 Introduction

Vascular basement membrane (BM) is essential for homeostasis of vascular cells and influences the patency of tissue-engineered vascular grafts (TEVG) [9]. Components of normal vascular BM are collagen IV, elastin, enactin/nidogen, heparin/sulfate proteoglycans and laminin, and they assemble as complex three-dimensional (3D) architectures consisting of orientated fibers and pores in submicron and nanoscale [9, 63]. These topographies have profound impact on the cell shape, growth/proliferation, migration and differentiation of endothelial cells (ECs) [9]. Furthermore, tunica media outwards BM consists of cells organised as a circumferential alignment and functions for maintaining the stress and stability of vascular vessels [40]. To function properly, engineering of vascular scaffolds must closely replicate these essential characteristics of the native vessels.

Geometric cues such as orientated fibers and anisotropic ridge/groove arrays have shown promise in aligning and regulating differentiation of cells (e.g. vascular smooth muscle cells [SMCs] and mesenchymal stem cells [MSCs]) for vascular TE [28, 113]. Chapter 2, Section 2.3.1 reviews the various geometric cues generated from methods

such as soft-lithography and direct-laser-writing. Chapter 2, Section 2.3.2 reviews the current findings that how these geometric cues influence cellular behaviour including morphology, migration, growth/proliferation, and differentiation as well as engineered tissue property. However, current geometric cues have been developed mainly based on the cubes and/or thick sheets, lacking sufficient interconnected pores.

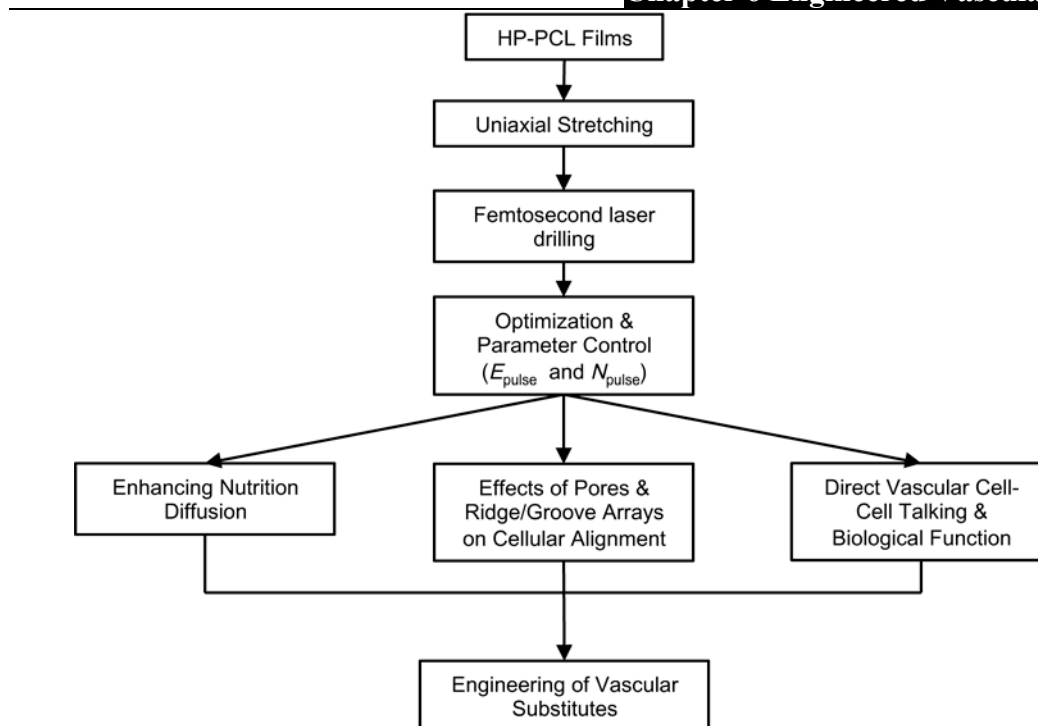
For vascular tissue regeneration, high porosity and pore connectivity of the scaffolds are required for providing sufficient gas and nutrient diffusion, and allow removal of metabolic products [274]. Furthermore, porous scaffolds appear to support cellular interaction across the substrates and promote cellular attachment and differentiation [9, 62, 275]. Therefore, geometric cues with the incorporation of pores could facilitate vascular tissue regeneration with similar organisation and function as *in vivo*. Chapter 2, Section 2.4.1 reviews the different techniques for introducing pores into scaffolds such as phase separation (e.g. freeze drying) and particulate leaching. In addition, needle-operated robot and laser beam punching have also been used [135]. Recent studies have demonstrated that by using the combination of soft-lithography/melt molding or soft-lithography/phase separation molding, pores have been successfully incorporated onto polymeric sheets [40, 62]. Despite the advantages achieved, pores generated from these methods were not homogeneous in size and shape, had poor interconnectivity, and were unable to control the pore positions, thus leading to interference on cellular alignment. As a comparison, laser beam is a promising technique for pore drilling *in situ*, and allows parameters such as pore size to be tunable [135].

In the work of Chapters 3, 4 and 5, uniaxial stretching has been demonstrated with capability of incorporating anisotropic 3D ridge/groove arrays on poly(ϵ -caprolactone) (PCL) films for biomimicking the anisotropy of vascular BM to regulate MSCs behaviour. Here, a combined method of using uniaxial stretching and femtosecond laser drilling, has been developed for creating complex architectures on PCL films including 3D orientated ridge/groove arrays and through-hole pore patterns. Such PCL films could be able to regulate cell organisation and simultaneously, allow direct cell-cell interaction, which has the potential to be used as an engineered BM for tunica media and intima regeneration.

6.2 Materials and Methods

6.2.1 Experimental Design

PCL films after uniaxial stretching were drilled using femtosecond laser beam (Scheme 6-1). Pore morphology, diameter and position at the top and bottom film surfaces were characterised to understand the influence of beam parameters on pore formation. Studies of nutrition diffusion, cellular alignment and direct cell-cell interaction were also performed to understand the designed biological performances.



Scheme 6-1: Schematic diagram illustrating the experimental design of this work. PCL films were subjected to uniaxial stretching for the generation of orientated ridge/groove arrays, and femtosecond laser drilling for perforation. Characterisations of morphology, nutrient diffusion, cellular alignment and direct cell-cell interaction were performed for evaluating the designed function. (E_{pulse} : pulse energy; N_{pulse} : pulse number)

6.2.2 Materials

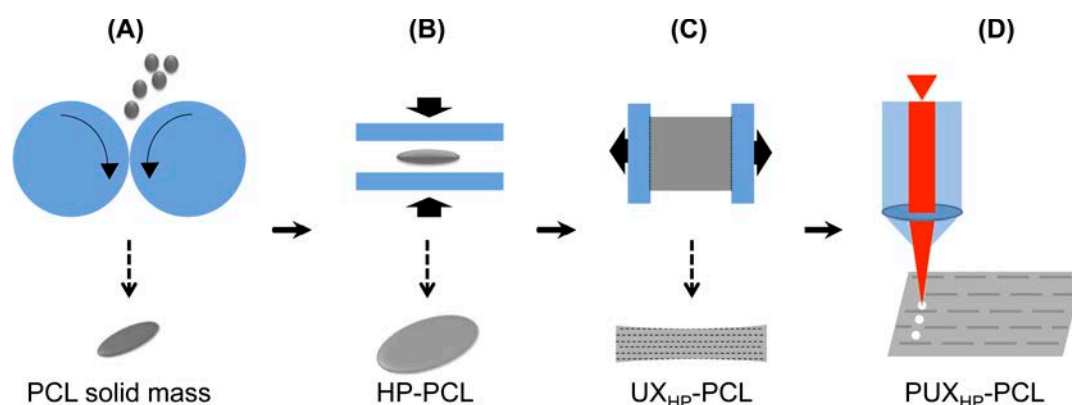
Endothelial growth medium (EGM) were purchased from Lonza (Singapore). Nitric oxide (NO) assays kit was purchased from Cell Biolabs, Inc. (USA). FITC-Dextran (MW: 40,000) and PHK cell linker dyes kit were purchased from Sigma-Aldrich (Singapore). Green fluorescent protein (GFP) labeled human umbilical vein endothelial cells (HUVECs) were provided as a gift from Dr. Mark Seow Khoon Chong (National University of Singapore). Other materials and mesenchymal stem cells (MSCs) in this work were obtained as described in Chapter 3, Section 3.2.2.

6.2.3 Sample Preparation

Heat-pressed PCL (HP-PCL) films were fabricated using a combined method of two-roll milling (80 °C) and heat pressing (300 MPa, 80 °C) (Chapter 3, Section 3.2.3).

Uniaxial-stretched PCL (UX_{HP} -PCL) films were then generated from HP-PCL at a stretching temperature of 54 °C and a draw ratio of 4.

Pores were drilled on HP-PCL and UX_{HP} -PCL using a spectra-physics millenia-pumped tsunami femtosecond laser. The femtosecond laser uses a Titanium (Ti):Sapphire doped crystal as the medium with a wavelength of 800 nm and pulse duration of 110 fs. Pore arrays were designed using a U500 MMI (Aerotech, UK) software. The femtosecond laser drilled films were named as PUX_{HP} -PCL.



Scheme 6-2: Schematic diagram illustrating the fabrication of PCL films. (A) PCL pallets were passed through a two-roll mill to obtain uniform PCL solid mass. (B) HP-PCL films with flat surfaces were obtained from heat press of PCL solid mass at 300 MPa and 80 °C. (C) UX_{HP} -PCL films were generated from uniaxial stretching of HP-PCL films at 54 °C and a draw ratio of 4. (D) PUX_{HP} -PCL films were obtained by program-controlled drilling of UX_{HP} -PCL using a femtosecond laser.

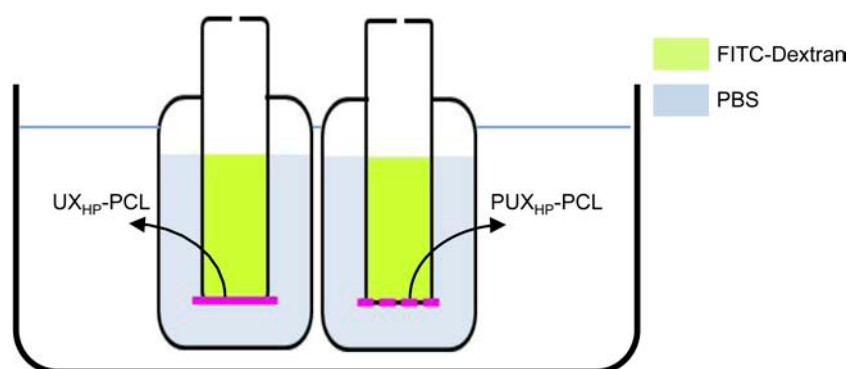
6.2.4 Field Emission Scanning Electron Microscopy (FESEM)

FESEM characterisation was performed as described in Chapter 3, Section 3.2.4.

6.2.5 Nutrition Diffusion Test

Nutrition diffusion of PUX_{HP} -PCL was evaluated using a marker of FITC-labeled Dextran. PCL films (UX_{HP} -PCL) without drilling were used as a control group. The setup was schematically shown in Scheme 6-3. Briefly, 1 ml (2 mg/ml) was injected via a small pore into the PCL film sealed tubes. The sealed tube was then put into a

black bottle, which contained 21 ml of PBS. The system was then immersed into a 37 °C water bath in a dark environment. Samples with a volume of 50 µl PBS were taken out at pre-determined time points of 1, 3, 7, 24, 50, 120 and 288 hrs. The samples were diluted 10 times with PBS, and fluorescence detection was performed using a microplate reader (Tecan Group Ltd, Infinite® M1000 PRO, Switzerland). Standard curves (FITC-Dextran concentrations ranged from 0.05 to 0.001563 mg/ml) were performed for each detection time point. Normalised cumulative concentration of FITC-Dextran was used to describe the film permeability ($C_{\text{cumulative}} = C_{\text{real}} / C_{\text{full-diffusion}} * 100 \%$). Six samples were used for each time point per group.



Scheme 6-3: Schematic diagram illustrating the measurement of FITC-dextran diffusion. UX_{HP}-PCL without drilling was set as a control. The diffusion system was under a constant temperature of 37 °C.

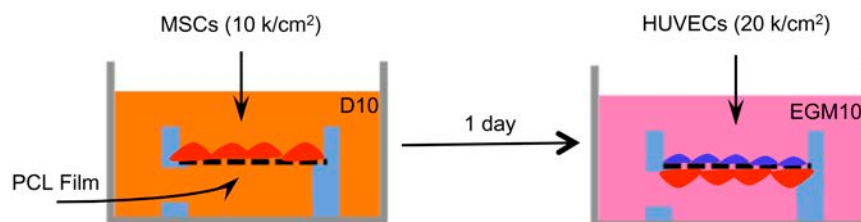
6.2.6 Cell Isolation and Culture

MSCs were isolated and expanded as described in Chapter 3, Section 3.2.9. HUVECs were cultured in EGM10 (EGM + 10 % FBS). Cells used were within Passage-6.

6.2.7 MSCs and HUVECs Co-culture

Co-culture of MSCs and HUVEC was performed using a ring as illustrated in Scheme 6-4. Briefly, PCL film was put at the middle of the ring, and MSCs (10k per cm²) were seeded firstly. After culturing in D10 for 1 day, films were turned over using a

sterilised forcep, and HUVECs were seeded onto the opposites of MSCs. MSCs and HUVECs were then co-cultured in EGM10.



Scheme 6-4: Schematic diagram illustrating the co-culture of MSCs and HUVECs. MSCs (10k per cm²) were firstly seeded onto the film. After 1 day culture in D10, the films were turned over, medium was changed to EGM10 and HUVECs were seeded onto the opposites of MSCs at a density of 20k per cm² for co-culture.

For direct cell-cell contact study, fluorescence-labeled cells were used. MSCs were labeled with red fluorescence using PHK26 kit. Briefly, once MSCs reached ~70 % confluence, they were collected by trypsinisation and centrifugation. Cells were washed with PBS twice to remove any FBS. Cellular pellets were then re-suspended in Diluent (2x final concentration, 0.5 ml). Meanwhile, PHK26 dye was diluted into 2x solution (0.5 ml), and immediately mixed with cell suspension. After incubation at room temperature for <5 min, FBS (1 ml) was added to stop the reaction, and cells were washed with D10 thrice. PHK26-labeled cells were examined using CLSM. HUVECs were labeled with GFP.

6.2.8 Confocal Laser Scanning Microscopy (CLSM)

For alignment study, cells after culturing for pre-determined time were visualised via cytoplasmic live-cell (FDA) and cytoskeletal fixed-cell (TRITC-conjugated phalloidin: F-actin; DAPI: DNA) staining. All fluorescence-labeled cells were examined using CLSM as described in Chapter 3, Section 3.2.10. Cell number was determined following a nucleus counting as described in previous reports [276, 277].

For characterisation of cell-cell contact, a Z-scanning was performed on CLSM, and 3D image construction was performed using the built-in function of Imaris (Bitplane, Switzerland).

6.2.9 Cellular Alignment

Cellular angles were analysed using the built-in function of ImageJ as described in Chapter 4, Section 4.2.10. Cells grew on UX_{HP}-PCL ridge/groove arrays and HP-PCL flat surfaces were set as a positive (P-Ctrl) and negative control (N-Ctrl), respectively. An isotropic sample would have an efficiency of ~11.7% of cells to be aligned.

6.2.10 NO Assay

The NO level of co-culture system was evaluated using a NO assay kit. Experiment was designed with five groups: (1) EGM10; (2) EGM10 + porous film + MSCs; (3) EGM10 + porous film +HUVECs; (4) EGM10 + non-porous film + MSCs + HUVECs; and (5) EGM10 + porous film + MSCs + HUVECs. Briefly, MSCs and HUVECs were seeded on UX_{HP}-PCL or PUX_{HP}-PCL with single- or co-culture in EGM10 (2.5 ml) for 8 days. At day 3 and 5, 0.5 ml EGM10 was added for nutrition supply. After 8 days of culture, the total nitrate/nitrite ($\text{NO}_3^-/\text{NO}_2^-$) level in culture medium was examined following the procedures of NO assay kit. Briefly, 10 μl sample (cell culture medium) was added to a 96-well plate, and adjusted to 80 μl using the assay buffer. 10 μl enzyme cofactors and 10 μl nitrate reductase were then added in sequence, and incubated at room temperature for 30 min to reduce nitrate into nitrite. 10 μl 2,3-diaminonaphthalene (DAN) was then added and incubated for further 10 min. 20 μl NaOH solution was added to end the reaction, with enhanced fluorescence intensity. For standard curve, 10 μl EGM10 with 70 μl assay buffer was

used as the blank. 10 μ l EGM10 with 20 μ l assay buffer and 50 μ l nitrate standard was used as gradient. Fluorescence detection was performed on a microplate reader at Ex/Em of 380/461 nm. Four samples were used.

6.2.11 Data Analysis

Data analysis was performed on Prism 5 software. Curve fitting for the FITC-dextran diffusion was implemented using Excel 2011 software with a R^2 value of 0.99. Results were reported as mean \pm SD. A value of $p < 0.05$ was considered to be statistically significant.

6.3 Results

6.3.1 Anisotropic Geometries and Pore Patterns on PCL Films

Figure 6-1 shows the morphologies of PCL films after uniaxial stretching and femtosecond laser drilling. Before stretching, HP-PCL exhibited relatively flat surfaces (Figure 6-1A). After uniaxial stretching, orientated micro-ridge/groove arrays were homogeneously presented on UX_{HP} -PCL (Figure 6-1B). When femtosecond laser beam was drilled onto UX_{HP} -PCL, pores were formed (Figure 6-1C). These circular pores distributed homogeneously on PCL films, with lip-like melting towards the ridge direction.

Figure 6-2A shows the morphologies of pores on both the top and bottom surfaces of UX_{HP} -PCL. FESEM images from the two surfaces demonstrated that the pores generated by femtosecond laser drilling were through-hole. The pores exhibited as an approximated circle on the top film surface, but an ellipse on the bottom film surface, with the long-axis perpendicular to the ridges. Furthermore, melting of PCL was

observed and exhibited as sprayed fibers around the pores. Comparatively, the sprayed melting was severer on film bottom surface accompanying with porous melting covered on ridges. Low magnified FESEM images of both PUX_{HP}-PCL surfaces further showed that the melting was restricted within the neighboring area (radius: <20 μm), and did not affect the ridge/groove arrays in other film regions. In contrast, the melting was more rounded on the top surface of HP-PCL with more ejection observed (Figure 6-2B).

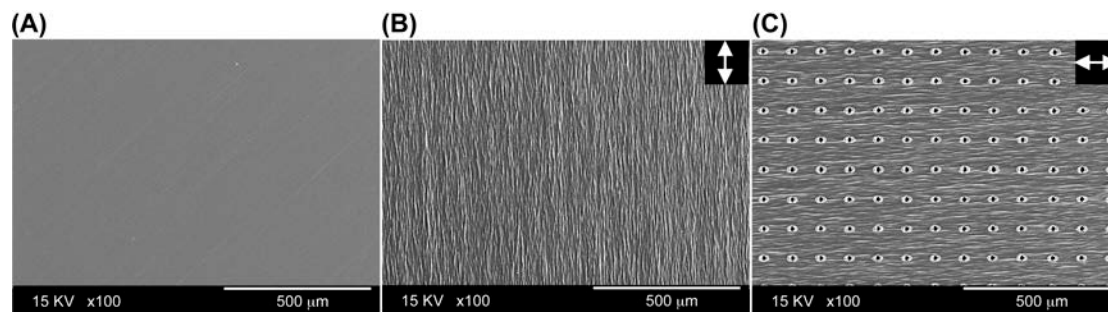


Figure 6-1: Uniaxial stretching and femtosecond laser drilling of PCL films resulted in orientated ridge/groove arrays and pore patterns. **(A)** HP-PCL flat surfaces. **(B)** UX_{HP}-PCL ridge/groove arrays (double-headed arrows: ridge direction). **(C)** PUX_{HP}-PCL with orientated ridge/groove arrays and pore patterns (Scale bar = 500 μm).

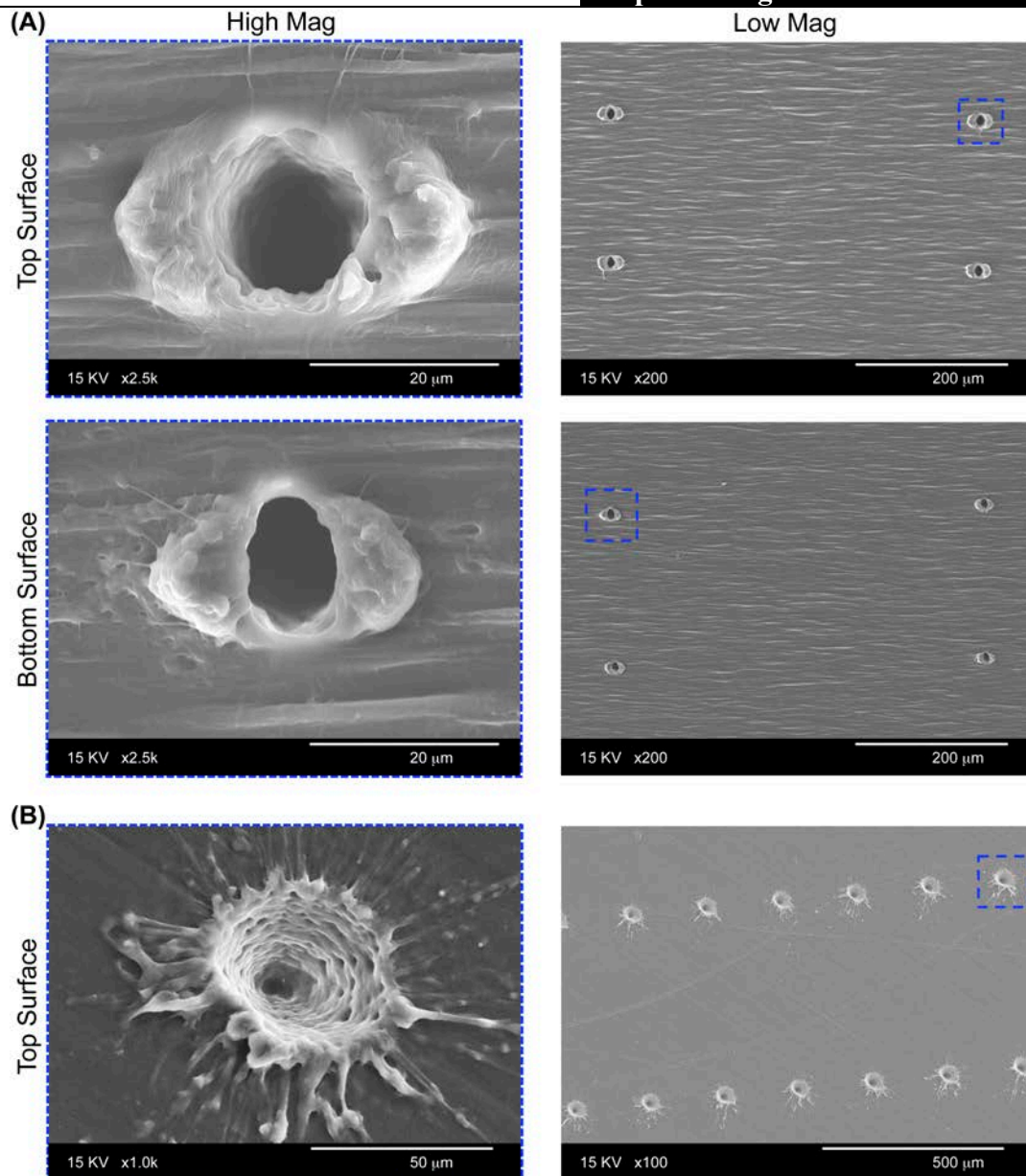


Figure 6-2: (A) Pore morphologies top and bottom film surfaces. FESEM images of PUX_{HP}-PCL reveal through-hole after femtosecond laser drilling, which was rounded with lip-like melting and formed into an ellipse-like shape towards ridges (Scale bar = 20 and 200 μm for high and low magnifications, respectively). (B) Pore morphologies on HP-PCL top film surface revealed more rounded and more ejection (Scale bar = 50 and 500 μm for the high and low magnifications, respectively).

6.3.2 Tailorability of Pore Position and Diameter

During the drilling process, pore position was adjusted by moving the stage, which was controlled via a program. As shown in Figure 6-3A, the direction along the ridges was defined as the x-axis, and the perpendicular direction as the y-axis. The pore patterns were realised through programming a path to guide the stage movement. Figure

6-3B shows the pore patterns on PUX_{HP}-PCL, with different inter-pore-distance in the x and y directions (e.g. X200Y200, X200Y500 and X500Y200). Pore position could be adjusted in both x and y directions, and pore shapes were homogeneous over the sample surface, without tailing phenotypes observed.

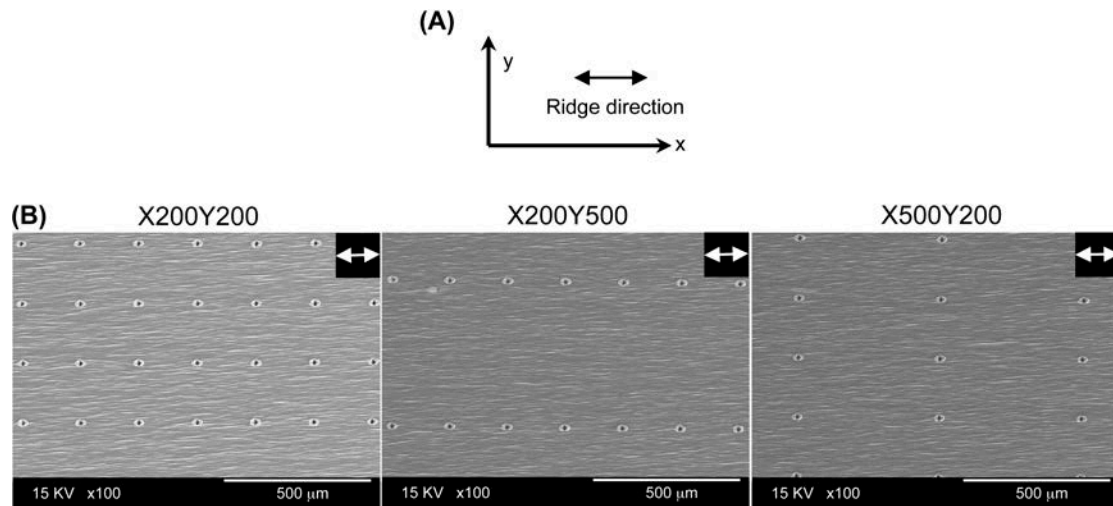


Figure 6-3: Control of pore position. (A) x-axis was defined as the ridge direction, while y-axis was perpendicular to ridges. (B) Different pore patterns on PUX_{HP}-PCL (Scale bar = 500 μm).

Figure 6-4A shows the changes of melting on film top surfaces. Higher pulse energy E_{pulse} tended to produce thicker ejection fibers, while a higher pulse number N_{pulse} resulted in a less melt ejection. Figure 6-4B shows the tailoring of pore size by controlling E_{pulse} and N_{pulse} . Results from the size measurement showed that pores of PUX_{HP}-PCL exhibited a larger diameter on film top surface and smaller one on film bottom surface. With increasing E_{pulse} from 10 to 80 μJ , the pore diameters on both the film top and bottom surfaces increased. When E_{pulse} was lower than 10 μJ , femtosecond laser beam resulted in less change to the pore diameter on film top surface, and mesh-like structures instead of a penetrated pore on film bottom surface (Figure 6-4B). Compared to E_{pulse} , N_{pulse} did not make any significant change to the pore diameters on both the film top and bottom surfaces (Figure 6-4A).

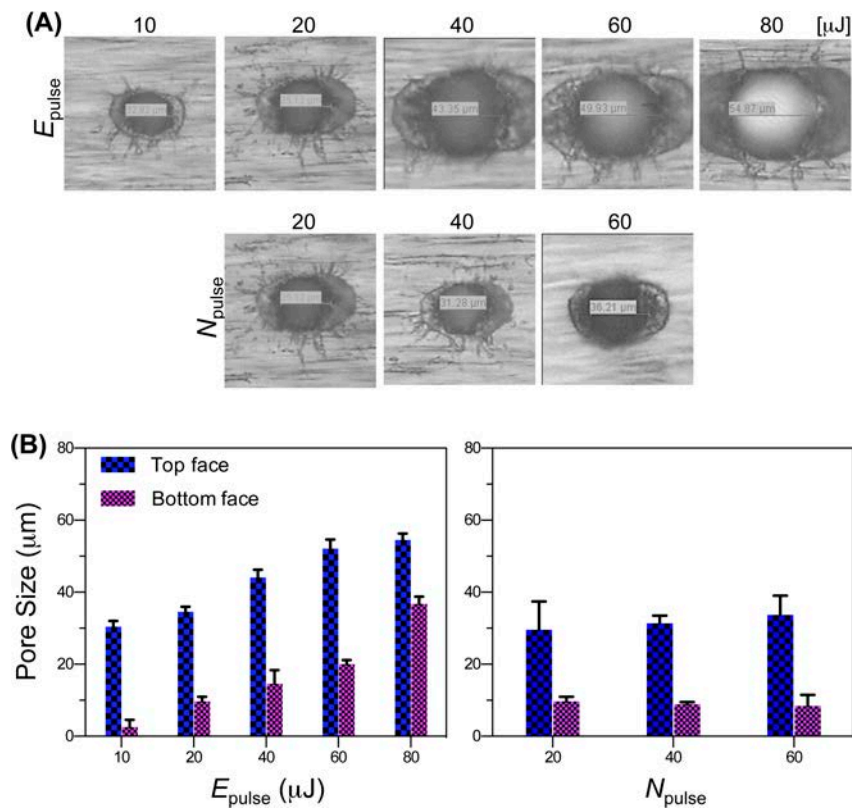


Figure 6-4: (A) Light microscopy images of melting ejection. Higher E_{pulse} produced thicker ejection fibers ($N_{\text{pulse}} = 20$), while higher N_{pulse} resulted in less ejection ($E_{\text{pulse}} = 20 \mu\text{J}$). (B) Influences of E_{pulse} and N_{pulse} . Pore diameters increased with raised E_{pulse} ($N_{\text{pulse}} = 20$), but exhibited less changes when N_{pulse} was varied ($E_{\text{pulse}} = 20 \mu\text{J}$; $n = 6$).

6.3.3 Enhanced Permeability for MSCs Adhesion and Proliferation

Figure 6-5 shows the evolution of permeability of PUX_{HP}-PCL. During 0 to 120 hrs, the curve of cumulative FITC-dextran concentration approximated to a line. After 120 hrs, the increase of cumulative FITC-dextran concentration was slower. FITC-dextran achieved ~100 % diffusion across PUX_{HP}-PCL at around 288 hrs (around 12 days). In contrast, no obvious diffusion was observed for UX_{HP}-PCL. The cumulative FITC-dextran concentration was around 0 % over the investigated period.

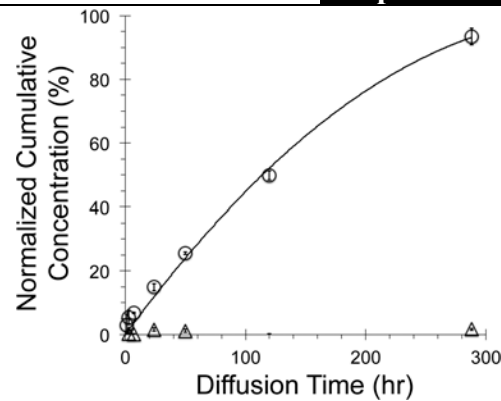


Figure 6-5: Permeability evolution of PUX_{HP}-PCL. Cumulative concentration of FITC-dextran increased with diffusion time, and achieved ~100 % of diffusion at 288 hrs (FITC-dextran: marker molecule; UX_{HP}-PCL: control group; n = 6).

The enhanced permeability of PUX_{HP}-PCL was further demonstrated. Figure 6-6A shows the experimental design. PCL films were sealed onto the rings to separate the testing (D0) and nutrition (D10) medium. MSCs seeded onto PUX_{HP}-PCL in D10 and D0 were set as the P-Ctrl and N-Ctrl, respectively. Results from cell nucleus counting showed that compared to UX_{HP}-PCL, MSCs seeded on PUX_{HP}-PCL in D0 achieved increased cell adhesion at culture day 1 (1.9x increase, $p < 0.001$), and exhibited an enhanced cellular proliferation at day 3 of culture (2.2x increase, $p < 0.001$), although both were lower than those cells in P-Ctrl. Furthermore, MSCs on UX_{HP}-PCL in D0 and PUX_{HP}-PCL in D0 showed similar cellular adhesion at day 1 ($p > 0.05$) and proliferation at day 3 ($p > 0.05$), suggesting that micropore patterns did not affect the cell adhesion.

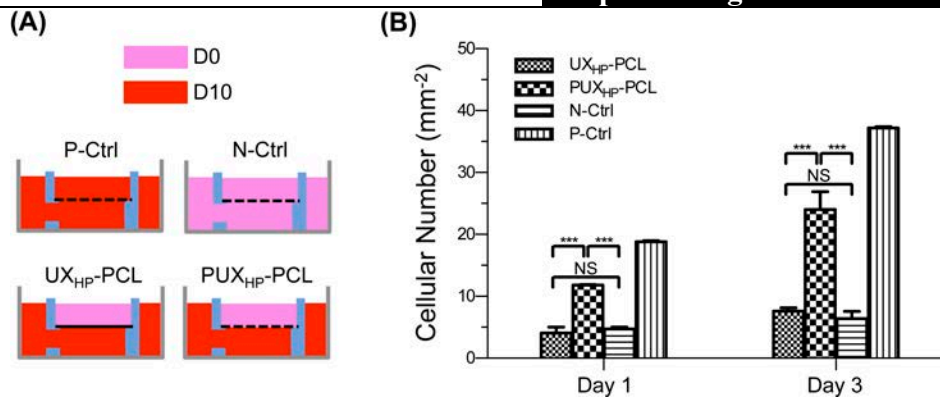


Figure 6-6: (A) Schematic diagram illustrating the experimental design. MSCs seeded on PUX_{HP}-PCL in D10 and D0 were set as positive (P-Ctrl) and negative (N-Ctrl) control, respectively. (B) Cellular adhesion and proliferation on PUX_{HP}-PCL. Cells (Passage-6, 5k per cm²) were seeded and cultured for 1 and 3 days. MSCs on PUX_{HP}-PCL achieved increased cell adhesion (day 1) and proliferation (day 3) as compared to those of UX_{HP}-PCL group (n = 3; ***, p < 0.001; NS, p > 0.05).

6.3.4 MSCs Alignment

Figure 6-7A shows the cell cytoskeletal organisation on UX_{HP}-PCL. CLSM images of F-actin exhibited that MSCs aligned along the UX_{HP}-PCL ridge/groove arrays, with highly orientated cytoskeletal stress filaments. MSCs on PUX_{HP}-PCL near the pores revealed three types of organisation. As shown in Figure 6-7B, MSCs retained alignment when cells were able to extend freely. If pores obstructed cellular extension at one end only, MSCs exhibited re-organised cytoskeleton fibers being confined to the pore shapes; MSCs still self-aligned the left half-part with orientated cytoskeletal fibers extended along the ridge/groove arrays (Figure 6-7C). However, cell alignment was disturbed if the other extension end of MSCs was attached to the ridges/grooves or cells that were not in the ridge direction (Figures 6-7C and E).

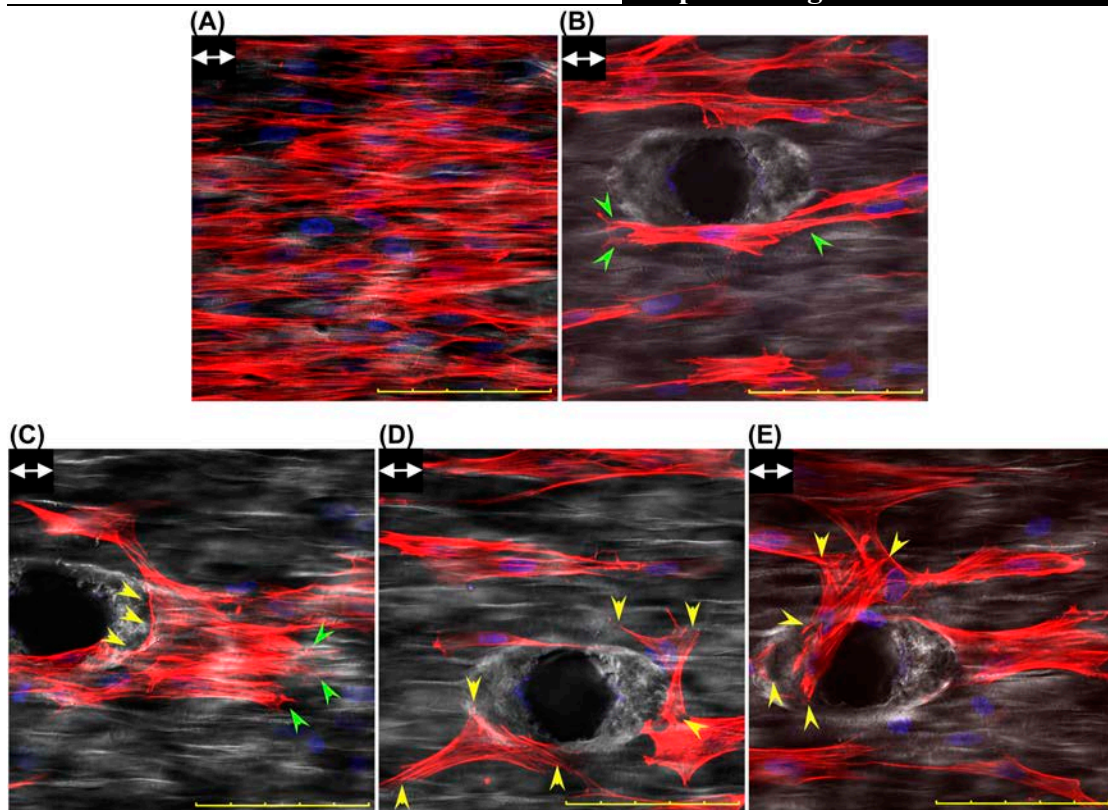


Figure 6-7: Pore influence on MSCs alignment. **(A)** UX_{HP} -PCL. MSCs aligned on UX_{HP} -PCL towards the ridge directions. **(B-E)** PUX_{HP} -PCL. MSCs exhibited aligned growth towards the ridge/groove arrays when they could extend freely, half-cell alignment when cellular extension was obstructed only at one end, and disturbed alignment when MSCs extension was obstructed at one end and the other end attached to substrate/cells that were not in ridge direction (Double-headed arrows: ridge direction; Green arrows: free extension of cells; Yellow arrows: cell extension being obstructed and attached to substrate or cells; Scale bar = 100 μ m).

Figure 6-8A shows the influence of pore patterns on MSCs alignment towards PUX_{HP} -PCL ridge/groove arrays. On X200Y200, CLSM images of cytoplasmic staining exhibited that MSCs between two pores tended to be deviated from the ridge directions. Comparatively, the pore pattern of X200Y500 showed more interference on MSCs alignment. Cells grew closely around the pores. Interestingly, MSCs on X500Y200 exhibited better alignment. Although MSCs tended to distribute around the pores, cells between the two pores were able to extend freely. Quantitative analysis of cellular angles showed that the presence of pores resulted in declined MSCs alignment (vs P-Ctrl: ~32-53 % reduction, $p < 0.001$). Compared to PUX_{HP} -PCL:X200Y200, MSCs on X200Y500 exhibited a lower alignment efficiency (p

>0.05), and a higher efficiency on X500Y200 ($p > 0.05$), although significant differences were not observed. Moreover, MSCs on PUX_{HP}-PCL:X500Y200 showed a higher alignment efficiency than that of cells on X200Y500 ($p < 0.001$).

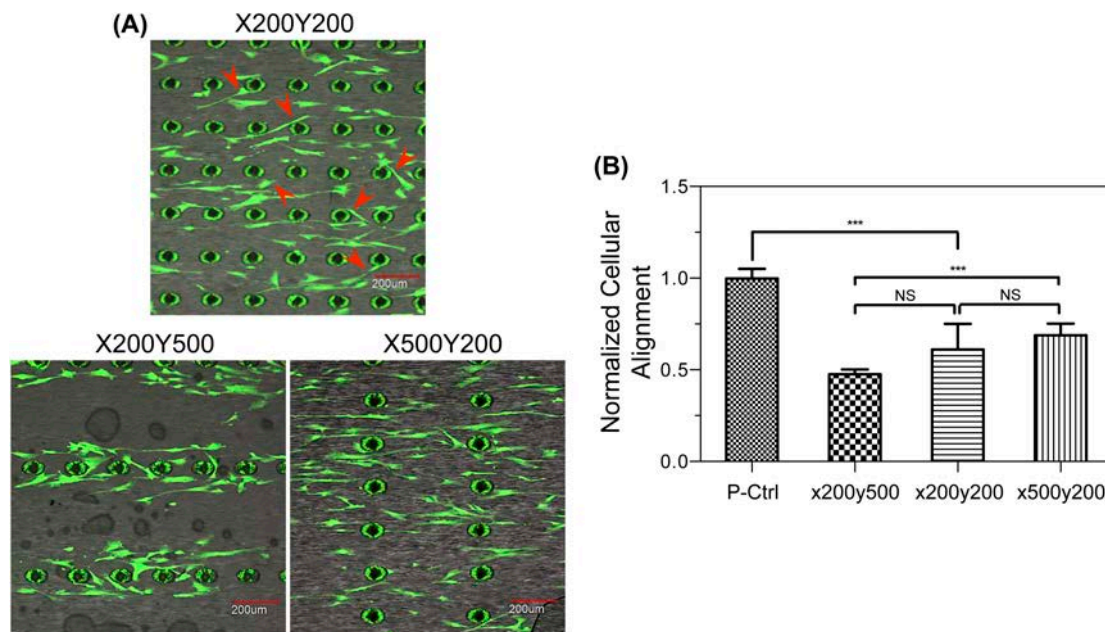


Figure 6-8: Influence of pore pattern on MSCs alignment. **(A)** CLSM images reveal different MSCs organisation on PUX_{HP}-PCL (Red arrows: cells disturbed by pores; Scale bar = 200 μm). **(B)** Normalised MSCs alignment efficiency. MSCs exhibited the declined degree of alignment efficiency towards ridge/grooves depending on pore patterns ($n = 3$; ***, $p < 0.001$; NS, $p > 0.05$).

Figure 6-9A shows the drilled pore patterns with a pore distance of 500 μm in both the x and y directions. Results from quantitative analysis of cellular angles showed that pores of X500Y500 did not affect MSCs alignment (Figure 6-9B). Cells grew on PUX_{HP}-PCL:X500Y500 achieved non-reduced cellular alignment efficiency as compared to those of UX_{HP}-PCL group for 1, 3 and 5 days of culture, respectively ($p > 0.05$).

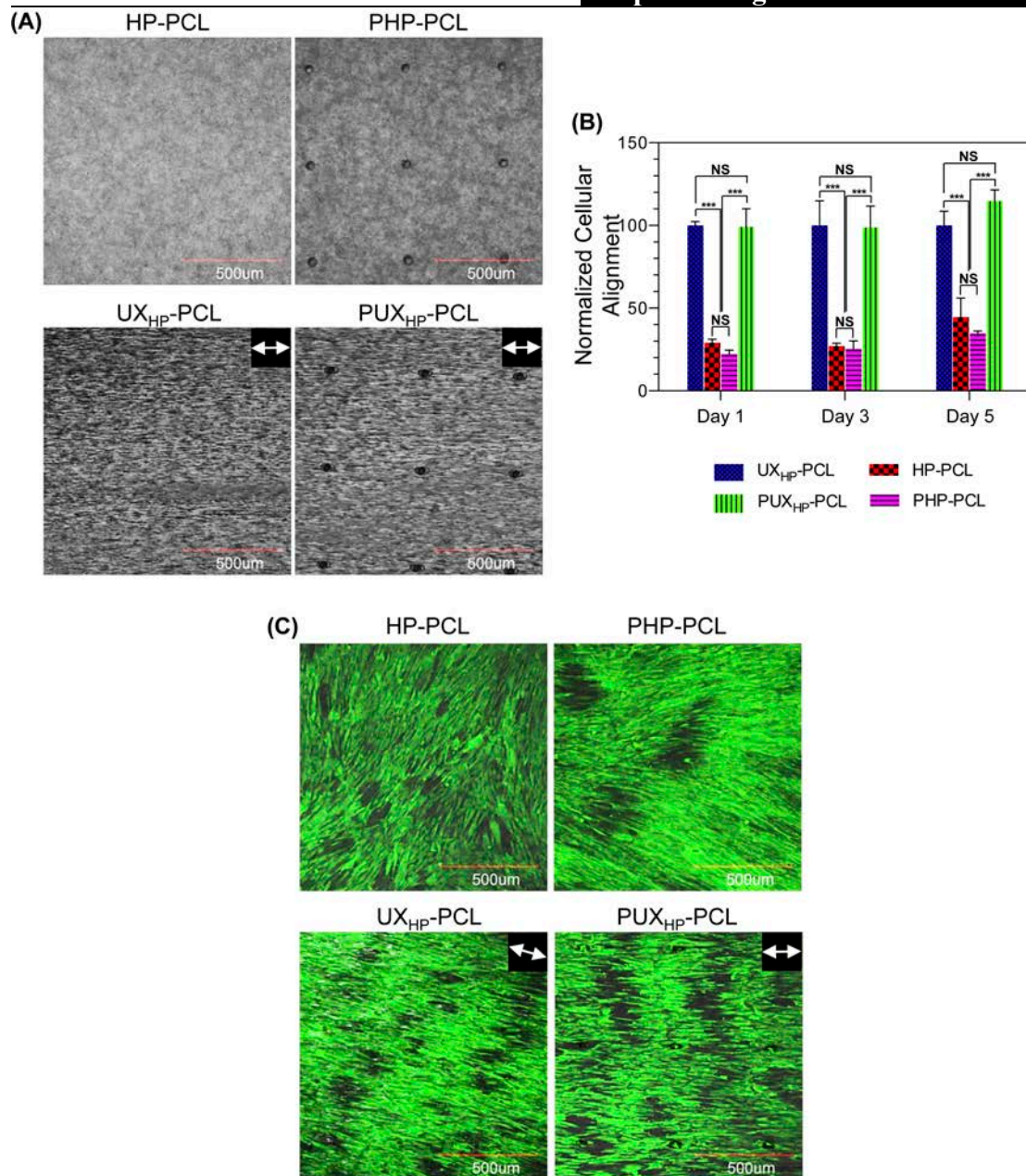


Figure 6-9: Non-interfered MSCs alignment on PUX_{HP}-PCL. Cells (Passage-6, 5k per cm²) seeded on PCL films were cultured for pre-determined time. **(A)** DIC images of HP-PCL, PHP-PCL, UX_{HP}-PCL and PUX_{HP}-PCL (Inter-pore-distance: 500 µm; Double-headed arrows: ridge direction). **(B)** Normalised cell alignment efficiency. MSCs alignment on PUX_{HP}-PCL achieved significant increase than that of PHP-PCL, and was non-reduced as compared to that of UX_{HP}-PCL (n = 3; ***, p <0.001; NS, p >0.05). **(C)** Cellular organisation at a confluence status. MSCs after 8 days of culture still retained aligned growth on UX_{HP}-PCL and PUX_{HP}-PCL in a controllable direction towards ridges (Double-headed arrows: ridge direction).

Compared to PHP-PCL, MSCs on PUX_{HP}-PCL showed considerable increase in cellular alignment efficiency (p <0.001). Meanwhile, MSCs exhibited similar lower alignment efficiencies on PHP-PCL and HP-PCL (p >0.05). MSCs retained

orientation-controlled alignment on UX_{HP} -PCL and PUX_{HP} -PCL, when cells got confluent (Figure 6-9C). However, MSCs still organised randomly on both HP-PCL and PHP-PCL.

6.3.5 Direct MSCs-HUVECs Interaction

Figure 6-10 shows the ingrowth of MSCs into the pores of PUX_{HP} -PCL after 3 days of culturing. FESEM images revealed three types of cellular ingrowth: (i) bridging: MSCs extended and bridged across the pores via two anchors (red arrows). Another cellular protrusion could extend into the pore depth (blue arrow) depending on the pore sidewall, (ii) sidewall depth: MSCs adhered well to the inner side of the pores, thereby extending along the surfaces (red arrows), and (iii) coverage: MSCs spread around the pores, and tended to cover the pores using several anchors (red arrows).

Figure 6-11A shows the direct contact between GFP-labeled HUVECs and PHK26-labeled MSCs. 3D construction of section-scanning CLSM images demonstrated that PUX_{HP} -PCL allowed HUVECs to grow into the pores from the top film surface and MSCs from the bottom film surface. The cells met each other within the pores and direct cell-cell contact occurred, presenting as yellow colour. To escape the false positivity due to different viewing angles, crossing-section view was performed (Figure 6-11B). Images showed that around the middle depth of the pores, GFP-labeled HUVECs co-localised with PHK26-labeled MSCs and exhibited as yellow areas. Interestingly, the yellow dots were found not only around the red or green colour areas, but also within each other.

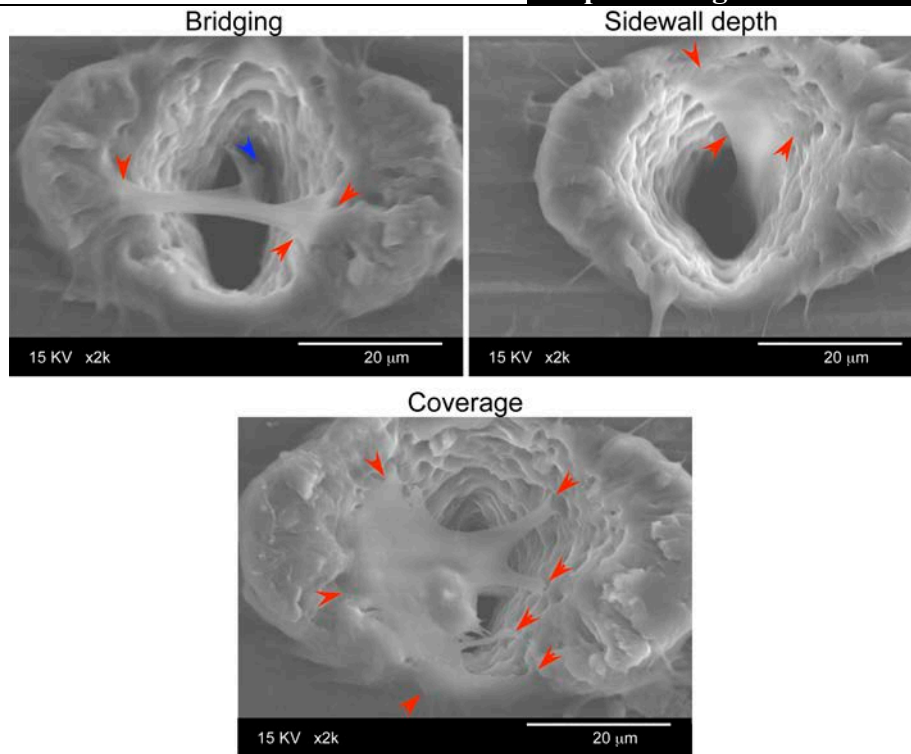


Figure 6-10: Cellular ingrowth of MSCs into PUX_{HP}-PCL via (i) bridging, (ii) sidewall depth and (iii) coverage. Cells (Passage-6, 5k per cm²) seeded on PUX_{HP}-PCL:X500Y500 were cultured for 3 days in D10 (Red arrows: cellular anchors that adhered to the pore sidewall; Blue arrows: cellular anchors that extended into the pore depth; Scale bar = 20 μm).

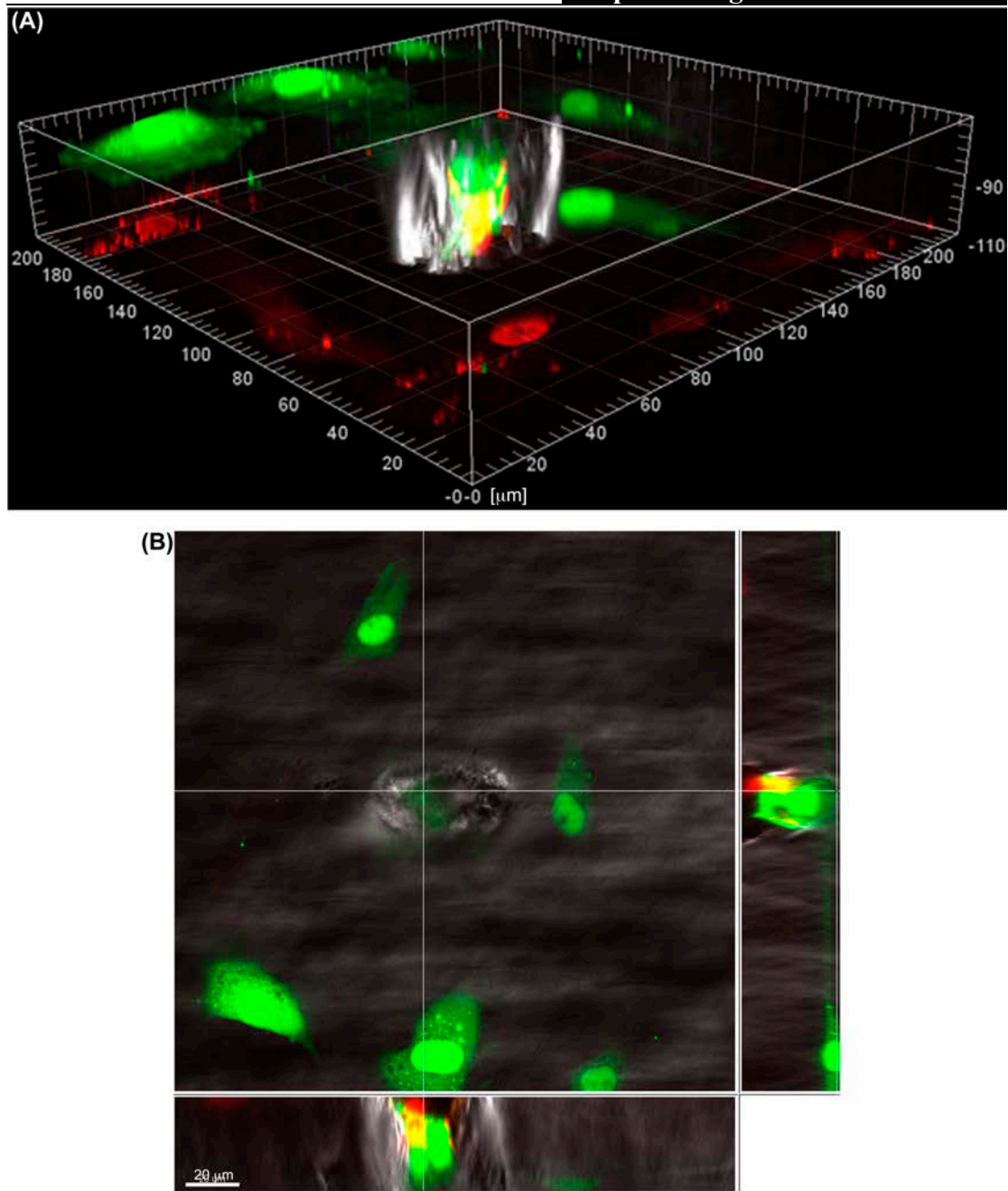


Figure 6-11: Direct MSCs-HUVECs contact. PHK26-labeled MSCs (Red colour; Passage-6, 10k per cm^2) seeded on one surface of PUX_{HP}-PCL:X500Y500 were cultured in D10 for 1 day, and GFP-labeled HUVECs (Green colour; Passage-6, 15k per cm^2) were then seeded onto the other film surface and co-cultured in EGM10 for further 3 days. **(A)** 3D construction of section-scanning CLSM images from DIC, Green and Red channels. Yellow colour represented the co-localisation of green and red colours. **(B)** Crossing-section view. Yellow colour distrusted not only around the green and/or red colour areas but also within each other (Scale bar = 20 μm).

Figure 6-12A shows the direct cell-cell contact between GFP-labeled HUVECs and PHK26-labeled MSCs. Direct cellular contact was found at 2 days of co-culturing. Pore number with positive cellular contact increased with increasing co-culturing

time. Quantitative analysis from pore counting of CLSM images exhibited that there was ~50 % of pores that occurred direct HUVECs-MSCs contact for 2 days of co-culturing, and ~84 % for 5 days of co-culturing (Figure 6-12B).

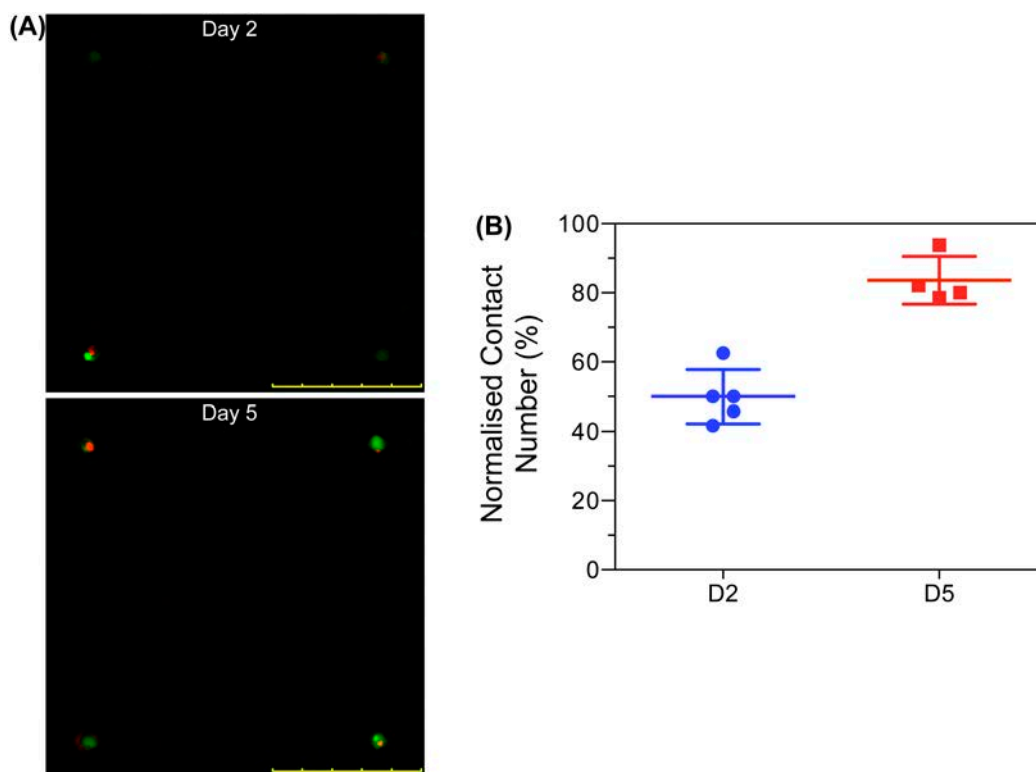


Figure 6-12: (A) CLSM images of cell-contact between GFP-labeled HUVECs (Green colour) and PHK26-labeled MSCs (Red colour) for 2 and 5 days of co-culture in EGM10 (Scale bar = 500 μ m). (B) Normalised pore number that occurred HUVECs-MSCs contact (n = 4).

Figure 6-13A shows the effects of direct cell-cell interaction on NO level of co-cultured system. Results exhibited that compared to EGM10, culturing of MSCs increased the total NO level ($p < 0.001$), while HUVECs declined the total NO level ($p < 0.01$). Co-culturing of MSCs and HUVECs through UX_{HP}-PCL resulted in reduced total NO level as compared to MSCs only ($p < 0.01$), but higher total NO level than that of HUVECs single-culture ($p < 0.05$). Interestingly, co-culture through PUX_{HP}-PCL resulted in significant increase in total NO level as compared to the single-culture of MSCs ($p < 0.01$) and/or HUVECs ($p < 0.01$) and co-culture via UX_{HP}-PCL

($p < 0.01$). Figure 6-13B shows the further effects of direct cell-cell interaction on HUVECs adhesion and proliferation. Results from cell nucleus counting exhibited that presence of MSCs reduced HUVECs adhesion as compared to that of HUVECs alone ($p < 0.05$). Presence of pores further reduced HUVECs adhesion. Compared to HUVECs alone, HUVECs adhesion at the presence of MSCs and pores (MSC/Pore: +/+) was lower than that of MSC/Pore: -/+ group ($p < 0.001$). After cellular proliferation for further 4 days, HUVECs in MSC/Pore: +/+ group exhibited much higher cell number as compared to both MSC/Pore: +/- (~27 % increase, $p < 0.001$) and MSC/Pore: -/+ (~17 % increase, $p < 0.001$) groups. Furthermore, HUVECs in MSC/Pore: +/- group continuously showed a lower cell number than that of MSC/Pore: -/+ group (~8 % reduction, $p < 0.001$).

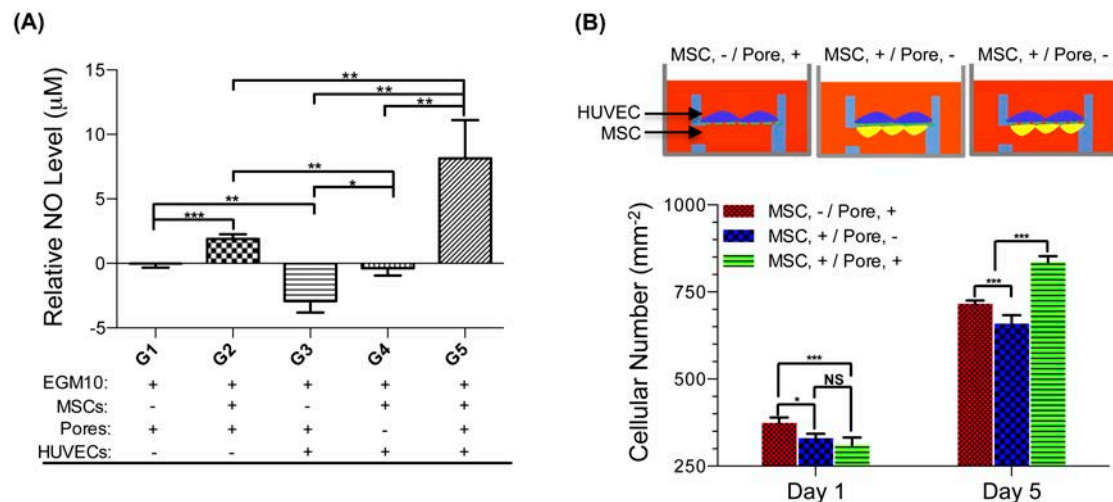


Figure 6-13: Influence of direct MSCs-HUVECs interaction. **(A)** Total system NO level. Direct cell-cell interaction increased the total NO level of HUVECs/MSCs co-culture system, while in-directed interaction declined the system total NO level ($n = 4$; *, $p < 0.05$; **, $p < 0.01$; ***, $p < 0.001$). **(B)** HUVECs adhesion and proliferation. Direct cell-cell interaction increased HUVECs proliferation as compared to that of co-culture system with in-direct cell-cell interaction and single-culture system ($n = 3$; *, $p < 0.05$; ***, $p < 0.001$; NS, $p > 0.05$).

6.4 Discussion

Geometric cues from soft-lithography, direct-laser-writing and electrospinning are inherently dense and lack of sufficient interconnected pores to facilitate mass transfer

and cell-cell interaction across the substrates, impeding their applications for vascular tissue regeneration. In this study, a novel PCL film with anisotropic ridge/groove arrays and micropore patterns were presented. Results showed that after femtosecond laser drilling, PUX_{HP}-PCL exhibited through-hole, with tunable position and diameter of pores. Compared to the control group, PUX_{HP}-PCL allowed nutrition diffusion across the PCL films for the enhanced MSCs adhesion and proliferation in D0. The presence of pores was found to interfere with the MSCs alignment. Cellular alignment efficiency was dependent on the pore-patterns, and non-reduced alignment efficiency could be achieved by controlling the inter-pore-distance. Furthermore, PUX_{HP}-PCL allowed direct HUVECs-MSCs contact, and resulted in an increase in the total NO level of co-culture system and HUVECs proliferation as compared to those of indirect interaction system, respectively.

The development of laser-assisted nano/micropatterning of polymer surfaces is a rapidly growing and developing field [135, 203, 278]. In femtosecond laser ablation, pulse energy has to be delivered with energy over than the binding energy of atoms for removing the atoms from bulk material [279]. Thus, pores were formed at the position where femtosecond laser beam interacted with the PCL film molecules. For polymeric materials, heat diffusion and energy loss of femtosecond laser beam are limited [135, 280]. Therefore, pore drilling of PUX_{HP}-PCL has been realised in a precise manner without severe thermal damage to the surrounding ridge/groove arrays. The melting effect was limited within the range of several micrometers. The melting was observed to form lip-like structures around the pores, and this phenomena probably due to the anisotropic residual stress from uniaxial stretching. During the drilling process, the residual stress at film surface lanced the melt and

pull them away from each other. This also explained the reason why laser drilling on HP-PCL and biaxial-stretched PCL films resulted in melts in a circular shape [135].

During the pores' perforation of PUX_{HP}-PCL, pulse energy E_{pulse} was observed to affect the diameter of femtosecond laser drilled pores. The pore diameter generally increased at a higher E_{pulse} as laser beam energy was in a Gaussian distribution [135]. The pore diameter and E_{pulse} followed in an approximate linear relationship during an E_{pulse} of 20-60 μJ , suggesting that the pore size could be properly tailored. Moreover, E_{pulse} determined whether the drilled pores were blind or through holes. In this study, the pores of PUX_{HP}-PCL (film thickness: $\sim 37.9 \mu\text{m}$) would become blind when E_{pulse} was less than 10 μJ . Because of the high energy of femtosecond laser pulse, previous study found that PCL films could be generated at a pulse number N_{pulse} of 2 [135]. Here, optimisation study further found that variation of N_{pulse} affected less on the pore diameter at both the film top and bottom surfaces. However, the ejection of melt tended to be reduced when N_{pulse} increased, suggesting that it would be preferable to perform femtosecond laser drilling at a higher N_{pulse} for less ejection generation.

While uniaxial stretching resulted in anisotropic ridge/groove, it simultaneously densified the PCL molecular chains, resulting in less hydrophilic permeability of UX_{HP}-PCL. Previously, perforated PCL films have been developed using a needle-operated robot [281]. However, the flaps that formed at the sites of needle punching tended to close when placed in a culturing medium [135]. Other techniques such as foaming and particulate leaching have also been used for pore generation, but have been found to exhibit limited inter-pore-connectivity [62]. Comparatively, the presenting technique using femtosecond laser drilling allowed the production of

through-hole. Because of the materials being removed, the flaps did not close when immersed in PBS and/or cell culture medium. Moreover, the FITC-dextran diffusion study demonstrated that PUX_{HP}-PCL had achieved enhanced hydrophilicity permeability, and was able to allow nutrition diffusion for MSCs growth in serum-free medium. Previously, ablation of femtosecond laser using a pre-fabricated stainless steel mask has been applied to perforate PCL films [135]. However, this method was time consuming, and due to the flexibility of PCL films, focusing of laser beam at a same height for all pores has become difficult, leading to un-homogeneous pore diameters in a large area. Furthermore, the using of mask made it become difficult if pores with different diameters and patterns were needed. In this work, femtosecond laser drilling at different pore sizes and positions was realised by simply adjusting the laser power and stage movement using a computer program. This method was mask-free, and allowed specific focus depths at certain pore positions as well as various pore patterns for different design requirements.

The combination of pore size in microscale and micropatterning for function-improved TE scaffolds has not been fully developed. One major reason was that the presence of pores was found to interfere the function of micropatterns to guide cellular organisation, in particularly for pores with diameters larger than 10 μm [40, 62, 282]. In this work, observations revealed how pores interfere cellular alignment along the geometric cues. On UX_{HP}-PCL, MSCs grew as an elongated and spindle-like shape. If cells on PUX_{HP}-PCL could extend freely, MSCs remained alignment in regardless of the pores. If one end of the cellular extension was obstructed, MSCs would conform partialy to the pore edges, and kept the left parts of cells remained in alignment along the ridges with the orientated F-actin cytoskeleton. If one cellular

extension end of MSCs was confined by pores, and meanwhile, the other extension ends contacted to other cells or surface features that were not in the ridge direction, MSCs would lose the alignment along ridge/groove arrays

Pores to interfere in cell alignment were found to be dependent on the inter-pore-distance. Edges of the substrate features have been proposed to facilitate cellular adhesion by acting as nucleation sites [212]. Here, MSCs on PUX_{HP}-PCL were also observed to distribute preferentially around the pores. Compared to pore patterns of X200Y200, the inter-pore-distance increased in either x or y direction resulted in more cells in the adjacent area of the pores. This could be attributed to the weakened attraction of pores to the cells [212]. Interestingly, although the inter-pore-distance for pore patterns of X200Y200 in the x and y axes were 200 μm (smaller than the length of elongated MSCs), MSCs have not been observed to anchor and bridge across the two adjacent pores in the y direction, suggesting that MSCs preferentially conformed to the ridge/groove arrays.

The interference of cellular alignment observed on different pore patterns of PUX_{HP}-PCL was explainable. A distance of 200 μm allowed MSCs to anchor at and bridge two adjacent pores in the x-axis. If cells were not able to extend over the pores along the ridges, they would adjust the extension direction and anchor at the other positions, resulting in a final cell extension deviating from ridges and a declined efficiency of cell alignment. An inter-pore-distance of 500 μm was sufficient to allow MSCs extension freely in the ridge directions and avoid cellular bridging of two adjacent pores. In addition, MSCs, although pores might confine their extension at one end, were able to crawl freely at the other extension end and retained alignment. These two

reasons explained why the alignment efficiency for MSCs on X500Y200 was larger than that on X200Y200. However, inter-pore-distance increase in the y-axis did not result in better MSCs alignment for pore patterns of X200Y500 as compared to that of X200Y200. This could be attributed to the more surrounded cell growth around the pores on PUX_{HP}-PCL for X200Y500. Such enhanced cellular growth could be due to the following two reasons: (i) reduced pore attraction in the y-axis direction, thus leading to more cells conforming to the ridge/groove arrays, and (ii) small inter-pore-distance in the x-axis direction, thus leading to confined cell extension. It was worth noting that compared to pore patterns of X500Y200, the inter-pore-distance increase in the y-axis direction resulted in increased cell alignment for pore patterns of X500Y500. This was probably because that the inter-pore-distance of 500 μm allowed MSCs to extend freely, and therefore, resulted in non-reduced efficiencies of cellular alignment as compared to positive control of UX_{HP}-PCL at cellular sub-confluence and confluence.

The design of PUX_{HP}-PCL has complex architectures consisting of anisotropic ridge/groove arrays and penetrated pore patterns in microscale. In Chapter 4, the alignment of MSCs on PCL ridge/groove arrays were found to couple with a contractile SMCs-like phenotype including spindle shapes, fewer but aligned cytoskeletal stress filaments, and up-regulated and orientated expression of SM- α -actin, calponin and SM-MCH filaments. In this work, PUX_{HP}-PCL with proper pore patterns such as X500Y500 retained MSCs alignment, which was similar to that on UX_{HP}-PCL. Meanwhile, the presence of pores enhanced the permeability of PCL films, and was sufficient to allow nutrition diffusion across the films for MSCs growth. All these suggested that PUX_{HP}-PCL was able to support MSCs growth,

forming aligned cellular organisation and differentiation towards a contractile phenotype as those observed in tunica media. Furthermore, MSCs on PUX_{HP}-PCL were found to contact via the pores with HUVECs on the opposite film surface. The observed colour dots superimposed with the other colour areas suggesting that MSCs and HUVECs did not just meet each other within the pores, but formed direct cell-cell interaction with complex interdigitated networks, resulting in up-regulated NO level of the co-culture system and increased HUVECs proliferation. Such findings suggested that PUX_{HP}-PCL through allowing direct cell-cell interaction could facilitate the endothelisation simultaneously and thus, was promising to act as an engineered BM for vascular tissue regeneration.

6.5 Summary

In this work, a combined method of uniaxial stretching and femtosecond laser drilling was used to generate complex PCL film architecture. PUX_{HP}-PCL consisted of anisotropic ridge/groove arrays and pore patterns. Drilling using femtosecond laser beam allowed perforative PCL films with regular pore shapes and tunable pore diameters and positions. Compared to UX_{HP}-PCL, PUX_{HP}-PCL exhibited an enhanced permeability of FITC-dextran, and allowed nutrition diffusion for increased cellular adhesion and proliferation. MSCs on PUX_{HP}-PCL aligned towards ridge/groove arrays following a manner depending on the pore patterns. Through fine-adjustment of pore distance, non-interfered MSCs alignment was achieved on PUX_{HP}-PCL as compared to that on UX_{HP}-PCL at sub-confluence and confluent status, respectively. PUX_{HP}-PCL allowed cell ingrowth into pores in three manners of "bridging", "sidewall depth" and "coverage", and facilitated MSCs-HUVECs interaction via direct cell-cell contact, leading to up-regulated total NO level of co-culture system

and increased HUVECs proliferation. This work demonstrates that multi-functional PCL films with anisotropic geometries and microporous patterns, could biomimic the complex architectures of vascular BM, and are promising for using as an engineered BM for the potential tunica media and lumen regeneration simultaneously. This work also suggests that a combination of uniaxial stretching and femtosecond laser drilling could be a suitable method for generating the complex film architectures for VTE application.

Chapter 7 Conclusions

Cardiovascular diseases are the leading cause of death worldwide, requiring surgical bypassing of effective vascular grafts to achieve good healing. However, current available vascular grafts cannot fulfill the clinical needs due to several significant drawbacks including the shortage of autografts, slow healing of allografts and xenografts, and poor long-term patency rates for small-diameter bypass grafting of synthetic grafts. Vascular tissue engineering (VTE) sets out to address the deficiency of effective vascular grafts. However, its further development has been beset. Current tissue-engineered vascular grafts (TEVG) cannot match the compliance of native vessels (e.g. distortion of ordered architecture, SMCs dedifferentiation, and poor endothelialisation). This project thus proposed a novel design for *de novo* TEVG through biomimicking the complex architecture of BM and using MSCs as an alternative cell source, and to realise the effective cell alignment, elevated differentiation of MSCs into a SMCs-like phenotype and rapid endothelialisation.

In the first part of this thesis, orientated ridge/groove arrays have been created on PCL thin films to biomimic the BM anisotropic architecture. PCL films after uniaxial stretching obtained 3D self-assembling micro-ridges and grooves that were highly orientated towards the stretching direction (angle variation: less than $\pm 1.56^\circ$) with homogeneous distribution of a large film area ($X_0 \rightarrow X_3$, Y_0 - Y_4 ; $\sim 2 \times 12 \text{ cm}^2$). The ridge/groove arrays allowed structural parameters (e.g. inter-ridge-distance and ridge-

length) to be varied by controlling the stretch temperature (T_s) and draw ratio (DR). The ridge/groove arrays further allowed modification of the desired surface properties (e.g. hydrolysis), while retaining the geometries intact. MSCs on stretched PCL films achieved an aligned organisation as cells arranged in tunica media. MSCs alignment was in a controllable direction and homogeneous over the film sample ($\sim 1 \times 1 \text{ cm}^2$), with significant increase in the cellular alignment efficiency ($>85 \%$) and elongation over a prolonged period (>2 weeks).

In the second part of this thesis, optimal PCL film was achieved for enhanced MSCs differentiation and TEVG scaffold construction. Uniaxial stretching was applied on various PCL films obtained via solvent casting, cast stretching and heat pressing. Among these films, uniaxial-stretched heat-pressed PCL (UX_{HP} -PCL) films showed the best mechanical properties, and the proper ridge-depth and inter-ridge-distance for the highest alignment efficiency of MSCs. Furthermore, UX_{HP} -PCL as compared to un-stretched films has achieved significant increase in yield stress (2.5x, $p < 0.001$), Yong's Modulus (2.1x, $p < 0.001$) and ultimate stress (2.6x, $p < 0.001$) with un-reduced elasticity. MSCs cultured on UX_{HP} -PCL showed a contractile SMCs-like phenotype, with up-regulated expressions of SM- α -actin, calponin and SM-MHC at protein and gene levels. UX_{HP} -PCL facilitated construction of small-diameter 3D vascular scaffolds, with a wall that allows the construction of orientated MSCs/PCL/MSCs multi-layers.

In the third part of this thesis, *in vitro* hydrolysis has been employed to evaluate the stability of UX_{HP} -PCL under erosive environment. UX_{HP} -PCL from uniaxial stretching obtained an enhanced stability against degradation, and experienced surface

erosion, with an overall geometries being retained even at ~45 % weight loss. Over the investigated period of degradation, UX_{HP}-PCL exhibited an "S-shape" behaviour of weight loss, more stable hydrophilicity and better retainment of mechanical properties than the un-stretched films. UX_{HP}-PCL could withstand up to ~20 % weight loss without causing reduction in cell alignment. At up to ~45 % weight loss, UX_{HP}-PCL could still retain increased cell alignment as compared to un-stretched PCL films. These findings represent the enhanced stability of UX_{HP}-PCL against erosive environment.

In the last part of this thesis, micropores have been further incorporated onto UX_{HP}-PCL (PUX_{HP}-PCL), to fully biomimic the complex architecture of BM. The pores drilled by femtosecond laser exhibited regular pore morphologies, and tunable pore sizes and positions. Compared to UX_{HP}-PCL, PUX_{HP}-PCL achieved an enhanced nutrient diffusion for MSCs proliferation. Through fine-adjustment of pore positions, un-interfered MSCs alignment has been obtained on PUX_{HP}-PCL at cellular sub-confluence and confluent status. PUX_{HP}-PCL supported MSCs ingrowth into pores and interaction with HUVECs on the opposite film surface via direct cell-cell contact, leading to up-regulated total NO level of the co-culture system and increased HUVECs proliferation.

This project explores the use of anisotropic geometric cues and micropore patterns to generate the engineered BM with demonstrated multi-functions, in incorporation of stem cells, for facilitating VTE applications. This work also provides two innovative techniques with benefits of reproducible, solvent-free and simple fabrication for applications in regenerative medicine.

Chapter 8 Future Work

This PhD project provided a novel strategy for *do novo* TEVG scaffold design, and has realised an engineered BM of PUX_{HP}-PCL to align and differentiate MSCs, and promote HUVECs proliferation. However, current research work remained limited on several specific aspects. Identification of these limitations may help the future work to be of great interest.

Recommendations for Uniaxial Stretching. There is a limited range for the inter-ridge-distance to be varied. The current variation could be from 6 to 17 μm , during which different sensing of MSCs might not be triggered. Further research work is required to systematically investigate the conditions (e.g. post annealing) that could affect the structural parameters generated from uniaxial stretching. This may enable multifaceted functions of UX_{HP}-PCL for not only the cellular alignment, but also allowing investigation of how cells adjust themselves towards the PCL topographical structures.

Recommendations for MSCs. UX_{HP}-PCL has differentiated MSCs with up-regulated expression of SMCs contractile markers. While both the ridge/groove arrays and film stiffness have been known to influence SMCs marker expression [28, 113], it is unknown how much each of them has contributed to promote MSCs differentiation. Further research work is needed to understand MSCs differentiation into SMCs on

micropatterned and flat surfaces for the same materials stiffness. This may reveal the intrinsic influence of geometric cues on MSCs differentiation, and the synergistic or antagonistic effects to those materials' stiffness.

Recommendations for *In Vivo* Degradation. The ridge/groove arrays of UX_{HP}-PCL have shown increased stability against erosive environment and capability of eliciting increased MSCs alignment even at ~45 % weigh loss. It is unknown whether UX_{HP}-PCL *in vivo* could present similar performances. This is because that experiments *in vitro* were performed using the direct cell seeding on the degraded UX_{HP}-PCL, and avoided the influence from degradation by-products, pH changes, mechanical flow, and various biochemical factors and cells. Further research work is needed to perform *in vivo* degradation study of UX_{HP}-PCL. This should help to understand the *in vivo* degradation behaviour of UX_{HP}-PCL, and may reveal better vascular tissue remodeling due to the surface erosion manner and ordered cell organisation.

Recommendations for Mechanical Compliance. It is unknown whether micropore patterns of PUX_{HP}-PCL can provide better compliance for TEVG scaffolds in regards to the mechanical matching. For VTE applications, grafts should be able to withstand a high physiological pressure and have mechanical properties close to those of human arteries (burst pressure: >2000 mmHg) [191]. Further research work is required to systematically investigate how micropore patterns influence PUX_{HP}-PCL mechanical properties. This would offer better understanding on the relationship between film mechanical properties and pore parameters (e.g. pore size, diameter and number around the circumference), facilitating the tailorable mechanical properties of PUX_{HP}-PCL for better vascular compliance.

Recommendations for PUX_{HP}-PCL. Future work with PUX_{HP}-PCL should not be limited to VTE. In human body, almost all-important tissues consist of highly ordered anisotropic organisation: the skins, bone, ligament, tendon, nerves, skeletal muscle, heart and vascular vessels [157]. Future work can use PUX_{HP}-PCL as the basic "unit" to engineer more complex TE scaffolds for various tissue regeneration such as rolling for TEVG, ligament, tendon and bone applications, and layer-by-layer stacking for skin, skeletal, and cardiac and smooth muscles. Anisotropic ridge/groove arrays could serve as cues for guiding the ordered architecture reconstruction, while microporous patterns support the transportation of nutrient/oxygen, cell-cell interaction, and tissue ingrowth with neovascularisation. A new concept of anisotropic tissue engineering (aTE) should be proposed for defining the important features of these applications.

References

- [1] Cardiovascular diseases (CVDs). World Health Organization; 2013.
- [2] Zorlutuna P, Vadgama P, Hasirci V. Both sides nanopatterned tubular collagen scaffolds as tissue-engineered vascular grafts. *Journal of tissue engineering and regenerative medicine*. 2010;4:628-37.
- [3] Zorlutuna P, Elsheikh A, Hasirci V. Nanopatterning of Collagen Scaffolds Improve the Mechanical Properties of Tissue Engineered Vascular Grafts. *Biomacromolecules*. 2009;10:814-21.
- [4] Hu J, Sun X, Ma H, Xie C, Chen YE, Ma PX. Porous nanofibrous PLLA scaffolds for vascular tissue engineering. *Biomaterials*. 2010;31:7971-7.
- [5] Stehouwer CDA, Clement D, Davidson C, Diehm C, Elte JW, Lambert M, et al. Peripheral arterial disease: A growing problem for the internist. *Eur J Intern Med*. 2009;20:132-8.
- [6] By 2030, cardiovascular disease and death rates in China will surge. American Heart Association; 2010.
- [7] Hill R, Bagust A, Bakhai A, Dickson R, Dunder Y, Haycox A, et al. Coronary artery stents: a rapid systematic review and economic evaluation. *Health Technol Asses*. 2004;8:1-+.
- [8] Chlupac J, Filova E, Bacakova L. Blood Vessel Replacement: 50 years of Development and Tissue Engineering Paradigms in Vascular Surgery. *Physiol Res*. 2009;58:S119-S39.
- [9] Liliensiek SJ, Nealey P, Murphy CJ. Characterization of Endothelial Basement Membrane Nanotopography in Rhesus Macaque as a Guide for Vessel Tissue Engineering. *Tissue Eng Pt A*. 2009;15:2643-51.
- [10] Gong Z, Niklason LE. Small-diameter human vessel wall engineered from bone marrow-derived mesenchymal stem cells (hMSCs). *FASEB journal : official publication of the Federation of American Societies for Experimental Biology*. 2008;22:1635-48.
- [11] Arrigoni C, Camozzi D, Remuzzi A. Vascular tissue engineering. *Cell transplantation*. 2006;15:S119-S25.

- [12] Thomas AC, Campbell GR, Campbell JH. Advances in vascular tissue engineering. *Cardiovasc Pathol*. 2003;12:271-6.
- [13] Swenne CL, Borowiec J, Carlsson M, Lindholm C. Prediction of and risk factors for surgical wound infection in the saphenous vein harvesting leg in patients undergoing coronary artery bypass. *Thorac Cardiovasc Surg*. 2006;54:300-6.
- [14] Cleary MA, Geiger E, Grady C, Best C, Naito Y, Breuer C. Vascular tissue engineering: the next generation. *Trends Mol Med*. 2012;18:394-404.
- [15] Naito Y, Shinoka T, Duncan D, Hibino N, Solomon D, Cleary M, et al. Vascular tissue engineering: Towards the next generation vascular grafts. *Adv Drug Deliver Rev*. 2011;63:312-23.
- [16] Zhang WJ, Liu W, Cui L, Cao YL. Tissue engineering of blood vessel. *Journal of cellular and molecular medicine*. 2007;11:945-57.
- [17] Woodruff MA, Hutmacher DW. The return of a forgotten polymer-Polycaprolactone in the 21st century. *Prog Polym Sci*. 2010;35:1217-56.
- [18] Zhang ZY, Teoh SH, Chong MSK, Lee ESM, Tan LG, Mattar CN, et al. Neo-vascularization and bone formation mediated by fetal mesenchymal stem cell tissue-engineered bone grafts in critical-size femoral defects. *Biomaterials*. 2010;31:608-20.
- [19] Rai B, Oest ME, Dupont KM, Ho KH, Teoh SH, Guldborg RE. Combination of platelet-rich plasma with polycaprolactone-tricalcium phosphate scaffolds for segmental bone defect repair. *J Biomed Mater Res A*. 2007;81A:888-99.
- [20] Chong MSK, Chan J, Choolani M, Lee CN, Teoh SH. Development of cell-selective films for layered co-culturing of vascular progenitor cells. *Biomaterials*. 2009;30:2241-51.
- [21] Chong MSK, Teoh SH, Teo EY, Zhang ZY, Lee CN, Koh S, et al. Beyond Cell Capture: Antibody Conjugation Improves Hemocompatibility for Vascular Tissue Engineering Applications. *Tissue Engineering Part A*. 2010;16:2485-95.
- [22] Iwasaki K, Kojima K, Kodama S, Paz AC, Chambers M, Umezu M, et al. Bioengineered three-layered robust and elastic artery using hemodynamically-equivalent pulsatile bioreactor. *Circulation*. 2008;118:S52-S7.
- [23] Woei K, Hutmacher DW, Schantz JT, Seng C, Too HP, Chye T, et al. Evaluation of ultra-thin poly(epsilon-caprolactone) films for tissue-engineered skin. *Tissue Engineering*. 2001;7:441-55.
- [24] Chung TW, Yang MC, Tseng CC, Sheu SH, Wang SS, Huang YY, et al. Promoting regeneration of peripheral nerves in-vivo using new PCL-NGF/Tirofiban nerve conduits. *Biomaterials*. 2011;32:734-43.
- [25] Noishiki Y, Yamane Y, Okoshi T, Tomizawa Y, Satoh S. Choice, isolation, and preparation of cells for bioartificial vascular grafts. *Artificial organs*. 1998;22:50-62.

- [26] Huang NF, Li S. Mesenchymal stem cells for vascular regeneration. *Regenerative medicine*. 2008;3:877-92.
- [27] Manson RJ, Unger JM, Ali A, Gage SM, Lawson JH. Tissue-Engineered Vascular Grafts: Autologous Off-the-Shelf Vascular Access? *Semin Nephrol*. 2012;32:582-91.
- [28] Williams C, Brown XQ, Bartolak-Suki E, Ma HW, Chilkoti A, Wong JY. The use of micropatterning to control smooth muscle myosin heavy chain expression and limit the response to transforming growth factor beta 1 in vascular smooth muscle cells. *Biomaterials*. 2011;32:410-8.
- [29] Stegemann JP, Hong H, Nerem RM. Mechanical, biochemical, and extracellular matrix effects on vascular smooth muscle cell phenotype. *J Appl Physiol*. 2005;98:2321-7.
- [30] Magro CM, Calomeni EP, Nadasdy T, Shusterman BD, Pope-Harman AL, Ross P. Ultrastructure as a diagnostic adjunct in the evaluation of lung allograft biopsies. *Ultrastruct Pathol*. 2005;29:95-106.
- [31] *Blood Vessels and Circulation*. University of Miami; 2013.
- [32] Stegemann JP, Kaszuba SN, Rowe SL. Review: Advances in vascular tissue engineering using protein-based Biomaterials. *Tissue engineering*. 2007;13:2601-13.
- [33] Chuang TW, Masters KS. Regulation of polyurethane hemocompatibility and endothelialization by tethered hyaluronic acid oligosaccharides. *Biomaterials*. 2009;30:5341-51.
- [34] Chong MS, Teoh SH, Teo EY, Zhang ZY, Lee CN, Koh S, et al. Beyond cell capture: antibody conjugation improves hemocompatibility for vascular tissue engineering applications. *Tissue engineering Part A*. 2010;16:2485-95.
- [35] Topper JN, Cai JX, Falb D, Gimbrone MA. Identification of vascular endothelial genes differentially responsive to fluid mechanical stimuli: Cyclooxygenase-2, manganese superoxide dismutase, and endothelial cell nitric oxide synthase are selectively up-regulated by steady laminar shear stress. *Proceedings of the National Academy of Sciences of the United States of America*. 1996;93:10417-22.
- [36] Deutsch M, Meinhart J, Fischlein T, Preiss P, Zilla P. Clinical autologous in vitro endothelialization of infrainguinal ePTFE grafts in 100 patients: A 9-year experience. *Surgery*. 1999;126:847-55.
- [37] Wagenseil JE, Mecham RP. Vascular Extracellular Matrix and Arterial Mechanics. *Physiol Rev*. 2009;89:957-89.
- [38] O'connell MK, Murthy S, Phan S, Xu C, Buchanan J, Spilker R, et al. The three-dimensional micro- and nanostructure of the aortic medial lamellar unit measured using 3D confocal and electron microscopy imaging. *Matrix Biol*. 2008;27:171-81.
- [39] L. BC, E. GS, F. RJ. Static mechanical properties of the developing and mature rat aorta. *Cardiovascular research*. 1975;9:10.

- [40] Sarkar S, Lee GY, Wong JY, Desai TA. Development and characterization of a porous micro-patterned scaffold for vascular tissue engineering applications. *Biomaterials*. 2006;27:4775-82.
- [41] Blit PH, Battiston KG, Yang ML, Santerre JP, Woodhouse KA. Electrospun elastin-like polypeptide enriched polyurethanes and their interactions with vascular smooth muscle cells. *Acta biomaterialia*. 2012;8:2493-503.
- [42] Park JS, Chu JSF, Cheng C, Chen FQ, Chen D, Li S. Differential effects of equiaxial and uniaxial strain on mesenchymal stem cells. *Biotechnology and bioengineering*. 2004;88:359-68.
- [43] Williams C, Xie AW, Yamato M, Okano T, Wong JY. Stacking of aligned cell sheets for layer-by-layer control of complex tissue structure. *Biomaterials*. 2011;32:5625-32.
- [44] Bujan J, Garcia-Honduvilla N, Bellon JM. Engineering conduits to resemble natural vascular tissue. *Biotechnol Appl Bioc*. 2004;39:17-27.
- [45] Beghi C, Nicolini F, Budillon AM, Borrello B, Ballore L, Reverberi C, et al. Midterm clinical results in myocardial revascularization using the radial artery. *Chest*. 2002;122:2075-9.
- [46] Sarjeant JM, Rabinovitch M. Understanding and treating vein graft atherosclerosis. *Cardiovasc Pathol*. 2002;11:263-71.
- [47] Johnson WC, Lee KK, Study DVAC. A comparative evaluation of polytetrafluoroethylene, umbilical vein, and saphenous vein bypass grafts for femoral-popliteal above-knee revascularization: A prospective randomized Department of Veterans Affairs cooperative study. *J Vasc Surg*. 2000;32:268-77.
- [48] Kieffer E, Gomes D, Chiche L, Fleron MH, Koskas F, Bahnini A. Allograft replacement for infrarenal aortic graft infection: Early and late results in 179 patients. *J Vasc Surg*. 2004;39:1009-17.
- [49] Schmidt CE, Baier JM. Acellular vascular tissues: natural biomaterials for tissue repair and tissue engineering. *Biomaterials*. 2000;21:2215-31.
- [50] Katzman HE, Glickman MH, Schild AF, Fujitani RM, Lawson JH. Multicenter evaluation of the bovine mesenteric vein bioprostheses for Hemodialysis access in patients with an earlier failed prosthetic graft. *J Am Coll Surgeons*. 2005;201:223-30.
- [51] Pascual G, Jurado F, Rodriguez M, Corrales C, Lopez-Hervas P, Bellon JM, et al. The use of ischaemic vessels as prostheses or tissue engineering scaffolds after cryopreservation. *Eur J Vasc Endovasc*. 2002;24:23-30.
- [52] Xue L, Greisler HP. Biomaterials in the development and future of vascular grafts. *J Vasc Surg*. 2003;37:472-80.
- [53] Lemson MS, Tordoir JHM, Daemen MJAP, Kitslaar PJEHM. Intimal hyperplasia in vascular grafts. *Eur J Vasc Endovasc*. 2000;19:336-50.

- [54] Glickman MH, Stokes GK, Ross JR, Schuman ED, Sternbergh WC, Lindberg JS, et al. Multicenter evaluation of a polyurethaneurea vascular access graft as compared with the expanded polytetrafluoroethylene vascular access graft in hemodialysis applications. *J Vasc Surg.* 2001;34:465-72.
- [55] Qin H, Ishiwata T, Wang R, Kudo M, Yokoyama M, Naito Z, et al. Effects of extracellular matrix on phenotype modulation and MAPK transduction of rat aortic smooth muscle cells in vitro. *Exp Mol Pathol.* 2000;69:79-90.
- [56] Beamish JA, He P, Kottke-Marchant K, Marchant RE. Molecular regulation of contractile smooth muscle cell phenotype: implications for vascular tissue engineering. *Tissue engineering Part B, Reviews.* 2010;16:467-91.
- [57] Narita Y, Yamawaki A, Kagami H, Ueda M, Ueda Y. Effects of transforming growth factor-beta 1 and ascorbic acid on differentiation of human bone-marrow-derived mesenchymal stem cells into smooth muscle cell lineage. *Cell and tissue research.* 2008;333:449-59.
- [58] Daculsi R, Remy-Zolghadri M, Grellier M, Conrad V, Fernandez P, Bareille R, et al. Signal transduction and procoagulant state of human cord blood-progenitor-derived endothelial cells after interleukin-1 alpha stimulation. *Endothelium-J Endoth.* 2007;14:163-71.
- [59] Liu WF. Mechanical regulation of cellular phenotype: implications for vascular tissue regeneration. *Cardiovascular research.* 2012;95:215-+.
- [60] Kurpinski K, Chu J, Hashi C, Li S. Anisotropic mechanosensing by mesenchymal stem cells. *Proceedings of the National Academy of Sciences of the United States of America.* 2006;103:16095-100.
- [61] Thakar RG, Ho F, Huang NF, Liepmann D, Li S. Regulation of vascular smooth muscle cells by micropatterning. *Biochemical and biophysical research communications.* 2003;307:883-90.
- [62] Papenburg BJ, Vogelaar L, Bolhuis-Versteeg LAM, Lammertink RGH, Stamatialis D, Wessling M. One-step fabrication of porous micropatterned scaffolds to control cell behavior. *Biomaterials.* 2007;28:1998-2009.
- [63] Iivanainen E, Kahari VM, Heino J, Elenius K. Endothelial cell-matrix interactions. *Microsc Res Techniq.* 2003;60:13-22.
- [64] Kalluri R. Basement membranes: Structure, assembly and role in tumour angiogenesis. *Nat Rev Cancer.* 2003;3:422-33.
- [65] Dockery P, Khalid J, Sarani SA, Bulut HE, Warren MA, Li TC, et al. Changes in basement membrane thickness in the human endometrium during the luteal phase of the menstrual cycle. *Hum Reprod Update.* 1998;4:486-95.
- [66] Lutter S, Xie S, Tatin F, Makinen T. Smooth muscle-endothelial cell communication activates Reelin signaling and regulates lymphatic vessel formation. *J Cell Biol.* 2012;197:837-49.

- [67] Hudson BG, Reeders ST, Tryggvason K. Type-IV Collagen - Structure, Gene Organization, and Role in Human-Diseases - Molecular-Basis of Goodpasture and Alport Syndromes and Diffuse Leiomyomatosis. *Journal of Biological Chemistry*. 1993;268:26033-6.
- [68] Scheppke L, Murphy EA, Zarpellon A, Hofmann JJ, Merkulova A, Shields DJ, et al. Notch promotes vascular maturation by inducing integrin-mediated smooth muscle cell adhesion to the endothelial basement membrane. *Blood*. 2012;119:2149-58.
- [69] Bou-Gharios G, Ponticos M, Rajkumar V, Abraham D. Extra-cellular matrix in vascular networks. *Cell proliferation*. 2004;37:207-20.
- [70] Hallmann R, Horn N, Selg M, Wendler O, Pausch F, Sorokin LM. Expression and function of laminins in the embryonic and mature vasculature. *Physiol Rev*. 2005;85:979-1000.
- [71] Durbeej M, Campbell KP. Muscular dystrophies involving the dystrophin-glycoprotein complex: an overview of current mouse models. *Curr Opin Genet Dev*. 2002;12:349-61.
- [72] Hultgardh-Nilsson A, Durbeej M. Role of the extracellular matrix and its receptors in smooth muscle cell function: implications in vascular development and disease. *Curr Opin Lipidol*. 2007;18:540-5.
- [73] Kanie K, Narita Y, Zhao Y, Kuwabara F, Satake M, Honda S, et al. Collagen type IV-specific tripeptides for selective adhesion of endothelial and smooth muscle cells. *Biotechnology and bioengineering*. 2012;109:1808-16.
- [74] Tsai SH, Liu YW, Tang WC, Zhou ZW, Hwang CY, Hwang GY, et al. Characterization of porcine arterial endothelial cells cultured on amniotic membrane, a potential matrix for vascular tissue engineering. *Biochemical and biophysical research communications*. 2007;357:984-90.
- [75] Mathews A, Columbus S, Krishnan VK, Krishnan LK. Vascular tissue construction on poly(ϵ -caprolactone) scaffolds by dynamic endothelial cell seeding: effect of pore size. *Journal of tissue engineering and regenerative medicine*. 2012;6:451-61.
- [76] Schaner PJ, Martin ND, Tulenko TN, Shapiro IM, Tarola NA, Leichter RF, et al. Decellularized vein as a potential scaffold for vascular tissue engineering. *J Vasc Surg*. 2004;40:146-53.
- [77] Dahan N, Zerbiv G, Sarig U, Karam T, Hoffman A, Machluf M. Porcine Small Diameter Arterial Extracellular Matrix Supports Endothelium Formation and Media Remodeling Forming a Promising Vascular Engineered Biograft. *Tissue Eng Pt A*. 2012;18:411-22.
- [78] Matsumura G, Miyagawa-Tomita S, Shin'oka T, Ikada Y, Kurosawa H. First evidence that bone marrow cells contribute to the construction of tissue-engineered vascular autografts in vivo. *Circulation*. 2003;108:1729-34.

- [79] Rosenman JE, Kempczinski RF, Pearce WH, Silberstein EB. Kinetics of Endothelial-Cell Seeding. *J Vasc Surg.* 1985;2:778-84.
- [80] Roh JD, Sawh-Martinez R, Brennan MP, Jay SM, Devine L, Rao DA, et al. Tissue-engineered vascular grafts transform into mature blood vessels via an inflammation-mediated process of vascular remodeling. *Proceedings of the National Academy of Sciences of the United States of America.* 2010;107:4669-74.
- [81] Mirza A, Hyvelin JM, Rochefort GY, Lermusianx P, Antier D, Awede B, et al. Undifferentiated mesenchymal stem cells seeded on a vascular prosthesis contribute to the restoration of a physiologic vascular wall. *J Vasc Surg.* 2008;47:1313-21.
- [82] Stegemann JP, Dey NB, Lincoln TM, Nerem RM. Genetic modification of smooth muscle cells to control phenotype and function in vascular tissue engineering. *Tissue engineering.* 2004;10:189-99.
- [83] Riha GM, Lin PH, Lumsden AB, Yao QZ, Chen CY. Application of stem cells for vascular tissue engineering. *Tissue engineering.* 2005;11:1535-52.
- [84] Krawiec JT, Vorp DA. Adult stem cell-based tissue engineered blood vessels: A review. *Biomaterials.* 2012;33:3388-400.
- [85] Huang NF, Li S. Mesenchymal stem cells for vascular regeneration. *Regenerative medicine.* 2008;3:877-92.
- [86] Pittenger MF, Mackay AM, Beck SC, Jaiswal RK, Douglas R, Mosca JD, et al. Multilineage potential of adult human mesenchymal stem cells. *Science.* 1999;284:143-7.
- [87] Wang C, Yin S, Cen L, Liu Q, Liu W, Cao Y, et al. Differentiation of adipose-derived stem cells into contractile smooth muscle cells induced by transforming growth factor-beta1 and bone morphogenetic protein-4. *Tissue engineering Part A.* 2010;16:1201-13.
- [88] Moby V, Labrude P, Kadi A, Bordenave L, Stoltz JF, Menu P. Polyelectrolyte multilayer film and human mesenchymal stem cells: An attractive alternative in vascular engineering applications. *J Biomed Mater Res A.* 2011;96A:313-9.
- [89] Wu W, Allen R, Gao J, Wang YD. Artificial Niche Combining Elastomeric Substrate and Platelets Guides Vascular Differentiation of Bone Marrow Mononuclear Cells. *Tissue Eng Pt A.* 2011;17:1979-92.
- [90] He W, Nieponice A, Soletti L, Hong Y, Gharaibeh B, Crisan M, et al. Pericyte-based human tissue engineered vascular grafts. *Biomaterials.* 2010;31:8235-44.
- [91] Finney MR, Greco NJ, Haynesworth SE, Martin JM, Hedrick DP, Swan JZ, et al. Direct comparison of umbilical cord blood versus bone marrow-derived endothelial precursor cells in mediating neovascularization in response to vascular ischemia. *Biol Blood Marrow Tr.* 2006;12:585-93.

- [92] Tse WT, Pendleton JD, Beyer WM, Egalka MC, Guinan EC. Suppression of allogeneic T-cell proliferation by human marrow stromal cells: Implications in transplantation. *Transplantation*. 2003;75:389-97.
- [93] Le Blanc K, Tammik C, Rosendahl K, Zetterberg E, Ringden O. HLA expression and immunologic properties of differentiated and undifferentiated mesenchymal stem cells. *Exp Hematol*. 2003;31:890-6.
- [94] Hashi CK, Zhu YQ, Yang GY, Young WL, Hsiao BS, Wang K, et al. Antithrombogenic property of bone marrow mesenchymal stem cells in nanofibrous vascular grafts. *Proceedings of the National Academy of Sciences of the United States of America*. 2007;104:11915-20.
- [95] Mariani E, Facchini A. Clinical Applications and Biosafety of Human Adult Mesenchymal Stem Cells. *Curr Pharm Design*. 2012;18:1821-45.
- [96] Gong ZD, Niklason LE. Small-diameter human vessel wall engineered from bone marrow-derived mesenchymal stem cells (hMSCs). *Faseb Journal*. 2008;22:1635-48.
- [97] Wang C, Cen L, Yin S, Liu Q, Liu W, Cao Y, et al. A small diameter elastic blood vessel wall prepared under pulsatile conditions from polyglycolic acid mesh and smooth muscle cells differentiated from adipose-derived stem cells. *Biomaterials*. 2010;31:621-30.
- [98] Zhang L, Zhou JY, Lu QP, Wei YJ, Hu SS. A novel small-diameter vascular graft: In vivo behavior of biodegradable three-layered tubular scaffolds. *Biotechnology and bioengineering*. 2008;99:1007-15.
- [99] Zhao YL, Zhang S, Zhou JY, Wang JL, Zhen MC, Liu Y, et al. The development of a tissue-engineered artery using decellularized scaffold and autologous ovine mesenchymal stem cells. *Biomaterials*. 2010;31:296-307.
- [100] Rodriguez LV, Alfonso Z, Zhang R, Leung J, Wu B, Ignarro LJ. Clonogenic multipotent stem cells in human adipose tissue differentiate into functional smooth muscle cells. *Proceedings of the National Academy of Sciences of the United States of America*. 2006;103:12167-72.
- [101] Kern S, Eichler H, Stoeve J, Kluter H, Bieback K. Comparative analysis of mesenchymal stem cells from bone marrow, umbilical cord blood, or adipose tissue. *Stem Cells*. 2006;24:1294-301.
- [102] Rebelatto CK, Aguiar AM, Moretao MP, Senegaglia AC, Hansen P, Barchiki F, et al. Dissimilar differentiation of mesenchymal stem cells from bone marrow, umbilical cord blood, and adipose tissue. *Exp Biol Med*. 2008;233:901-13.
- [103] Su ZY, Li Y, Zhao XL, Zhang M. All-trans retinoic acid promotes smooth muscle cell differentiation of rabbit bone marrow-derived mesenchymal stem cells. *J Zhejiang Univ-Sc B*. 2010;11:489-96.

- [104] Lee MR, Kwon KW, Jung H, Kim HN, Suh KY, Kim K, et al. Direct differentiation of human embryonic stem cells into selective neurons on nanoscale ridge/groove pattern arrays. *Biomaterials*. 2010;31:4360-6.
- [105] Oswald J, Boxberger S, Jorgensen B, Feldmann S, Ehninger G, Bornhauser M, et al. Mesenchymal stem cells can be differentiated into endothelial cells in vitro. *Stem Cells*. 2004;22:377-84.
- [106] Boyd NL, Nunes SS, Jokinen JD, Krishnan L, Chen YL, Smith KH, et al. Microvascular Mural Cell Functionality of Human Embryonic Stem Cell-Derived Mesenchymal Cells. *Tissue Eng Pt A*. 2011;17:1537-48.
- [107] Kurpinski K, Lam H, Chu JL, Wang AJ, Kim A, Tsay E, et al. Transforming Growth Factor-beta and Notch Signaling Mediate Stem Cell Differentiation into Smooth Muscle Cells. *Stem Cells*. 2010;28:734-42.
- [108] Tamama K, Sen CK, Wells A. Differentiation of Bone Marrow Mesenchymal Stem Cells into the Smooth Muscle Lineage by Blocking ERK/MAPK Signaling Pathway. *Stem cells and development*. 2008;17:897-908.
- [109] Giddens DP, Zarins CK, Glagov S. The Role of Fluid-Mechanics in the Localization and Detection of Atherosclerosis. *J Biomech Eng-T Asme*. 1993;115:588-94.
- [110] Kurpinski K, Park J, Thakar RG, Li S. Regulation of vascular smooth muscle cells and mesenchymal stem cells by mechanical strain. *Molecular & cellular biomechanics : MCB*. 2006;3:21-34.
- [111] Kobayashi N, Yasu T, Ueba H, Sata M, Hashimoto S, Kuroki M, et al. Mechanical stress promotes the expression of smooth muscle-like properties in marrow stromal cells. *Exp Hematol*. 2004;32:1238-45.
- [112] Wang H, Riha GM, Yan SY, Li M, Chai H, Yang H, et al. Shear stress induces endothelial differentiation from a murine embryonic mesenchymal progenitor cell line. *Arterioscl Throm Vas*. 2005;25:1817-23.
- [113] Park JS, Chu JS, Tsou AD, Diop R, Tang ZY, Wang AJ, et al. The effect of matrix stiffness on the differentiation of mesenchymal stem cells in response to TGF-beta. *Biomaterials*. 2011;32:3921-30.
- [114] Wang PY, Yu J, Lin JH, Tsai WB. Modulation of alignment, elongation and contraction of cardiomyocytes through a combination of nanotopography and rigidity of substrates. *Acta biomaterialia*. 2011;7:3285-93.
- [115] Cao Y, Poon YF, Feng J, Rayatpisheh S, Chan V, Chan-Park MB. Regulating orientation and phenotype of primary vascular smooth muscle cells by biodegradable films patterned with arrays of microchannels and discontinuous microwalls. *Biomaterials*. 2010;31:6228-38.
- [116] Boon RA, Leyen TA, Fontijn RD, Fledderus JO, Baggen JMC, Volger OL, et al. KLF2-induced actin shear fibers control both alignment to flow and JNK signaling in vascular endothelium. *Blood*. 2010;115:2533-42.

- [117] Flaibani M, Boldrin L, Cimetta E, Piccoli M, De Coppi P, Elvassore N. Muscle Differentiation and Myotubes Alignment Is Influenced by Micropatterned Surfaces and Exogenous Electrical Stimulation. *Tissue Eng Pt A*. 2009;15:2447-57.
- [118] Li D, Xia YN. Electrospinning of nanofibers: Reinventing the wheel? *Adv Mater*. 2004;16:1151-70.
- [119] Lanfer B, Hermann A, Kirsch M, Freudenberg U, Reuner U, Werner C, et al. Directed Growth of Adult Human White Matter Stem Cell-Derived Neurons on Aligned Fibrillar Collagen. *Tissue Eng Pt A*. 2010;16:1103-13.
- [120] Sun JR, Ding YF, Lin NJ, Zhou J, Ro H, Soles CL, et al. Exploring Cellular Contact Guidance Using Gradient Nanogratings. *Biomacromolecules*. 2010;11:3067-72.
- [121] Yeong WY, Yu HY, Lim KP, Ng KLG, Boey YCF, Subbu VS, et al. Multiscale Topological Guidance for Cell Alignment via Direct Laser Writing on Biodegradable Polymer. *Tissue Eng Part C-Me*. 2010;16:1011-21.
- [122] Shimizu K, Fujita H, Nagamori E. Alignment of Skeletal Muscle Myoblasts and Myotubes Using Linear Micropatterned Surfaces Ground With Abrasives. *Biotechnology and bioengineering*. 2009;103:631-8.
- [123] Xu CY, Inai R, Kotaki M, Ramakrishna S. Aligned biodegradable nanotibrous structure: a potential scaffold for blood vessel engineering. *Biomaterials*. 2004;25:877-86.
- [124] Baker BM, Gee AO, Metter RB, Nathan AS, Marklein RA, Burdick JA, et al. The potential to improve cell infiltration in composite fiber-aligned electrospun scaffolds by the selective removal of sacrificial fibers. *Biomaterials*. 2008;29:2348-58.
- [125] Li D, Wang YL, Xia YN. Electrospinning nanofibers as uniaxially aligned arrays and layer-by-layer stacked films. *Adv Mater*. 2004;16:361-6.
- [126] Wang ZY, Teo EY, Chong MS, Zhang QY, Lim J, Zhang ZY, et al. Biomimetic Three-Dimensional Anisotropic Geometries by Uniaxial Stretch of Poly(ϵ -Caprolactone) Films for Mesenchymal Stem Cell Proliferation, Alignment, and Myogenic Differentiation. *Tissue engineering Part C, Methods*. 2013;19:538-49.
- [127] Sill TJ, von Recum HA. Electro spinning: Applications in drug delivery and tissue engineering. *Biomaterials*. 2008;29:1989-2006.
- [128] Lanfer B, Freudenberg U, Zimmermann R, Stamov D, Korber V, Werner C. Aligned fibrillar collagen matrices obtained by shear flow deposition. *Biomaterials*. 2008;29:3888-95.
- [129] Roach P, Parker T, Gadegaard N, Alexander MR. Surface strategies for control of neuronal cell adhesion: A review. *Surf Sci Rep*. 2010;65:145-73.

- [130] Karuri NW, Liliensiek S, Teixeira AI, Abrams G, Campbell S, Nealey PF, et al. Biological length scale topography enhances cell-substratum adhesion of human corneal epithelial cells. *J Cell Sci.* 2004;117:3153-64.
- [131] Xie JW, MacEwan MR, Li XR, Sakiyama-Elbert SE, Xia YN. Neurite Outgrowth on Nanofiber Scaffolds with Different Orders, Structures, and Surface Properties. *ACS Nano.* 2009;3:1151-9.
- [132] Lu Y, Chen SC. Micro and nano-fabrication of biodegradable polymers for drug delivery. *Adv Drug Deliver Rev.* 2004;56:1621-33.
- [133] Ferrari A, Faraci P, Cecchini M, Beltram F. The effect of alternative neuronal differentiation pathways on PC12 cell adhesion and neurite alignment to nanogratings. *Biomaterials.* 2010;31:2565-73.
- [134] Hwang SY, Kwon KW, Jang KJ, Park MC, Lee JS, Suh KY. Adhesion Assays of Endothelial Cells on Nanopatterned Surfaces within a Microfluidic Channel. *Anal Chem.* 2010;82:3016-22.
- [135] Tiaw KS, Goh SW, Hong M, Wang Z, Lan B, Teoh SH. Laser surface modification of poly(epsilon-caprolactone) (PCL) membrane for tissue engineering applications. *Biomaterials.* 2005;26:763-9.
- [136] Bozkurt A, Deumens R, Beckmann C, Damink LO, Schugner F, Heschel I, et al. In vitro cell alignment obtained with a Schwann cell enriched microstructured nerve guide with longitudinal guidance channels. *Biomaterials.* 2009;30:169-79.
- [137] Tocce EJ, Smirnov VK, Kibalov DS, Liliensiek SJ, Murphy CJ, Nealey PF. The ability of corneal epithelial cells to recognize high aspect ratio nanostructures. *Biomaterials.* 2010;31:4064-72.
- [138] Kim DH, Han K, Gupta K, Kwon KW, Suh KY, Levchenko A. Mechanosensitivity of fibroblast cell shape and movement to anisotropic substratum topography gradients. *Biomaterials.* 2009;30:5433-44.
- [139] Jeon H, Hidai H, Hwang DJ, Healy KE, Grigoropoulos CP. The effect of micronscale anisotropic cross patterns on fibroblast migration. *Biomaterials.* 2010;31:4286-95.
- [140] Sarkar S, Dadhania M, Rourke P, Desai TA, Wong JY. Vascular tissue engineering: microtextured scaffold templates to control organization of vascular smooth muscle cells and extracellular matrix. *Acta biomaterialia.* 2005;1:93-100.
- [141] Dang JM, Leong KW. Myogenic induction of aligned mesenchymal stem cell sheets by culture on thermally responsive electrospun nanofibers. *Adv Mater.* 2007;19:2775-+.
- [142] Tsai WB, Lin JH. Modulation of morphology and functions of human hepatoblastoma cells by nano-grooved substrata. *Acta biomaterialia.* 2009;5:1442-54.

- [143] Wang HB, Mullins ME, Cregg JM, Hurtado A, Oudega M, Trombley MT, et al. Creation of highly aligned electrospun poly-L-lactic acid fibers for nerve regeneration applications. *J Neural Eng.* 2009;6.
- [144] Prodanov L, te Riet J, Lamers E, Domanski M, Luttge R, van Loon JJWA, et al. The interaction between nanoscale surface features and mechanical loading and its effect on osteoblast-like cells behavior. *Biomaterials.* 2010;31:7758-65.
- [145] Lamers E, Walboomers XF, Domanski M, te Riet J, van Delft FCMJM, Luttge R, et al. The influence of nanoscale grooved substrates on osteoblast behavior and extracellular matrix deposition. *Biomaterials.* 2010;31:3307-16.
- [146] Aubin H, Nichol JW, Hutson CB, Bae H, Sieminski AL, Cropek DM, et al. Directed 3D cell alignment and elongation in microengineered hydrogels. *Biomaterials.* 2010;31:6941-51.
- [147] Hoffman-Kim D, Mitchel JA, Bellamkonda RV. Topography, Cell Response, and Nerve Regeneration. *Annu Rev Biomed Eng.* 2010;12:203-31.
- [148] Ohara PT, Buck RC. Contact guidance in vitro. A light, transmission, and scanning electron microscopic study. *Experimental cell research.* 1979;121:235-49.
- [149] Yang JY, Ting YC, Lai JY, Liu HL, Fang HW, Tsai WB. Quantitative analysis of osteoblast-like cells (MG63) morphology on nanogrooved substrata with various groove and ridge dimensions. *J Biomed Mater Res A.* 2009;90A:629-40.
- [150] Fujita S, Ohshima M, Iwata H. Time-lapse observation of cell alignment on nanogrooved patterns. *J R Soc Interface.* 2009;6:S269-S77.
- [151] Fraser SA, Ting YH, Mallon KS, Wendt AE, Murphy CJ, Nealey PF. Sub-micron and nanoscale feature depth modulates alignment of stromal fibroblasts and corneal epithelial cells in serum-rich and serum-free media. *J Biomed Mater Res A.* 2008;86A:725-35.
- [152] Nisbet DR, Rodda AE, Horne MK, Forsythe JS, Finkelstein DI. Neurite infiltration and cellular response to electrospun polycaprolactone scaffolds implanted into the brain. *Biomaterials.* 2009;30:4573-80.
- [153] Teixeira AI, Abrams GA, Bertics PJ, Murphy CJ, Nealey PF. Epithelial contact guidance on well-defined micro- and nanostructured substrates. *J Cell Sci.* 2003;116:1881-92.
- [154] Liliensiek SJ, Wood JA, Yong JA, Auerbach R, Nealey PF, Murphy CJ. Modulation of human vascular endothelial cell behaviors by nanotopographic cues. *Biomaterials.* 2010;31:5418-26.
- [155] Thakar RG, Cheng Q, Patel S, Chu J, Nasir M, Liepmann D, et al. Cell-shape regulation of smooth muscle cell proliferation. *Biophysical journal.* 2009;96:3423-32.
- [156] Lu J, Rao MP, MacDonald NC, Khang D, Webster TJ. Improved endothelial cell adhesion and proliferation on patterned titanium surfaces with rationally designed, micrometer to nanometer features. *Acta biomaterialia.* 2008;4:192-201.

- [157] Kim HN, Jiao A, Hwang NS, Kim MS, Kang DH, Kim DH, et al. Nanotopography-guided tissue engineering and regenerative medicine. *Adv Drug Deliver Rev.* 2013;65:536-58.
- [158] Philip JT, Dahl KN. Nuclear mechanotransduction: Response of the lamina to extracellular stress with implications in aging. *J Biomech.* 2008;41:3164-70.
- [159] Dalby MJ, Yarwood SJ. Analysis of focal adhesions and cytoskeleton by custom microarray. *Methods Mol Biol.* 2007;370:121-34.
- [160] Tay CY, Koh CG, Tan NS, Leong DT, Tan LP. Mechanoregulation of stem cell fate via micro-/nano-scale manipulation for regenerative medicine. *Nanomedicine-Uk.* 2013;8:623-38.
- [161] Xie JW, Willerth SM, Li XR, Macewan MR, Rader A, Sakiyama-Elbert SE, et al. The differentiation of embryonic stem cells seeded on electrospun nanofibers into neural lineages. *Biomaterials.* 2009;30:354-62.
- [162] Li HQ, Wen F, Wong YS, Boey FYC, Subbu VS, Leong DT, et al. Direct laser machining-induced topographic pattern promotes up-regulation of myogenic markers in human mesenchymal stem cells. *Acta biomaterialia.* 2012;8:531-9.
- [163] Li H, Wong YS, Wen F, Ng KW, Ng GK, Venkatraman SS, et al. Human mesenchymal stem-cell behaviour on direct laser micropatterned electrospun scaffolds with hierarchical structures. *Macromolecular bioscience.* 2013;13:299-310.
- [164] Yang Y, Relan NK, Przywara DA, Schuger L. Embryonic mesenchymal cells share the potential for smooth muscle differentiation: myogenesis is controlled by the cell's shape. *Development.* 1999;126:3027-33.
- [165] Jana S, Zhang MQ. Fabrication of 3D aligned nanofibrous tubes by direct electrospinning. *Journal of Materials Chemistry B.* 2013;1:2575-81.
- [166] Baker BM, Mauck RL. The effect of nanofiber alignment on the maturation of engineered meniscus constructs. *Biomaterials.* 2007;28:1967-77.
- [167] Vert M, Li SM, Spenlehauer G, Guerin P. Bioresorbability and Biocompatibility of Aliphatic Polyesters. *J Mater Sci-Mater M.* 1992;3:432-46.
- [168] Kundu B, Rajkhowa R, Kundu SC, Wang XG. Silk fibroin biomaterials for tissue regenerations. *Adv Drug Deliver Rev.* 2013;65:457-70.
- [169] Tillman BW, Yazdani SK, Lee SJ, Geary RL, Atala A, Yoo JJ. The in vivo stability of electrospun polycaprolactone-collagen scaffolds in vascular reconstruction. *Biomaterials.* 2009;30:583-8.
- [170] Eglin D, Mortisen D, Alini M. Degradation of synthetic polymeric scaffolds for bone and cartilage tissue repairs. *Soft Matter.* 2009;5:938-47.
- [171] Li SM, Chen XH, Gross RA, McCarthy SP. Hydrolytic degradation of PCL/PEO copolymers in alkaline media. *J Mater Sci-Mater M.* 2000;11:227-33.

- [172] Meseguer-Duenas JM, Mas-Estelles J, Castilla-Cortazar I, Ivirico JLE, Vidaurre A. Alkaline degradation study of linear and network poly(epsilon-caprolactone). *J Mater Sci-Mater M*. 2011;22:11-8.
- [173] Theiler S, Teske M, Keul H, Sternberg K, Moller M. Synthesis, characterization and in vitro degradation of 3D-microstructured poly(epsilon-caprolactone) resins. *Polym Chem-Uk*. 2010;1:1215-25.
- [174] Chen DR, Bei JZ, Wang SG. Polycaprolactone microparticles and their biodegradation. *Polym Degrad Stabil*. 2000;67:455-9.
- [175] Castilla-Cortazar I, Mas-Estelles J, Meseguer-Duenas JM, Ivirico JLE, Mari B, Vidaurre A. Hydrolytic and enzymatic degradation of a poly(epsilon-caprolactone) network. *Polym Degrad Stabil*. 2012;97:1241-8.
- [176] Pektok E, Nottelet B, Tille JC, Gurny R, Kalangos A, Moeller M, et al. Degradation and Healing Characteristics of Small-Diameter Poly(epsilon-Caprolactone) Vascular Grafts in the Rat Systemic Arterial Circulation. *Circulation*. 2008;118:2563-70.
- [177] Pena J, Corrales T, Izquierdo-Barba I, Serrano MC, Portoles MT, Pagani R, et al. Alkaline-treated poly(epsilon-caprolactone) films: Degradation in the presence or absence of fibroblasts. *J Biomed Mater Res A*. 2006;76A:788-97.
- [178] Khatiwala VK, Shekhar N, Aggarwal S, Mandal UK. Biodegradation of Poly(epsilon-caprolactone) (PCL) Film by *Alcaligenes faecalis*. *J Polym Environ*. 2008;16:61-7.
- [179] Lu L, Peter SJ, Lyman MD, Lai HL, Leite SM, Tamada JA, et al. In vitro and in vivo degradation of porous poly(DL-lactic-co-glycolic acid) foams. *Biomaterials*. 2000;21:1837-45.
- [180] Bolgen N, Menciloglu YZ, Acatay K, Vargel I, Piskin E. In vitro and in vivo degradation of non-woven materials made of poly(epsilon-caprolactone) nanofibers prepared by electrospinning under different conditions. *J Biomat Sci-Polym E*. 2005;16:1537-55.
- [181] Lee SJ, Liu J, Oh SH, Soker S, Atala A, Yoo JJ. Development of a composite vascular scaffolding system that withstands physiological vascular conditions. *Biomaterials*. 2008;29:2891-8.
- [182] Lam CXF, Teoh SH, Huttmacher DW. Comparison of the degradation of polycaprolactone and polycaprolactone-(beta-tricalcium phosphate) scaffolds in alkaline medium. *Polym Int*. 2007;56:718-28.
- [183] Tsuji H, Ishida T, Fukuda N. Surface hydrophilicity and enzymatic hydrolyzability of biodegradable polyesters: 1. Effects of alkaline treatment. *Polym Int*. 2003;52:843-52.
- [184] Makadia HK, Siegel SJ. Poly Lactic-co-Glycolic Acid (PLGA) as Biodegradable Controlled Drug Delivery Carrier. *Polymers-Basel*. 2011;3:1377-97.

- [185] Cao Y, Mitchell G, Messina A, Price L, Thompson E, Penington A, et al. The influence of architecture on degradation and tissue ingrowth into three-dimensional poly(lactic-co-glycolic acid) scaffolds in vitro and in vivo. *Biomaterials*. 2006;27:2854-64.
- [186] Wu LB, Ding JD. Effects of porosity and pore size on in vitro degradation of three-dimensional porous poly(D,L-lactide-co-glycolide) scaffolds for tissue engineering. *J Biomed Mater Res A*. 2005;75A:767-77.
- [187] Sung HJ, Meredith C, Johnson C, Galis ZS. The effect of scaffold degradation rate on three-dimensional cell growth and angiogenesis. *Biomaterials*. 2004;25:5735-42.
- [188] Jeong SI, Kim BS, Kang SW, Kwon JH, Lee YM, Kim SH, et al. In vivo biocompatibility and degradation behavior of elastic poly(L-lactide-co-epsilon-caprolactone) scaffolds. *Biomaterials*. 2004;25:5939-46.
- [189] Kaushiva A, Turzhitsky VM, Backman V, Ameer GA. A biodegradable vascularizing membrane: A feasibility study. *Acta biomaterialia*. 2007;3:631-42.
- [190] Hashizume R, Hong Y, Takanari K, Fujimoto KL, Tobita K, Wagner WR. The effect of polymer degradation time on functional outcomes of temporary elastic patch support in ischemic cardiomyopathy. *Biomaterials*. 2013.
- [191] Goonoo N, Bhaw-Luximon A, Bowlin GL, Jhurry D. An assessment of biopolymer- and synthetic polymer-based scaffolds for bone and vascular tissue engineering. *Polym Int*. 2013;62:523-33.
- [192] Serrano MC, Chung EJ, Ameer GA. Advances and Applications of Biodegradable Elastomers in Regenerative Medicine. *Adv Funct Mater*. 2010;20:192-208.
- [193] Wu LB, Ding JD. In vitro degradation of three-dimensional porous poly(D,L-lactide-co-glycolide) scaffolds for tissue engineering. *Biomaterials*. 2004;25:5821-30.
- [194] Onuma Y, Serruys PW, Perkins LEL, Okamura T, Gonzalo N, Garcia-Garcia HM, et al. Intracoronary Optical Coherence Tomography and Histology at 1 Month and 2, 3, and 4 Years After Implantation of Everolimus-Eluting Bioresorbable Vascular Scaffolds in a Porcine Coronary Artery Model An Attempt to Decipher the Human Optical Coherence Tomography Images in the ABSORB Trial. *Circulation*. 2010;122:2288-300.
- [195] Gao J, Crapo P, Nerern R, Wang YD. Co-expression of elastin and collagen leads to highly compliant engineered blood vessels. *J Biomed Mater Res A*. 2008;85A:1120-8.
- [196] Fry WJ, Deweese MS, Kraft RO, Ernst CB. Importance of Porosity in Arterial Prostheses. *Arch Surg-Chicago*. 1964;88:836-42.
- [197] Doi K, Nakayama Y, Matsuda T. Novel compliant and tissue-permeable microporous polyurethane vascular prosthesis fabricated using an excimer laser ablation technique. *J Biomed Mater Res*. 1996;31:27-33.

- [198] Jun HW, West JL. Endothelialization of microporous YIGSR/PEG-modified polyurethaneurea. *Tissue engineering*. 2005;11:1133-40.
- [199] Mata A, Kim EJ, Boehm CA, Fleischman AJ, Muschler GF, Roy S. A three-dimensional scaffold with precise micro-architecture and surface micro-textures. *Biomaterials*. 2009;30:4610-7.
- [200] Bettinger CJ, Weinberg EJ, Kulig KM, Vacanti JP, Wang YD, Borenstein JT, et al. Three-dimensional microfluidic tissue-engineering scaffolds using a flexible biodegradable polymer. *Adv Mater*. 2006;18:165-+.
- [201] Safinia L, Wilson K, Mantalaris A, Bismarck A. Through-thickness plasma modification of biodegradable and nonbiodegradable porous polymer constructs. *J Biomed Mater Res A*. 2008;87A:632-42.
- [202] Yucel D, Kose GT, Hasirci V. Polyester based nerve guidance conduit design. *Biomaterials*. 2010;31:1596-603.
- [203] Aguilar CA, Lu Y, Mao S, Chen SC. Direct micro-patterning of biodegradable polymers using ultraviolet and femtosecond lasers. *Biomaterials*. 2005;26:7642-9.
- [204] Tiaw KS, Hong MH, Teoh SH. Precision laser micro-processing of polymers. *J Alloy Compd*. 2008;449:228-31.
- [205] Zacchi V, Soranzo C, Cortivo R, Radice M, Brun P, Abatangelo G. In vitro engineering of human skin-like tissue. *J Biomed Mater Res*. 1998;40:187-94.
- [206] Lootz D, Behrend D, Kramer S, Freier T, Haubold A, Benkiesser G, et al. Laser cutting: influence on morphological and physicochemical properties of polyhydroxybutyrate. *Biomaterials*. 2001;22:2447-52.
- [207] Khung YL, Barritt G, Voelcker NH. Using continuous porous silicon gradients to study the influence of surface topography on the behaviour of neuroblastoma cells. *Experimental cell research*. 2008;314:789-800.
- [208] Wang L, Murthy SK, Fowle WH, Barabino GA, Carrier RL. Influence of micro-well biomimetic topography on intestinal epithelial Caco-2 cell phenotype. *Biomaterials*. 2009;30:6825-34.
- [209] Gasiorowski JZ, Liliensiek SJ, Russell P, Stephan DA, Nealey PF, Murphy CJ. Alterations in gene expression of human vascular endothelial cells associated with nanotopographic cues. *Biomaterials*. 2010;31:8882-8.
- [210] Salem AK, Stevens R, Pearson RG, Davies MC, Tendler SJB, Roberts CJ, et al. Interactions of 3T3 fibroblasts and endothelial cells with defined pore features. *J Biomed Mater Res*. 2002;61:212-7.
- [211] Zeltinger J, Sherwood JK, Graham DA, Mueller R, Griffith LG. Effect of pore size and void fraction on cellular adhesion, proliferation, and matrix deposition. *Tissue engineering*. 2001;7:557-72.

- [212] Karuri NW, Porri TJ, Albrecht RM, Murphy CJ, Nealey PF. Nano- and microscale holes modulate cell-substrate adhesion, cytoskeletal organization, and β 1 integrin localization in SV40 human corneal epithelial cells. *Ieee T Nanobiosci.* 2006;5:273-80.
- [213] Dalby MJ, Gadegaard N, Tare R, Andar A, Riehle MO, Herzyk P, et al. The control of human mesenchymal cell differentiation using nanoscale symmetry and disorder. *Nat Mater.* 2007;6:997-1003.
- [214] O'Brien FJ, Harley BA, Yannas IV, Gibson LJ. The effect of pore size on cell adhesion in collagen-GAG scaffolds. *Biomaterials.* 2005;26:433-41.
- [215] Hu JA, Sun XA, Ma HY, Xie CQ, Chen YE, Ma PX. Porous nanofibrous PLLA scaffolds for vascular tissue engineering. *Biomaterials.* 2010;31:7971-7.
- [216] Nakayama Y, Nishi S, Ueda-Ishibashi H, Matsuda T. Fabrication of micropored elastomeric film-covered stents and acute-phase performances. *J Biomed Mater Res A.* 2003;64A:52-61.
- [217] Lutolf MP, Gilbert PM, Blau HM. Designing materials to direct stem-cell fate. *Nature.* 2009;462:433-41.
- [218] Beachley V, Wen X. Polymer nanofibrous structures: Fabrication, biofunctionalization, and cell interactions. *Progress in Polymer Science.* 2010;35:868-92.
- [219] Prodanov L, te Riet J, Lamers E, Domanski M, Luttge R, van Loon JJ, et al. The interaction between nanoscale surface features and mechanical loading and its effect on osteoblast-like cells behavior. *Biomaterials.* 2010;31:7758-65.
- [220] Papadaki M, Bursac N, Langer R, Merok J, Vunjak-Novakovic G, Freed LE. Tissue engineering of functional cardiac muscle: molecular, structural, and electrophysiological studies. *Am J Physiol-Heart C.* 2001;280:H168-H78.
- [221] Krizmanich WJ, Lee RM. Correlation of vascular smooth muscle cell morphology observed by scanning electron microscopy with transmission electron microscopy. *Exp Mol Pathol.* 1997;64:157-72.
- [222] Chong MSK, Chan J, Choolani M, Lee C-N, Teoh S-H. Development of cell-selective films for layered co-culturing of vascular progenitor cells. *Biomaterials.* 2009;30:2241-51.
- [223] Jin G, Prabhakaran MP, Ramakrishna S. Stem cell differentiation to epidermal lineages on electrospun nanofibrous substrates for skin tissue engineering. *Acta Biomater.* 2011;7:3113-22.
- [224] Kilian KA, Bugarija B, Lahn BT, Mrksich M. Geometric cues for directing the differentiation of mesenchymal stem cells. *Proceedings of the National Academy of Sciences of the United States of America.* 2010;107:4872-7.

- [225] Nuzzo RG. The future of electronics manufacturing is revealed in the fine print. *Proceedings of the National Academy of Sciences of the United States of America*. 2001;98:4827-9.
- [226] Xie J, MacEwan MR, Li X, Sakiyama-Elbert SE, Xia Y. Neurite outgrowth on nanofiber scaffolds with different orders, structures, and surface properties. *Acs Nano*. 2009;3:1151-9.
- [227] Sarkar S, Lee GY, Wong JY, Desai TA. Development and characterization of a porous micro-patterned scaffold for vascular tissue engineering applications. *Biomaterials*. 2006;27:4775-82.
- [228] Tiaw KS, Teoh SH, Chen R, Hong MH. Processing methods of ultrathin poly(epsilon-caprolactone) films for tissue engineering applications. *Biomacromolecules*. 2007;8:807-16.
- [229] Zhang ZY, Teoh SH, Chong MS, Schantz JT, Fisk NM, Choolani MA, et al. Superior osteogenic capacity for bone tissue engineering of fetal compared with perinatal and adult mesenchymal stem cells. *Stem Cells*. 2009;27:126-37.
- [230] Tocce EJ, Smirnov VK, Kibalov DS, Liliensiek SJ, Murphy CJ, Nealey PF. The ability of corneal epithelial cells to recognize high aspect ratio nanostructures. *Biomaterials*. 2010;31:4064-72.
- [231] Serrano M-C, Pagani R, Vallet-Regí M, Peña J, Comas J-V, Portolés M-T. Nitric oxide production by endothelial cells derived from blood progenitors cultured on NaOH-treated polycaprolactone films: A biofunctionality study. *Acta Biomaterialia*. 2009;5:2045-53.
- [232] Kim SH, Ha HJ, Ko YK, Yoon SJ, Rhee JM, Kim MS, et al. Correlation of proliferation, morphology and biological responses of fibroblasts on LDPE with different surface wettability. *J Biomater Sci Polym Ed*. 2007;18:609-22.
- [233] Giraud MN, Armbruster C, Carrel T, Tevæarai HT. Current state of the art in myocardial tissue engineering. *Tissue Engineering*. 2007;13:1825-36.
- [234] Chew SY, Mi R, Hoke A, Leong KW. The effect of the alignment of electrospun fibrous scaffolds on Schwann cell maturation. *Biomaterials*. 2008;29:653-61.
- [235] Greener J, Tsou AH, Blanton TN. Physical and microstructural effects of heat setting in polyester films. *Polym Eng Sci*. 1999;39:2403-18.
- [236] Tokiwa Y, Calabria BP, Ugwu CU, Aiba S. Biodegradability of Plastics. *Int J Mol Sci*. 2009;10:3722-42.
- [237] Tschoegl NW, Knauss WG, Emri I. Poisson's ratio in linear viscoelasticity - A critical review. *Mech Time-Depend Mat*. 2002;6:3-51.
- [238] Sweeney J, Ward IM. The Modeling of Multiaxial Necking in Polypropylene Using a Sliplink Cross-Link Theory. *J Rheol*. 1995;39:861-72.

- [239] Drevelle O, Bergeron E, Senta H, Lauzon MA, Roux S, Grenier G, et al. Effect of functionalized polycaprolactone on the behaviour of murine preosteoblasts. *Biomaterials*. 2010;31:6468-76.
- [240] Wolansky G, Marmur A. Apparent contact angles on rough surfaces: the Wenzel equation revisited. *Colloid Surface A*. 1999;156:381-8.
- [241] Kim GH. Electrospun PCL nanofibers with anisotropic mechanical properties as a biomedical scaffold. *Biomedical Materials*. 2008;3.
- [242] Zhang ZY, Teoh SH, Hui JH, Fisk NM, Choolani M, Chan JK. The potential of human fetal mesenchymal stem cells for off-the-shelf bone tissue engineering application. *Biomaterials*. 2012;33:2656-72.
- [243] Lim JY, Donahue HJ. Cell sensing and response to micro- and nanostructured surfaces produced by chemical and topographic patterning. *Tissue Engineering*. 2007;13:1879-91.
- [244] Tsai WB, Ting YC, Yang JY, Lai JY, Liu HL. Fibronectin modulates the morphology of osteoblast-like cells (MG-63) on nano-grooved substrates. *J Mater Sci Mater Med*. 2009;20:1367-78.
- [245] Williams C, Xie AW, Yamato M, Okano T, Wong JY. Stacking of aligned cell sheets for layer-by-layer control of complex tissue structure. *Biomaterials*. 2011;32:5625-32.
- [246] Li HQ, Wen F, Wong YS, Boey FYC, Subbu VS, Leong DT, et al. Direct laser machining-induced topographic pattern promotes up-regulation of myogenic markers in human mesenchymal stem cells. *Acta Biomaterialia*. 2012;8:531-9.
- [247] Gomez N, Chen SC, Schmidt CE. Polarization of hippocampal neurons with competitive surface stimuli: contact guidance cues are preferred over chemical ligands. *Journal of The Royal Society Interface*. 2007;4:223-33.
- [248] Tay CY, Yu H, Pal M, Leong WS, Tan NS, Ng KW, et al. Micropatterned matrix directs differentiation of human mesenchymal stem cells towards myocardial lineage. *Experimental cell research*. 2010;316:1159-68.
- [249] Wang C, Yin S, Cen L, Liu QH, Liu W, Cao YL, et al. Differentiation of Adipose-Derived Stem Cells into Contractile Smooth Muscle Cells Induced by Transforming Growth Factor-beta 1 and Bone Morphogenetic Protein-4. *Tissue Eng Pt A*. 2010;16:1201-13.
- [250] Jana S, Zhang M. Fabrication of 3D aligned nanofibrous tubes by direct electrospinning. *Journal of Materials Chemistry B*. 2013;1:2575.
- [251] Wang ZY, Teo EY, Chong MS, Zhang QY, Lim J, Zhang ZY, et al. Biomimetic Three-Dimensional Anisotropic Geometries by Uniaxial Stretch of Poly(varepsilon-Caprolactone) Films for Mesenchymal Stem Cell Proliferation, Alignment, and Myogenic Differentiation. *Tissue engineering Part C, Methods*. 2013.

- [252] Chan-Park MB, Shen JY, Cao Y, Xiong Y, Liu YX, Rayatpisheh S, et al. Biomimetic control of vascular smooth muscle cell morphology and phenotype for functional tissue-engineered small-diameter blood vessels (vol 88a, pg 1104, 2009). *J Biomed Mater Res A*. 2009;91A:629-34.
- [253] Zhang ZY, Teoh SH, Hui JHP, Fisk NM, Choolani M, Chan JKY. The potential of human fetal mesenchymal stem cells for off-the-shelf bone tissue engineering application. *Biomaterials*. 2012;33:2656-72.
- [254] Konig G, McAllister TN, Dusserre N, Garrido SA, Iyican C, Marini A, et al. Mechanical properties of completely autologous human tissue engineered blood vessels compared to human saphenous vein and mammary artery. *Biomaterials*. 2009;30:1542-50.
- [255] Curtis A, Wilkinson C. Topographical control of cells. *Biomaterials*. 1997;18:1573-83.
- [256] Lim JY, Donahue HJ. Cell sensing and response to micro- and nanostructured surfaces produced by chemical and topographic patterning. *Tissue engineering*. 2007;13:1879-91.
- [257] Chan-Park MB, Shen JY, Cao Y, Xiong Y, Liu YX, Rayatpisheh S, et al. Biomimetic control of vascular smooth muscle cell morphology and phenotype for functional tissue-engineered small-diameter blood vessels. *J Biomed Mater Res A*. 2009;88A:1104-21.
- [258] McNamara LE, McMurray RJ, Biggs MJ, Kantawong F, Oreffo RO, Dalby MJ. Nanotopographical control of stem cell differentiation. *Journal of tissue engineering*. 2010;2010:120623.
- [259] Pek YS, Wan ACA, Ying JY. The effect of matrix stiffness on mesenchymal stem cell differentiation in a 3D thixotropic gel. *Biomaterials*. 2010;31:385-91.
- [260] Sarkar S, Schmitz-Rixen T, Hamilton G, Seifalian AM. Achieving the ideal properties for vascular bypass grafts using a tissue engineered approach: a review. *Med Biol Eng Comput*. 2007;45:327-36.
- [261] Takahashi H, Nakayama M, Shimizu T, Yamato M, Okano T. Anisotropic cell sheets for constructing three-dimensional tissue with well-organized cell orientation. *Biomaterials*. 2011;32:8830-8.
- [262] Lee IC, Lee YT, Yu BY, Lai JY, Young TH. The behavior of mesenchymal Stem cells on micropatterned PLLA membranes. *J Biomed Mater Res A*. 2009;91A:929-38.
- [263] Pena J, Corrales T, Izquierdo-Barba I, Doadrio AL, Vallet-Regi M. Long term degradation of poly(epsilon-caprolactone) films in biologically related fluids. *Polym Degrad Stabil*. 2006;91:1424-32.
- [264] Hoglund A, Hakkarainen M, Albertsson AC. Degradation profile of poly(epsilon-caprolactone) - the influence of macroscopic and macromolecular biomaterial design. *J Macromol Sci A*. 2007;44:1041-6.

- [265] Nguyen VN, Vauthier C, Huang N, Grossiord JL, Moine L, Agnely F. Degradation of hydrolyzable hydrogel microspheres. *Soft Matter*. 2013;9:1929-36.
- [266] Geng Y, Discher DE. Hydrolytic degradation of poly(ethylene oxide)-block-polycaprolactone worm micelles. *J Am Chem Soc*. 2005;127:12780-1.
- [267] Kim SH, Ha HJ, Ko YK, Yoon SJ, Rhee JM, Kim MS, et al. Correlation of proliferation, morphology and biological responses of fibroblasts on LDPE with different surface wettability. *J Biomat Sci-Polym E*. 2007;18:609-22.
- [268] McGonigle EA, Liggat JJ, Pethrick RA, Jenkins SD, Daly JH, Hayward D. Permeability of N₂, Ar, He, O₂ and CO₂ through biaxially oriented polyester films - dependence on free volume. *Polymer*. 2001;42:2413-26.
- [269] Saha SK, Tsuji H. Effects of rapid crystallization on hydrolytic degradation and mechanical properties of poly(L-lactide-co-epsilon-caprolactone). *React Funct Polym*. 2006;66:1362-72.
- [270] Cheneler D, Bowen J. Degradation of polymer films. *Soft Matter*. 2013;9:344-58.
- [271] Li X, Koller G, Huang J, Di Silvio L, Renton T, Esat M, et al. A novel jet-based nano-hydroxyapatite patterning technique for osteoblast guidance. *J R Soc Interface*. 2010;7:189-97.
- [272] Li X, Huang J, Edirisinghe MJ. Novel patterning of nano-bioceramics: template-assisted electrohydrodynamic atomization spraying. *J R Soc Interface*. 2008;5:253-7.
- [273] Li XA, Huang J, Edirisinghe M, Bonfield W. An electrically driven jetting technique for diverse high-resolution surface structures of nanometre hydroxyapatite crystals. *Colloid Surface B*. 2011;82:562-70.
- [274] Yang SF, Leong KF, Du ZH, Chua CK. The design of scaffolds for use in tissue engineering. Part 1. Traditional factors. *Tissue engineering*. 2001;7:679-89.
- [275] Hollister SJ. Porous scaffold design for tissue engineering. *Nat Mater*. 2005;4:518-24.
- [276] Lee M, Wu BM, Dunn JC. Effect of scaffold architecture and pore size on smooth muscle cell growth. *J Biomed Mater Res A*. 2008;87:1010-6.
- [277] Karuri NW, Liliensiek S, Teixeira AI, Abrams G, Campbell S, Nealey PF, et al. Biological length scale topography enhances cell-substratum adhesion of human corneal epithelial cells. *J Cell Sci*. 2004;117:3153-64.
- [278] Tay CY, Irvine SA, Boey FYC, Tan LP, Venkatraman S. Micro-/Nano-engineered Cellular Responses for Soft Tissue Engineering and Biomedical Applications. *Small*. 2011;7:1361-78.
- [279] Gamaly EG, Rode AV, Tikhonchuk VT, Luther-Davies B. Electrostatic mechanism of ablation by femtosecond lasers. *Appl Surf Sci*. 2002;197:699-704.

References

[280] Serafetinides AA, Makropoulou MI, Skordoulis CD, Kar AK. Ultra-short pulsed laser ablation of polymers. *Appl Surf Sci.* 2001;180:42-56.

[281] Htay HS, Teoh, S. H. , Hutmacher, D. W. Development of a novel perforated ultra thin poly(e-caprolactone) membrane for epidermal skin tissue engineering. *Proceedings of ICBME.* Singapore 2002.

[282] Flemming RG, Murphy CJ, Abrams GA, Goodman SL, Nealey PF. Effects of synthetic micro- and nano-structured surfaces on cell behavior. *Biomaterials.* 1999;20:573-88.

Appendices - List of Related Publications

INTERNATIONAL JOURNAL PUBLICATIONS

1. ZY Wang, J Lim, YS Ho, M Chong, QY Zhang, M Chong, M Tang, MH Hong, J Chan, SH Teoh, ES Thian. Biomimetic Three-Dimensional Anisotropic Geometries by Uniaxial Stretching of Poly(ϵ -caprolactone) Films: Degradation and Mesenchymal Stem Cell Responses. **Journal of Biomedical Materials Research Part A**. (DOI: 10.1002/jbm.a.34899)
2. ZY Wang, E Teo, M Chong, QY Zhang, J Lim, ZY Zhang, MH Hong, ES Thian, J Chan, SH Teoh. Biomimetic Three-Dimensional Anisotropic Geometries by Uniaxial Stretch of Poly(ϵ -Caprolactone) Films for Mesenchymal Stem Cell Proliferation, Alignment, and Myogenic Differentiation. **Tissue Engineering Part C: Methods**. 19 (7), 538-549. (*Featured Press, Press News of MARY ANN LIEBERT, INC., Top 1 of the Most Read Articles*)

INTERNATIONAL CONFERENCE PUBLICATIONS

1. ZY Wang, J Lim, QY Zhang, E Teo, F Wen, J Chan, MH Hong, SH Teoh. Responses of Human Fetal Mesenchymal Stem Cells to Various Poly(ϵ -caprolactone) Films: A Comparison Study. **Defense Science Research Conference and Expo (DSR)**. 2011, 1-5.
2. J Lim, ZY Wang, QY Zhang, E Teo, F Wen, SH Teoh. Blending of Poly(3-hydroxybutyrate-co-3-hydroxyhexanoate) and Polycaprolactone: Characterization and Degradation Studies. **Defense Science Research Conference and Expo (DSR)**. 2011, 1-5.
3. QY Zhang, ZY Wang, J Lim, J Li, F Wen, SH Teoh. Tailoring of Poly(vinyl alcohol) Hydrogels Properties by Incorporation of Crosslinked Acrylic Acid. **Defense Science Research Conference and Expo (DSR)**. 2011, 1-5.

INTERNATIONAL CONFERENCES & AWARDS

Oral Presentations

1. ZY Wang, J Lim, QY Zhang, M Chong, E Teo, ZY Zhang, MH Hong, J Chan, SH Teoh. Direct Cellular Contact and Alignment of Human Fetal Mesenchymal Stem Cells and Umbilical Vein Endothelial Cells Based on Micro-patterned Porous Poly(ϵ -caprolactone) Film for Tissue Engineering Applications. **9th World Biomaterials Congress**. 1-6 June 2012, China.
2. ZY Wang, J Lim, QY Zhang, E Teo, F Wen, J Chan, MH Hong, SH Teoh. Responses of Human Fetal Mesenchymal Stem Cells to Various Poly(ϵ -caprolactone) Films: A Comparison Study. **Defense Science Research Conference and Expo (DSR)**. 3-5 August 2011, Singapore.
3. QY Zhang, ZY Wang, SH Teoh, J Li, L Ren, ES Thian. Synthesis of Nitric-Oxide-Releasing S-nitrosothiol-modified Gelatin-Siloxane Nanoparticles. **6th East Asian Pacific Student Workshop on Nano-Biomedical Engineering**. 23-24 March 2013, Singapore.
4. QY Zhang, ZY Wang, J Lim, E Teo, L Ren, CN Lee, J Li, ES Thian, SH Teoh. Nitric-Oxide-Releasing System Based on Gelatin-Siloxane Nanoparticles for Cardiovascular Applications. **9th World Biomaterials Congress**. 1-6 June 2012, China.
5. J Lim, ZY Wang, QY Zhang, E Teo, F Wen, SH Teoh. Blending of Poly(3-hydroxybutyrate-co-3-hydroxyhexanoate) and Polycaprolactone: Characterization and Degradation Studies. **Defense Science Research Conference and Expo (DSR)**. 3-5 August 2011, Singapore.
6. QY Zhang, ZY Wang, J Lim, J Li, F Wen, SH Teoh. Tailoring of Poly(vinyl alcohol) Hydrogels Properties by Incorporation of Crosslinked Acrylic Acid. **Defense Science Research Conference and Expo (DSR)**. 3-5 August 2011, Singapore.

Poster Presentations

1. ZY Wang, QY Zhang, J Lim, E Teo, MH Hong, J Chan, ES Thian, SH Teoh. Bioresorbable 3D Micro-Topographical Structures for Vascular Cellular Pattern and Differentiation Control. **International Conference of Young Researchers on Advanced Materials**. 1-5 July 2012, Singapore.
2. ZY Wang, YS Ho, J Lim, QY Zhang, MH Hong, JKY Chan, SH Teoh. Highly Orientated 3D Micro-Topographical Structures for Bone Tissue Engineering Applications: A Degradation Study. **9th World Biomaterials Congress**. 1-6 June 2012, China.
3. QY Zhang, FSH Goh, ZY Wang, J Lim, E Teo, J Li, ES Thian, SH Teoh. Properties of Physical Crosslinked Polyvinyl Alcohol Hydrogel for Controlled Release of Nitric-Oxide-Releasing Nanoparticles. **1st International Conference for Young Researchers in Advanced Materials**. 1-5 July 2012, Singapore.

4. QY Zhang, FSH Goh, J Lim, ZY Wang, ES Thian, J Li, SH Teoh. Physical Properties of Freeze-Thawed Polyvinyl Alcohol Hydrogel for Cartilage Tissue Engineering Applications. **9th World Biomaterials Congress**. 1-6 June 2012, China
5. E Teo, J Lim, ZY Wang, J Chan, SH Teoh. Multi-Layered Aligned Cell Sheet Construct with Micro Topographical Cues. **Annual Tissue Engineering and Regenerative Medicine International Society-Asia Pacific Region (TERMIS-AP)**. 5-8 September 2012, Austria.

Awards

1. Best Poster Award. **9th World Biomaterials Congress (9th WBC)**. 1-6 June 2012; Chendu, China.